

https://dspace.org/

Fluxon pinning and geometrical effects in a type 2 superconductor

Doyle, Terence Brian

2015-03-05
http://hdl.handle.net/10539/17192

Downloaded from a DSpace repository. https://dspace.org/

FLUXON PINNING AND GEOMETRICAL EFFECTS IN A TYPE II SUPERCONDUCTOR

Terence Brian Doyle

A Thesis submitted to the Faculty of Science,

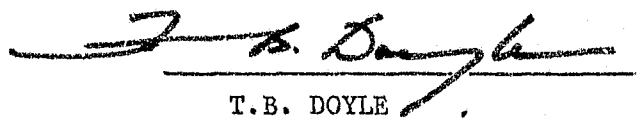
University of the Witwatersrand, Johannesburg,

for the degree of Doctor of Philosophy.

Johannesburg, 1975.

DECLARATION

I declare that this thesis is my own work, that no part of it has been or will be submitted for a degree at any other university and that no information in it has been obtained while I have been employed by, or working under the aegis of, any person or organisation other than this University.



T.B. DOYLE

ACKNOWLEDGEMENTS

The author wishes to thank his supervisor Professor F.R.N. Nabarro for his interest, criticism and stimulating discussion during the preparation of this thesis.

Sincere thanks are also due to Professor R. Labusch for considerable theoretical assistance with the geometry problem; Mr J.L. Crawford for assistance with computing; Mr D.L. James for assistance with electronics; Mr R.P. Badenhorst for assaying the specimens for hydrogen content; Professor F.R.L. Schöning, Dr A.G. Every, Dr A.T. Quintanilha, Dr A. Ball, Dr D.S. McLachlan, Professor H.J. Fink, Dr E.J.H. Wessels, Dr M.J. Witcomb, Dr I. Joffe and numerous other colleagues and friends for discussion, advice and encouragement; Mrs K.M. Peach for most of the figures; Mrs F.R. Higgins for a great job of typing under trying conditions; Miss A. Strauss for the photographs; and Mr R. Nel, Mr W.J. Watts and the workshop staff for construction of much of the apparatus.

The author also wishes to thank the Council for Scientific and Industrial Research and the University of the Witwatersrand for supporting this work and, in particular, Professor F.R.N. Nabarro, Professor J.H.N. Loubser and Professor J.W. Brommert for their general interest and for supporting an application for an appointment as Research Fellow during the early stages of this work.

Finally the author is deeply indebted to his wife and children for their encouragement and forbearance during the course of this work and to his parents for their continuing interest and encouragement.

ABSTRACT

The fluxon pinning behaviour in lightly deformed niobium single crystal specimens is investigated in order to identify (i) the particular features of the dislocation structure which are effective as pinning sites and (ii) the predominant mechanism of interaction between the fluxon lattice and the pinning site. For this purpose 'parent' crystals were deformed in uniaxial compression along [110] to produce predominantly edge dislocation debris along $[1\bar{1}0]$ in the (110) planes. Disc specimens (axial orientation [110]) and small square sectioned rectangular specimens (long axis along $[1\bar{1}0]$ and [001]) were cut from the deformed parent specimens. (During cutting and polishing of these specimens hydrogen is absorbed to a concentration of about 50 ppm-atomic.) From magnetization measurements made on these specimens, after various sub-room temperature ageing procedures, the bulk pinning force density is obtained as a function of the deformation parameters, the configurational distribution of the interstitial hydrogen and the local induction and temperature in the specimen. The results of the experiments show the existance of two distinct classes of behaviour. In the first class, which occurs in all the specimens, the pinning sites are identified with small regions of tangled dislocation. At any particular value of the local induction B only those regions which have dimensions (2R), normal to $\bar{B}$, in a narrow range centered at $2R \simeq 0.7a_o$, where a_o is the fluxon lattice parameter, are effective. These sites apparently pin by the so-called $\delta\kappa$ mechanism if they consist of tangled edge dislocation segments and by the so-called second-order elastic mechanism if the dislocations are of screw type aligned normal to $\bar{B}$. A detailed formulation of the

interaction force due to the $\delta\kappa$ mechanism for these sites and use of the point force, dilute-limit lattice approximation summation method of Labusch (1969b) makes predictions for the bulk pinning force density which are in excellent qualitative agreement with experiment in all respects. In the second class, which occurs only where the fluxons are parallel to the edge dislocations and the dislocations are sufficiently dressed with Cottrell atmospheres of interstitial hydrogen (Cottrell, 1948), the pinning sites are identified with straight segments of Cottrell atmosphere. A model is formulated which is based on the postulate of Campbell and Evetts (1972) that fluxon lattice dislocations may provide sufficient plasticity in the fluxon lattice to allow for independent fluxon pinning and hence the so-called synchronous pinning mechanism. The $\delta\kappa$ interaction between the Cottrell atmosphere sites and the fluxon lattice is shown to provide some of the required conditions for this mechanism and the final predictions of the model are in good qualitative agreement with experiment, particularly in respect of the lack of dependence on the extent of deformation in lightly deformed specimens. This is a consequence of the fact that the pinning is due almost entirely to the Cottrell atmospheres and depends linearly on the concentration of the hydrogen in the atmospheres which in turn is inversely proportional to the edge dislocation density. As expected ageing of the specimen at temperatures near 90K, where the mobility of the interstitial hydrogen is significant but the solubility in solid solution is very small, leads to precipitation of the hydrogen in the Cottrell atmospheres into the dislocation cores and consequent disappearance of this class of behaviour. The model allows for the determination, from isochronal ageing experiments, of the diffusion coefficient D for hydrogen in niobium at low temperatures. At 90K the determined value is

$D(90K) \simeq 0.9 \times 10^{-9}$ cm^{-2} sec. which agrees favourably with expectation.

Various anomalies and small deviations of the experimental results from the prediction of the above models are discussed. In particular the so-called 'peak effect' which occurs predominantly in the specimens containing hydrogen in solid solutions is found to be in good agreement, in a self consistent manner for both of the above classes of behaviour, with the Pippard model (see Campbell and Evetts, 1972).

In a separate series of experiments on undeformed disc shaped specimens of various axial ratios, in transverse applied magnetic field, a previously unsuspected geometry effect is investigated. This effect is manifest by a delay in the penetration of fluxons into the interior of the specimens to an applied field H_o which is larger than the value predicted for the inscribed spheroid and by non-equilibrium behaviour for $H_o \leq H_{c1}$ where H_{c1} is the field for initial penetration in an infinitely long specimen. A model for this behaviour is formulated by setting up the boundary conditions for the superconducting specimen explicitly and then determining the position dependent thermodynamic field $H_e(\underline{r})$ in the specimen. $H_e(\underline{r})$ is found, as expected, to be a decreasing function of the radial distance r from the axis of the disc and consequently fluxons, after entering the specimen at its perimeter, move rapidly and dissipatively to the middle of the disc where they form a 'pool' which grows in radius with increasing H_o until $H_o = H_{c1}$ when the pool fills the disc. The model makes an accurate prediction for the field of initial fluxon penetration $H_o = H_{c1}^*$ as a function of the axial ratio for disc shaped specimens and also predicts, in agreement with experiment, equilibrium behaviour, for suitable 'barrelled' specimens, for all H_o decreasing.

Non-equilibrium behaviour occurs when the pool does not completely fill the specimen.

Finally, the pinning and deformation behaviour in disc shaped specimens, with their axes collinear with the <111> direction, which are 'punched' to produce a narrow annular region of deformation, are investigated. The deformation behaviour is of particular interest since it convincingly demonstrates the asymmetry of cross-slip behaviour on the {211} planes in B.C.C. niobium (Ball and Doyle, 1974).

CONTENTS PAGE

1. INTRODUCTION 1

2. APPARATUS AND EXPERIMENTAL METHOD 14
   - 2.1 Introduction 14
   - 2.2 Description of the apparatus 17
     - 2.2.1 The magnetometer 17
     - 2.2.2 Temperature measurement and control .. 28
     - 2.2.3 The superconducting solenoid magnet .. 34
     - 2.2.4 Field regulation and measurement . .. 39
     - 2.2.5 The magnetometer cryostat 39
     - 2.2.6 Resistivity measurement 41
   - 2.3 System layout 45
   - 2.4 Modus operandi 47

3. THEORY OF FLUXON PINNING 51
   - 3.1 Introduction 51
   - 3.2 The basic interaction mechanisms 54
     - 3.2.1 The $\delta\kappa$ basic interaction 59
     - 3.2.2 The stress dependent (elastic) basic interaction 70
       - (a) The first-order interaction . .. 70
       - (b) The second-order interaction .. 77
   - 3.3 The summation problem 82
     - 3.3.1 The dilute limit 83
     - 3.3.2 The concentrated limit 89
   - 3.4 Conclusions 97

4. THE INFLUENCE OF HYDROGEN ON THE BULK SUPERCONDUCTING PROPERTIES OF NIOBIUM 98
   - 4.1 Introduction 98
   - 4.2 The phase diagram 101
   - 4.3 Low temperature diffusion 103
   - 4.4 Interstitial atmospheres on dislocations . .. 107
   - 4.5 The effect of interstitial solute on ρ_N, κ, T_c and H_c 111

CONTENTS

		PAGE
5.	THE FLUXON-DISLOCATION INTERACTION IN NIOBIUM	115
	5.1 Introduction	115
	5.2 Experimental	118
	5.2.1 Specimen preparation	118
	5.2.2 Deformation and dislocation configuration	122
	5.2.3 The magnetization measurements	123
	5.3 Experimental results	126
	5.4 Theoretical considerations	165
	5.4.1 The basic pinning sites	165
	5.4.2 The detailed low temperature behaviour of the interstitial hydrogen	175
	5.4.3 Summary	178
	5.5 Models for the bulk pinning force density and comparison with experiment	179
	5.5.1 Introduction	179
	5.5.2 Class I behaviour	179
	(a) The multiple dislocation site	179
	(b) The summation problem	181
	5.5.3 Class II behaviour	196
	(a) The Cottrell atmosphere site	196
	(b) The summation problem	197
	5.5.4 Anomalous behaviour	212
	5.5.5 Summary and conclusions	221
6	THE MACROSCOPIC MAGNETIZATION BEHAVIOUR OF CYLINDERS OF IDEAL TYPE II SUPERCONDUCTORS	225
	6.1 Introduction	225
	6.2	
	6.2.1 Experimental	230
	6.2.2 Experimental results	231
	6.3 Theory	244
	6.3.1 Equilibrium magnetization behaviour for a type II superconducting spheroidal specimen	244
	6.3.2 Macroscopic equations for the description of non-reversible superconductors of arbitrary shape	248
	6.3.3 Calculation of the field $H_e(r)$ in a cylindrical specimen	250

CONTENTS PAGE

6.3.4 Calculation of the reduced field $h^* = H^*_{c1}/H_{c1}$ for initial fluxon penetration into a cylindrical specimen .. 258

6.3.5 Magnetization behaviour for a type II superconducting cylinder in a longitudinal applied field 262

6.4 Discussion and comparison with experiment . .. 269

6.5 Conclusions 282

7. FLUXON PINNING IN DEFORMED DISC-SHAPED NIOBIUM SINGLE CRYSTAL SPECIMENS 284

7.1 Introduction 284

7.2 Experimental 285

7.2.1 Specimen preparation and deformation .. 285

7.2.2 Magnetization measurements 287

7.2.3 Experimental results 287

7.3 Theory 291

7.4 Determination of the bulk pinning force density $P_v(B,T)$ from the experimental results . 295

7.5 Discussion and conclusions 297

APPENDICES

A1(a) The Ginzburg-Landau expression for the free energy .. 302

A1(b) The relationship between the stress tensor in cartesian and cylindrical coordinates 303

A1(c) The second-order elastic interaction between the fluxon lattice and a perpendicular screw dislocation 304

A1(d) The elastic properties of the fluxon lattice 307

A1(e) Analysis of the experimental magnetization curves for the determination of $P_v(B,T)$. 311

A1(f) The magnetic moment of a fluxon 317

A1(g) Proof of an identity.. 319

A1(h) An approximate calculation of the interaction force on the fluxon lattice as a function of the dimensions of a spherical or cylindrical region of uniform density 320

CONTENTS PAGE

A2 THE MAGNETOMETER.. 325
A2.1 The detection coils 325
A2.2 The vibrating capacitor system 329
A2.3 The magnetometer circuit 330
A2.4 Magnetometer set-up procedure 334
A2.5 Specimen rods and holder stages 337

A3 TEMPERATURE REGULATION 339
A3.1 A.C. bridge temperature regulator 339
A3.2 Thermocouple temperature regulator 343

A4 TEMPERATURE SENSORS AND MEASUREMENT 344
A4.1 Carbon resistor 345
A4.2 Gold-iron chromel thermocouple 345
A4.3 Germanium resistance thermometer 345

A5 SUPERCONDUCTING MAGNET AND ANCILLARY APPARATUS 352
A5.1 Coil design 352
A5.2 NMR calibration of the magnet 356
A5.3 Hall probe and ancillary apparatus 358

A6 CONTINUOUS READING DEPTH GAUGE 363

A7 RESISTIVITY MEASUREMENT 366

A8 COMPUTER PROGRAMS 370

A9 A NEW EXPERIMENT TO STUDY THE DEFORMATION OF BODY-CENTRED CUBIC CRYSTALS (Ball and Doyle, 1974). 379

REFERENCES 387

LIST OF FIGURES

		PAGE
2.1	The magnetometer; showing the electro-mechanical transducer, reference capacitor, detection coils and the temperature controlled 'calorimeter'. Labels are referred to in the text	18
2.2	Two views of the transducer-vibrating capacitor integral assembly	20
2.3	View of tail section with outer tube removed ..	22
2.4	Schematic diagram of the electronic layout for the magnetometer	24
2.5	Schematic diagram of the electronic layout for the A.C. bridge temperature regulator	32
2.6	The superconducting solenoid magnet	36
2.7	View of the superconducting solenoid and support assembly	37
2.8	The variation of $B(z)/B(z = 0)$ with displacement z along the axis of the superconducting solenoid	38
2.9	The magnetometer cryostat assembly showing the magnetometer, superconducting magnet and magnet support system	40
2.10	The variable temperature cryostat for resistivity measurements	43
2.11	Schematic diagram of the system for resistivity measurement and temperature regulation in the variable temperature cryostat	44
2.12	Schematic diagram of the vacuum and helium lines for the low temperature systems	46
2.13	Schematic diagram of the electronic layout for the magnetometer and peripheral systems. Labels are clarified in the relevant appendices (as indicated)	48

LIST OF FIGURES (Cont.) PAGE

3.1 The variation of ψ, $|\psi|^2$, $|\psi|^4$ and $|\psi|^2-|\psi|^4$ (from Neumann and Tewordt, 1966) for an isolated fluxon as a function of the reduced distance r/λ_L from the fluxon axis. λ_L is the London penetration length 62

3.2 The co-ordinate system for the description of the fluxon lattice 64

3.3 The variation of $|\psi|^2-|\psi|^4$ versus the reduced distance along the y axis of figure 3.2 for various values of the reduced induction $b = B/B_{c2}$ (full curves). The points have been obtained from equations 3.8 and 3.9 with $b = 0.6$. The dashed curve shows the variation along the x axis. 65

3.4 From the results of figure 3.3 and equations 3.8 and 3.9 the maximum gradient in $[|\psi|^2-|\psi|^4]a_o$ along the y axis is shown (solid curve) as a function of the reduced induction. 68

3.5 The variation in the maximum gradient in $B_{c2}^{-\frac{1}{2}}[|\psi|^2-|\psi|^4]$ along the y axis as a function of the reduced induction 69

3.6 The forces due to the interaction between an edge dislocation at r_o with a Burgers vector in the negative x direction and a fluxon collinear with the $r = 0$ axis. 73

3.7 The interaction energy, at 4.2K in niobium, between a fluxon collinear with the z axis and a parallel edge dislocation as a function of its position on the y axis. The first order (E_1), second order (E_2) and combined ($E_1 + E_2$) interaction energies are shown. (From Kramer and Bauer, 1967.) 73

3.8 The variation in the reduced bulk pinning force density, due to an elementary pinning site, as a function of the reduced displacement of fluxon.

LIST OF FIGURES (Cont.) PAGE

For small displacements, i.e. small p_m or d the pinning sites become ineffective and the bulk pinning force density falls to zero. (From Labusch, 1969b.).. 86

4.1a Niobium-hydrogen phase diagram (From Walter and Chandler, 1965). 102

4.1b The boundary between the α and α + β phases as obtained by various methods. (From Buck, Thompson and Wert, 1971). 102

4.2 Arrhenius plot of the diffusion coefficient for hydrogen in niobium showing the deviation of the experimental results from simple exponential behaviour (from Cantelli, Mazzolai and Nuovo, 1969) 105

4.3 A schematic representation for the description of the hydrostatic stress field of an edge dislocation. In isotropic elastic continuum theory lines of constant stress are circles as shown .. 108

4.4 Variation in the critical temperature as a function of dilation of the unit cell in the niobium lattice and also of the hydrogen concentration in the niobium lattice (From Wiseman, 1965). 114

5.1 Stress-strain curves obtained for the niobium single crystals in compression along <110> at 295K. The arrows indicate the terminal strain for each crystal. 121

5.2 Heating-time and cooling-time characteristics for the temperature controlled specimen stage (see text). 124

5.3a Magnetization curves for the [001] undeformed niobium rod specimen at a few of the temperatures of measurement 127

LIST OF FIGURES (Cont.) PAGE

5.3b Magnetization curves for the $[1\bar{1}0]$ and [001] 1 per cent (nominal) deformed rod specimens 128

5.3c Magnetization curves for the $[1\bar{1}0]$ and [001] 2 per cent (nominal) deformed rod specimen. 129

5.3d Magnetization curves for the $[1\bar{1}0]$ and [001] 4 per cent (nominal) deformed specimens. 130

5.4 The field-temperature phase diagram for the [001] undeformed rod specimens. The variation of H_{c2} with temperature for the 4 per cent deformed [001] specimen is included to show that $H_{c2}(T)$ is unaffected by the deformation. Tc is obtained from this figure by extrapolating the curves to $H_o = 0$ as shown. 131

5.5 The variation of the critical fields H_{c1}, H_c and H_{c2} with t^2 where $t = T/T_c$. Extrapolation of the curves to $t^2 = 0$ gives $H_{c1}(0)$, $H_c(0)$ and $H_{c2}(0)$. . 132

5.6 The variation of the reduced Maki parameters κ_1/κ and κ_2/κ with the square of the reduced temperature. The inset shows the variation of κ_1 and κ_2 with t^2 near $t = 1$ and gives the Ginsburg-Landau parameter $\kappa(\kappa = \kappa_1(t = 1) = \kappa_2(t = 1))$ as 0.785. 135

5.7 The variation at various reduced temperatures of the critical current density with reduced induction for the as-quenched $[1\bar{1}0]$ 4 per cent deformed rod specimen. 136

5.8 As for figure 5.7 for the as-quenched $[1\bar{1}0]$ 2 per cent deformed specimen. 137

5.9 As for figure 5.7 for the as-quenched $[1\bar{1}0]$ 1 per cent deformed specimen 138

5.10 As for figure 5.7 for the as-quenched [001] 4 per cent deformed rod specimen. 139

LIST OF FIGURES (Cont.) PAGE

5.11 The variation at T = 4.05K of the critical current density with reduced induction for the [1$\bar{1}$0] 4 per cent deformed rod specimen after various isochronal ageing treatment 140

5.12 As for figure 5.11 for the [001] 4 per cent deformed specimen 141

5.13a and b The derived variation of the bulk pinning force density with reduced induction for the as-quenched [1$\bar{1}$0] 4 per cent deformed rod specimen at various reduced temperatures 142 143

5.14a and b As for figure 5.13 for the as-quenched [1$\bar{1}$0] 2 per cent deformed specimen. 144 145

5.15a and b As for figure 5.13 for the as-quenched [1$\bar{1}$0] 1 per cent deformed specimen 146 147

5.16a and b As for figure 5.13 for the as-quenched [001] 4 per cent deformed specimen 148 149

5.17 The anisotropy of the bulk pinning force density with the applied field in the (110) plane for the as-quenched deformed disc specimens at T = 4.05K and b = B/B_{c2} = 0.6 (solid curves) and b = 0.8 (points). 150

5.18 The anisotropy of the upper critical field in the (110) plane of the as-quenched disc specimen at T = 4.05K. 151

5.19 The variation of the bulk pinning force density, at b = 0.6, with ageing temperature in the isochronal ageing experiments on the undeformed and 4 per cent deformed [001] and [1$\bar{1}$0] rod specimens 153

5.20 The variation in the bulk pinning force density with reduced induction, after 10 minute isochronal ageing procedures at various temperatures, for the [110] 4 per cent deformed specimen. Included is the result for a 20 hour anneal at 90K. 154

LIST OF FIGURES (Cont.) PAGE

5.21 The variation in the bulk pinning force density with reduced induction, after successive 15 minute isochronal ageing procedures at 90K 155

5.22 The variation in the bulk pinning force density with reduced induction in class (i) (see text). .. 157

5.23 The variation of the bulk pinning force density with reduced induction for the deformed specimens at T = 4.5K showing the difference in behaviour between the $[1\bar{1}0]$ (class (ii)) and the [001] (class (i)) as-quenched specimens. 159

5.24a The variation of the bulk pinning force density normalized at b = 0.4, with the reduced induction b for the [001] 4 per cent deformed specimen, as-quenched and aged for 20 hours at 90K, showing class (i) behaviour and the anomaly at b = 0.8 .. 161

5.24b As for (a) but normalized at b = 0.6 for the $[1\bar{1}0]$ 4 per cent deformed specimen as-quenched showing class (ii) behaviour.. 161

5.25a and b As for figures 5.24b and for $[1\bar{1}0]$ 2 per cent and 1 per cent deformed specimens respectively. 162

5.26 log-log plots of the bulk pinning force density at b = 0.6 versus the upper critical field (induction) for various specimens and also at b = 0.8 for the [001] 4 per cent deformed specimen. From these plots the temperature dependences of the bulk p pinning force density have been obtained approximately in terms of an exponent n, i.e. $P_v(t) \propto B_{c2}^n(t)$, which is given in the figure for the various plots. 164

5.27 The variation of the bulk pinning force density at T = 4.05K with the reduced induction in class II (see text) after isochronal ageing at various ageing temperatures. 171

LIST OF FIGURES (Cont.) PAGE

5.28 As for figure 5.27 after successive isochronal ageing for 15 minute periods at an ageing temperature $T_a = 90K$.. 172

5.29 The variation of the natural logarithm of the ratio of the pinning force density after a time t and at t = 0 with $t^{2/3}$ at reduced inductions b = 0.45, 0.6 and 0.7 (at T = 4.05K from the class II results of figure 5.28). The average gradient $\Delta[\ln(P_v(t)/P_v(0)]/\Delta t^{2/3}$ is S = -0.783 ± 0.25 seconds$^{-2/3}$.. 174

5.30 A plot of the temperature invariant component of the bulk pinning force density (in accordance with the model for class I), against t^2 showing a maximum relative deviation from theory of approximately 10 per cent (except near $t^2 = 1$). 191

5.31 The variation of the bulk pinning force density with deformation ε, in class I at b = 0.5, 0.6 and 0.7, showing an approximately linear dependence. : 193

5.32 Comparison of the predicted b dependence of the bulk pinning force density, from the model for class I, with experiment on the as-quenched and aged [001] 4% deformed specimen (class (i)) and also with the experimental results of Good and Kramer at t ≃ 0.48. 195

5.33 A plot of the temperature invariant component of the bulk pinning force density, in accordance with the model for class II, against t^2 for the 4 per cent, 2 per cent, and 1 per cent deformed $[1\bar{1}0]$ specimens. The relative deviation from the prediction of the model is small except at t → 1.. 209

5.34 Comparison of the predicted b dependence of the bulk pinning force density, from the model for class II (solid curve - b > 0.6), with experiment on the as-quenched and aged $[1\bar{1}0]$ 4 per cent

deformed specimen (class (ii) and class II respectively). Also shown is the prediction of Kramer's (1972) model with appropriate choice of parameters. 210

5.35 A plot of the variations of the ratio of the bulk measured bulk pinning force density at $b = 0.6$ and $b = 0.8$ for class (i) and class (ii) against respectively $\kappa_1^4(t)/\kappa_2^3(t)$ (which is the ratio of the predicted temperature dependences for class I and the peak effect model) and $\kappa_1^2(t)/\kappa_2^2(t)$ (which is the ratio of the predicted temperature dependences for class II and the peak effect model). 219

6.1 Magnetization curves obtained at $T = 4.05K$ for <111> oriented niobium disc-specimens of constant radius $R \simeq 5.9mm$ and various thicknesses 232

6.2 As for figure 6.1. 233

6.3 As for figure 6.1 for discs of constant thickness $d \simeq 0.36mm$ and various radii. 234

6.4 Derived absolute magnetization curves at $T = 4.05K$ for the thin discs of constant radius and various thicknesses... 235

6.5 As for figure 6.4 for the discs of constant thickness and various radii. The fine and dashed curves will be referred to in the text. 236

6.6 Magnetization curve for a niobium disc-specimen (orientation <123> along the cylindrical axis and $R/d = 3.0$) at $T = 8.69K$ after annealing at 1900K for 15 hours in a vacuum of 10^{-9}mm Hg (solid curve) and subsequently after bevelling off the rims as shown (dashed curve) 239

6.7 Magnetization curves at $T = 4.05K$ for a disc-specimen (solid curve) and for a ring specimen ($R/d = 3.26$ mean ring thickness 0.5mm) (dashed

curve) obtained by trepanning the disc-specimen. The field of first penetration H_{c1}^{*} is apparently the same for both specimens 240

6.8 Magnetization curves at T = 4.05K for a ring specimen (R/d = 2.32, mean t = 0.2mm). In this case t is apparently too small (at some point along the ring) to allow usual behaviour (dashed curve). 241

6.9 Magnetization curves at T = 4.05K for a disc-specimen (R/d = 2.26, orientation <123>) which was scratched on its peripheral surface 242

6.10 As for figure 6.9 with the specimen scratched on its planar surfaces. 243

6.11 The magnetization behaviour ($M\text{-}H_o$) for a disc-specimen (R/d = 11.0, orientation <111>) at T = 4.05K (solid curve) is compared with the behaviour for a spheroidal-specimen (dashed curve (a)) of the same axial ratio and volume as the disc specimen, derived by 'shearing' the curve for an infinite long specimen (shown approximately by dashed curve (b)) by an amount $4\pi MD$ as shown. 247

6.12a Co-ordinate system for the description of the charge distribution over the surface of a disc-specimen (radius R, thickness d) when a fluxon is situated at $r = r_F$. 251

6.12b Schematic diagram to illustrate the manner in which a fluxon penetrates the rims of a cylindrical or disc specimen. 251

6.13 The variation of the reduced thermodynamic field Ψ on the end and the equatorial planes of a cylinder as a function of the reduced radial position of a fluxon for various values of R/d. The dashed curve shows the mean value of $\Psi(r_F)$. 257

LIST OF FIGURES (Cont.) PAGE

6.14 A plot of the reduced field of initial penetration of fluxons into the bulk of a cylindrical specimen versus the reduced radius of penetration of a flux spot on the planar end-surface of the specimen (see figure 6.12b) for the various values of R/d for which numerical calculations were made. The figure shows minima in $h^*(r_o)$ which are expected to be the critical $h^*(r_c)$ 260

6.15 A comparison of the predictions of the present model for the equilibrium behaviour in cylindrical specimens with the prediction for a spheroidal specimen with demagnetizing factor D_m - in the limit $B \to 0$ from above (points) 267

6.16 The predicted (see figure 6.14) reduced penetration distance as a function of R/d showing that for most of the range of R/d this distance is small. • and o show the mean reduced ring thicknesses for the two ring specimens. 271

6.17 A comparison of the experimentally determined slopes of the magnetization curves in the Meissner regime ($B = 0$) with the equilibrium predictions using $D = D_m$ (solid curve) and $D = D_e$ (dashed curve) respectively (see text). The figure shows that the use of $D = D_m$ is the better approximation. 272

6.18 A comparison of the critical reduced field of initial fluxon penetration as a function of d/R as determined from the model (solid curve) with the experimentally determined values for the two series of <111> disc-specimens (o and Δ). 274

6.19 The variation of the square of the reduced field of initial penetration as determined experimentally (o and Δ) is compared with the predictions of the model (heavy curve) as a function of $(1 + R/d)^{-1}$ showing the remarkable empirical

relationship $h^{*2} = (1 + R/d)^{-1}$ over the range of R/d investigated. [The predictions for a spheroid (from section 6.3.1) are shown by the dashed curve.] 275

6.20 A schematic diagram illustrating the behaviour of the fluxon lattice pool and the penetration regions in the rims of a disc specimen with increasing and decreasing applied field H_o in the range $H_o \sim H_{c1}$. 278

7.1 The experimentally determined variations of the upper critical field and the field of initial fluxon penetration with temperature in bevelled niobium single crystal disc-specimens (R/d = 0.46 orientation <111>) as-prepared and after deformation by punching (see text). 288

7.2a Magnetization curves normalised to H_{c1}^* for the disc-specimen (figure 7.1) at reduced temperatures t = 0.975, 0.860 and 0.435. 289

7.2b As for (a) in the specimen deformed by punching (see text) for t = 0.970, 0.860 and 0.435. 289

7.3a A direct comparison of the magnetization curves at t = 0.435 in the disc-specimen as-prepared (curve (a)) and deformed (curve (b)) showing the increase in hysteresis in the deformed specimen. For $H_o \rightarrow H_{c2}$ the deformed specimen shows a small peak affect. 290

7.3b The calculated reversible curve for a very long specimen in longitudinal applied field (D = 0 - see text). 290

7.4 The variation, with the induction, in the deformed region, of the difference in the induction across the deformed annular region, (as determined from the magnetization curves for the deformed and undeformed disc-specimens at t = 0.435) and the equilibrium dH(B)/dB (as determined from the

magnetization curve of figure 7.3b). The behaviour for $B(r_o) < 160$ gauss is explained in the text .. 296

7.5 The calculated variation in the bulk pinning force density with reduced induction at $t = 0.435$ in the deformed annular region. The maximum in P_v occurs at $b \simeq 0.18$. 298

7.6 The variation with temperature, determined from the magnetization curves of the deformed and undeformed specimens, of the difference in the magnetic moment at constant H_o (and hence in ΔB across the deformed annular region (see text) of radius r_o at such a field that $b(r_o) = 0.1$). .. 299

7.7 A log-log plot of the bulk pinning force density at $b(r_o) = 0.1$ (in the deformed annular region) versus the upper critical field (induction). The plot shows two linear regions: for $t < 0.885$ $P_v \propto B_{c2}^{2.3}$ and for $t > 0.885$ $P_v(t) \propto B_{c2}^{1.3}$ 300

A1.1 The experimentally determined variation of C_{11}, C_{44}, C_{66} with reduced induction in the range $0.35 < b < 1.0$. 309

A1.2a Schematic representation of the distribution of the induction inside a long superconducting specimen in longitudinal field. 313

A1.2b Schematic representation of the magnetization curve for a deformed specimen showing the method for obtaining the average induction in increasing and decreasing applied field. 313

A1.3 The variation of the reduced induction with temperature for various values of the reduced applied field H_o/H_{c2} in the range $0.55 < H_o/H_{c2} < 0.95$.. 315

A1.4 The variation with temperature of the equilibrium value of dH/dB for various values of the reduced induction in the range $0.3 < b < 0.95$. 316

magnetization curve of figure 7.3b). The behaviour for $B(r_o) < 160$ gauss is explained in the text .. 296

7.5 The calculated variation in the bulk pinning force density with reduced induction at $t = 0.435$ in the deformed annular region. The maximum in P_v occurs at $b \simeq 0.18$. 298

7.6 The variation with temperature, determined from the magnetization curves of the deformed and undeformed specimens, of the difference in the magnetic moment at constant H_o (and hence in ΔB across the deformed annular region (see text) of radius r_o at such a field that $b(r_o) = 0.1$). .. 299

7.7 A log-log plot of the bulk pinning force density at $b(r_o) = 0.1$ (in the deformed annular region) versus the upper critical field (induction). The plot shows two linear regions: for $t < 0.885$ $P_v \propto B_{c2}^{2.3}$ and for $t > 0.885$ $P_v(t) \propto B_{c2}^{1.3}$ 300

A1.1 The experimentally determined variation of C_{11}, C_{44}, C_{66} with reduced induction in the range $0.35 < b < 1.0$. 309

A1.2a Schematic representation of the distribution of the induction inside a long superconducting specimen in longitudinal field. 313

A1.2b Schematic representation of the magnetization curve for a deformed specimen showing the method for obtaining the average induction in increasing and decreasing applied field. 313

A1.3 The variation of the reduced induction with temperature for various values of the reduced applied field H_o/H_{c2} in the range $0.55 < H_o/H_{c2} < 0.95$.. 315

A1.4 The variation with temperature of the equilibrium value of dH/dB for various values of the reduced induction in the range $0.3 < b < 0.95$. 316

LIST OF FIGURES (Cont.) PAGE

A1.5 The maximum pinning force due to a spherical site of uniform non-zero pinning potential density Ω within a radius R is shown as a function of $2R/a_o$ (dashed). The solid line is a plot of the 'correction factor' required for generalizing the pinning force calculated for a site with $R << a_o$ to arbitrary R (see text). 323

A2.1 Co-ordinate system for the description of the scalar potential of a dipole M situated at the origin and pointing along the z axis. 326

A2.2 The spatial configuration in the x-z plane of the time varying component of the magnetic field due to a dipole pointing and vibrating along the z direction. 326

A2.3 The coil configuration for optimal detection of the time varying field of the vibrating dipole as shown 328

A2.4 Equivalent circuit for the vibrating capacitor reference system 328

A2.5 Schematic circuit diagram for the comparator unit of the magnetometer 331

A2.6 The low noise preamplifier circuit (A1 in figure A2.5) (from Fairchild Application Report 159). .. 332

A2.7 Various specimen rods and stages (including the temperature regulated stage) for use with the magnetometer 338

A3.1 Electronic circuit diagram for the A.C. bridge temperature regulator 340

A4.1 Calibration curve for the (Au - 0.03 per cent Fe)-Chromel Thermo-couple in the range $0 < T < 295K$... 346

A4.2 Calibration curve in the range $2.5 < T < 10K$ for the germanium resistance thermometer (Solatron Devices Incorporated, Series 5, Model SP5401-1814) 349

LIST OF FIGURES (Cont.) PAGE

A4.3 Circuit diagram for the germanium resistance thermometer constant current source and power supply for a potentiometer circuit 350

A5.1 Schematic diagram of the superconducting magnet coils showing dimensions and the co-ordinate system for the calculation of the spatial configuration of the magnetic field.. 353

A5.2 Schematic diagram of the NMR probe and electronics for the calibration of the superconducting solenoid magnet 357

A5.3 The calibration H-I curve for the superconducting magnet obtained from the NMR results in increasing and decreasing I 359

A5.4 Circuit diagram for the Hall probe electronics and the magnetic power supply programmer 361

A5.5 Circuit diagram for the magnet current monitor and selection unit 362

A6.1 Schematic diagram of the continuous reading liquid helium depth probe and associated electronics .. 364

A7.1 Schematic diagram of the apparatus and electronics for measurements of resistivity by the eddy current decay method (from Clarke and Mordike, 1966). .. 368

A7.2 The results of experiments to determine the resistivity of a copper and a niobium specimen by the eddy current decay method and to demonstrate the relative accuracy obtainable 369

CHAPTER 1

1. Introduction

The subject of type II superconductivity has its origin in a paper by Abrikosov (1957) in which, by a complete analysis of the Ginzburg-Landau equations (Ginzburg and Landau, 1950), he predicts all the essential features of ideal superconductors intrinsically of this type. The phenomenon of type II superconductivity, in particular with regard to non-ideal irreversible magnetic properties, has been intensively studied since the discovery at the beginning of the last decade of superconducting materials capable of supporting very high current densities in high magnetic fields (Kunzler, 1961). These materials (for example Nb-Zr, Nb-Ti, Nb_3Sn and Mo_3Re) are of great technological interest and have found various low temperature device applications. The ability to carry large transport current densities depends, in a manner as yet incompletely understood, on the extent of crystal lattice imperfection in these materials which are usually heavily cold worked or sintered. The effectiveness of various types and configurations of imperfection has been investigated and in some cases the underlying physical processes have been elucidated*. The present investigation is concerned mainly with the processes involved in intrinsically type II superconducting niobium single crystals which

---

* Excellent review articles have been written by, inter alia; Livingston and Schadler (1964), Dew-Hughes (1966, 1972), and Campbell and Evetts (1972).

CHAPTER 1

1. Introduction

The subject of type II superconductivity has its origin in a paper by Abrikosov (1957) in which, by a complete analysis of the Ginzburg-Landau equations (Ginzburg and Landau, 1950), he predicts all the essential features of ideal superconductors intrinsically of this type. The phenomenon of type II superconductivity, in particular with regard to non-ideal irreversible magnetic properties, has been intensively studied since the discovery at the beginning of the last decade of superconducting materials capable of supporting very high current densities in high magnetic fields (Kunzler, 1961). These materials (for example Nb-Zr, Nb-Ti, Nb_3Sn and Mo_3Re) are of great technological interest and have found various low temperature device applications. The ability to carry large transport current densities depends, in a manner as yet incompletely understood, on the extent of crystal lattice imperfection in these materials which are usually heavily cold worked or sintered. The effectiveness of various types and configurations of imperfection has been investigated and in some cases the underlying physical processes have been elucidated*. The present investigation is concerned mainly with the processes involved in intrinsically type II superconducting niobium single crystals which

---

* Excellent review articles have been written by, inter alia; Livingston and Schadler (1964), Dew-Hughes (1966, 1972), and Campbell and Evetts (1972).

have been pre-deformed to produce dilute arrays of edge dislocations with a predominantly common Burgers vector.

The relative diversity of the contents of this thesis necessitates introductory material at the beginning of most chapters and therefore only a brief outline of introductory theory of general relevance and an outline of the scope of this investigation will be given here.

1.1 Equilibrium behaviour

The M-H phase diagram of the bulk of a type II superconductor is characterized by three temperature dependent critical fields (first measured and reported by Shubnikov, Khotkevich, Shepelev and Riabinin, 1937 for Pb-Tl and Pb-In alloys) viz; $H_c(T)$, $H_{c1}(T)$ and $H_{c2}(T)$ where $H_{c1}(T) < H_c(T) < H_{c2}(T)$ and $-H_c^2/8\pi$ is the condensation energy density of the superconducting electrons in zero applied field. For ideal type II specimens with zero demagnetizing factor the magnetization behaviour is reversible and has the following characteristics: for an applied magnetic field H_o, in the range $H_o < H_{c1}$, the induction B in the specimen is zero ($B = H_o + 4\pi M$ and therefore the magnetization $M = -H_o/4\pi$) and the specimen is in the so-called Meissner state (Meissner and Ochsenfeld, 1933). In the range $H_{c1} < H_o < H_{c2}$ the specimen is in the Shubnikov or mixed state with $H_o > B > o$ and B increasing with H_o until $H_o = H_{c2}$ when $B = H_o$ and the specimen undergoes a second order transition to the normal state. (For $H_o > H_{c2}$ superconductivity persists near the surfaces parallel to the applied field. At $H_o = H_{c3} \simeq 1.69\ H_{c2}$ this surface superconductivity ceases and the specimen is fully in the normal state (Saint James and de Gennes, 1963). Abrikosov's (loc. cit.) solutions to the Ginzburg-Landau equations (in the regime $\kappa > 1/\sqrt{2}$ where κ is the so-called Ginzburg-Landau parameter - see appendix 1(a)), correctly predicts this

behaviour and also predicts that in the mixed state the magnetic flux in the specimen should be quantized in microscopic flux tubes or supercurrent vortices (henceforth referred to as fluxons in the present work). Each fluxon contains one flux quantum, $\phi_o = ch/2e = 2.07 \times 10^{-7}$ gauss cm^2, and in ideal superconductors the fluxons form a regular two dimensional array with a line density (B/ϕ_o) which is a single valued function of the applied field H_o. The structure of the fluxon is described in terms of two characteristic lengths ξ and λ. ξ is the coherence distance of the super-electron condensate and is the characteristic range over which the condensate order parameter may vary. It is explicitly related to the coherence length of Pippard (1953). λ is the characteristic range of magnetic field penetration into the superconductor and is explicitly related to the London penetration length λ_L (London and London, 1935). The temperature dependences of ξ and λ are known (see for example de Gennes, 1966) to be approximately the same and therefore their ratio $\kappa = \lambda(T)/\xi(T)$ (the Ginzburg-Landau parameter)* is independent of temperature. ξ and λ also have a dependence on the normal electronic mean free path which is not the same for each so that κ depends on the resistivity of the material in the normal state (Goodman, 1961).

The fluxon consists in essence of a cylindrical region in which superconductivity is partially suppressed (the order parameter $|\psi|^2$ (see appendix 1(a)) - increasing from zero on the axis of an isolated fluxon to its equilibrium value over the characteristic distance ξ).

---

* $\kappa > 1/\sqrt{2}$ in the Ginzburg-Landau equations implies a negative interface energy between the superconducting and normal phases.

Supercurrents flow around this region generating one quantum (ϕ_o) of flux. At large distances (r) from the fluxon axis the field strength h(r) falls off as $\exp(-r/\lambda_L)$ (London, 1961). Associated with the fluxon is a line energy which has three components, viz; the magnetic energy of the enclosed flux, the kinetic energy of the circulating supercurrent, and the loss of condensation energy in the fluxon core. The line tension of a fluxon is given (see for example de Gennes, 1966) for $\kappa >> 1$ by

$$\tau = (\phi_o/4\pi\lambda_L)^2(\ln \kappa + \varepsilon) \qquad 1.1(a)$$

$$\simeq (\phi_o H_c/2^{5/2}\pi) \ln \kappa/\kappa \qquad 1.1(b)$$

where ε is a small correction for the 'core' energy of the fluxon and is of order 0.1. (According to equation 1.1(b) the line tension τ is a decreasing function of κ and a fluxon will therefore be attracted to regions of locally enhanced κ. The thermodynamic considerations of Keesom (1924), Gorter (1933) and Gorter and Casimir (1934) on the superconducting normal transition indicate that there should be very small differences in the crystal lattice parameter and elastic moduli between the essentially normal core of a fluxon and the surrounding superconducting matrix. Thus the fluxon will behave as an elastic inhomogeneity and will therefore also interact with various other elastic inhomogeneities such as dislocations and grain boundaries in the crystal lattice (see later)).

The mixed state of an ideal specimen with zero demagnetizing factor may be explained as follows: In increasing applied field when $H_o = H_{c1}$ the line energy of a fluxon just equals the reduction in the magnetic energy of the specimen due to the presence of a fluxon. From equation 1.1(b) therefore (for $\kappa >> 1$)

$$(\phi_o H_c/2^{5/2}\pi) \ln \kappa/\kappa \simeq H_{c1} \cdot \phi_o/4\pi$$

so that

$$H_{c1} \simeq (H_c/2^{5/2}\pi) \ln \kappa/\kappa. \qquad 1.2$$

For applied fields in the range $H_{c1} < H_o < H_{c2}$, i.e. in the mixed state, the equilibrium induction $B[H_o]$ may be determined by minimizing the Gibbs function

$$G = n_L \tau + \tfrac{1}{2} \sum_{i,j} U_{ij} - n_L \phi_o H_o/4\pi \qquad 1.3$$

where $n_L = B/\phi_o$ (i.e. the fluxon density) and U_{ij} is the energy of interaction between the ith and jth fluxons in the lattice (see later).

As the applied field approaches H_{c2} the cores of the fluxon begin to overlap so that eventually at $H_o = H_{c2}$ the order parameter is everywhere zero in the bulk of the specimen which then undergoes a second order transition to the normal state. H_{c2} is given (e.g. Saint James, Thomas and Sarma, 1969) by

$$H_{c2} = (1/2\pi\xi^2)\phi_o \qquad 1.4$$

The behaviour of a type II superconductor as predicted by Abrikosov and outlined above, is qualitatively correct for all $\kappa < 1/\sqrt{2}$ and $T < T_c$ (where T_c is the critical temperature). However, it is quantitatively exact only in the Ginzburg-Landau domain (i.e. as $T \to T_c$) and is analytically tractable only for $\kappa \gg 1$. Subsequent numerical calculations and generalizations of the theory* have extended its range of quantitative applicability [near H_{c2}; for all $\kappa > 1/\sqrt{2}$ and all $t = T/T_c \leqslant 1$, near H_{c1}; for $\kappa \sim 1$ and $t \to 1$ by numerical methods

---

* For a complete review see Fetter and Hohenberg (1969).

(e.g. Harden and Arp, 1963) and for $t \lesssim 1$ (e.g. Tewordt, 1964 and Neumann and Tewordt, 1966a,b)]. In order to generalise Abrikosov's theory to all temperatures Maki (1964) introduced three dimensionless temperatures dependent parameters $\kappa_1(T)$, $\kappa_2(T)$ and $\kappa_3(T)$ which all converge and become equal to the G-L parameter κ at $T=T_c$. These parameters have proved to be very useful in comparing theory with experiment and in classifying various type II behaviour. [For an intrinsic type II superconductor $\kappa_2 > \kappa_1 > \kappa_3$ (see for example Serin, 1969 and Jacobs, 1971)] The Maki parameters are defined by the following equations:

$$\kappa_1(T) = H_{c2}(T)/(2^{\frac{1}{2}}H_c(T)) \qquad 1.5$$

$$\left[dM/dH\right]_{H_{c2}} = 1/[4\pi\beta(2\kappa_2^2(T) - 1)] \qquad 1.6$$

and

$$H_{c1}(T) = H_c(T)\ f(\kappa_3(T)) \qquad 1.7$$

where $f(\kappa_3) \simeq .\ln \kappa_3/(2^{\frac{1}{2}}\kappa_3)$ for $\kappa \gg 1$ and has been numerically calculated for arbitary κ by Harden and Arp (loc. lit). β is a numerical constant which depends on the symmetry of the fluxon lattice. For large κ Kleiner, Roth and Autler (1964) and Eilenberger (1964) show that a triangular fluxon arrangement is more favourable than the square lattice originally proposed by Abrikosov (loc. cit.). For $\kappa \to 1/\sqrt{2}$ and $B > 0.3H_c$ Kramer (1966) finds the free energy of the square lattice to be lower than that of the triangular lattice. This is supposed to be due to an attractive interaction between fluxons, resulting from fluxon core overlap, which modifies the form of the normal electromagnetic repulsive interaction (which gives an adequate description in the high κ case). A consequence of this attractive

interaction in specimens with $\kappa \lesssim 1$ and with finite demagnetizing factors is the occurrence of the so-called mixed-intermediate state (see for example Seeger, 1970 and also Chapter 6) . A triangular fluxon lattice was first observed in a superconducting niobium specimen by Cribier, Jacrot Rao, Madhav and Farnoux (1964) using neutron diffraction techniques and subsequently by Essmann and Träuble (1967) by means of an elegant Bitter pattern replica technique. Obst (1969) finds, using this technique, both triangular and square fluxon lattices in Pb-In allows specimens with finite demagnetizing factors and κ only just greater than $1/\sqrt{2}$. He also finds that the fluxon lattice symmetry in these specimens is influenced by the crystal symmetry.

Finally, a property of the fluxon lattice which needs consideration because of its relevance to non-equilibrium behaviour is its elasticity. Early calculations of the compressive elastic constants were made by Silcox and Rollins (1963) and by Friedel, de Gennes and Matricon (1963). More recently Labusch (1968 , 1969a), using continuum theory, has derived all the relevant matrix elements of the elastic modulus in terms of measurable parameters of the reversible magnetization curve and has also derived the effective moduli for various pinning force configuration (see Chapters 3 and 5).

1.2 Non-equilibrium behaviour

Non-equilibrium behaviour in the mixed state of a type II superconducting specimen under isothermal and quasi-static conditions arises from (i) 'bulk fluxon pinning' mechanisms, i.e. from dissipative interactions between crystal lattice inhomogeneities and fluxons, (ii) 'surface effects', i.e. dissipative pinning interactions and/or barrier effects in the specimen surface and (iii) 'geometry effects' in specimens with a finite demagnetizing factor.

These effects will now be outlined briefly in relation to the present investigation.

Bulk fluxon pinning is generally understood in terms of the critical state model due to Bean (1962) and Kim, Hempstead and Strnad (1962, 1963). Essentially the model states that any gradient in the fluxon lattice density, arising from the action of pinning forces and not from some slow (w.r.t. the fluxon spacing) spatially varying property of the superconducting matrix, has some critical maximum value everywhere. Stated another way: the effective pinning force density is everywhere equal to the driving force density which, for straight fluxons, is proportional to the local fluxon lattice density gradient and therefore to some current which is then defined as the critical current.

A complete general treatment of the critical state has been given by Evetts, Campbell and Dew-Hughes (1968) and Campbell and Evetts (1972). Aspects of the theory which are relevant to the present investigation will be reviewed in Chapter 3. These will be used in Chapter 5 to determine the bulk pinning force density P_v from the magnetization curves experimentally obtained as a function of B,T and the microstructure configuration on specially prepared niobium specimens. These specimens were cut from larger single crystals of niobium which had been deformed in compression along a <110> direction to produce predominantly edge dislocation arrays. The final specimens are of millimeter dimensions and as a consequence of the cutting and polishing processes contain interstitial hydrogen as a concentration of about 50 ppm (atomic). The presence of the hydrogen proved very useful: since by means of low temperature ageing procedures it was found that the magnitude and form of the measured $P_v(B,T)$ could under certain circumstances be altered to a very large extent thus providing

information about the character of the basic pinning sites.

These experiments, in fact, allowed two distinct classes of behaviour to be distinguished. One class obtains in all the specimens, regardless of the orientation of the fluxons with respect to the predominant direction of the edge dislocations, when the hydrogen is completely precipitated out of solution by suitable low temperature ageing. The other class obtains only in specimens for which the edge dislocations have Cottrell atmospheres associated with them and are parallel to the fluxons.

The relevant theory for the low temperature behaviour of interstitial hydrogen in niobium is given in Chapter 4.

In Chapter 3 a brief introduction to the theory of pinning is given and several pertinent models for possible basic pinning mechanisms of the elementary pinning sites and also models for the overall fluxon lattice response to arrays of basic pinning sites (i.e. summation models) are reviewed and formulated.

In the light of the theoretical considerations of chapters 3 and 4 specific mutually consistent proposals are made for the salient physical processes responsible for the observed pinning behaviour in the two classes mentioned above. Specific models are then formulated which are in good agreement with experiment in each class. Application of the model pertaining in the former class to experimental results on lightly deformed materials, as reported by various other authors, also gives good agreement and resolves certain problems and inconsistencies which have previously been associated with the application of prevailing theoretical ideas to this pinning situation. This agreement, taken in conjunction with the severe restrictions resulting from the requirements of mutual consistency in the above

models, is considered to be an unambiguous and unqualified affirmation of the assumed basic physical processes in either class. The conclusions of the investigation on bulk pinning in niobium ($\kappa \simeq 1$) may be summarised as follows:

(i) Isolated edge dislocation segments, i.e. with no significant strain field overlap, in either perpendicular or parallel interaction with the fluxon lattice are not effective as pinning sites and therefore do not give rise to a bulk pinning force. This is probably true of screw dislocations also.

(ii) In lightly deformed low to intermediate κ materials containing 'clean' (i.e. free of interstial atmospheres) dislocations the basic pinning sites are small regions (10^3 - 5.10^3Å) of tight... ...gled dislocation segments, dipoles or multipoles or otherwise ...slocation pile-up configurations. These sites will be re... ...rred to as 'multiple dislocation' sites. In the present investigati... the former type is operative and its interaction with the fluxon lattice is by the so-called $\delta\kappa$ mechanism (i.e. due to a local variation in the Ginzburg-Landau parameter κ). For the perpendicular interaction with screw dislocation tangles (see for example Freyhardt, 1967) the so-called second order elastic interaction obtains. The number density of the multiple dislocation sites, in the cases considered, is sufficiently low that they interact independently with the fluxon lattice and theory in the so-called dilute limit is appropriate.

(iii) The parallel interaction between a Cottrell atmosphere (Cottrell, 1948) of hydrogen on an edge dislocation segment is effective, by the $\delta\kappa$ mechanism, as a pinning site. These sites will be called 'Cottrell atmosphere sites'. Their high density in the present case is consistent with the use of concentrated limit theory.

These conclusions are compatible with the long held, but incompletely understood, contention that for strong pinning by dislocations highly inhomogeneous networks are necessary (see for example Narlikar and Dew-Hughes, 1964, 1966). The experiment also constitutes the first critical assessment of Labusch's threshold criterion (Labusch, 1969b) which requires, for pinning due to an array of non-correlating small sites (i.e. having dimensions small with respect to the fluxon separation) a certain minimum ratio between the basic pinning force and the effective elastic constant of the fluxon lattice. For ratios below this minimum value the interaction is elastic, i.e. non dissipative, and therefore no bulk pinning results. The results and conclusions of the present investigation are definitely in at least qualitative agreement with this prediction.

Pinning and barrier effects in surfaces parallel to the applied field must also be considered because under certain circumstances they can be large and, in the experimental situation, must be distinguished from bulk effects which they tend to mask. There are several such surface mechanisms, notably; (i) fluxon pinning due to an anomalously high concentration of crystal defects in the specimen surface (Campbell, 1969, Fournet and Mailfert, 1970 and Melville, 1971). (ii) A surface barrier effect for fluxons which is due to the interaction between a fluxon and its image in a parallel plane surface which must be smooth on a scale of λ (Bean and Livingston, 1964 and de Gennes, 1965). This effect is manifest by a delay, in increasing applied field, of the onset of initial flux penetration into the specimen and by hysteretic magnetic behaviour in the region $H_{c1} < H_o < H_c$. (iii) Surface sheath currents (Saint James and de Gennes, 1963. Fink, 1966 and Park, 1969) associated with surface

superconductivity in applied fields $H_o \leqslant H_{c3} = 1.69\ H_{c2}$. These surface effects have not been explicitly studied in this investigation but adequate precautions have been taken to eliminate the former two and the latter was not found to be significant.

In short cylindrical specimens a purely geometrical effect has been found which is also manifest by a delayed onset of fluxon penetration above the expected applied field for transition to a mixed state, viz: $H_o = H_{c1}(1-D)$ (where D is the demagnetizing factor for the enclosed spheroid) and also by a hysteretic magnetization phenomenon. A theoretical model for this effect is developed in Chapter 6 and the predictions of the model for disc-shaped specimens (with the applied field along the cylindrical axis) are compared with experimental results. In essence the model predicts that the magnetic moment of a fluxon is a decreasing function of its distance from the cylindrical axis of the disc. The negative magnetostatic energy of the fluxon is therefore also a decreasing function of this distance. Thus after initial fluxon penetration at an applied field $H_o = H^*_{c1}(R,d)$ (where R and d are respectively the radius and thickness of the disc) the fluxons move to the middle of the disc to form a 'pool' which grows in radius with increasing applied fields until at $H_o = H_{c1}$ it fills the disc. In decreasing applied field the radius of the pool must obviously remain equal to the radius of the disc in order for the fluxons to escape from the disc. Quantitative predictions are made for this process which are in good agreement with experiment.

This aspect of the present investigation was initiated to account* for the results of a fluxon pinning experiment which was performed on specially deformed disc-specimens (Chapter 7). These disc specimens were lightly deformed by 'punching' (as described in Chapter 7 and in appendix A9) to produce a narrow annular region of deformation concentric with the cylindrical axis of the disc. When the cylindrical axis of the single crystal disc-specimens is along a [111] direction, i.e. parallel to the Burgers vector for dislocations in B.C.C. niobium, the resulting deformation on punching is very interesting and has been investigated in some detail (Ball and Doyle, 1974 - included in appendix A9). The rationale behind these pinning experiments (which preceded the other pinning experiments already mentioned) in the [illegible]ned discs was to find an experiment which would unambiguously show the relative importance of various surface and bulk effects.

---

* The prediction of the model is however of particular relevance to a class of experiments on disc samples to investigate the mixed - intermediate state. This will be discussed in Chapter 6.

CHAPTER 2

2. Apparatus and Experimental Method

2.1 Introduction

Several experimental methods have been used to determine the pinning force density P_v in type II superconductors. These include direct measurement of the critical applied transport current density perpendicular to an applied magnetic field, A.C. susceptibility measurements and also magnetization measurements using ballistic, torque, integrating or vibrating sample magnetometers. Factors governing the choice of method are, inter alia, the size, geometry and susceptibility of the specimen. Each method has certain disadvantages (see for example Campbell and Evetts, 1972 and Livingston and Schadler, 1964).

The choice of method in the present investigation was dictated by the following considerations, viz:

(i) since the investigation is not of a simple exploratory nature there is a need for high accuracy and reproducibility,

(ii) the size of the specimens would necessarily be small due to the high cost of single crystal material (in the absence of suitable facilities to prepare such crystals) and because of the nature of the envisaged investigation,

(iii) the desirability of investigating geometry effects, and

(iv) general applicability as a magnetometer facility of high accuracy, reproducibility and sensitivity.

These considerations suggest a vibrating sample magnetometer.

The two main disadvantages of this type of magnetometer are:

(i) Image effects - the vibrating magnetic moment of the magnetized specimen gives rise to eddy currents in conducting materials and to a vibrating image in magnetic materials in the vicinity of the specimen. These effects give rise to a spurious signal in the detection coils which are placed near the specimen to detect the time varying component of the field due to the vibrating dipole.

(ii) A spurious signal will be induced if the detection coils are in an inhomogeneous field and any vibration is transmitted to them.

The former effect has been considered in detail by Stoner and Herbert (1970) for the case of a specimen vibrating normally to the axis of the poles of an iron core electromagnet and for various detection coil configurations. In this case the magnetic image effect predominates over eddy current effects at low values of the magnetic field and gives rise to a spurious signal of a few per cent which goes to zero as the iron core of the magnet saturates. Stoner and Herbert find that the magnitude for the first order pair of images associated with the vibrating dipole is proportional to $(\mu_e - 1)\cdot(\mu_e + 1)$ where $\mu_e = dB/dH$ (for the pole pieces). The case of a magnetized specimen vibrating along the axis of a superconducting solenoid has been investigated, inter alia, by Richards, Edwards, Cornforth and Legvold (1970). These authors measure the moment of an iron sample in a solenoid constructed of Nb_3Sn ribbon wound on a non-conducting bobbin. The only electrically conducting closed loop in the vicinity of the specimen is a thin brass tube. With detection coils close to the specimen they observe only a 1 per cent change in spurious signal as the field is swept from 10 to 100 kilo-oersted. They conclude that the effect should be reduced if a good electrical

conductor is placed between the detection coils and the solenoid.

The spurious signal due to vibration of the detection coils is fairly easily reduced to an insignificant level by ensuring that they are rigid relative to the magnet which should have a high field homogeneity. This effect is in any case proportional to the magnitude of the magnetic field and is therefore easily corrected for.

An unknown factor, at the time of choosing a vibrating sample magnetometer, was the effect that the vibration of the superconducting specimen would have on the fluxon lattice dynamics, and in particular, in reducing the efficacy of the pinning sites. This was later shown to be insignificant.

An important advantage of this type of magnetometer is that it allows, with suitable design, convenient and fast removal and replacement of the specimen at all times. This permitted quenching of the specimen from room temperature to 4K and low temperature annealing experiments which would otherwise have been long and expensive (in terms of liquid helium).

The design criteria for the superconducting solenoid included high field homogeneity, and a moderately high maximum field strength (above 40 kilo-oersted) to allow for general use. This latter criterion has the slight disadvantage that the magnet tends to 'trap' a small amount of flux when cycled to fields in excess of about 3 kilo-oersted at a temperature of 4K. This was however rarely necessary in the experiments on the niobium specimens.

Specimen temperature in the range $T < 30K$ is measured by means of germanium resistance thermometer, and in the rante $30 < T < 400K$ by a gold-iron chromel thermocouple.

In this chapter the apparatus will be considered in terms of the separate components and as an integrated assembly. The general description of the principles of operation, specifications and modus operandi will be given briefly. Detailed design considerations, circuits and set-up procedures will be given in appendices.

2.2 Description of the apparatus

2.2.1 The magnetometer

The first published design of a vibrating sample magnetometer is due to Foner (1959) whose name is now always associated with this type of magnetometer. The present design is similar in principle but differs in a number of respects from Foner's original design.

The operation of the magnetometer depends on the detection of the time varying component of the dipole (or linearly superimposed multipole) field of an harmonically vibrating sample by the signal induced in a set of stationary coils in the vicinity of the sample. This signal is proportional to the magnetic moment of the sample and also to its amplitude and frequency of vibration. A suitable null method of signal detection is therefore required in order to eliminate these latter dependences. Foner (1959) discusses some of the possible methods. The method offering the greatest versatility, convenience and dynamic range, involves the generation of a synchronous reference signal by means of a vibrating plate capacitor which is coupled mechanically to the vibrating specimen. This reference signal is used to cancel, either manually or automatically, the signal from the detection coils.

The mechanical design of the present magnetometer is shown in figure 2.1. It consists in essence of an electro-mechanical transducer, the vibrating plate capacitor reference system and the

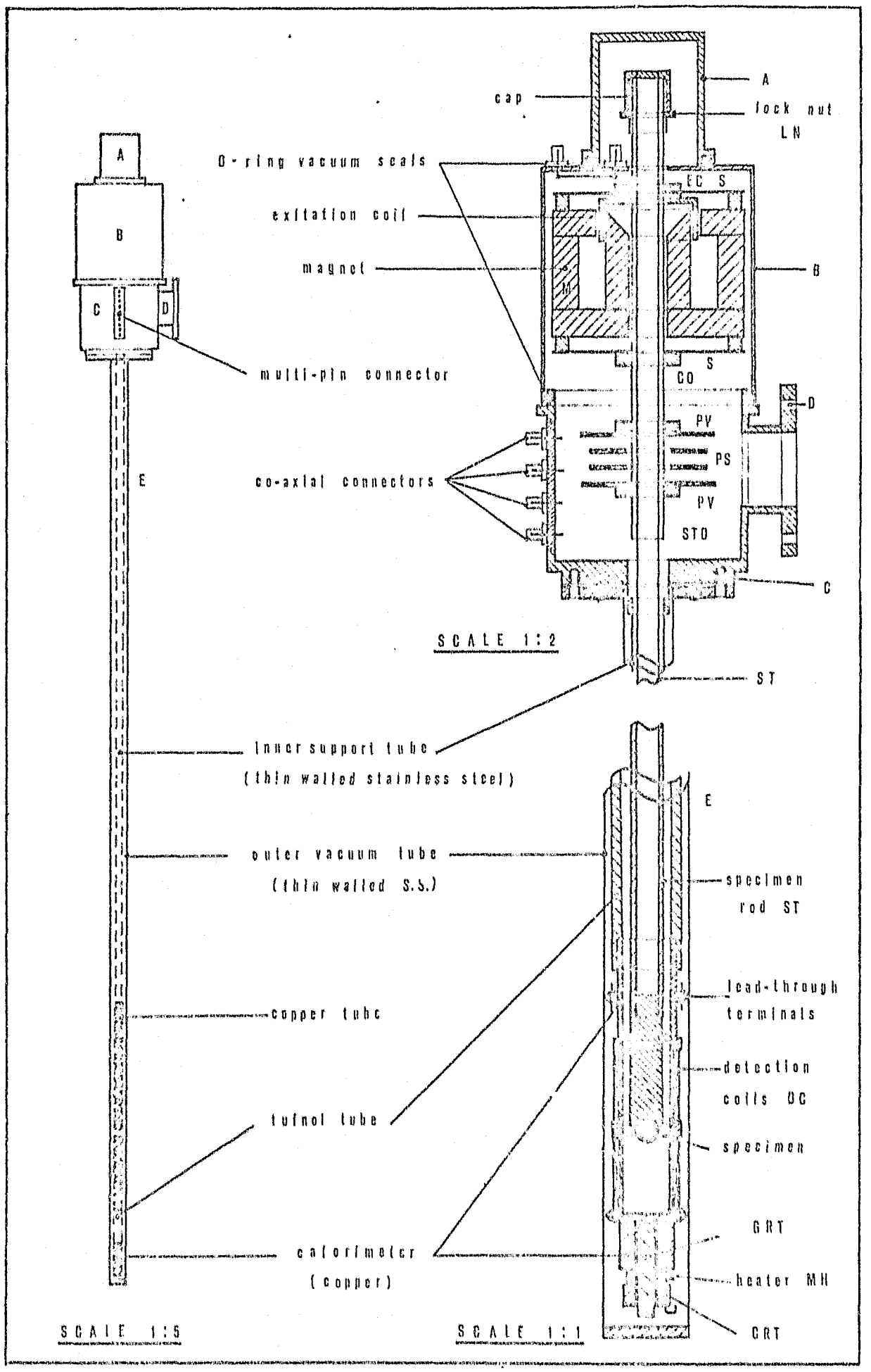


Figure 2.1. The magnetometer; showing the electro-mechanical transducer, reference capacitor, detection coils and the temperature controlled 'calorimeter'.

signal detection system. The transducer assembly consists of a modified loudspeaker magnet M through which a hole has been drilled to accommodate the $\frac{3}{8}$ inch diameter thin wall stainless steel support tube STO. This tube is clamped to the transducer excitation coil former EC which, for the sake of keeping reaction forces as low as possible, is made of epoxy resin with aluminium clamping rings secured to it. The excitation coil is wound onto the epoxy former. Below the magnet the tube STO is clamped to the collar CO which is also made of aluminium. STO, EC and CO are elastically suspended and axially centered by means of two copper-beryllium 'spider' springs S.

The capacitor assembly consists of two moving annular plates PV and two stationary annular plates PS: all of which are fabricated from aluminium and are plated with gold. The plates PV are clamped to the support tube STO by means of electrically insulating (tufnol) rings. The stationary plates PS are suspended from the magnet on insulating supports which are not shown in figure 2.1 but which may be seen in the photographs of figure 2.2, which are two perspective views of the integrated transducer-capacitor assembly. When in situ in the magnetometer this assembly is clamped onto three vertical posts which fit into the holes on the lower side of the magnet. These posts are not shown in figure 2.1. Finally the support tube STO has a threaded collar at its upper end onto which the cap of the specimen tube ST may be screwed and locked against the lock nut LN. The entire vibrating assembly, including the specimen tube and specimen holder, is designed to have a very low mass in order to minimize reaction forces which may be transmitted to the detection coils.

The detection system is situated in the 'tail' of the magnetometer which is designed to fit into the superconducting solenoid. With

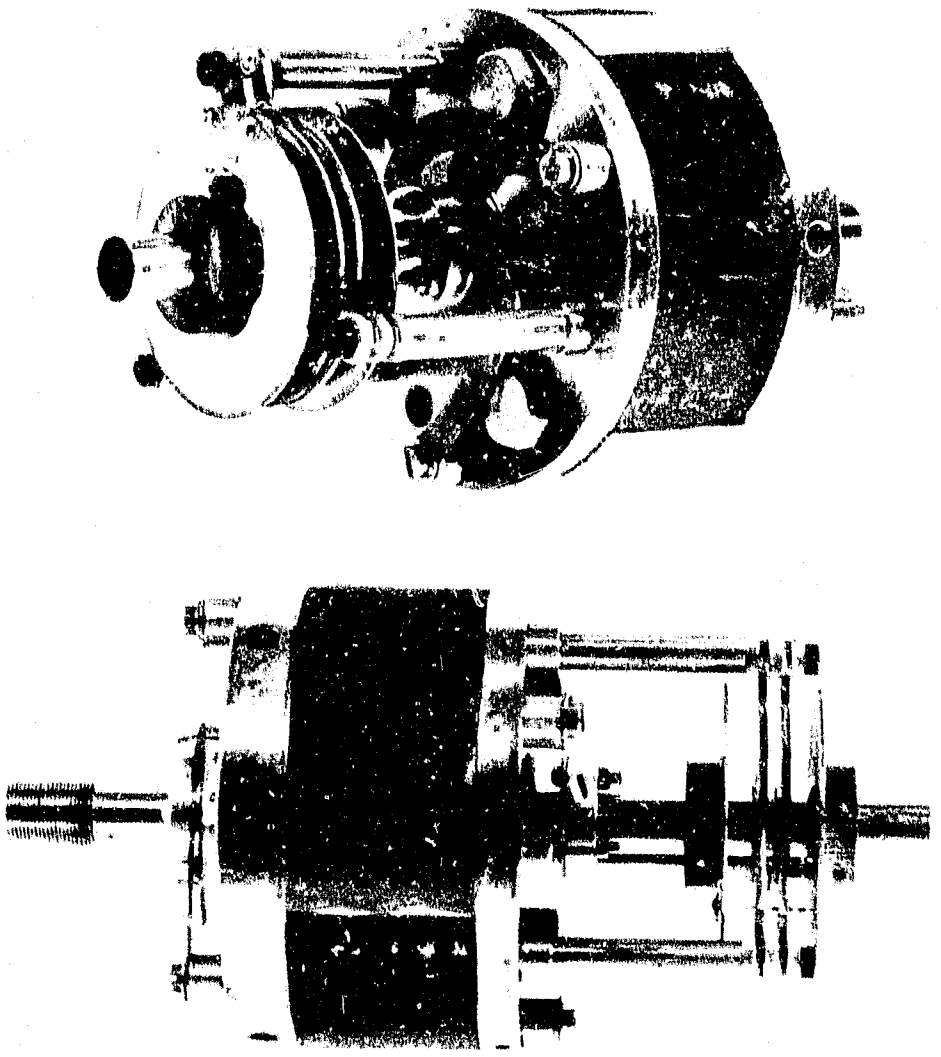


Figure 2.2. Two views of the transducer-vibrating capacitor integral assembly.

reference to figure 2.1 this consists of the detection coils DC which are two coaxial windings of about 18,000 turns each connected in series opposition. The coils are wound on a copper 'calorimeter' onto which a germanium resistance thermometer GRT, a carbon resistance thermometer CRT and a very small non-inductive manganin heater MH are thermally attached. Good thermal contact between the thermometers and the calorimeter is made by pressing the thermometer, after application of silicone vacuum grease, into close fitting holes in the calorimeter. The fine leads for the thermometers and the heater are also thermally anchored to the calorimeter in the usual manner and fixed with G.E.C.7031 varnish. A photograph of the tail section with outer tube removed is shown in figure 2.3.

The copper calorimeter is fixed to the end of a guide tube which consists of a length of thin wall stainless steel tube, a length of copper tube and finally a short length of tufnol tube as indicated in figure 2.1. The tufnol tube thermally isolates the calorimeter from higher sections of the guide tube. The copper tube acts as a thermal anchor for the electrical leads and also via helium gas (as an exchange medium) for the specimen tube. The screened lead from the detection coils is ducted up a thin wall stainless steel ($\frac{1}{8}$ inch diameter) tube outside the guide tube (and is not shown in the figure).

Finally, the outer casing of the magnetometer, consisting of the removable lid A, the removable section B, the base C and the removable tail E, comprises a vacuum tight system which may be pumped utilizing the flange D. (The calorimeter is constrained to be coaxial with the outer tail tube E by teflon rings which are slotted to allow evacuation. The guide tube also has several holes drilled through it for the same purpose.)



Figure 2.3. View of tail section with outer tube removed.

The entire magnetometer assembly is self contained and is fixed onto a flange at the top of the cryostat (described later).

With reference to figure 2.4 the principle of operation of the magnetometer is as follows:

The transducer TR is driven by the oscillator OSC and the power amplifier A6 at fixed frequency (approximately 82Hz). This causes the capacitor plates PV, the specimen tube ST, and therefore also the specimen to vibrate synchronously. The vibration amplitude is small (approximately 0.1-0.3mm). The capacitor plate assembly is accurately set to be symmetrical by means of a small DC current which is applied to the transducer TR and adjusted by means of the potentiometer P.

The time varying component of the field due to the specimen vibrating in the magnetic field (generated by the solenoid SM) induces a signal, in the detection coils DC, given (see appendix A2) by

$$v_s = \alpha a \nu M \cos(2\pi\nu t + \phi_s) \qquad 2.1$$

where α is a constant relating to the coils DC,

a is the vibration amplitude,

ν is the vibration frequency,

M is the magnetic moment of the specimen,

and ϕ_s is the phase of the signal relative to the oscillator OSC.

Thus v_s = CONST. x M only if the product $a\nu$ is a constant.

In practice the vibration amplitude (a) cannot be kept exactly constant. This problem is overcome by means of the null method which will now be described.

If a DC potential V is placed on the vibrating plates (PV) a signal will be generated on each of the two stationary plates (PS) of the capacitor which will be given approximately (see appendix A2) by

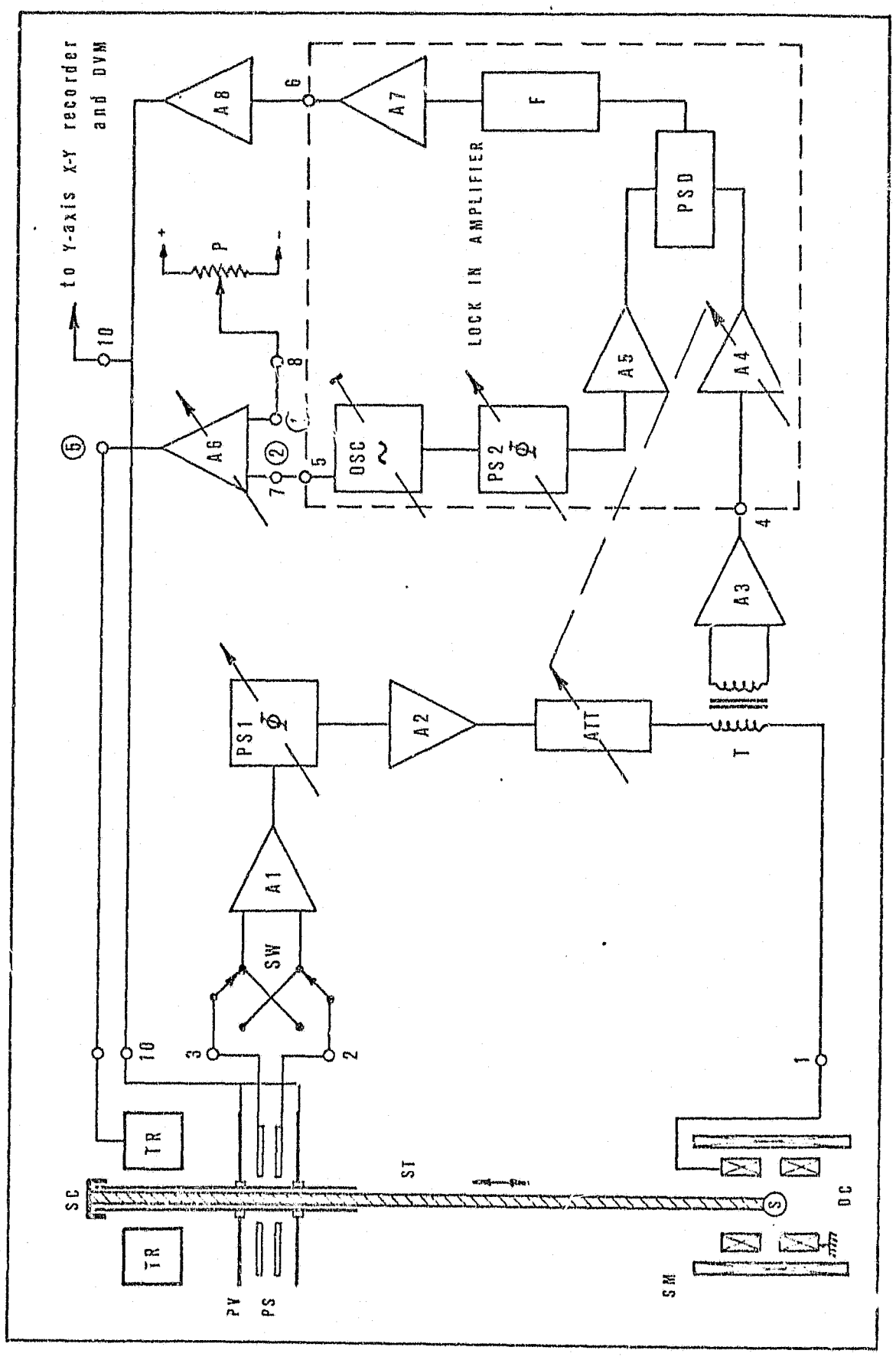


Figure 2.4. Schematic diagram of the electronic layout for the magnetometer.

$$v_R = \pm\beta a\nu V \cos(2\pi\nu t + \phi_R) \qquad 2.2$$

respectively where β is a constant relating to the capacitor geometry and ϕ_R is the phase relative to the oscillator OSC. Again v_R = CONST. x V only if the product $a\nu$ is a constant.

The reference signal v_R is passed through a series of amplifiers and an attenuator (A1, A2 and AT respectively) and its phase is adjusted (by means of the switch SW and the phase shifter PS1) to be identical with that of the signal v_S from the detection coils. It is then mixed with the signal V_S in the primary winding of transformer T. The 'error' signal v_E appearing across the secondary winding of the transformer T is then given by

$$v_E = v_S - G_1 v_R \qquad 2.3$$

where G_1 is the overall gain of the reference channel (comprising A1, PS1, A2 and AT). If v_E is set to zero by suitable adjustment of the D.C. potential V on the vibrating plates PV (equation 2.2) then from equations 2.3, 2.2 and 2.1 the magnetic moment is given by

$$M = AV \qquad 2.4$$

where $A = G_1\beta/\alpha$ is a constant of the system. (Actually G_1 is made variable in decade steps by means of the attenuator AT to give the magnetometer a wide dynamic range). The null method therefore gives the magnetic moment directly in terms of the D.C. potential V independently of the product $a\nu$. V may be adjusted either manually, or automatically by a servo system, which will be described. Both options have been built into the actual design. For automatic operation and error signal v_E must be non zero but may be made arbitrarily small. This will be discussed later. Thus with reference to figure 2.4: the error signal is amplified in the low noise amplifier

A3 and the tuned amplifier A4. It is then synchronously rectified in the phase sensitive detector PSD which is driven by the master oscillator OSC and the amplifier A5. The D.C. output of the phase sensitive detector is proportional to $v_E \cos\theta$ where θ is the phase difference between the signal and reference inputs to the phase sensitive detector. [θ is adjusted by means of the phase shifter PS2 to be zero for $V_S > G_1 V_R$.] This D.C. output signal is then fed through an adjustable low pass filter F which determines the band width or time constant of the system and hence also the signal to noise ratio (see appendix A2). The D.C. signal is then amplified in the amplifiers A7 and A8 and finally applied to the vibrating plates PV. The output voltage of amplifier A8 is in the range $-30 < V < +30$ volts. (This bi-polar output is of great advantage since it allows the magnetic moment of the specimen to change polarity without the necessity of changing the phase of v_R by - using the switch SW).

From the foregoing $V \propto |v_E|$ and the system is in equilibrium when

$$V = \gamma |(v_S - G_1 v_R)| \times \text{sign}(v_S - G_1 v_R) \qquad 2.5$$

where γ is the gain of the detection system (i.e. through T_1, A_3, A_4, PSD, F, A_7 and A_8). v_S and v_R are in phase with each other as discussed previously. Substituting from equations 2.1 and 2.2 for v_S and v_R respectively into equation 2.5 gives

$$V = \gamma[\alpha a\nu M - G_1 \beta a\nu V]$$

$$= [\gamma\alpha a\nu/(1 + G_1\gamma\beta a\nu)]\, M \qquad 2.6(a)$$

In the limit $G_1\gamma\beta a\nu \gg 1$, M is given by

$$M = V(\beta G_1/\alpha) \qquad 2.6(b)$$

which is independent of the product $a\nu$ as expected. (See also

equation 2.4). It is easily shown by substitution that the product $G_1\gamma\beta a\nu$ is equal to v_R/v_E which may be defined as the 'loop gain' of the system. In practice this loop gain is set to be 50 or 100 and is kept constant when G_1 is varied (attenuator AT) by simultaneously varying γ (by altering the gain of amplifier A4). On the most sensitive range the lower loop gain is used. The attenuator AT covers a range of 10^4:1 in five decade steps.

Finally the D.C. potential V (which is proportional to the magnetic moment M) is applied to the Y axis of an X-Y recorder and to a multi-channel digital voltmeter data acquisition system with visual and paper tape output.

Detailed circuit diagrams and the set-up procedure for the magnetometer electronics are given in appendix A2. The ultimate sensitivity and noise figure for the system depend on the design of the detection coils and this is also discussed in appendix A2.

The overall specifications of the magnetometer are as follows:

Dynamic Range:

1:10^4 in decade steps.

Differential Sensitivity:

The system is capable, under ideal conditions, of detecting a change in specimen magnetic moment of less than 10^{-4}emu.

Stability:

Once set up: if the specimen is not disturbed the stability is better than 1 per cent over a 6 hour period.

Reproducibility:

Under the same conditions as above; better than 1 per cent.

Accuracy:

Under the same conditions as above; better than 2 per cent.

Maximum specimen size:

6mm diameter sphere.

2.2.2 Temperature measurement and control

Under working conditions the tail of the magnetometer (see figure 2.1) is immersed over more than one third of its length in liquid helium. Thermal contact between the specimen and the helium bath is achieved by means of helium gas, at reduced pressure (approximately 1mm Hg) which acts as an exchange medium. The gas is admitted via flange D (figure 2.1) after the magnetometer has been thoroughly evacuated and purged with helium gas several times before the system is cooled down. Thermal contact between the outer stainless steel tube E (when immersed in liquid helium) and the copper 'calorimeter' is relatively poor (even with exchange gas in the system) because of the coils of fine wire wound onto it and also because most of its length is covered with several layers of teflon tape for this purpose and also to protect the delicate coil windings. The calorimeter is also thermally isolated from the guide tube by the length of insulating tufnol tubing which supports it. Thus by means of the small heater MH (figure 2.1) the temperature of the calorimeter may be raised rapidly to temperature well above the helium bath temperature (4.05K) without undue loss of heat to the liquid helium. In practice the calorimeter is not raised above 30K. [Direct heating of the specimen is used at higher temperatures.] The calorimeter almost completely surrounds the specimen which is supported at the end of a thermally insulating specimen rod (see appendix A2). For the small power dissipation in the specimen, due to magnetic hysteresis, and in the specimen holder, due to friction of its teflon guide ring on the inside of the calorimeter, the thermal contact between the

specimen and the calorimeter via the exchange gas is sufficient to keep the specimen temperature almost identical to the calorimeter temperature. This was thoroughly checked as will be explained in a later section. The temperature of the calorimeter, and therefore of the specimen also, is measured by means of the germanium resistance thermometer. This thermometer and several others were simultaneously calibrated (J.C. Brock, J.L. Crawford and the author) against two secondary standard germanium thermometers which were calibrated by the courtesy of Professor N.E. Phillips of the Department of Chemistry, University of California, Berkley, U.S.A. Details are given in appendix A4 together with circuits and measuring techniques.

The specifications of temperature measurement are as follows:

Accuracy:

Absolute: depends on the calibration of secondary standard (see Appendix A4), and on calibration against this standard. Should be within ±5mK of the secondary standard.

Relative:

±2mK (at 4K), limited by the resolution and drift of the D.V.M. used to measure the resistance of the thermometer.

Germanium resistance thermometers have a significant magnetoresistance and therefore all temperature measurements were made in zero applied magnetic field.

Two separate systems were used for continuous automatic regulation of the specimen temperature, viz:

(i) For temperatures below about 30K (i.e. for all magnetization measurements on niobium specimens: the carbon resistance thermometer CRT (figure 2.1) and the small manganin heater MH together with a

specially designed A.C. resistance bridge which will be described. The carbon resistance thermometer consists of a carbon resistor (Allen Bradley 47ohm ½ watt with most of its outer insulating jacket removed) which has an insignificant magneto-resistance for H < 10 Koe. (See for example White, 1959 and appendix A4). It is therefore suitable as a sensor for continuous temperature control in varying magnetic fields. The well known disadvantage of a carbon resistance thermometer, namely its irreproducibility with temperature cycling between 300K and 4K, is obviously not important in this application.

(ii) For specimen temperatures in the range 30 < T < 400K (in the present investigation used only for in situ ageing of the specimen) a thermometer and heater are in intimate contact with a special specimen stage (see figure A2.7). In this case the thermometer is a fine (Au-0.3 per cent Fe)-chromel thermocouple with the 'hot' junction at room temperature. The heater is a very small non-inductively wound ultra-fine manganin wire coil (resistance 50ohms). Details of the thermo-couple and a calibration curve, are given in appendix A4. When this system is used the helium exchange gas is pumped from the magnetometer in order to reduce the power requirements of the heater. [With the specimen stage maintained at a temperature of 300K the helium boil-off rate is less than one litre per hour.] In this case the thermo-couple potential is used both for monitoring and for controlling the specimen temperature.

The two systems will now be considered in detail.

(i) Temperature regulation using the carbon resistance thermometer

The properties of the carbon resistor as a low temperature thermometer are discussed in appendix A4.

The design of the A.C. bridge controller is based on long

established techniques (for example, White loc. cit.). The present design however is particularly successful and it is therefore included herein.

With reference to figure 2.5 the principle of operation is as follows:

The carbon resistance thermometer R(CRT) forms one arm of the Wheatstone bridge WB. Compensation for variations due to thermal effects in the long leads to the thermometer in the cryostat is made by using the three lead system as shown. [In practice the three leads are twisted together so that any temperature fluctuation along their length affects all three leads equally.] The bridge is driven via the isolation transformer T at a fixed frequency of about 300Hz by the oscillator OSC and the amplifier A3. The error signal V_E from the bridge ($|V_E| \propto |R-R(CRT)$ near balance) is amplified in the low noise amplifier A1 and the tuned amplifier A2. It is then synchronously rectified in the phase sensitive detector PSD which is driven by the oscillator OSC and the amplifier A3 and A4. The phase difference between the signal and reference inputs to the phase sensitive detector is set to zero by means of the phase shift network PS1. (The output of the phase sensitive detector is continuously monitored at point 5 on a C.R.O.). The rectified output of PSD is then passed through the low pass filter F and unipolar amplifier A5. The output of A5 is applied to the heater MH and is either proportional to the error signal from the bridge or zero depending on the phase of the error signal from the bridge. The carbon resistance thermometer CRT has a negative temperature coefficient so that the switch SW is set to give an output from A5 only when R(CRT)>R. The operation of the system will be considered in detail in appendix A3 where circuit

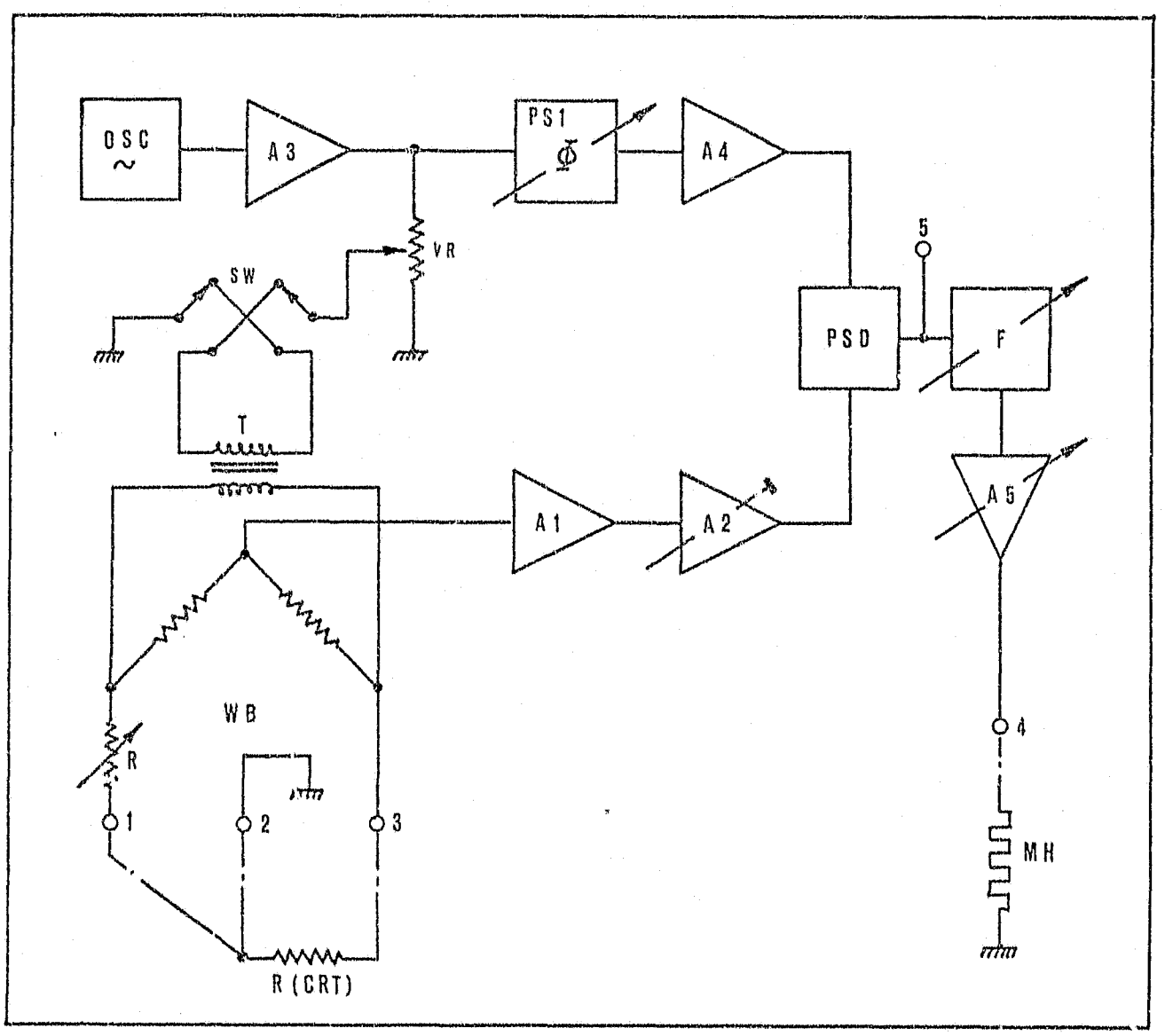


Figure 2.5. Schematic diagram of the electronic layout for the A.C. bridge temperature regulator.

details and the set-up procedures are also given. In practice the current in the bridge (and therefore also the A.C. gain of the system) is determined by the maximum allowable power dissipation in the resistance thermometer. This current is adjustable by means of the potentiometer VR. The D.C. gain is then increased (amplifier A5) and the band width adjusted (F) to give optimum performance within the area of stability of the system.

The overall specifications for the system are as follows:

Oscillation frequency:

Nominally 300Hz.

Bridge current:

0-100μA approximately.

Output:

4.5 watts (15 volts into 50 ohms).

Temperature stability of system:

(Sensor 47ohm Allen Bradley ½ watt resistor).

Short term:

±1mK at 4K.

(ii) Temperature regulation using the thermo-couple

At temperatures above 30K measurement to an accuracy of ±2K is considered to be adequate for the present purposes. For this reason no special care was taken to select 'good' lengths of thermo-couple wire and the 'hot' junction is at room temperature. The gold-iron chromel thermo-couple has a high sensitivity (averaging about 15μV/K between 4K and 300K-see appendix A4) so that the resolution of a temperature difference of 1K in 300K is relatively easy to achieve. The main source of error is due to temperature variations in the 'hot' junction.

The thermo-couple potential is monitored on a Hewlett Packard 3420B D.C. differential Voltmeter/Ratiometer. The voltmeter has a resolution of 1μV and gives an output signal which is proportional to the error voltage when operating in the differential mode. This output is fed to a power amplifier which drives the heater on the sample stage. The principle of operation is then similar to that of the A.C. bridge controller. In operation the desired thermo-couple potential is programmed on the differential voltmeter and the voltmeter gain (or error signal resolution) is increased while the band width of the power amplifier is simultaneously adjusted until optimum performance is obtained.

Further details and circuits are given in appendix A3.

The specifications on measurement and control are as follows:

Accuracy of measurement:

Better than ±2K.

Temperature stability:

Short term : ±0.5K.

Long term : Depends on temperature stability of the hot junction.

Output power:

4.5 watts (15 volts into 50 ohms).

2.2.3 The superconducting solenoid magnet

The solenoid was designed according to the following criteria, viz: (i) a maximum field of about 40 kilo-oersted requiring a maximum current of about 30 amperes (which is the manufacturers expected critical current for the type of wire and magnetic field proposed), (ii) high field homogeneity, particularly axial, (iii) a clear access bore diameter of about 2cm.

The design formulae and the computer program (J.L. Crawford and the author) for figuring the magnet to obtain high axial homoeneity

are given in appendix A5. The final design is shown in figure 2.6 and a photograph of the magnet and its power leads and support assembly is shown in figure 2.7. The main coil and the compensation windings were wound from a single length (approximately 5,000 feet) of Supercon A25 (Nb - 25 per cent Zr) wire (diameter 0.0100" ± 0.0002" plus 0.001" pure electrolytic copper on the radius plus 0.001" nylon on the radius) supplied by Supercon Division of National Research Corporation, Massachusetts, U.S.A. Between each layer is an 0.001" thick nylon film which was cut extra wide to allow for take up during the winding of the coils which was done at a tension of approximately 5 pounds force. All flying leads between coils and current terminals are ducted through gentle curves, grooved or cut into the former material, and are fixed in place with an epoxy resin having a low thermal expansion coefficient. The current terminals consist of grooved copper blocks. The magnet leads, having been stripped of their nylon insulator and tinned with indium, are pressed into the grooves in the copper blocks (which are also filled with indium) as indicated in figure 2.6.

The magnet calibration and homogeneity were checked against the nuclear magnetic resonance (N.M.R.) line in aluminium. The specimen used for this purpose was a moulded pellet of powdered aluminium in an epoxy resin matrix. The specimen and transmitting and receiving coil assembly were designed to allow for accurate positioning, along the axis of the solenoid, from the outside of the cryostat. [illegible]ils of the N.M.R. set up are given in appendix A5. The axial f[illegible] profile obtained from these results is shown in figure 2.8.

The specifications for the magnet are as follows:

Bore diameter:

17mm clear.

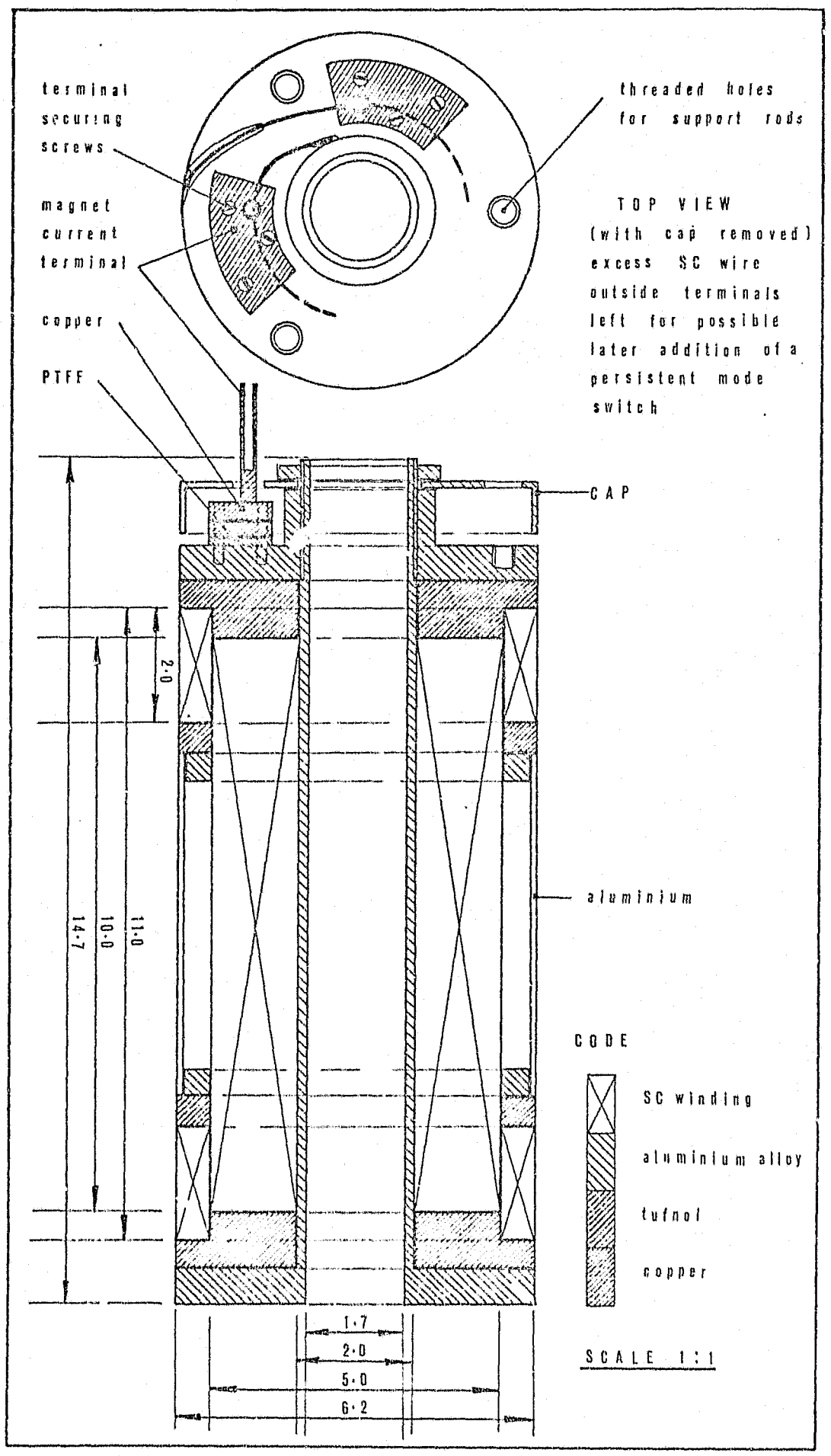


Figure 2.6. The superconducting solenoid magnet.

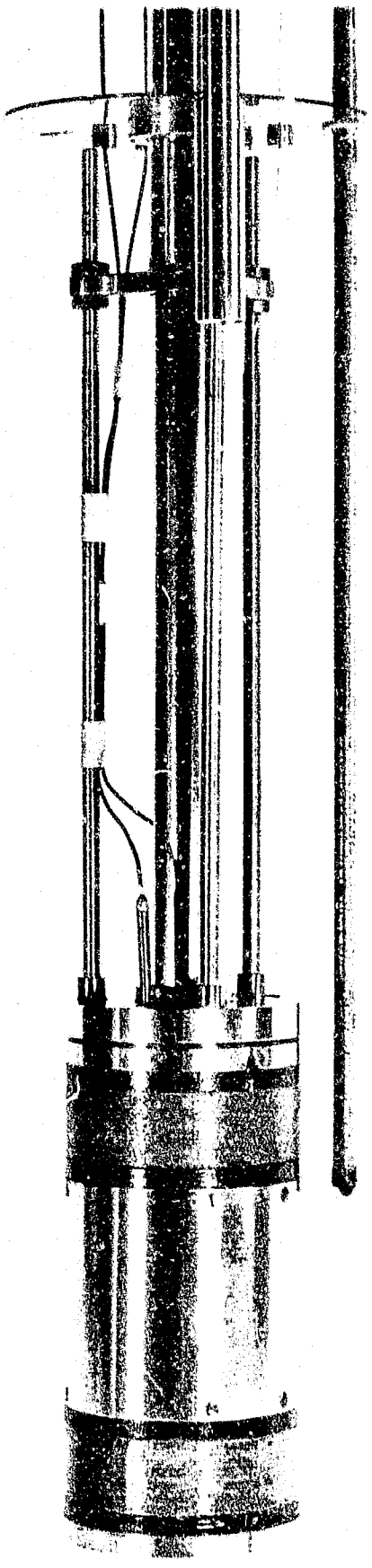


Figure 2.7. View of the superconducting solenoid and support assembly.

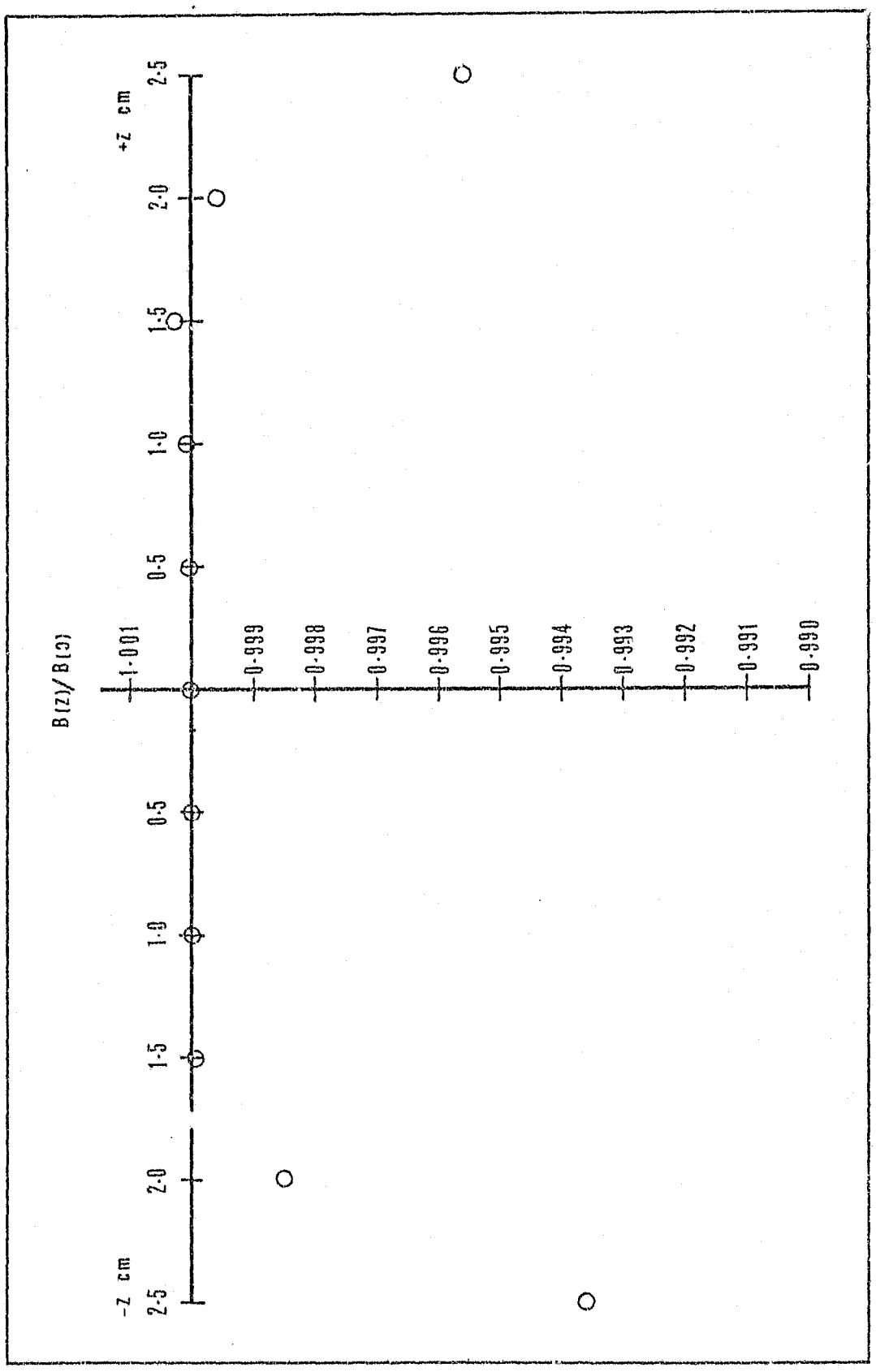


Figure 2.8. The variation of B(z)/B(0) with displacement z along the axis of the superconducting solenoid.

Maximum field:

Greater than 40 kilo-oersted at 4.05K (Actual maximum has not been determined).

Calibration:

1.385 amperes per kilo-oersted (see also appendix A5).

Homogeneity:

Axial: Better than $1:10^4$ over 2cm (see figure 2.8).

Radial: (design) $1 : 10^3$ over 1cm.

2.2.4 Field control and measurement

The power for the superconducting magnet is supplied by an Oxford Instruments Superconducting Magnet Power Supply (0-40amps) which is programmed by an external variable speed motor-driven potentiometer. The magnet current, and therefore the field, is measured by monitoring the voltage across a precision 0.01 ohm 10 watt resistor (in series with the magnet) at high currents and across a 0.1 ohm 5 watt resistor at low currents. This voltage is applied to the X axis of the X-Y recorder and also to the Data Acquisition system.

Circuit details for the programmer and monitoring units together with details of a general purpose Hall probe at the lower end of the solenoid are given in appendix A5.

Specifications:

Power supply : Long term stability : better than $1:10^4$.

2.2.5 The magnetometer cryostat

The basic dewar system is an all metal British Oxygen Company Cryoproducts Model SCM 5. A detailed drawing of the entire cryostat assembly is given in figure 2.9. The magnetometer is shown cross hatched and in outline only and may be removed simply by removing bolts under the 'top flange' and then lifting it out. This leaves the

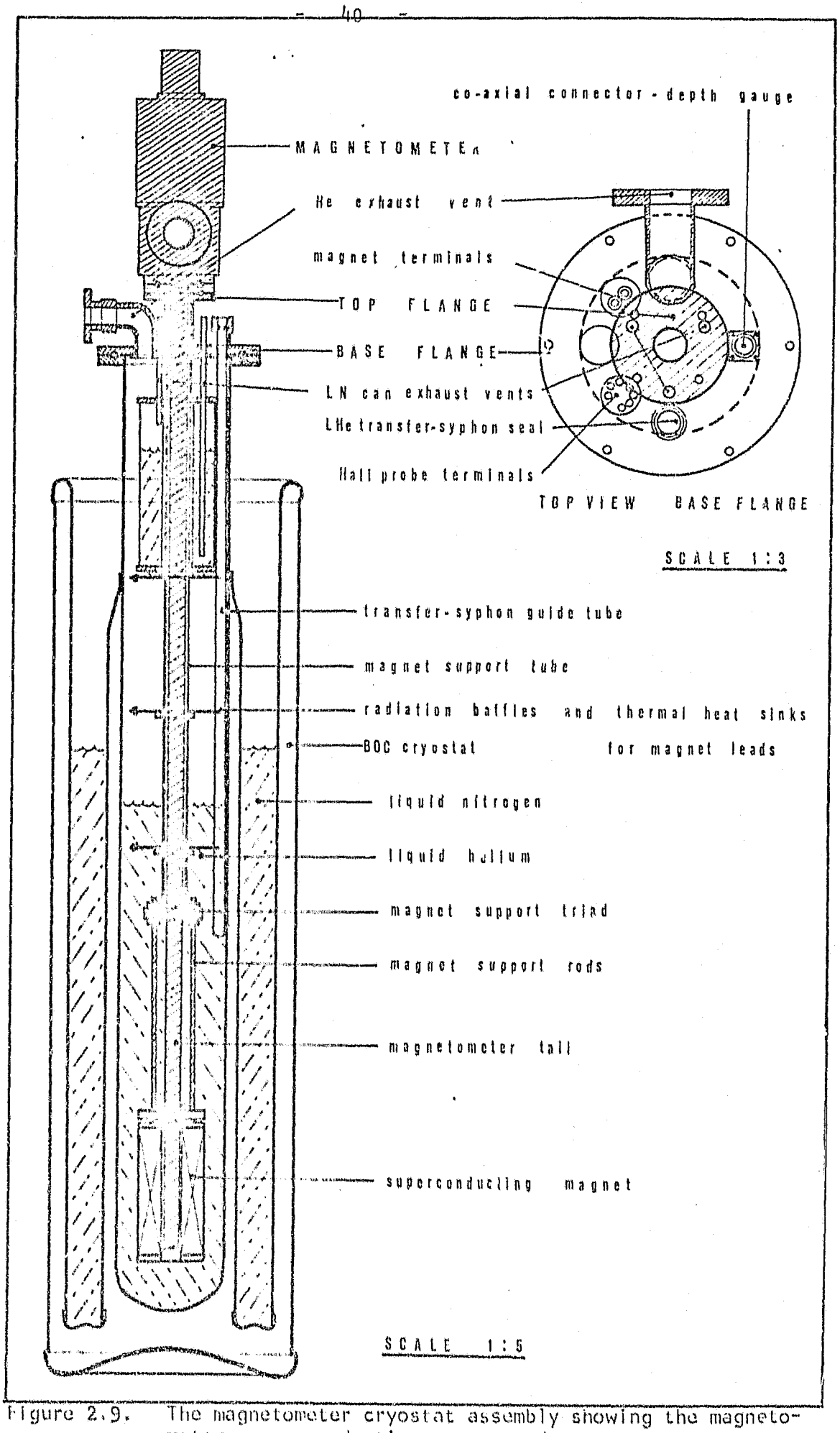


Figure 2.9. The magnetometer cryostat assembly showing the magnetometer, superconducting magnet and magnet support system.

magnet facility free for other applications. (Alternatively other experiments could be done in the temperature regulated calorimeter of the magnetometer.) The diagram is self explanatory but there are several omissions and details which will now be given. The current leads for the magnet are two 22 S.W.G. formvar insulated copper wires. These are soldered into the magnet terminals and then pass through thermal heat sinks in a radiation baffles up to the 'nitrogen' can around which they are wound several times before being connected to feed-through terminals in the base flange. The wire gauge was chosen to minimize thermal conduction and dissipation into the helium bath at currents below about 10 amperes. Also not shown is the helium depth gauge. This is a continuous reading device and is described in appendix A6.

Thermal-acoustic oscillations which will occur in the annular space between the magnetometer tail and the magnet support tube were damped by means of a series of teflon rings (not shown) unevenly spaces along the tail in the annular space.

After an overnight pre-cool (liquid nitrogen in the outer dewar) about 2-3 litres of liquid helium are required before transfer commences and the boil-off rate is less than 3/4 litre per hour under normal working conditions.

2.2.6 Resistivity measurements

A variable temperature cryostat, for the range $4K < T < 300K$ has been designed to measure resistivity by the eddy current decay method described by Bean, De Blois and Nesbitt (1951) using the electronic circuitry of Clarke and Mordike (1966). A brief outline of the method and the theory is given in appendix A7. The method is best suited to specimens of awkward geometry or when it is inconvenient to connect leads to the specimen.

The cryostat is shown in figure 2.10. It consists in essence of an outer liquid nitrogen dewar (glass), a vacuum jacket, an inner liquid helium vessel and the specimen chamber and guide tube. The specimen chamber is a hollow cylinder (made of a plastic of low thermal coefficient of expansion) onto which the primary and secondary coils for the resistivity measurement are wound. A rod of pure silicon which has a high thermal conductivity between 4K and room temperature is fixed into the cylinder with epoxy resin as shown in the figure. The cylinder is fixed to the lower end of the specimen guide tube and the specimen chamber and guide tube are vacuum tight. The silicon rod is connected thermally to the helium can by means of a thin copper wire. This thermal link is adequate to keep the silicon rod at about 5K under normal conditions with no power supplied to the heater on the silicon rod (see later). The temperature of the rod is monitored by two fine gold-iron chromel thermo-couples with 'cold' junctions at 4K and 77K respectively. Several inches of the thermo-couple leads are wound onto the rod to ensure good thermal contact of the junction with the rod. To ensure that the specimen temperature is approximately the same as that of the silicon rod the specimen is lightly smeared with silicone grease and pressed against the silicon rod which is maintained at a temperature of about 300K during this process. The lower end of the specimen rod is made of perspex which is a poor thermal conductor for all temperatures and therefore the thermal input to the specimen is very small.

Temperature regulation is achieved using the regulator which has already been described. A schematic diagram of the system is shown in figure 2.11. R1, R2, R3 in the figure are small carbon resistors which are used for monitoring the depth of liquid helium in the helium

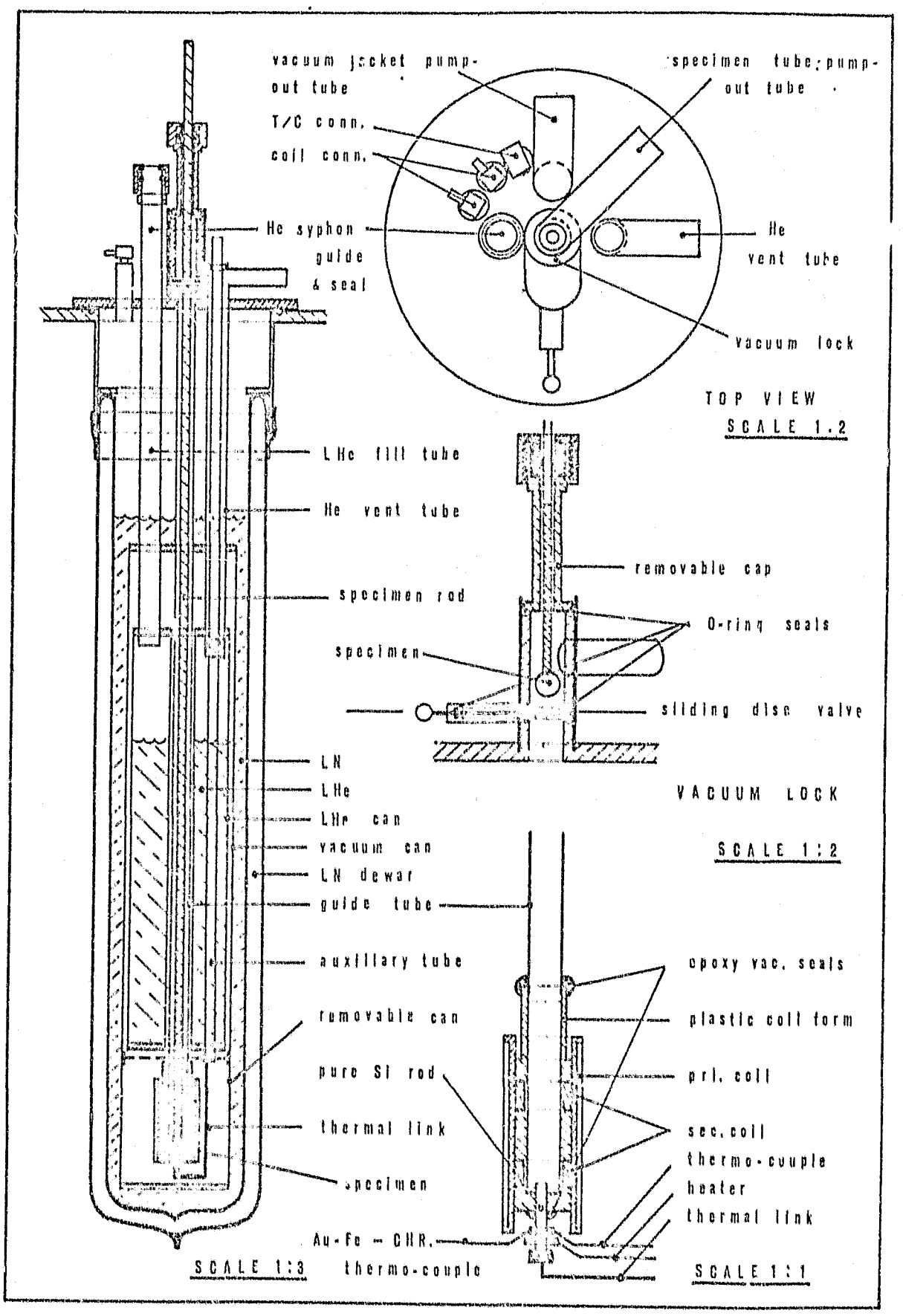


Figure 2.10. The variable temperature cryostat for resistivity measurements.

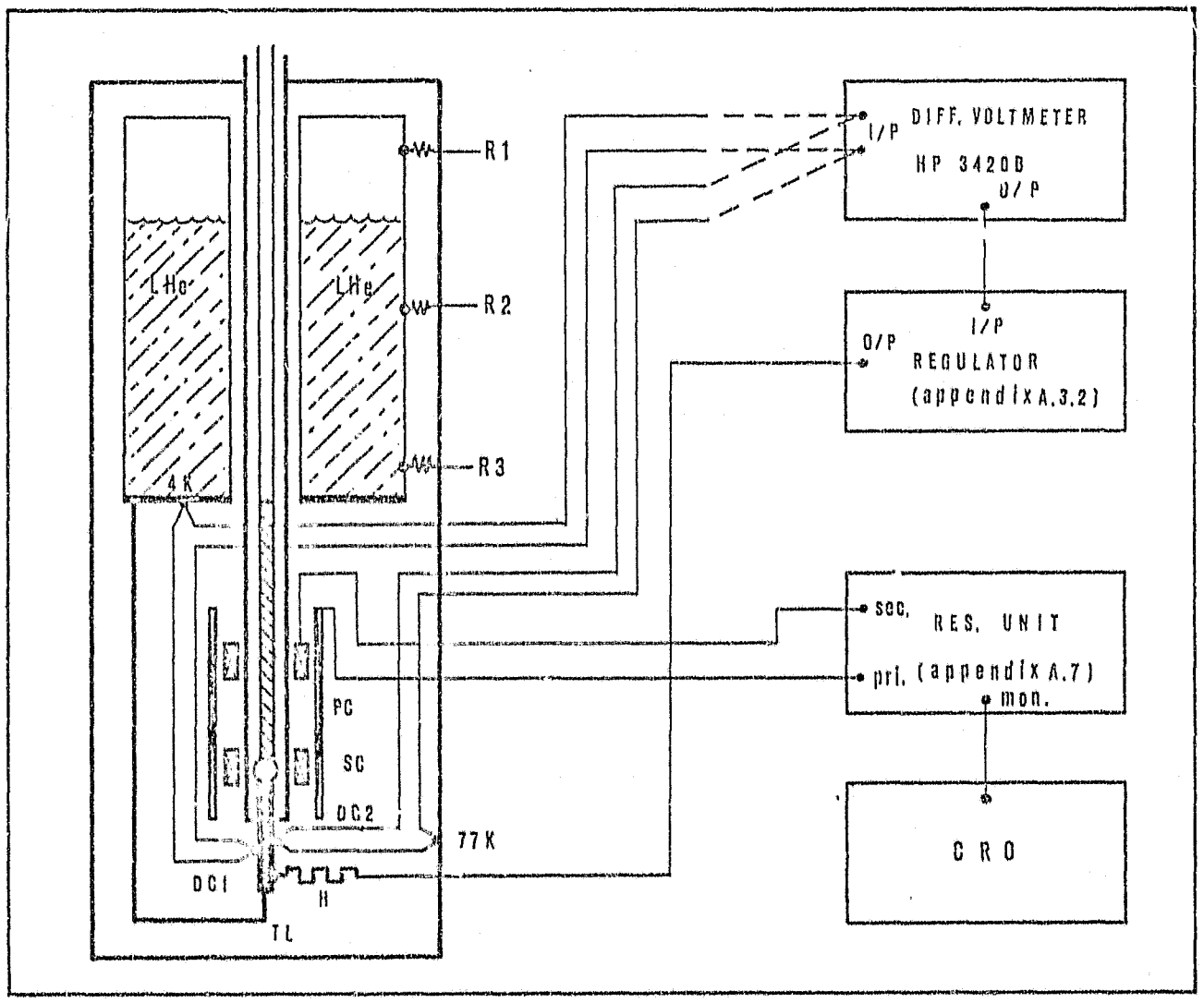


Figure 2.11. Schematic diagram of the system for resistivity measurement and temperature regulation in the variable temperature cryostat.

can. TL represents the thermal link, PC the primary coil, SC the secondary coils, S the specimen, H the heater and DC1 and DC2 the thermo-couples.

Again with reference to figure 2.10 specimen removal is effected by heating the specimen to about 200K when the silicone grease softens. The specimen is then pulled up into the 'vacuum lock', the 'sliding disc valve' is closed and the 'removable cap' is lifted off with the sample. To replace the sample the 'removable cap' is replaced, the lock is evacuated, the sliding valve is opened and sample is finally pushed to the bottom of the cryostat.

The copper wire thermal link is not very satisfactory but suffices for short experiments where a high liquid helium boil-off rate can be tolerated. For long experiments the 'ancillary tube' has been provided so that one of the many variable conduction thermal-link methods may be used. The lower end of the vacuum can is soft soldered into place and may therefore be removed for easy access to the specimen chamber area.

Specifications for the system and the operating methods for resistivity measurements are given in appendix A7.

2.3 System layout

The overall plumbing arrangement for vacuum, helium boil-off recovery and helium purging is shown in figure 2.12. V1 to V16 are vacuum valves. V12 is the sliding valve on the resistivity cryostat and V6, V8 and V13 are free-flow type valves. MV1 is a solenoid vacuum valve which is remotely operated. RP1, RP2 and RP3 are rotary vacuum pumps and DP is an oil diffusion pump with a liquid nitrogen cold trap. G1 and G2 are Bourdon vacuum and pressure gauges respectively. G3 is a cold cathode ionization gauge and G4,

can. TL represents the thermal link, PC the primary coil, SC the secondary coils, S the specimen, H the heater and DC1 and DC2 the thermo-couples.

Again with reference to figure 2.10 specimen removal is effected by heating the specimen to about 200K when the silicone grease softens. The specimen is then pulled up into the 'vacuum lock', the 'sliding disc valve' is closed and the 'removable cap' is lifted off with the sample. To replace the sample the 'removable cap' is replaced, the lock is evacuated, the sliding valve is opened and sample is finally pushed to the bottom of the cryostat.

The copper wire thermal link is not very satisfactory but suffices for short experiments where a high liquid helium boil-off rate can be tolerated. For long experiments the 'ancillary tube' has been provided so that one of the many variable conduction thermal-link methods may be used. The lower end of the vacuum can is soft soldered into place and may therefore be removed for easy access to the specimen chamber area.

Specifications for the system and the operating methods for resistivity measurements are given in appendix A7.

2.3 System layout

The overall plumbing arrangement for vacuum, helium boil-off recovery and helium purging is shown in figure 2.12. V1 to V16 are vacuum valves. V12 is the sliding valve on the resistivity cryostat and V6, V8 and V13 are free-flow type valves. MV1 is a solenoid vacuum valve which is remotely operated. RP1, RP2 and RP3 are rotary vacuum pumps and DP is an oil diffusion pump with a liquid nitrogen cold trap. G1 and G2 are Bourdon vacuum and pressure gauges respectively. G3 is a cold cathode ionization gauge and G4,

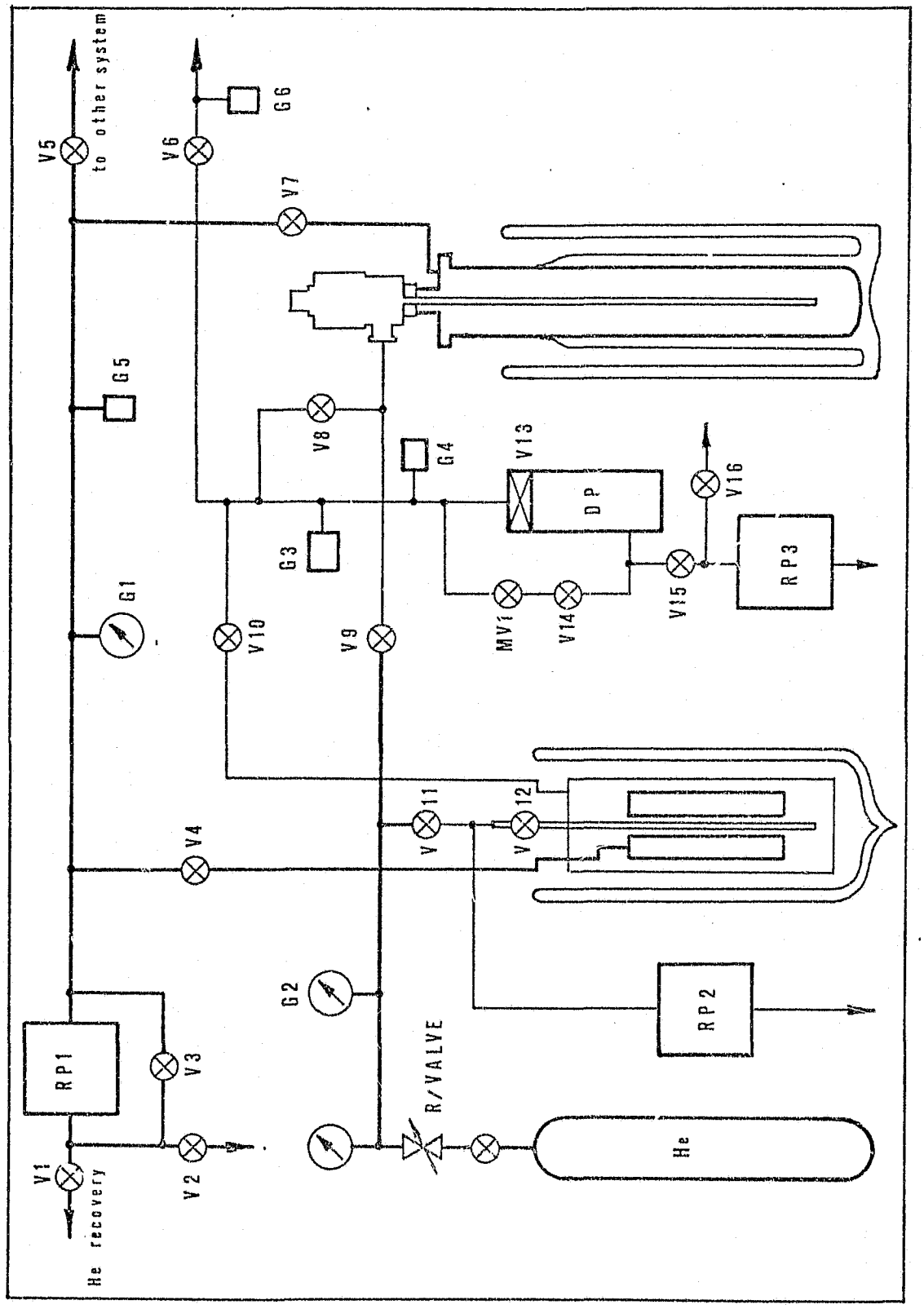


Figure 2.12. Schematic diagram of the vacuum and helium lines for the low temperature systems.

G5 and G6 are thermo-couple vacuum gauges. The heavy line represents helium recovery and other helium gas lines.

The pump RP1 is used for purging and for pumping on the helium bath when desired.

In normal use with the magnetometer the diffusion pump DP is not used. Valves V16 and V13 are kept closed and valves V15 and V14 and V8 open. The valve MV1 is then used to evacuate the magnetometer to the correct exchange gas pressure (~1mm Hg) and valve V9 to flood the magnetometer with helium gas (from the helium cylinder) to a pressure slightly in excess of atmospheric so that the magnetometer lid may be removed without admission of air. [Even small quantities of frozen air in the magnetometer tail are sufficient to cause binding of the specimen holder.]

The diffusion pump is used when a hard vacuum is required - for example when specimen temperatures above 30K are used.

The overall electrical layout for the magnetometer and ancillary equipment is shown schematically in figure 2.13. The diagram is self explanatory if reference is made to figures 2.1 and 2.9 and to the appendices indicated for the various components.

All high impedance and A.C. lines are screened cables.

2.4 Modus operandi (magnetometer)

The helium vessel of the cryostat and the magnetometer are initially thoroughly purged with helium gas by alternatively pumping and flusing and are finally left at atmospheric pressure. The system is then precooled by filling the liquid nitrogen space and then leaving for approximately 16 hours. Helium is transferred and the system is allowed to settle while the electronics are simultaneously warmed up for a period of about 30 minutes. The transducer drive

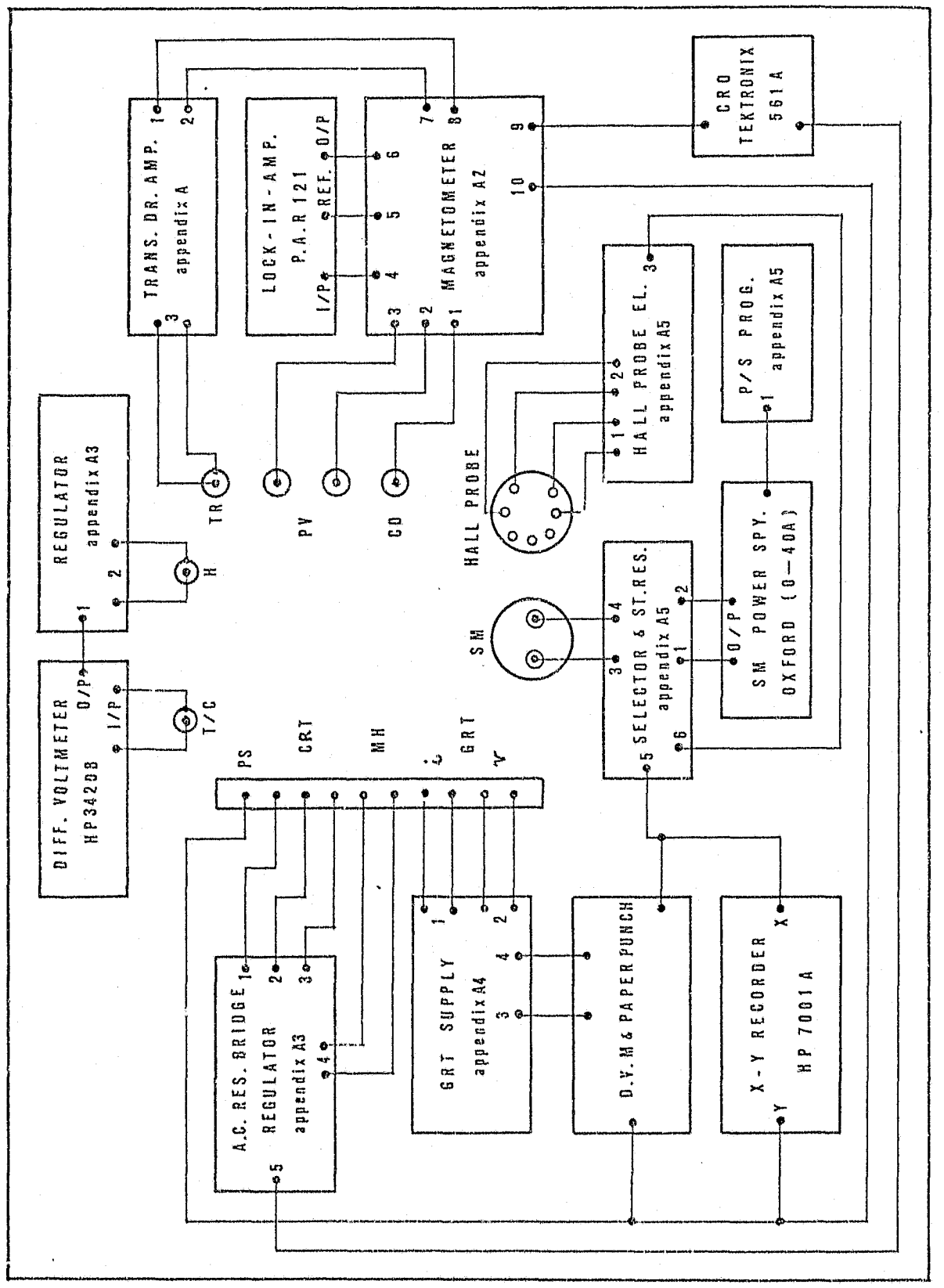


Figure 2.13. Schematic diagram of the electronic layout for the magnetometer and peripheral systems. Labels are clarified in the relevant appendices (as indicated).

amplifier is then switched off. The helium gas pressure in the magnetometer is raised above atmospheric, the lid removed and the specimen rod is lowered into place and screwed down against the locking nut. (The position of the locking nut must previously have been adjusted so that the specimen will be in the saddle point of the detection system (see appendix A2).) The lid is then replaced, the helium gas pressure is reduced to $\sim$ 1mm Hg and the magnetometer is isolated. The transducer drive amplifier is switched on again and the set-up procedure described in appendix A2 is followed. (For subsequent removal and replacements of specimens the set-up procedure need not be repeated.) The calorimeter or specimen temperature is adjusted to the desired value.using one or the other of the temperature regulators,and a suitable sweep-rate is chosen on the magnet power supply programmer. The magnetic field may now be swept up or down, in either sense, and a plot of magnetic moment versus magnetic field can now be obtained on the X-Y recorder and simultaneously, together with the temperature parameters for the GRT, in digitial form on paper tape using the Data Acquisition System.

The sensitivity of the magnetometer may be altered in decade steps, as previously described, but finer steps are obtainable by altering the sensitivity of the Y axis of the X-Y recorder, which also allows a 1000% back-off, so that small regions of the magnetization curve can be expanded.

Finally, when recording magnetic hysteresis loops for type II superconductors, it is desirable to return the specimen to the Meissner state, after each loop, by raising the sample temperature above its critical value T_c in zero applied magnetic field. For this purpose the A.C. bridge temperature regulator is designed to supply power to

the heater (MH), without alteration of its set point, merely by closing a spring loaded push button switch for a suitable short period of time.

CHAPTER 3

3. Theory of Fluxon Pinning

3.1 Introduction

The subject of fluxon pinning has recently been reviewed in excellent articles by Campbell and Evetts (1972) and less specifically by Dew-Hughes (1972). In this chapter only the considerations important for the present work will be dealt with. Special attention will be given to the theory of pinning due to dislocations in the crystal lattice, and to areas of uncertainty where the present investigation has relevance.

Models for the pinning behaviour in type II superconductors are generally based on the concept of the critical state which was first introduced by Bean (1962), Bean and Doyle (1962), Kim, Hempstead and Strnad (1962), London (1963), and Bean (1964). Thus spatial variations in the fluxon lattice density, due to pinning interactions between fluxons and imperfections in the crystal lattice, give rise to a Lorentz driving force density P_L which acts in the opposite direction to the local pinning force density and is given (see for example Evetts, Campbell and Dew-Hughes, 1968) by

$$\vec{P}_L(B) = -(1/4\pi)\vec{B} \times \nabla \times \vec{H}$$

$$-(1/c)\vec{B} \times \vec{J}$$

where B and H are local values for the induction and field respectively and J is a macroscopic current density. In the critical state model the Lorentz force density approaches the pinning force density $P_V(B)$, i.e. $P_L(B) \simeq P_V(B)$, as the fluxon lattice approaches some

static equilibrium condition with no fluxon movement. This condition cannot be fully realized in practice because of the so-called phenomenon of flux-creep which results from thermal activation of 'bundles' of fluxons over pinning barriers (Anderson, 1962 and developed by Anderson and Kim, 1964). In the usual experimental situation however, the duration time for the experiment is sufficiently short that the effect of flux-creep may be neglected but is still sufficiently long that the fluxon lattice may be considered to be in quasi-static equilibrium. In magnetization experiments the current density J is thus either zero or some critical value $J_c(B)$ everywhere in the superconductor and can be determined from the above expressions (see also appendix 1(e)). This model has been amply verified experimentally and the dependence of J_c on B has been found to vary considerably for different fluxon pinning situations.

The fundamental problem is then to predict the dependence of J_c on the induction B and on the temperature T for any particular pinning situation. This involves the problem of relating the pinning force density to the interaction between a lattice of self interacting fluxons and a distribution of pinning sites in the superconductor. The solution will depend on the volume density, distribution and geometry of the pinning sites, their basic interaction mechanism with the fluxons, co-operative effects between pinning sites and finally on the elastic properties of the fluxon lattice.

It is usual to treat the problem of formulating a model for the prediction of $P_v(B,T)$ as two separate problems, viz: (i) that of establishing the basic pinning mechanism at an elementary pinning site and obtaining an explicit expression and (ii) the determination of the overall fluxon lattice response to the elementary pinning site array, i.e. the method of summing the elementary pinning forces to

obtain the bulk pinning force density P_v.

In the case of fluxon pinning in lightly deformed materials however, the elementary pinning sites which are associated with the dislocations have not previously been definitely identified. (The reason for this will become apparent later.) This particular pinning situation is apparently rather complicated and most of the insight to date can be attributed to the rigorous statistical treatment of Labusch (Labusch, 1969b). This treatment will be briefly reviewed later. For the moment however, it will be useful to outline a few conclusions of Labusch's calculation. Thus: It is necessary first to distinguish between so-called 'dilute' and 'concentrated' arrays of randomly distributed pinning sites. In essence for the former case the force fields of the pinning sites do not overlap so that the distortion of the fluxon lattice due to a particular site is negligibly small at an adjacent site. In the dilute limit - 'lattice approximation' (see later) Labusch predicts a threshold requirement for the strength of a point-like pinning site, relative to a certain function of the elastic constants of the fluxon lattice, for which the pinning site is effective. It is well known (and later demonstrated) however, that a screw or edge dislocation segment at any orientation with respect to the fluxon lattice apparently does not satisfy this threshold requirement. In accordance with Labusch's model it must therefore be concluded that dislocations can only pin fluxons either by a diffuse co-operative interaction (i.e. in the concentrated limit) or otherwise the pinning sites must constitute small discrete regions of relatively high local dislocation density (due to statistical fluctuations - see for example Labusch (1969b) and Fietz and Webb, 1969, or dislocation tangles) which for lightly deformed materials may

then satisfy the dilute limit criterion (see later). Labusch indicates how, in general, the concentrated limit may be treated but gives an explicit expression for P_v only in the dilute limit - 'lattice approximation'. It will become apparent later that some confusion as to the basic pinning sites in lightly deformed materials has resulted through the use of this expression outside its range of validity and through substitution of incorrect expressions for the basic pinning force at an elementary fluxon-site interaction.

Various other dilute-limit summation methods which should be mentioned, but will not be required in this investigation, include the statistical model of Lowell (1972) and the so-called dynamical models of Yamafuji and Irie (1967), Lowell (1970) and Good and Kramer (1970). In this latter model the frictional force due to pinning interactions (interaction energy E_s) is obtained by assuming that a uniform fluxon lattice velocity $\langle v \rangle$ will result from a steady applied pressure P on the fluxon lattice. The work done (Pv per unit volume) is then equated to the power dissipated as the fluxons are released from their pinning sites. Thus $P\langle v \rangle / N_A = 2E_s \langle v \rangle . a_o$ where N_A is the density of sites per unit area and a_o is the fluxon lattice parameter.

The relevant aspects of the problem outlined above will now be treated separately and in detail.

3.2 The basic interaction mechanisms

As discussed in Chapter 1 the fluxon consists of a core region (radius ξ), in which the order parameter $|\psi|^2$ is depressed, and a magnetic region (radius λ) in which the magnetic field is finite. Currents circulating in this region support the radial gradient in the magnetic field.

Associated with the depressed order parameter in the fluxon is a crystal lattice dilation $\delta\varepsilon_{ij}$ and also a change in the crystal lattice

elastic moduli δC_{ij} relative to the surrounding superconducting matrix. The magnetic field in the fluxon also gives rise to a small local magneto-striction in the crystal lattice.

A fluxon may therefore interact with dislocations by the following mechanisms:

(i) The stress field associated with a dislocation interacts with the strain field of the fluxon. (It is however mathematically more tractable to calculate the interaction between the strain field of the dislocation and the stress field of the fluxon (Kramer and Bauer, 1967).) The interaction is linear in the strain of the dislocation and it is therefore known as the first-order elastic interaction.

(ii) The stress or strain field of a dislocation interacts with the changed elastic moduli associated with the fluxon. This interaction energy is quadratic in the strain of the dislocation and is therefore known as the second-order elastic interaction.

(iii) Strain gradients and the presence of atmospheres of an impurity solute (which reduce the associated stresses) in the vicinity of the dislocations locally reduce the mean free path of normal electrons. This leads to an increase in κ and H_{c2} (see chapter 4), and therefore to change in the local line tension of a fluxon (equation 1.1).

Various other contributions due to strain gradient and non-linear elastic effects have also been considered (Seeger and Kronmuller, 1968 and Kronmuller and Seeger, 1969). Fluxons may also be pinned by magnetic image effects across the boundary separating two regions of different κ, H_c or H_{c2}.

Order of magnitude calculations have been made (see later) of the absolute magnitudes of the various pinning interaction contributions

for various dislocation - fluxon lattice interaction configurations. For an isolated dislocation however, at any orientation with respect to the fluxon lattice, these interaction contributions apparently all fail by more than an order of magnitude to satisfy Labusch's threshold condition. The basic pinning site may therefore involve co-operative effects between several dislocation segments. For a random or non-uniform dislocation distribution a comprehensive treatment of the basic pinning interaction including all of the interaction mechanisms is prohibitively and unnecessarily complex. The usual practice has therefore been to attempt to establish the predominant mechanism. This will depend on the dislocation type and configuration and also on the Ginzburg-Landau parameter κ for the superconductor. Although it is often possible from theory to establish the approximate relative importance between the first and second-order elastic interaction mechanisms the relative contribution of these latter mechanisms compared with the contribution due to local variations in κ and H_{c2} in non-uniform dislocation distributions has not previously been established with any certainty. Previous experimental evidence in this regard is also inconclusive (see the introduction to chapter 5). This latter problem should however be easily resolvable by experiment since the temperature and field dependences of the elastic and the $\delta\kappa$ or δH_{c2} mechanisms are not the same (see later).

The most comprehensive approach to the basic interaction problem has been through the Ginzburg-Landau theory. A brief outline of this approach will now be given: Thus it is convenient to separate the problem into two parts, viz:

(i) The calculation of the variation in the free energy of the mixed state due to a local perturbation in the parameters κ, H_c and/or

H_{c2} only, i.e. neglecting all changes in the elastic energy associated with the defects giving rise to the changes these parameters and

(ii) the calculation of changes in the elastic energy.

The free energy variation, to first order, due to the former is given (Campbell and Evetts, 1972 and see appendix A1a) by

$$\delta E = (1/4\pi)\int H_c^2(-\frac{\delta H_{c2}}{H_{c2}}\left|\psi\right|^2 + \frac{1}{2}\cdot\frac{\delta\kappa^2}{2\kappa^2}\left|\psi\right|^4)d^3r \qquad 3.1$$

where ψ is the unperturbed relative order parameter or wave function and the integration is taken over all space. The free energy variation due to the latter is determined from the full strain dependent Ginzburg-Landau theory. The treatment outlined below is due to Labusch (1968) (see also Miyahara, Irie and Yamafuji, 1969). Thus the Ginzburg-Landau expression (see appendix A1a) for the free energy is extended to include the strain dependences to second-order in terms of a strain tensor ε_{ij} which is defined to be zero in an unconstrained perfect crystal in the normal state. Variational methods are then used to obtain the so-called modified Ginzburg-Landau equations for the vector potential $\vec{A}$ and wave function ψ and also the modified elasticity equations. (From these latter equations Labusch derives useful equations which relate the changes in the elasticity constants and the dilation of the material, which occur at the superconducting-normal transition, to experimentally determinable parameters - see later.) To determine the interaction between fluxons and the strain field of a defect the exact solutions ψ_o, $\vec{A}_o$ and ε_{oij} are first obtained for the modified Ginzburg-Landau and the modified elasticity equations. From the changes in the boundary conditions for the elasticity equations, which result with the introduction of a defect (strain η_{oij} in the normal state) new equations for $\vec{A}$ and ψ are obtained by substitution

of $\varepsilon_{ij} = \varepsilon_{oij} + \eta_{ij}$ into the modified Ginzburg-Landau equations. The terms containing η_{ij} are then treated as perturbations and the solutions of these equations are given in terms of perturbation series of the form $\psi = \psi_o + \sum_{n=1}^{\infty} \phi_n$ and $A = A_o + \sum_{n=1}^{\infty} \alpha_n$ where ϕ_n and α_n are proportional to the nth power of η_{ij}. These new solutions for ψ and $\vec{A}$ and $\varepsilon_{ij} = \varepsilon_{oij} + \eta_{ij}$ are then substituted back into the expression for G which now includes terms in powers of η. The first and second-order contributions to the Gibbs free energy in terms of η are then obtained from this expression. The first-order interaction is given (using the Einstein notation for summation over repeated indices) by

$$\delta E_1 = \int \eta_{oij} [C^n_{ijk\ell} \varepsilon_{ok\ell} - (H_c^2/4\pi) [a_{ij} |\psi_o|^2 - \tfrac{1}{2} b_{ij} |\psi_o|^4]] d^3r \quad 3.2$$

where η_{ij} has been replaced by η_{oij} (since $\eta_{oij} \simeq \eta_{ij}$), $C^n_{ijk\ell}$ is the elastic constant tensor in the normal state,

$$a_{ij} = (1/H_{c2}) \partial H_{c2}/\partial \varepsilon_{ij} \text{ and } b_{ij} = (1/\kappa^2) \partial \kappa^2/\partial \varepsilon_{ij}.$$

The two terms in the square brackets of equation 3.2 are of the same order. The first term is the stress arising solely from the imposed strain and the second term corrects for the spontaneous relaxation of the crystal lattice. In the absence of any external or defect strain therefore

$$C^n_{ijk\ell} \varepsilon^f_{k\ell} = (H_c^2/4\pi) [a_{ij} |\psi_o|^2 - \tfrac{1}{2} b_{ij} |\psi_o|^4]. \quad 3.3$$

The expression for the second-order interaction is very complicated and involves the perturbation parameters ϕ and α which are very difficult to obtain. However, for the special case of a defect strain field η_{ij} which has only shear components the terms containing

ϕ and α vanish and Labusch gives for the second order interation in this case

$$\delta E_2 = \int \eta_{ij}\,\eta_{k\ell}\left[\tfrac{1}{2}c^{n}_{ijk\ell} - (H_c^{\,2}/8\pi)\left[a_{ijk\ell}|\psi_o|^2 - \tfrac{1}{2}b_{ijk\ell}|\psi_o|^4\right]\right] d^3r \qquad 3.4$$

where $a_{ijk\ell} = (1/H_{c2})\partial^2 H_{c2}/\partial\varepsilon_{ij}\partial\varepsilon_{k\ell}$ and $b_{ijk\ell} = (1/k^2)\partial^2\kappa^2/\partial\varepsilon_{ij}\partial\varepsilon_{k\ell}$

For a quantitative comparison of the above expressions for the first and second-order elastic interactions with experiment the values of the coefficients a_{ij}, b_{ij}, $a_{ijk\ell}$ and $b_{ijk\ell}$ are required. Labusch gives these coefficients in terms of experimentally measurable parameters but because a_{ij} and b_{ij} and $a_{ijk\ell}$ and $b_{ijk\ell}$ are usually not measured separately and are moreover very small there is still some doubt about their absolute magnitudes and temperature dependences. (The will be discussed in more detail later and for a complete review see Campbell and Evetts, 1972).

The interaction force between a pinning defect and the fluxon lattice is found by evaluating δE (from the pertinent equations) as a function of the position of the fluxons relative to the defect. The pinning force is then given by the gradient in δE at the point of elastic instability (i.e. where the threshold condition is satisfied - see later).

In the following two sections approximate expressions for the $\delta\kappa$ and the elastic pinning mechanisms will be derived (from the two parameter Ginzburg-Landau treatment outlined above) in order to establish their approximate absolute magnitudes and dependences on field and temperature.

3.2.1 The $\delta\kappa$ basic interaction

For an isolated dislocation the $\delta\kappa$ interaction is easily shown to be insignificant. However for dislocation braids, tangles, for

cell walls and for dislocations with associated atmospheres of solute atoms the elastic or stress dependent interactions will be modified and augmented by the so-called stress independent interactions which may predominate. These latter interactions result from local variations in the electronic mean free path and therefore in κ and H_{c2} or from local variations in the density of electronic states and therefore in T_c and H_c (see chapter 4).

The variety and number of published expressions for the pinning force due to interactions of this type are manifold (see for example the review articles cited previously). For the present purposes however only interactions due to variations in $\delta\kappa$ need be considered (this will be justified in chapter 5). The published expressions for this case are valid only in the limit as the reduced induction $b = B/B_{c2} \to 1$ and usually only for high κ materials. They are therefore not considered to be adequate and a more detailed treatment will be formulated here.

Thus consider equation 3.1 for the difference in the local Helmholtz free energy (excluding elastic contributions) between the mixed and normal states to first-order in the perturbations in the material-dependent coefficients α and β in the Ginzburg-Landau theory (see appendix 1a). In the derivation of this expression it was assumed that H_c is not perturbed by the variations in the material properties. (This will be justified for the present pinning sites later.) Now since $H_{c2}(T) = \sqrt{2}\,\kappa_1 H_c(T)$, $H_{c2} = B_{c2}$ and assuming that $\delta\kappa_1(T)/\kappa_1(T) = \delta\kappa/\kappa$*: δE(from equation 3.1) may be expressed as:

---

* This assumption is probably fair but is difficult to justify. For discussion of κ_1 and its relationship to κ see for example Tewordt (1965), Neumann and Tewordt 1966a, 1966b, Eilenberger (1967) and Jacobs (1971a and 1971b).

$$\delta E(t) = -(B_{c2}^2(t)/8\pi\kappa_1^2(t)) \int (\delta\kappa/\kappa)\left[\,|\psi|^2 - |\psi|^4\right] d^3r \qquad 3.5$$

where $t = T/T_c$ is the reduced temperature. [In previous treatments it has effectively been assumed that $|\psi|^2 >> |\psi|^4$ and that therefore the term in $|\psi|^4$ may be neglected. This is valid as $b \to 1$ but it will become apparent that it is a very poor approximation for a large range of b at all values of $\kappa > 1/\sqrt{2}$.]

The spatial variation of $\left[\,|\psi|^2 - |\psi|^4\right]$ will now be determined as a function of the reduced induction b. At low values of b the numerical calculations of Neumann and Tewordt (1966) for the radial dependence of the zero order Ginzburg-Landau solution for the normalized order parameter f_o about an isolated fluxon will be used. These calculations have been made for various values of κ and the results for $f_o(r/\lambda_L)$ at $\kappa = 1$ are reproduced in figure 3.1. Also shown in the figure are the derived curves for $|\psi|^2 = f_o^2$ and $|\psi|^2 - |\psi|^4$ as a function of r/λ_L. As expected $|\psi|^2 - |\psi|^4$ at the centre of the fluxon and also at large distances from an isolated fluxon is zero. Thus variations of κ near the centre of a fluxon and also, for low values of b, in the regions far from any fluxon cause no variation in the free energy (equation 3.5). The equilibrium position for a sufficiently small region with $\delta\kappa > 0$ is at $r/\lambda_L \simeq 1$ in the present case. It is also apparent from these results that significant fluxon core overlap does not occur until the reduced fluxon separation $a_o/\lambda_L \lesssim 2r/\lambda_L \simeq 4.5$. The corresponding value for the reduced induction b is easily obtainable in terms of a_o/λ_L from the following expressions, viz:

$a_o(t) = (2/\sqrt{3})^{\frac{1}{2}} \cdot (\phi_o/B_{c2}(t))^{\frac{1}{2}}$, $B_{c2} = \phi_o/(2\pi\xi^2)$ and $\kappa = \lambda/\xi$,

and is given by

$$b(t) = (2.68\lambda(t)/\kappa a_o(t))^2 \qquad 3.6$$

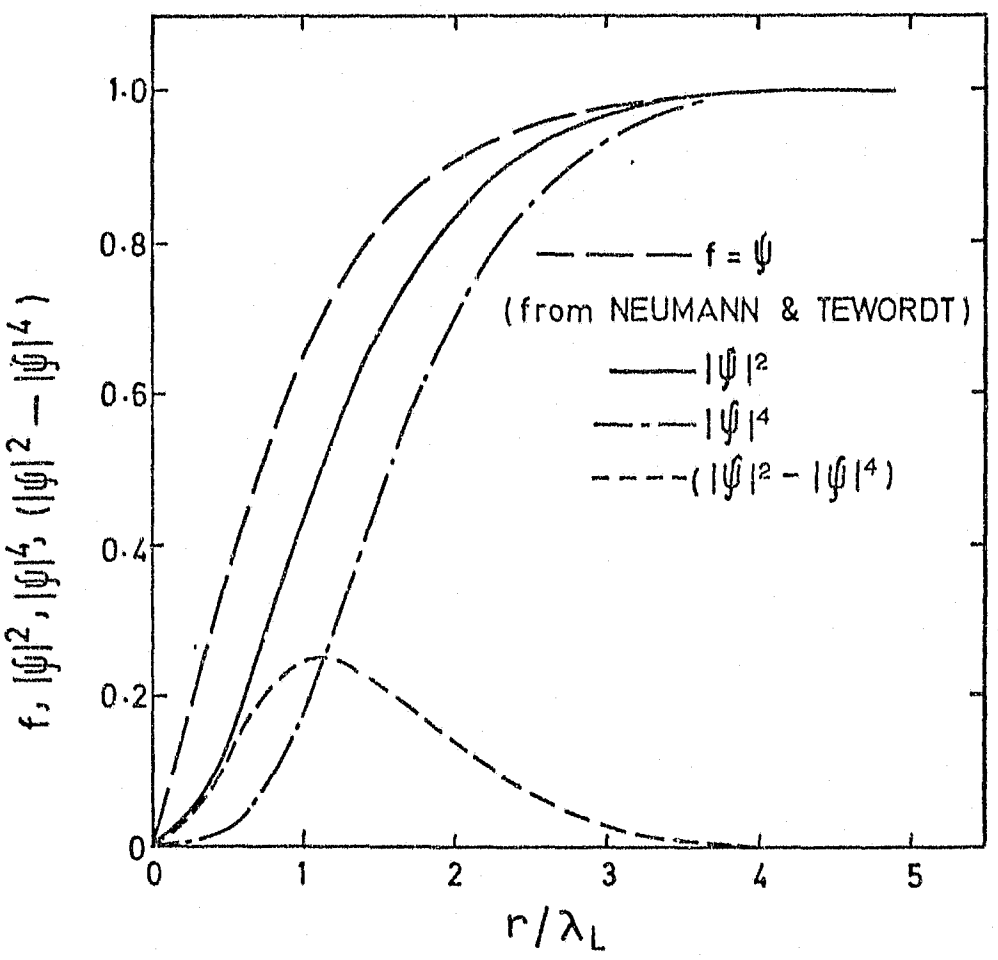


Figure 3.1. The variation of ψ, $|\psi|^2$, $|\psi|^4$ and $|\psi|^2-|\psi|^4$ (from Neumann and Tewordt, 1966) for an isolated fluxon as a function of the reduced distance r/λ_L from the fluxon axis. λ_L is the London penetration length.

Putting $a_o/\lambda_L = 4.5$ and $\kappa = 1$ gives $b = 0.35$. [For $\kappa = 5$ the value of a_o/λ_L for significant core overlap, estimated directly from the results of Neumann and Teword (loc. cit.) is approximately 0.8 giving $b = 0.45$.]

For low values of b it may be assumed that the spatial variation of $[\,|\psi|^2 - |\psi|^4]$ can be obtained from the total depression in the order parameter (i.e. $1 - |\psi|^2$) at a particular point by linearly summing the contributions to this depression due to each of the surrounding nearest fluxons. Thus with reference to figure 3.2 the value of $1 - |\psi|^2$ at a distance y/a_o along the y axis is given by

$$\begin{aligned} \langle 1 - |\psi|^2 \rangle_{(y/a_o)} = {} & A_1(y/a_o) + A_1(\sqrt{3}/2 - y/a_o) \\ & + 2A_1(1/4 + (\sqrt{3}/2 - y/a_o))^{\frac{1}{2}} \\ & + 2A_1(1 + (y/a_o)^2)^{\frac{1}{2}} \end{aligned} \qquad 3.7$$

where $A_1(x) = (1 - |\psi|^2)_x$, for an isolated fluxon.

The variation of $(|\psi|^2 - |\psi|^4)$ along the y axis can then be determined from the expression

$$[\,|\psi|^2 - |\psi|^4]_{y/a_o} = \langle 1 - |\psi|^2 \rangle_{y/a_o} [\,1 - \langle 1 - |\psi|^2 \rangle_{y/a_o}] \qquad 3.8$$

Using the results of figure 3.1 and equations 3.6, 3.7 and 3.8 $[\,|\psi|^2 - |\psi|^4]_{y/a_o}$ has been determined for various values of the reduced induction in the range $0 < b \leq 0.6$. These results are shown by the solid curves in figure 3.3. (The dashed curves show the behaviour $[\,|\psi|^2 - |\psi|^4]$ along the x axis.)

At larger values of b, $|\psi|^2$ varies approximately sinusoidally through the fluxon lattice and may be approximated by its first harmonic. Saint James, Sarma and Thomas (1969) have calculated $|\psi|^2$ in this approximation and their result (in cartesian co-ordinates - see figure 3.2) may be expressed as

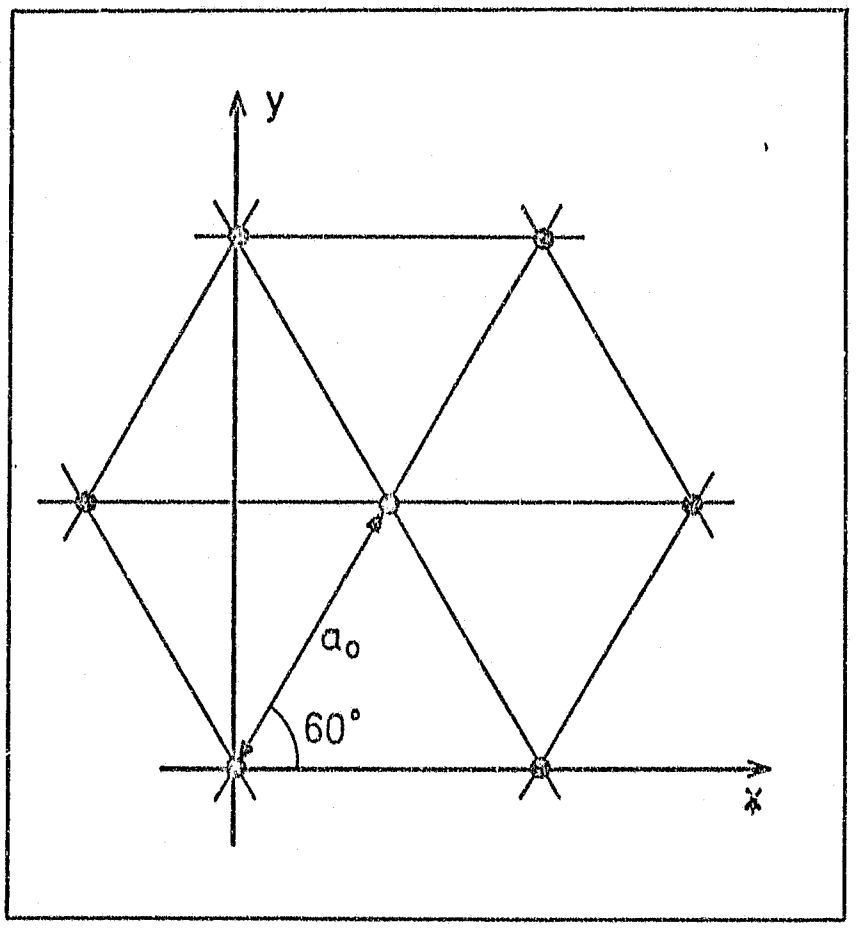


Figure 3.2. The co-ordinate system for the description of the fluxon lattice.

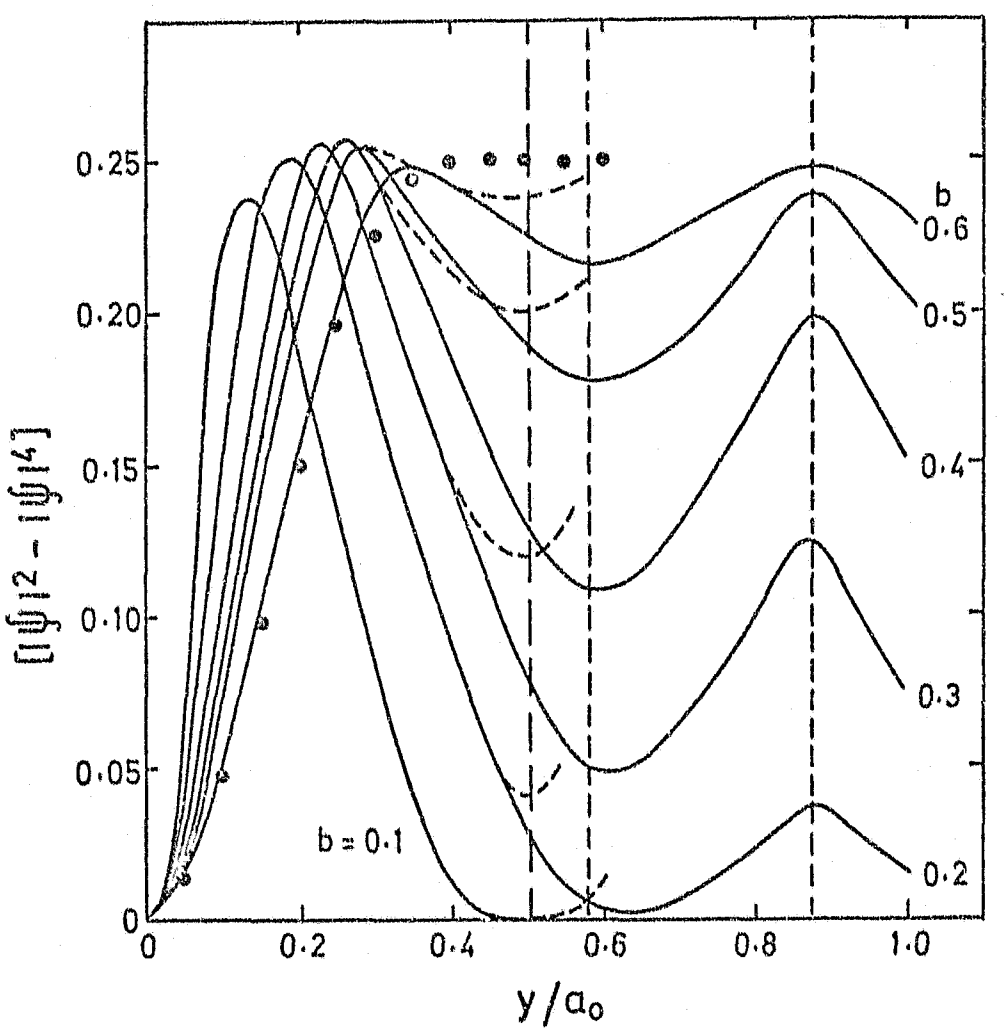


Figure 3.3. The variation of $|\psi|^2-|\psi|^4$ versus the reduced distance along the y axis of figure 3.2 for various values of the reduced induction $b=B/B_{c2}$ (full curves). The points have been obtained from equations 3.8 and 3.9 with $b = 0.6$. The dashed curves show the variation along the x axis.

$$|\psi|^2 = (1-b)\left[1-1/3\left[\cos(2\pi(x+y/\sqrt{3})/a_o) + \cos(2\pi.2y/\sqrt{3}a_o) + \cos(2\pi(x-y/\sqrt{3})/a_o)\right]\right] \qquad 3.9$$

The results for $\left[|\psi|^2 - |\psi|^4\right]$ as determined from this equation at $b = 0.6$ (see also equation 3.6) are shown by the points in figure 3.3.

[In this approximation if $\left[|\psi|^2 - |\psi|^4\right]_{r/a_o}$ is substituted into equation 3.5 and the integration taken over unit volume the free energy density change δE_v due to a change $\delta\kappa$ in κ over the entire volume is given approximately by

$$\delta E_v \sim (B_{c2}(t)/\kappa_1^2(t))(\delta\kappa/\kappa)\left[(1 - b) - (1 - b)^2\right]$$

The free energy change per unit length of fluxon is therefore given by

$$\delta E_f = \delta E_v(\phi_o/B) \sim (B_{c2}(t)/\kappa_1^2(t))(\delta\kappa/\kappa)(1 - b)$$

This is substantially the same as the result obtained by Hampshire and Taylor (1972) using the high κ, high field expression of Goodman (1966) for the free energy difference between the mixed and the normal states and it will become apparent that its validity is restricted to this regime.]

The interaction force between a fluxon and a region of different κ is given by the gradient in the interaction energy. For effective pinning, i.e. dissipation, an elastic instability is required however and the exact determination of the effective pinning force is not generally possible without a detailed knowledge of the shape of the pinning potential. This obviously involves the characteristics of the pinning site. However, an expression for the maximum pinning force should be obtainable with sufficient accuracy, given an approximate knowledge of the pinning site characteristics, to experimentally test models for the bulk pinning force density and to permit observations

concerning Labusch's threshold criterion (i.e. for the elastic instability (see section 3.3)).

In this approximation the pinning force due to a region of disparate κ is given (from equation 3.5) by

$$p_m(b,t) = \left[dE/dr\right]_{max} = -\left[B_{c2}^2(t)/8\pi\kappa_1^2(t)\right]\left[\, d/dr\left(\int(\delta\kappa/\kappa)\quad|\psi|^2 - |\psi|^4\quad d^3r\right)\right]_{max} \qquad 3.10$$

where the integration is taken over the volume of the region. For small regions, i.e. having dimensions, normal to the direction of the fluxon $\langle R\rangle \ll a_o$ this expression for p_m may be simplified to fair approximation, thus:

$$p_m(b,t) \simeq -\left[\, B_{c2}^2(t)/8\pi\kappa_1^2(t)\,\right]\left[\,\delta\kappa/\kappa\,\right]_{eff.} V\left[\, d/dr\,(|\psi|^2 - |\psi|^4)\right]_{max} \qquad 3.11$$

where V is the volume of the region, $\left[\delta\kappa/\kappa\right]_{eff.}$ is the mean effective value in the region (see chapter 4) and $Z = \left[\, d/dr\,(|\psi|^2 - |\psi|^4)\right]_{max}$ the gradient at the spatial point where it is a maximum. This point is relatively close to the axis of the fluxon (see figure 3.3a) in the region where $|\psi|^2$ is approximately cylindrically symmetric about the fluxon.

In figure 3.4 values of Za_o obtained directly from figure 3.3 (points) and by differentiation of equation 3.8 on substitution for $|\psi|_y^2$ from equation 3.9 (circles) have been plotted against b. The solid curve shows the overall behaviour. From this result $Z(\phi_o/B)^{\frac{1}{2}} = Za_o b^{\frac{1}{2}}$ is plotted and tabulated against b in figure 3.5. The solid curve (a) in the figure is a plot of $Z = \alpha B_{c2}^{1/2}(t)$ and curve (b) is a plot of $Z = \beta B_{c2}^{\frac{1}{2}}(1-b)$ where α and β are constants. The transition from the former to the latter behaviour occurs at $b = 0.4$. Thus finally, on substitution for Z into equation 3.11, the basic

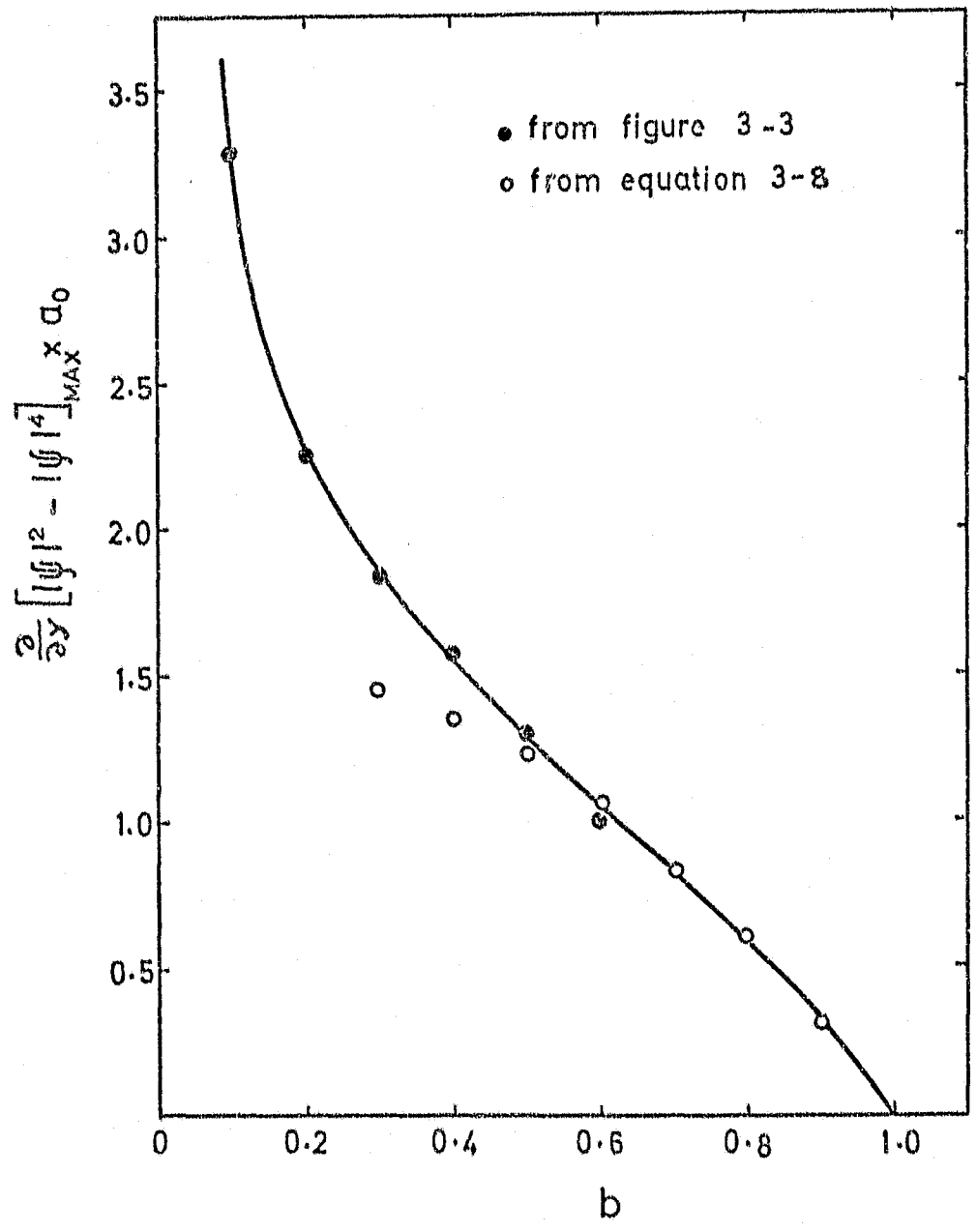


Figure 3.4. From the results of figure 3.3 and equations 3.8 and 3.9 the maximum gradient in $[|\psi|^2-|\psi|^4]a_o$ along the y axis is shown (solid curve) as a function of the reduced induction.

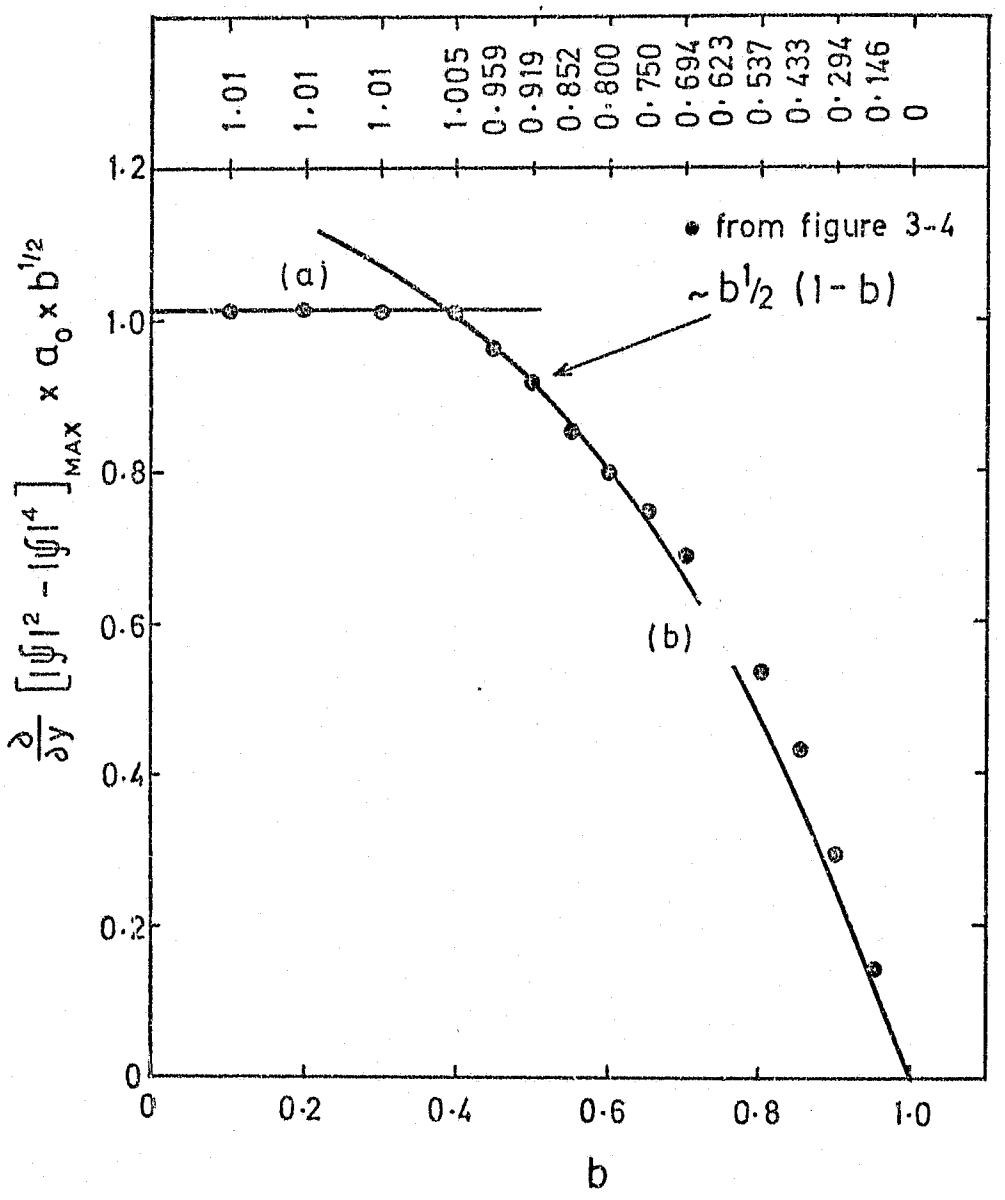


Figure 3.5. The variation in the maximum gradient in $B_{c2}^{-\frac{1}{2}}[|\psi|^2-|\psi|^4]$ along the y axis as a function of the reduced induction.

pinning force p_m behaves as follows:

for $b \lesssim 0.4$

$$p_m(b,t) \propto [\, B_{c2}{}^{5/2}(t)/\kappa_1^2(t)\,][\, \delta\kappa/\kappa\,]_{\text{eff.}}{}^{V} \qquad 3.12a$$

and for $b \gtrsim 0.4$

$$p_m(b,t) \propto [\, B_{c2}{}^{5/2}(t)/\kappa_1^2(t)\,] \,.\, b^{\frac{1}{2}}(1-b)[\, \delta\kappa/\kappa\,]_{\text{eff.}}{}^{V} \qquad 3.12b$$

3.2.2 The stress dependent (elastic) basic pinning interactions

(a) The first-order interaction

For the cubic isotropic case the first-order elastic interaction energy (equation 3.2) may be expressed (Labusch, 1968) as

$$\delta E_1 = \int \eta_{oij}\sigma_{ij}^{f}\, d^3r \qquad 3.13$$

where σ_{ij}^{f} is the nett unperturbed stress field of the fluxons (corresponding to the term in the square brackets of equation 3.2).

On the assumption that b_{ij} (in equation 3.2) is negligibly small σ_{ij}^{f} has been determined for an isolated fluxon by Kramer and Bauer (1967) from the exact analogy of the thermal stress due to a cylindrically symmetric temperature gradient in an infinite isotopic cylinder. Thus the dilation at a radial distance r from the axis of a fluxon is assumed to be given by

$$\delta\varepsilon_v(r) = \delta\varepsilon_{vo}.\tilde{\omega}(r) \qquad 3.14$$

where $\delta\varepsilon_{vo}$ is the relative dilation between the normal and the superconducting states in zero field and in the analogy corresponds to the volume coefficient of thermal expansion. $\tilde{\omega}(r)$ is a disorder parameter corresponding in the analogy to the temperature change. Kramer and Bauer use the reasonable very low field or isolated fluxon assumption viz:

$$\tilde{\omega}(r) = 1 - |\psi|^2 \simeq [\ 1 - \exp(-r^2/\xi^2)\ ] \qquad r > \xi$$

and obtain expressions (within the analogy - from Timoshenko and Goodier, 1951) for the stresses σ_{ij}^{f}. These are given (in cylindrical co-ordinates) by

$$\sigma_{rr} = A(\xi^2/r^2)\ [\ 1 - \exp(-r^2/\xi^2)\ ]$$

$$\sigma_{\theta\theta} = A\ [\ (2 + \xi^2/r^2)\ \exp(-r^2/\xi^2) - (\xi^2/r^2)\ ] \qquad 3.16$$

and $\sigma_{zz} = 2A\ \exp(-r^2/\xi^2)$

where $A = -\delta\varepsilon_o\mu(1 + \nu)/3(1 - \nu)$ and μ and ν are the shear modulus and Poisson's ratio respectively.

The corresponding stress tensor $\vec{\sigma}$ consists of the following components (in cartesian co-ordinates):

$$\vec{\sigma} = \begin{bmatrix} \sigma_{xx} & \sigma_{xy} & o \\ \sigma_{yx} & \sigma_{yy} & o \\ o & o & \sigma_{zz} \end{bmatrix} \qquad 3.17$$

where the z co-ordinate is collinear with the axis of the fluxon. (Formulae relating these cartesian components to the stresses in cylindrical co-ordinates (i.e. σ_{rr}, $\sigma_{\theta\theta}$ and $\sigma_{r\theta}$) are derived in appendix A1(b).

Kramer and Bauer (loc. cit.) determine the interaction force between the stress tensor $\vec{\sigma}$ and the strain field of a dislocation (for various interaction configurations of both edge and screw dislocation) using the well known Peach - Koehler equation, viz:

$$\vec{F} = -\ \vec{\sigma}.\ \vec{b}_o \times \vec{t} \qquad 3.18$$

where $\vec{b}_o$ is the Burgers vector for the dislocation and $\vec{t}$ is a unit vector collinear with the dislocation line.

$$\tilde{\omega}(r) = 1 - |\psi|^2 \simeq [\ 1 - \exp(-r^2/\xi^2)\ ] \qquad r > \xi$$

and obtain expressions (within the analogy - from Timoshenko and Goodier, 1951) for the stresses σ^{f}_{ij}. These are given (in cylindrical co-ordinates) by

$$\sigma_{rr} = A(\xi^2/r^2)\ [\ 1 - \exp(-r^2/\xi^2)\ ]$$

$$\sigma_{\theta\theta} = A\ [\ (2 + \xi^2/r^2)\ \exp(-r^2/\xi^2) - (\xi^2/r^2)\ ] \qquad 3.16$$

and $\sigma_{zz} = 2A\ \exp(-r^2/\xi^2)$

where $A = -\delta\varepsilon_o\mu(1 + \nu)/3(1 - \nu)$ and μ and ν are the shear modulus and Poisson's ratio respectively.

The corresponding stress tensor $\vec{\vec{\sigma}}$ consists of the following components (in cartesian co-ordinates):

$$\sigma = \begin{bmatrix} \sigma_{xx} & \sigma_{xy} & o \\ \sigma_{yx} & \sigma_{yy} & o \\ o & o & \sigma_{zz} \end{bmatrix} \qquad 3.17$$

where the z co-ordinate is collinear with the axis of the fluxon. (Formulae relating these cartesian components to the stresses in cylindrical co-ordinates (i.e. σ_{rr}, $\sigma_{\theta\theta}$ and $\sigma_{r\theta}$) are derived in appendix A1(b).

Kramer and Bauer (loc. cit.) determine the interaction force between the stress tensor $\vec{\vec{\sigma}}$ and the strain field of a dislocation (for various interaction configurations of both edge and screw dislocation) using the well known Peach - Koehler equation, viz:

$$\vec{F} = -\ \vec{\sigma}.\ \vec{b}_o \times \vec{t} \qquad 3.18$$

where $\vec{b}_o$ is the Burgers vector for the dislocation and $\vec{t}$ is a unit vector collinear with the dislocation line.

The most significant and important first-order interaction results when an edge dislocation is parallel to the fluxon. For this case (following the scheme of Kramer and Bauer - see figure 3.6), defining orthogonal unit vectors $\vec{i}$, $\vec{j}$ and $\vec{k}$ to be collinear to the x, y and z axes respectively, the edge dislocation is characterized by $\vec{b}_o = - b_o \vec{i}$ and $\vec{t} = \vec{k}$, the fluxon is parallel to $\vec{k}$ at $x = y = o$ and the radial distance between the dislocation and the fluxon is $\vec{r}_o$ where $\vec{i}.\vec{r}_o = r_o \theta \cos$. The interaction force per unit length is then given using equation 3.18, by

$$\vec{p}^{\ell} = - b_o \begin{bmatrix} \sigma_{xx} & \sigma_{xy} & 0 \\ \sigma_{yx} & \sigma_{yy} & 0 \\ 0 & 0 & \sigma_{zz} \end{bmatrix} \begin{bmatrix} -1 \\ 0 \\ 0 \end{bmatrix} \times \begin{bmatrix} 0 \\ 0 \\ 1 \end{bmatrix}$$

$$= b_o \left[\sigma_{xy} \vec{i} - \sigma_{xx} \vec{j} \right] \qquad 3.19$$

substituting for σ_{xy} and σ_{xx} from appendix A1(b) gives

$$\vec{p}^{\ell} = -b_o \left[((\sigma_{\theta\theta} - \sigma_{rr})\cos\theta\sin\theta)\vec{i} + (-\sigma_{rr} - (\sigma_{\theta\theta} - \sigma_{rr})\cos^2\theta)\vec{j} \right] .$$

If the relative movement between the fluxon and the dislocation is only along the y axis ($\theta = \pi/2, 3\pi/2$) then

$$\vec{p}^{\ell} = \pm b_o \sigma_{rr} \vec{j} \qquad 3.20$$

Substituting for σ_{rr} from equation 3.16 gives

$$\vec{p}^{\ell} = \pm b_o A \left[(\xi^2/r^2)(1 - \exp(- r^2/\xi^2)) \right] \vec{j}$$

For $r \lesssim \xi/2$ and $= \pi/2$, $\pi/2$ the magnitude $|\vec{p}^{\ell}|$ has its maximum attainable value, viz:

$$|\vec{p}^{\ell}_{m}| = A b_o \qquad 3.21$$

and is repulsive for $\theta = \pi/2$ and attractive for $\theta = 3\pi/2$.

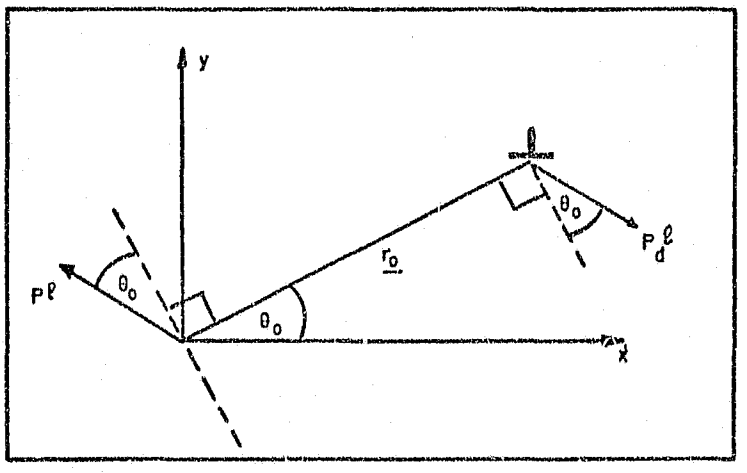


Figure 3.6. The forces due to the interaction between an edge dislocation at r_o with a Burgers vector in the negative x direction and a fluxon collinear with the r=0 axis.

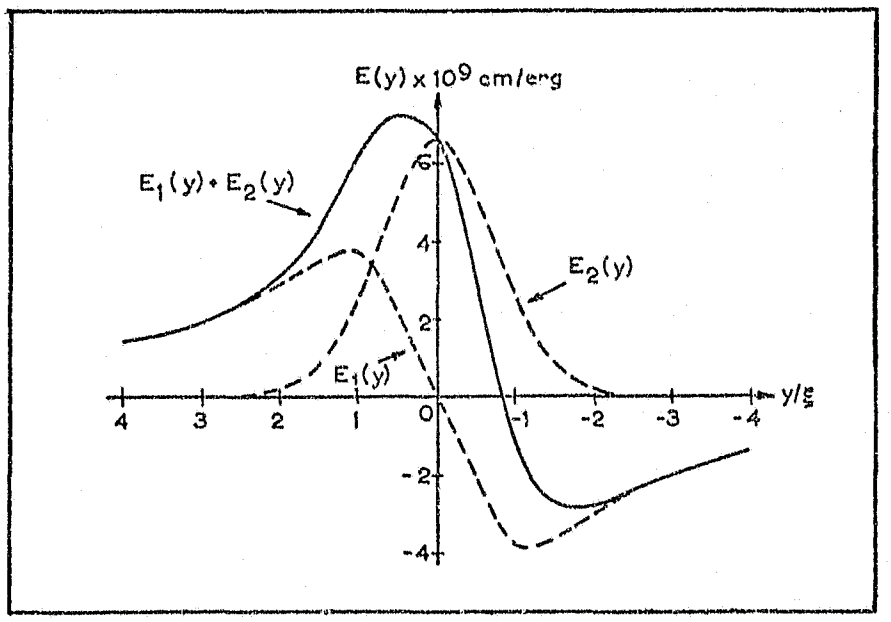


Figure 3.7. The interaction energy, at 4.2K in niobium, between a fluxon collinear with the z axis and a parallel edge dislocation as a function of its position on the y axis. The first order (E_1), second order (E_2) and combined ($E_1 + E_2$) interaction energies are shown. (From Kramer and Bauer, 1967.)

For relative movement along the x axis ($\theta = 0, \pi$)

$$\vec{p}^{\ell} = b_o \, \sigma_{\theta\theta} \cdot \vec{J}$$

and $$p_m^{\ell} = Ab_o \quad \text{for } r \leqslant \xi/2 \qquad 3.22$$

These results for p_m^{ℓ} are valid only for an isolated fluxon or at low b. At moderate to high inductions (i.e. $b \gtrsim 0.4$) when the fluxon cores overlap it is necessary to consider the stress field of the fluxon lattice rather than that of an isolated fluxon. Using the high field approximation for $|\psi|^2$ given by equation 3.9 (and see figure 3.2) Campbell and Evetts (1972) derive the stress function ϕ from the thermal analogy and obtain

$$\phi = (A/2)(1-b)\left(\frac{a_o}{2\pi}\right)^2 \left[\cos\left[\frac{2\pi}{a_o} (x+y/\sqrt{3}) \right] + \cos\left[\frac{2\pi}{a_o} \cdot \frac{2y}{\sqrt{3}} \right] + \cos\left[\frac{2\pi}{a_o} (x - y)\sqrt{3}) \right] \right] \qquad 3.23$$

The stresses are then given by

$$\sigma_{xx} = (A/18)(1-b)\left[\cos\left[\frac{2\pi}{a_o} (x+y/\sqrt{3}) \right] + 4 \cos\left[\frac{2\pi}{a_o} \frac{2y}{\sqrt{3}} \right] + \cos\left[\frac{2\pi}{a_o} (x - y/\sqrt{3}) \right] \right]$$

$$\sigma_{yy} = (A/2)(1-b)\left[\cos\left[\frac{2\pi}{a_o} (x + y)/\sqrt{3}) \right] + \cos\left[\frac{2\pi}{a_o} (x - y/\sqrt{3}) \right] \right] \qquad 3.24$$

$$\sigma_{xy} = (A/2\sqrt{3})(1 - b)\left[\cos\left[\frac{2\pi}{a_o} (x - y/\sqrt{3}) \right] - \cos\left[\frac{2\pi}{a_o} (x + y/\sqrt{3} \right] \right]$$

$$= 0 \quad \text{for } x = 0 \text{ or } y = 0$$

For an edge dislocation with $\vec{b}_o = b_o \hat{j}$ and $\vec{t} = \vec{k}$ (using previous definitions) the Peach-Koehler formula gives

$$\vec{p}^{\ell} = \left[\sigma_{yy} \, \vec{i} + \sigma_{xy} \vec{j} \right] b_o$$

and therefore

$$\vec{p}^{\ell} = \vec{p}_m^{\ell} = \pm b_o \, A(1 - b)\vec{i} \qquad 3.25$$

for $x \simeq 0$ and $x = a_o/2$ respectively and $y = 0$. This prediction differs in magnitude from that of equation 3.21 for the low field limit only by a factor of (1-b).

For niobium at 4.2K, substituting for A from equation 3.16 into equation 3.25 with $\delta\varepsilon_{vo} = 3 \times 10^{-7}$, $\mu = C_{44} = 3 \times 10^{11}$ dynes cm^{-2}, $b_o = 3 \times 10^{-8}$cm, $\nu = 1/3$ and $b = 0.5$ gives

$$p_m^{\ell} = 10^{-3} \text{ dynes cm}^{-1}.$$

The first-order elastic interaction due to crystal defects other than isolated dislocations, where the Peach-Koehler formula cannot be used directly, results in a maximum pinning force (see equation 3.13 and previous section) given by

$$\vec{P}_m = \left[(\vec{i}\partial/\partial x + \vec{j}\partial/\partial y) \int \eta_{oij}\sigma_{ij}^{f}\, d^3r \right]_{max} \qquad 3.26$$

Expanding the term under the integral and discarding components which are zero or irrelevant gives finally (in the co-ordinate system used above)

$$\vec{P}_m = \left[(\vec{i}\partial/\partial x + \vec{j}\partial/\partial y) \int_o^{\infty}\int_o^{\infty}\int_o^{\infty} \left[\eta_v\sigma_v{}^{f} + \sigma_{xy}(\eta_{xy} + \eta_{yx}) \right] dxdydz \right]_{max} \qquad 3.27$$

where η_v is the trace of the defect strain tensor ($\eta_v = \Delta V/V$) and σ_v^f is the trace of the fluxon or fluxon lattice stress tensor. Thus from equation 3.16:

for $b < 0.4$:

$$\sigma_v^f = (\sigma_{xx} + \sigma_{yy} + \sigma_{zz}) = 4A \exp(-r^2/\xi^2) \qquad 3.28a$$

and for $b > 0.4$ from equation 3.24:

$$\sigma_v^f = \frac{2}{9} A(1-b)\left[5 \cos\left[\frac{2\pi}{a_o} (x - y/\sqrt{3})\right] + 2 \cos\left[\frac{2\pi}{a_o} \cdot \frac{2y}{\sqrt{3}}\right]\right.$$

$$\left. + 2 \cos\left[\frac{2\pi}{a_o} (x + y/\sqrt{3})\right]\right] \qquad 3.28b$$

The strain tensors η_{ij} for coherent and non-coherent precipitates and for various dislocation networks are obtainable from the literature. For coherent pricipitates which have dimensions ($x_o < a_o$, $y < a_o$, z_o) (i.e. either small spheres or needle shaped) the calculation of p_m from equation 3.27 is relatively straight-forward. Also for small spherical precipitates the stress tensor may be conveniently expressed in terms of a misfit parameter α (Kramer and Bauer, 1967). In this case the pinning force is given by

$$\vec{p}_m = \left[(\vec{i}\partial/\partial x + \vec{j}\partial/\partial y) V.\alpha\sigma_v \right]_{max} \qquad 3.29$$

where V is the volume of the spherical precipitate.

Finally, to complete the present description of the first-order interaction it is necessary to specify the magnitude and the temperature dependence of $\delta\varepsilon_{vo}$. This is somewhat problematical (see the review by Campbell and Evetts, 1972). $\delta\varepsilon_{vo}$ is known (Labusch, 1968) to be given by

$$\delta\varepsilon_{vo} = 3(H_c(t)/4\pi)\left[\partial H_c/\partial P \right]_v \qquad 3.30$$

The temperature variation of $\partial H_c/\partial P$ is slow and has been found to be given approximately by $(c+dt^2)$ where c and d are positive constants with c > d. (White, 1962, Andres, Olsen and Rohrer, 1962). [According to White (loc. cit.) $(\partial Hc/\partial P)_{T=T_c} = -(1.2\pm0.3) \times 10^{-9}$ Oe dyne^{-1} cm^2 and $(\partial Hc/\partial P)_{T=0} = -(1.2\pm0.1) \times 10^{-9}$ Oe. dyne^{-1} cm^2.] Substituting for $\left[\partial Hc/\partial P\right]_{T=0}$ in equation 3.30 and multiplying by $Hc(0) = 1.95 \times 10^3$ oersted gives

$$\delta\varepsilon_{vo}(t) \simeq 5.5 \times 10^{-7}.\ H_c(t)/H_c(0) \qquad 3.31$$

neglecting the apparently small temperature dependence of $\partial H_c/\partial P$.

3.2.2 (b) The second-order elastic interaction

Equation 3.4 for the second-order interaction is valid only for defects having no dilation strain components. According to Labusch this equation becomes identical with the usual classical equation for a defect in a material with local variations $\delta C_{ijk\ell}(r)$ of the elastic constants if the perturbation of the wave function ψ in the modified elasticity equations is neglected (see section 3.2). In this case δC is given by

$$\delta C_{ijk\ell} = -(H_c^2/4\pi)\left[\, a_{ijk\ell}|\psi_o|^2 - \tfrac{1}{2}\, b_{ijk\ell}|\psi_o|^4 \right] \qquad 3.32$$

Webb (1963) and Toth and Pratt (1964), in their calculations for the interaction between an isolated fluxon and respectively a screw dislocation and the shear strain due to a coherent precipitate, effectively use this model with the additional assumption that $b_{ijk\ell} = 0$. This latter assumption has no real justification in general but is apparently reasonable in the case of some lead-indium alloys (see Labusch (loc. cit.) where values for $a_{ijk\ell}$ and $b_{ijk\ell}$ are given from measurements by Alers). Nabarro and Quintanilha (1970) and Quintanilha (1972) in their formulation of the first and second-order interactions use the usual expressions from elasticity theory (i.e. neglecting the perturbations to ψ due to the imposed strain) and then use perturbation techniques on the total free energy to determine the first and second-order interactions in the perturbed approximation. They conclude that the unperturbed approximation is probably valid for $t \lesssim 0.9$. This is certainly in agreement with Labusch (1968) for the first-order interaction but may not be for the second-order.

For the present, in this investigation, the second-order interaction will be considered only in the unperturbed approximation. [In chapter 5 experimental results will be investigated to establish whether any anomalous behaviour occurs for $t > 0.9$. The perturbation is expected to enhance the interaction (Quintanilha, 1972).]

In this approximation

$$\delta E_2 = - \int n_i^2 \, \delta C_{ij}^n \, d^3r \qquad 3.33$$

where the tensor notation of equations 3.4 and 3.32 has been replaced by the matrix notation so that the indices i and j now run from 1 to 6.

For a cubic material (e.g. niobium) the only non-vanishing elastic constants C_{ij} are C_{11}, $C_{12} = C_{21}$ and C_{44}. These have been measured for niobium in the superconducting and normal states by Alers and Waldorf (1962) and their temperature dependence in the superconducting state is apparently similar to that for $\delta\varepsilon_{vo}$ (see previous section) except that there are no discontinuities in the shear constants at $t = 1$ (Pippard, 1955 and for further discussion see Campbell and Evetts, 1972).

In accordance with the above considerations the spatial and temperature dependences of δC_{ij}^n will be assumed with some confidence to be given by

$$\delta C_{ij}^n(t) = \delta C_{ij}^n(t \to 0) . \left[H_c(t)/H_c(0) \right] |\psi|^2 \qquad 3.34$$

[For convenience the elastic constants are usually expressed in terms of the combinations C_{44}, $C' = (C_{11}-C_{12})/2$ and $C_B = (C_{11} + 2C_{12})/3$ which give respectively the resistance to deformation by shear across a {100} plane in the <010> direction, across a {110} plane in the <110> direction and by uniform hydrostatic pressure. The changes which occur in these constants at the normal-superconducting transition in zero magnetic field are inferred by Quintanilha (1972), from the

experimental results of Armstrong, Dickenson and Brown (1966) and Alers and Waldorf (1962), to be $\delta C_B(t = 0) \simeq 2.3 \times 10^7$ dynes cm^{-2}, $\delta C_B(1) \simeq 1.7 \times 10^6$ dynes cm^{-3}, $\delta C'(0) \simeq 1.1 \times 10^7$ dynes cm^{-2}, $\delta C'(1) = 0$, $\delta C_{44} \simeq 4.0 \times 10^7$ dynes cm^{-2} and $\delta C_{44}(1) = 0$.]

Finally substituting for $\delta C_{ij}(t)$ from equation 3.34 into equation 3.33 and expanding gives (ignoring vanishing terms) for the second-order interaction

$$\delta E_2 = \int [\, 3(n_1^2 + n_2^2 + n_3^2)(\delta C_{11} + 2\delta C_{12}) + (n_4^2 + n_5^2 + n_6^2)\delta C_{44}] \, |\psi|^2 d^3r \qquad 3.35$$

Reverting to usual notation, making appropriate substitutions and differentiating with respect to $\vec{r} = \vec{x} + \vec{y}$ gives the maximum second-order pinning force as

$$\vec{p}_m = (H_c(t)/H_c(0)) \left[\left(\vec{i}\,\frac{\partial}{\partial x} + \vec{j}\,\frac{\partial}{\partial y}\right)\left(\int [\, n_v^2\, \delta C_B(0) + (n_{xy}^2 + n_{xz}^2 + n_{yz}^2) \delta C_{44}(0)] \, |\psi_o|^2 d^3r \right]_{max} \qquad 3.36$$

where $|\psi_o|^2$ is given approximately by equation 3.9 in the high field regime ($b > 0.4$) and by equations 3.7 or 3.15 at low fields. The second-order interaction is always repulsive since it is quadratic in the strain and $\delta C_{ij} = C_{ij}^n - C_{ij}^s \geq 0$.

The interaction energy δE_2 for an isolated fluxon and a parallel edge dislocation has been determined in the above unperturbed approximation by Kramer and Bauer (1967). For $|\psi|^2$ they use the result of equation 3.15 which is due to them. For this case Kramer and Bauer give a figure which compares δE_1, δE_2 and $\delta E_1 + \delta E_2$ along the y axis (see figure 3.6) and which is reproduced here in figure 3.7. As expected δE_2 falls off far more rapidly than δE_1. In accordance with previous considerations it is expected that the resultant pinning force

due to the combined interaction (i.e. $\delta E_1 + \delta E_2$) will have approximately (except as $t \to 1$) the same temperature dependence as the first-order pinning force, viz; approximately as $H_c(t)$ (equations 3.21 and 3.31). It is moreover obvious from figure 3.7 even allowing for some uncertainty in the magnitude of δE_2 that the first and second-order pinning forces are of the same magnitude.

The model of Webb (1963) for the second-order interaction between an isolated fluxon and a perpendicular screw dislocation predicts a temperature dependence for the pinning force which is the same as that obtained above. With the exception of Fietz and Webb (1969), who state that it should vary as $H_{c2}^{3/2}$ it has generally been assumed therefore that for the elastic interactions $p_m(t) \propto H_c(t)$. This assumption is not justified however, as it is based on interactions between isolated fluxons and dislocations. Thus consider the case of the perpendicular interaction mentioned above : Even at moderate fluxon densities a single segment of screw dislocation may interact with more than one fluxon. The total interaction force* will therefore increase in proportion to $a_o^{-1} \simeq \left[b.B_{c2}(t)/\phi_o \right]^{\frac{1}{2}}$. To illustrate this the pinning force per unit length of screw dislocation is derived in appendix A1(c) from equation 3.36 for the regime $b \geq 0.4$. The final result (equation C6a) gives

$$\vec{p}_m^{\ell}(b,t) = (1/3\sqrt{3}) \left[C_{44} b_o\right]^2 \left[\sqrt{2}\, H_{c2}(t)/\kappa_1(t)\, H_c(0)\right] \delta C_{44}(0) \times (1 - b) b^{\frac{1}{2}} (B_{c2}(t)/\phi_o)^{\frac{1}{2}} \vec{\ } \qquad 3.37$$

---

* This result is in reality quite trivial and predicts simply that the pinning force increases in proportion to the number of fluxon interactions along the length of the dislocation segment. However, if this length is of order a_o this result is probably better used in the regime $b > 0.4$ than the result of Webb (loc. cit.).

or

$$p_m^{\ell}(b,t) \propto \left[B_{c2}{}^{3/2}(t)/\kappa_1(t)\right] \cdot b^{\frac{1}{2}}(1-b) \qquad 3.38$$

As another example, consider the case of a small region (dimensions $\langle R\rangle < a_o$) of tightly tangled dislocation consisting of dislocation dipoles or multipoles. The long range strain field for such a region is very small. Within the region the first-order interaction contributions will tend to cancel while the second-order contribution may be very large. To a first approximation the interaction energy in this case may be expressed as

$$\delta E_2 \simeq \left[\langle \eta_v^2 . \delta C_B \rangle + \sum_{i=4}^{6} \langle \eta_i . \delta C_{44} \rangle \right] V \qquad 3.39$$

where the quantities between the bras and ketts are the average values of the parameters over the volume V of the region. In the range $b < 0.4$: since $\delta C \propto |\psi|^2$ the characteristic distance over which δC will vary is $\xi = (\phi_o/2\pi H_{c2})^{\frac{1}{2}}$ and the maximum pinning force will be

$$p_m(b,t) \propto \delta E_2/\xi \propto Hc(t) H_{c2}{}^{\frac{1}{2}}(t) \propto H_{c2}{}^{3/2}(t)/\kappa_1(t) \qquad 3.40a$$

In the range $b > 0.4$: the characteristic distance will be $a_o = (\phi_o/bB_{c2})^{\frac{1}{2}}$ and again (see equation 3.37)

$$p_m \propto \left[H_{c2}{}^{3/2}(t)/\kappa_1(t) \right] b^{\frac{1}{2}}(1-b) \qquad 3.40b$$

This case will be considered in more detail in chapter 5. From previous considerations however it will be noted that this type of site will also give rise to a $\delta\kappa$ interaction which will be attractive (see later).

In conclusion it should be restated that the above discussion of the various pinning interactions is not exhaustive. However, all th salient features are included and various other possible mechanisms, some of which are certainly not applicable in the present investigation,

are discussed in the excellent review articles previously mentioned.

3.3 The summation problem

Consider a specimen containing a volume density N_v of randomly distributed discrete pinning sites which may be point-like or short line segments and which have dimensions, normal to the fluxons, which are smaller than the fluxon spacing a_o. Allow each pinning site to be capable of exerting, under ideal conditions, a maximum pinning force p_m on a fluxon. An obvious way to express the expected pinning force density (see for example Fietz and Webb, 1969) is then

$$P_v = N_v \, p_m \, \nu \qquad 3.41$$

where ν is some efficiency factor which must be determined for each pinning situation. In general ν will depend explicitly on p_m, on the geometry of the pinning sites and on the fluxon lattice elastic moduli and implicitly on the pinning site density, N_v.

In the dilute limit ν can be determined from the model of Labusch (1969b) (see for example Fietz and Webb, (loc. cit.) Campbell and Evetts, 1972, Section 3.3.1 and chapter 5). In the concentrated limit the determination of ν is very difficult except in some very special cases which will be discussed in section 3.3.2.

The criterion for the dilute limit in the case of a random distribution of small (relative to a_o) point-like pinning sites, according to Campbell and Evetts (1972), is that the mean pinning site separation is such that the distance between two sites which may operate simultaneously is $10a_o$, so that

$$N_v < 7 \times 10^{-5}/a_o d^2 \qquad 3.42$$

where d is the effective pinning range of the pinning site. (For niobium at $B = 2$Kgauss taking $d \simeq a_o \simeq 10^{-5}$cm gives $N_v \leqslant 10^{11}\text{cm}^{-3}$.)

are discussed in the excellent review articles previously mentioned.

3.3 The summation problem

Consider a specimen containing a volume density N_v of randomly distributed discrete pinning sites which may be point-like or short line segments and which have dimensions, normal to the fluxons, which are smaller than the fluxon spacing a_o. Allow each pinning site to be capable of exerting, under ideal conditions, a maximum pinning force p_m on a fluxon. An obvious way to express the expected pinning force density (see for example Fietz and Webb, 1969) is then

$$P_v = N_v\, p_m\, \nu \qquad 3.41$$

where ν is some efficiency factor which must be determined for each pinning situation. In general ν will depend explicitly on p_m, on the geometry of the pinning sites and on the fluxon lattice elastic moduli and implicitly on the pinning site density, N_v.

In the dilute limit ν can be determined from the model of Labusch (1969b) (see for example Fietz and Webb, (loc. cit.) Campbell and Evetts, 1972, Section 3.3.1 and chapter 5). In the concentrated limit the determination of ν is very difficult except in some very special cases which will be discussed in section 3.3.2.

The criterion for the dilute limit in the case of a random distribution of small (relative to a_o) point-like pinning sites, according to Campbell and Evetts (1972), is that the mean pinning site separation is such that the distance between two sites which may operate simultaneously is $10a_o$, so that

$$N_v < 7 \times 10^{-5}/a_o d^2 \qquad 3.42$$

where d is the effective pinning range of the pinning site. (For niobium at B = 2Kgauss taking $d \simeq a_o \simeq 10^{-5}$cm gives $N_v \leq 10^{11}\text{cm}^{-3}$.)

3.3.1 The dilute limit

As previously mentioned there are two approaches which have been used to obtain expressions for the bulk pinning force density P_v in this limit, viz: the statistical and the dynamical methods. In this section only the statistical method will be discussed since the final result does not depend on the method if the assumptions, which are usually made concerning the geometry and distribution of the basic pinning sites, are used (see Campbell and Evetts, 1972). These assumptions may be summarized as follows:

(i) The sites behave as point forces.

(ii) The interaction range d of a site is much less than the fluxon lattice parameter (i.e. $d << a_o$).

(iii) The site satisfies the threshold criterion (see later).

(iv) The sites are sufficiently weak and/or well separated that their force fields do not overlap, i.e. they are in the dilute limit.

It will be argued in chapter 5 however that assumption (ii) is, in practice, not tenable in low κ materials and is of only limited applicability in high κ materials and that this has resulted in inconsistencies in the application of the above models to certain experimental situations. For the present however the usual expression for P_v as predicted by the statistical model with all of the above assumptions will be derived and various other considerations will be discussed later in chapter 5.

The basis for the statistical model may be understood from the following argument: Consider a random three dimensional array of point-force pinning sites in a rigid regular fluxon lattice. On average if each interaction force between a site and a fluxon is summed vectorially the nett result will be zero and the bulk pinning force will therefore

also be zero. Thus in order to obtain a finite P_v it is necessary for the fluxon lattice to distort inhomogeneously in response to the basic interaction forces due to the pinning sites. This concept and its formulation, analysis and solution are due to Labusch (1969b). It is too long and complex for more than a very brief summary. Thus in essence, Labusch calculates a response function G'(0) which is the displacement of a fluxon (stabilised in its equilibrium position by a parabolic potential due to the surrounding fluxons) in response to a point force acting at the centre of the fluxon. G'(0) is calculated for three regimes of a parameter α which is defined as the mean value of $\nabla^2 u$ over all the fluxons where u is the interaction potential per unit length between the pinning sites and the fluxons. For α small (compared with the fluxon lattice shear constant C_{66}) the interaction with the pinning sites does not significantly effect the triangular symmetry of the fluxon lattice and the so called 'lattice approximation' obtains. For higher values of α the so called 'fluid' and 'single fluxon' approximations obtain. These latter are not considered to be important except at very low fluxon densities, i.e. near H_{c1} and also near H_{c2} where C_{66} decreases quadratically to zero (see Appendix A1(d)). For the lattice approximation ($\alpha/C_{66} \ll 1$) Labusch gives

$$G'(0) = (1/4\pi^{\frac{1}{2}})(B/\phi_o)^{\frac{1}{2}} \left[(C_{44}C_{11})^{-\frac{1}{2}} + (C_{44}C_{66})^{-\frac{1}{2}} \right] \qquad 3.43$$

which is independent of α.

A complex statistical analysis is then done to determine a function

$$\rho(\xi) = \rho_o \ \mathrm{Det}(1 + G'(0)\nabla^2 \varepsilon(\xi)) \qquad 3.44$$

which is the distribution function for fluxon elements, after the interaction has been switched on, at a distance ξ from a pinning site,

for which the density is ρ and the pinning force is

$$p = \nabla_\xi \varepsilon = \nabla_\xi \int_{-\infty}^{+\infty} u(\xi) dz$$

where z is collinear with the fluxons .

The critical state, i.e. when the bulk pinning force is equal to the driving force, is now obtained by summing over positive values of $\rho(\xi)$ with the driving force increasing until a maximum value ρ_c is reached. The bulk pinning force density P_v is then given by

$$P_v = (B/\phi_o) p_c = (B/\phi_o) \int \nabla\varepsilon(\xi) \rho_c(\xi) d\xi \qquad 3.45$$

[This expression is valid only in the dilute limit since it has been carried out only to first-order in the defect density $\rho_o(\xi)$. Labusch points out that as the defect concentration increases higher order functions are required so that, for example, a second-order calculation would require the auxiliary function $\rho(\xi_1, \xi_2)$ which is the probability that pinning sites will be found simultaneously at distances ξ_1 and ξ_2 from the fluxon element.]

Finally, in order to obtain an explicit analytic expression for the bulk pinning force, Labusch chooses a convenient form for the pinning potential viz:

$$\varepsilon(\xi) = \varepsilon_o [\, 1 - (2/3)(\xi^2/d^2) + (1/9)(\xi^4/d^4)\,] \quad \text{for } \xi/d < \sqrt{3}$$

and $\varepsilon(\xi) = 0$ for $\xi/d > \sqrt{3}$. 3.46

where d characterises the width of the site.

The final result is shown graphically in figure 3.8 (modified from Labusch, 1969b). [$2N_v d = \rho_o$ is the density of sites per unit area.]

Thus according to the model: for $G'(0) p_m/d \lesssim 2/3$; $P_v = 0$, i.e.

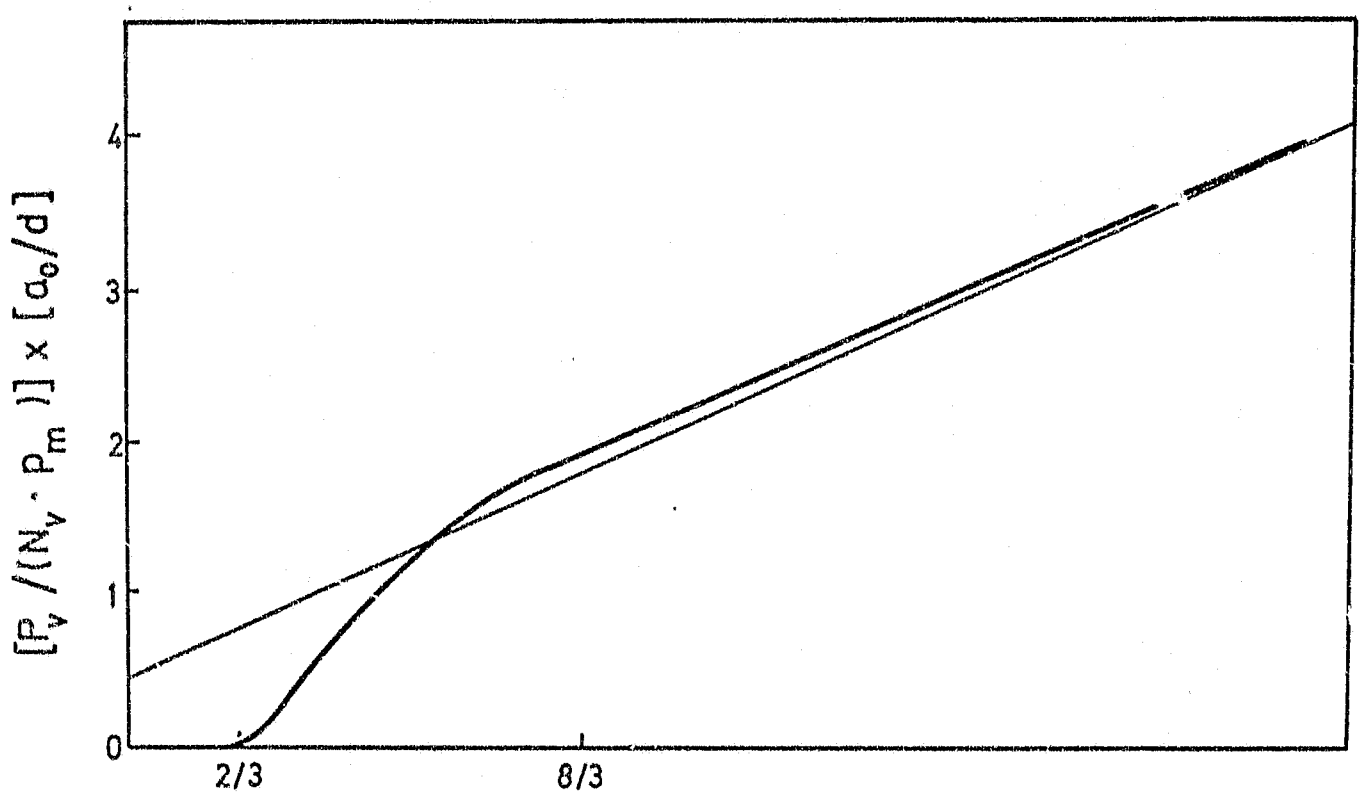


Figure 3.8. The variation in the reduced bulk pinning force density, due to an elementary pinning site, as a function of the reduced displacement of a fluxon. For small displacements, i.e. small p_m or d the pinning sites become ineffective and the bulk pinning force density falls to zero. (From Labusch, 1969b).

there is no elastic instability and consequently no dissipation, and for $G'(0)p_m/d \geq 8/3$: P_v is given by

$$P_v \simeq .2N_v d\ p_m^2 G'(0)/a_o^2$$

Substituting for $G'(0)$ from equation 3.43 and $a_o^2 = (\phi_o/bB_{c2})$ gives

$$P_v = (1/2\pi^{\frac{1}{2}})N_v d\ p_m^2(bB_{c2}/\phi_o)^{3/2}\left[(C_{44}C_{11})^{-\frac{1}{2}} + (C_{44}C_{66})^{-\frac{1}{2}}\right] \quad 3.47$$

The efficiency factor ν (see previous section 3.3, equation 3.41) can easily be seen to be given in this case by

$$\nu \simeq 2p_m\ G'(0)d/a_o^2$$

$$\simeq 2u_o d/a_o^2 \quad 3.48$$

where $u_o = p_m G'(0)$ is the average displacement of a fluxon in response to a pinning site. This expression for ν can be interpreted physically (see also Fietz and Webb (loc. cit.) and Webb, 1971) in the following rather over-simplified manner. Thus: the probability that a site is within interaction distance d of a fluxon is approximately d^2/a_o^2 (it will be recalled that the lattice approximation obtains) and the remaining factor, i.e. u_o/d, is related to the threshold condition which requires a certain minimum relative distortion of the fluxon for an inelastic interaction. From figure 3.8 the threshold condition is seen to be given approximately by

$$G'(0)\ p_m/d \geq 2/3 \quad \text{or} \quad u_o/d \geq 2/3$$

and the critical pinning force p_{mc} is therefore given, substituting for $G'(0)$ from equation 3.43, by

$$p_{mc} \geq (8\pi^{\frac{1}{2}}/3)d\ (\phi_o/B_{c2})^{\frac{1}{2}}\left[(C_{44}C_{11})^{-\frac{1}{2}} + (C_{44}C_{66})^{-\frac{1}{2}}\right] \quad 3.49a$$

or using the approximation of appendix A1(d)

$$p_{mc} \geq 0.1d\ \phi_o^{\frac{1}{2}}\left[B_{c2}^{3/2}(t)/\kappa_2(t)\right]\ b^{\frac{1}{2}}(1-b) \quad 3.49b$$

Substituting $d \simeq a_o/5 = 0.2(\phi_o/bB_{c2})^{\frac{1}{2}}$, $b = 0.5$ and for niobium at $T = 4.2K$ (see chapter 5); $B_{c2} = 2.7 \times 10^3$ gauss and $\kappa_2 = 1.73$. gives

$$p_{mc} \gtrsim 4.3 \times 10^{-6} \text{dynes}$$

which is a factor of approximately 4×10^2 larger than Webb's (1963) prediction for the perpendicular fluxon-screw dislocation interaction. Also on the very crude approximation that the critical pinning force per unit length of line force p^{ℓ}_{mc} for a line of effective length 10^{-4}cm is then $p^{\ell}_{mc} \simeq 4.3 \times 10^{-2}$ dynes cm^{-1}, which is a factor of approximately 50 larger than the prediction for the parallel fluxon-edge dislocation interaction (equation 3.25).

The model outlined above may be modified, under certain conditions, to make predictions for the pinning force density due to an array of line-force pinning sites which are long relative to a_o. The displacement u_o of an isotropic continuum at the point of application of a line force p^{ℓ}_m per unit length is well known and is given by

$$u_o = [\ (3 - \nu)p^{\ell}_m \ln(R/r)\ ]\ /8\pi\mu e \qquad 3.50$$

where μ_e is the appropriate elastic modulus and R and r are respectively the outer and inner cut-off radii of the force field. For a line force perpendicular to the fluxon lattice μ_e is given (see for example Campbell and Evetts, 1972) by

$$\mu_{e_\perp} = (5/4)C_{11} \qquad 3.51$$

For the parallel case μ_e is given (Good and Kramer, 1970) by

$$\mu_{e_{||}} = [\ (5/16)\ p^{\ell}_m \ln(R/a_o)\ ]\ /C_{66} \qquad 3.52$$

where R is taken to be half the distance between the line forces and C_{66} is the shear modulus (see appendix A(d)). Good and Kramer (loc.

cit.), using the dynamic approach, obtain an expression for the pinning force density for this case (assuming the line forces are dislocations) which they give as

$$P_v = \left[0.1\ \rho (p_m^{\ell})^2 . (B/\phi_o)^{\frac{1}{2}} \ln(R/a_o) \right] / C_{66} \qquad 3.53$$

where ρ is the dislocation density (cm^{-2}). However, for niobium with $b \geq 0.4$, $C_{66} \propto (1-b)^2$ (appendix A1d) and $p_m \propto (1-b)$ (section 3.2) equation 3.53 predicts $P_v \propto b^{\frac{1}{2}} \ln(Rb^{\frac{1}{2}})$ i.e. P_v monotonically increasing with b for all b. This has not been observed experimentally under any circumstances and emphasizes two aspects which should be considered, viz:

(i) The logarithmic dependence of u_o on R (equations 3.52 and 3.53) implies that the force fields of the pinning sites overlap even at moderate line density thus precluding the use of a dilute limit model.

(ii) Dislocations are rarely straight and parallel along distances of more than 10^{-4} to 10^{-3} cm so that a proper line force response is not likely to occur. However, a fluxon may interact with many short segments of line pinning sites (for example dislocations) along its length and the response of the fluxon lattice may then be intermediate between the point and line force predictions. Synchronous pinning effects may also occur in this case. This will be discussed in the next section.

3.3.2 The concentrated limit

Campbell and Evetts (1972) discuss this limit and the related so-called 'matching' and 'synchronous effects' in some detail. Except for these latter two cases the problem of the concentrated limit is extremely complicated. An indication of how for the general case, the problem may be approached has been given by Labusch (1969b). The majority of models which have been developed for this limit however

simplify the problem by ignoring the fluxon lattice rigidity (i.e. effectively putting $\nu = 1$ in equation 3.41). Exceptions to this are the models of Nabarro and Quintanilha (1970) and Quintanilha (1972) and also of Kramer (1973). These will be discussed later.

Matching effects occur when the distribution or physical size of the pinning sites is approximately uniform and also scales with an integer multiple of the fluxon lattice parameter a_o. This effect was not expected or observed in the present investigation and will therefore not be considered further.

Synchronous pinning may result when the strength or density of the pinning sites is very large or when one or more of the elastic moduli of the fluxon lattice becomes very small. The shear modulus C_{66} is small relative to C_{44} and C_{11} and moreover decreases quadratically with b for $b > 0.4$ (see appendix 1A(d)). Synchronous pinning is therefore likely to occur when the pinning sites are line forces (or segments of line forces along individual fluxons) aligned parallel to the fluxons since the fluxon lattice response in this case is inversly proportional to C_{66} (equation 3.52). Pippard (1969) suggests that the so-called 'peak effect', which occurs for $b \lesssim 1$ is due to this mechanism.

Generally synchronous pinning occurs when it is favourable for the entire fluxon lattice to relax onto the available pinning sites in such a manner that the pinning sites realize their maximum effectiveness (i.e. $\nu \to 1$ in equation 3.41) so that

$$P_v \cong N_v p_m \qquad 3.54$$

This will be discussed further in chapter 5.

A few of the more relevant models for the prediction of the bulk pinning force density $P_v(b,t)$ due to high density arrays o dis-

location will now be outlined briefly.

Coffey (1967) calculates the pinning force density on the assumption that all pinning sites are active and that the basic pinning is due to electron kinetic energy effects. He obtains

$$P_v(b,t) = B_p(\pi/\phi_o)^{\frac{1}{2}}(B_{c2}{}^{3/2}(t)/\kappa_1^2(t)).b^{\frac{1}{2}}(1-b) \qquad 3.55$$

where B_p is the induction at which the fluxon density is equal to the pinning site density per unit area. However, when the pinning site density is greater than the fluxon density, B_p must be replaced by B and then

$$P_v(b,t) \propto B_{c2}{}^{5/2}(t)\ b^{3/2}(1-b) \qquad 3.56$$

Baramidze and Saralidze (1970) calculate the pinning force density due to the first-order elastic interaction resulting from a high density of randomly distributed edge dislocations aligned parallel to the fluxons. The dilation in the crystal lattice due to the dislocations expressed in terms of a probability density function and the pinning force density is obtained by direct summation i.e. ignoring the fluxon lattice rigidity ($\nu = 1$ in equation 3.41). Their final result may be expressed as

$$P_v(b,t) \simeq (\Delta V/V)Kb_o.(b.B_{c2}/\phi_o)\ f(x) \qquad 3.57$$

where $\Delta V/V$ is the relative change in the volume of a unit cell at the superconducting - normal phase transition, k is the bulk modulus, b_o is the Burgers vector and f(x) is the probability density function where $x \simeq (\xi\rho)^{-\frac{1}{2}}$ and ρ is the dislocation density. Now $\Delta V/V = \delta\varepsilon_v \propto (H_{c2}(t)/\kappa_1(t))(1-b)$ (section 3.2) and for $\kappa >> 1$ the pinning force density dependences on b and t are given approximately by

$$P_v(b,t) \propto (B_{c2}(t)/\kappa_1(t)).b(1-b) \qquad 3.58$$

The model predicts a maximum in interaction energy per fluxon of approximately 10^{-8} ergs cm^{-1} when the average separation between the fluxons is 1.7ξ. This latter result is important and reflects the fact that the pinning forces cannot vary over distance smaller than ξ since any variation in the superconducting parameters (due to stress or otherwise) over such distances will be effectively smoothed out by the coherence effects.

Nabarro and Quintanilha (1970) calculate the first and second-order interactions for a uniform array of edge dislocations (aligned parallel with the fluxons) which is assumed to produce a periodic strain field in an xy plane given by

$$\varepsilon^d = \varepsilon_o^d \, (\sin kx + \sin ky) \qquad \cdot 3.59$$

where $k^2 = \rho$ is the dislocation density.

Quintanilha (1972) discusses the model in more detail and extends the calculation to include the perpendicular fluxon-dislocation interaction (i.e. fluxons along x or y). The elasticity of the fluxon lattice is implicitly included in the model and perturbation effects due to the strain field ε^d on the current contours around the fluxon are also considered and are found to be important only for $t > 0.99$. The final expressions for the pinning force density in these works are in terms of specially defined parameters and therefore for the present purpose the expressions have been reduced to show the dependences of P_v on $B_{c2}(t)$, $\kappa_1(t)$, b and ρ. Thus:

For $\xi\rho^{\frac{1}{2}}$ small

$$P_{v_{11}}(b,t) \propto P_{v_\perp}(b,t) \propto \rho^{\frac{1}{2}} B_{c2}(t)\kappa_1(t)b \text{ for } \quad < b_{cr},\ x(1-b) \text{ for } b > 0.4 \qquad 3.60a$$

and $P_{v_{11}}(b,t) \propto P_{v_\perp}(b,t) \propto \rho^{3/2} B_{c2}^{-1}(t)$ for $b < b_{cr}$, $x(1-b)^2$ for $b > 0.4$

For $\xi\rho^{\frac{1}{2}}$ large:

$$P_{v_{11}}(b,t) \propto P_{v_{\perp}}(b,t) \propto \rho^{-2} B_{c2}^{7/2}(t)\kappa_1(t) \quad \text{for } b < b_{cr}$$

and $$P_{v_{11}}(b,t) \propto P_{v_{\perp}}(b,t) \propto \rho^{-7/2} B_{c2}{}^{4}(t) \quad \text{for } b > b_{cr} \qquad 3.60b$$
$$\times (1-b)^2 \quad b > 0.4$$

where b_{cr} is some critical value of b which depends on temperature and on the orientation of the fluxons with respect to the dislocations and is typically between 0.1 and 0.4. Also $P_{v_{11}} > P_{v_{\perp}}$ and the first-order interaction predominates. Quintinilha (loc. cit.) finds a maximum in $P_{v_{11}}$ when the wavelength of the strain field is approximately 3.4ξ. This is in close agreement with the result of Baramidze and Saralidze (loc. cit.).

A feature of the majority of the models for P_v considered so far is that they make predictions of the form

$$P_v(b,t) \propto G.g(b)\left[B_{c2}^{n}(t)/\kappa^{m}(t) \right] \qquad 3.61$$

where G is some function of the microstructure responsible for the basic pinning interaction.

g(b) is a function of $b = B/B_{c2}$ which for high κ materials is usually of the form $b^x(1-b)^y$ where x and y have integer or half-integer values. $\kappa = \kappa_1$ or κ_2 or some function of κ_1 and κ_2. For high κ materials the temperature dependance of κ_1 and κ_2 is relatively small and is usually not considered when comparisons with experiment are made. However for niobium this cannot be considered to be the case (see chapter 5).

Fietz and Webb (1969) were the first to establish that the pinning force density in some heavily cold-worked niobium alloys appear to obey

a scaling law of the form given by equation 3.61. This behaviour has subsequently been confirmed in many investigations, in particular, on hard or high κ materials. There is however a fundamental problem associated with the scaling law of equation 3.61. Thus: the form of g(b) found for the various theoretical pinning models precicts, as expected, a maximum in $P_v(b)$ at some $b = b_p$ and that $P_v(b = 0) = P_v(b = 1) = 0$. However the precise form of g(b) and, in particular, the value of b_p is found from experiment to depend on variations in the crystal microstructure (responsible for the fluxon pinning) in a manner which apparently cannot be readily accounted for by these models. Kramer (1973) discusses this problem in some detail and formulates a model which is in apparently good agreement with a number of experimental investigations on hard superconductors. The model will be briefly discussed here because although it is primarily formulated for high κ materials there is no apparent aspect of it which precludes its qualitative validity in low κ materials.

Thus Kramer (loc. cit.) demonstrates that for the high pinning site densities normally associated with hard superconductors the response of the fluxon lattice tends to a line force limit. [The criterion is given by

$$\omega^{-1} << \left[C_{44}\, \phi_o / C_{66} B \right]^{\frac{1}{2}}$$

where ω^{-1} is the pinning site separation distance.] It is now argued that for $b << b_p$ fluxon motion occurs as fluxons break away from the weaker of these line forces and for $b >> b_p$ the motion occurs by a synchronous shearing process of the fluxon lattice around the line forces which are too strong to be broken. The pinning force densities for these two regimes are calculated and then summed assuming a statistical distribution for the strength of the basic

interaction force per pinning site. Solutions for $P_v(b,t)$ are obtained for Gaussian, Poisson and double-Poisson distribution functions. The result for the Poisson distribution, which is quantitatively similar to the result for the Gaussian distribution, is given as

$$P_v(b,t) = \langle K_p(t)\rangle b^{\frac{1}{2}}(1-b)\left[1-\left[1+(K_{pm}(t)/\langle K_p(t)\rangle)\right]\right.$$
$$\left. \times \exp(-K_{pm}(t)/\langle k_p(t)\rangle)\right] + K_s(t)b^{\frac{1}{2}}(1-b)$$
$$\times \exp(-k_{pm}(t)/\langle K_p(t)\rangle) \qquad 3.62$$

where $\langle K_p\rangle$ is the average value of K_p and K_p and K_s are the field independent components of the pinning force density for $b \ll b_p$ and $b \gg b_p$ respectively and K_{pm} is defined by $K_{pm} = K_s(1-b)^4$. Physically K_{pm} represents a borderline pinning density (i.e. between low b and high b).

K_p is determined, using the dynamical approach, for a density ρ of initially strong line pinning forces which are assumed to have a strength

$$f_p = \beta\omega(H_{c2}(t)/\kappa_1(t))^2(1-b) \qquad 3.63$$

where β is a constant. K_p is given as:

$$K_p(t) = 5.10^6(\rho P\omega^4\beta^4 H_{c2}^{5/2}(t))/(\phi_o^{\frac{1}{2}}\kappa_1^2(t)) \qquad 3.64$$

in dynes cm^{-3}, where P is approximately a constant. Kramer allows that for different types of defect the dependence of f_p on H_{c2} and κ may be different from that given in equation 3.63 (see later).

K_s is determined from the maximum shear stress of the fluxon lattice and is given as

$$K_s(t) = C_s H_{c2}^{5/2}(t)/(\phi_o^{\frac{1}{2}}\kappa_1^2(t)) \qquad 3.65$$

where C_s is a function of ρ and the fluxon lattice parameter a_o and

varies between 0.14 for small ρ and 0.56 for the largest value of ρ which is consistent with the model used to formulate K_s. This C_s is only weakly dependent on pinning site density and the field. Also K_s and K_p both scale with temperature as $H_{c2}^{5/2}(t)/\kappa_1^2(t)$ (but see later comments).

The characteristic behaviour of equation 3.62 for $P_v(b,t)$ can now be described as follows:

(i) The equation obeys a scaling law of the same form as equation 3.61 for all $0 \leqslant b \leqslant 1$.

(ii) The term in $\langle K_p \rangle$ is an increasing function of b and is a sensitive function of the density and strength of the pinning sites.

(iii) The term in K_s is a decreasing function of b for $b \gtrsim 0.2$ and depends only weakly on the density of the pinning sites and not at all on their strength.

(iv) Equation 3.62 therefore predicts a maximum in $P_v(b)$. This occurs at a value of b given by

$$b_p \simeq 1 - (\langle K_p \rangle / K_s)^{1/4} \qquad 3.66$$

which is therefore (from (ii) and (iii)) a sensitive function of the density and strength of the pinning sites. Weak or widely spaced pinning sites result in a small peak in P_v at high b and strong closely spaced pinning sites give rise to a large peak in P_v at low b. The form of $P_v(b)$ for $b > b_p$ is similar in both cases.

Kramer points out that since b_p depends on the 1/4 power of the ratio K_p/K_s the position of the peak does not depend sensitively on the temperature dependence of K_p/K_s and therefore other forms for f_p (equation 3.63) may be used without significantly influencing the model. Also if $K_p \propto H_{c2}{}^p(t)$ and $K_s \propto H_{c2}{}^s(t)$ then the exponent that would be obtained from an experimental log $P_{v_{max}}(t)$ versus log $H_{c2}(t)$ plot will

be approximately $\frac{1}{2}(p + s)$.

This model is apparently in good agreement with several experiments and also accounts for the so-called 'peak effect' in hard superconductors. The lack of sensitivity of $P_v(b,t)$ on the exponent p however suggests that an unambiguous identification of the basic pinning site interaction mechanism (i.e. elastic or $\delta\kappa$) is not easily obtained from experimental results.

3.4 Conclusions

The theory outlined in the preceding sections makes definite predictions for the pinning force density only for certain idealized pinning situations. In real materials, especially when the pinning is due to cold work, the pinning site geometry may be very complicated and several pinning mechanisms may operate simultaneously. Further complications are associated with low κ superconducting materials (for example niobium). This will be discussed further in chapter 5 where experimental results on fluxon pinning in specially deformed niobium specimens are reported and compared with models based on the considerations of this chapter and chapter 4.

CHAPTER 4

4. The Influence of Interstitial Hydrogen on the Bulk Superconducting Properties of Niobium

4.1 Introduction

It is well known that the presence of an interstitial solute in a type II superconductor alters the Ginzburg-Landau parameter κ and also the critical temperature T_c of the host latice (Livingston and Schadler, 1964 and Dew-Hughes, 1972). For a dilute, random distribution of interstitial solute the change in κ results from a reduction in the mean free path of the normal electrons and the change in T_c from changes in the superconducting energy gap which depends on the density of states for the super-electron Cooper pairs.

Local changes in κ and/or T_c or H_c due to precipitates and other ordered and sub-ordered interstitial phases, will, under certain circumstances, cause fluxon pinning. (See for example Campbell and Evetts, 1972 and also chapter 3.) It is generally found that the pinning is strongest when the fluxons are parallel to the habit planes of precipitates or otherwise to crystal planes which favour clustering of the solute. The pinning effectiveness of ordered or sub-ordered phases of oxygen in niobium and nitrogen in vanadium has been investigated, inter alia, by Rose and Jones (1969) and Milne and Gibbons (1972) respectively. In both cases maxima in the critical current density (and therefore in the bulk pinning force density P_v) were found when the applied field H_o was parallel to the <110> and <001> directions in the {110} planes. Rose and Jones also find a much

larger maximum in J_c for H_o along <210> and conclude that pinning occurs when the fluxons are parallel to internal anti-phase boundaries which are then supposed to be parallel to the {100} and {210} planes in agreement with the electron-microscope studies of Van Landuyt, Gevers and Amelinckx (1966). (These authors actually find that the habit plane for the oxygen precipitate is {310} which is close to the {210} plane and also that the boundary between adjacent domains is the {001} plane.) Milne and Gibbons interpret their results by noting that the elastic anisotropy in vanadium (and also niobium) is less than one so that the <111> direction in these elements is 'soft'. Thus if there is a tendency for solution demixing the solute will segregate such that composition fluctuations will occur on planes normal to these elastically 'soft' directions. These compositions modulations are then manifest as solute enriched planes. For demixing along <111> directions solute enrichment occurs on {111} planes which intersect along <110> directions to produce a three-dimensional array of rods and the pinning force density is therefore a maximum when the applied field is parallel to <110>.

The only explicit mention in the literature, of the influence of hydrogen on fluxon pinning is that due to Essmann (1971) who suggests that pinning he observes, by means of his fluxon decoration technique, in a niobium disc-specimen is due to precipitates of hydride. (Essmann supposes that the presence of hydrogen in his specimen is due to electro-polishing.)

The presence of an interstitial solute also implies the possible existence of solute atmospheres on dislocations (see later) and this should influence the intrinsic pinning properties of the dislocations. (Kramer and Bauer, 1967 and Tedmon, Rose and Wulff 1964, 1965.) No

mechanism for this process has previously been published however and it will therefore be considered in chapter 5 using theory which will be reviewed and developed in this chapter.

The solubility and mobility, at sub-ambient temperatures, of interstitial oxygen and nitrogen in niobium are negligibly small (see for example Fast, 1971). Consequently even slow quenching from room temperatures to 4K will cause virtually no configurational change of these interstitials in the host lattice. The case of interstitial hydrogen in niobium is very difficult however. The solubility and mobility are relatively high at sub-ambient temperatures. Quenching to 4K from room temperature will therefore give rise to large configurational changes of the interstitial hydrogen in the host lattice and the rate of cooling will influence the size and distribution of hydride precipitates, ordered and sub-ordered phases and also the extent of development of interstitial atmospheres around dislocations. This latter effect is found, in the present investigation, to have a large effect on the fluxon pinning behaviour. For a concentration of hydrogen in niobium of approximately 50 ppm (atomic) almost an order of magnitude change in the pinning force density can be induced by certain low temperature ageing procedures (see chapter 5).

The absorption of hydrogen into niobium takes place, at room temperature and even in very low partial pressures of hydrogen, if a surface of the niobium specimen is freed of its usual stable oxide layer. Such conditions should obtain during spark-erosion machining under liquid paraffin, during chemical and electro-polishing (Westlake and Gray, 1966) and even after ultra high vacuum outgassing in oil-diffusion pumped systems with cold traps (Christian and Taylor 1967, Hananda, Suganuma and Kimura, 1972 and Faber and Schultz, 1972).

Hanada et al. (loc. cit.) find a hydrogen concentration of 50 ppm (atomic) in tantalum samples after U.H.V. outgassing.

It is possible that a number of previously reported experimental results on pinning in B.C.C. superconductors, especially when cold worked, are spurious as a result of effects due to interstitial hydrogen. The results of this investigation lead to mutually consistent models for the fluxon pinning behaviour and for the low temperature behaviour of hydrogen in niobium. Although the latter behaviour is fairly well understood certain useful quantitative deductions and predictions can be made from the results of the pinning experiments described in chapter 5. A brief review of the relevant aspects of the subject is therefore given here. (general references, Fast, 1971 and Nabarro, 1967).

4.2 The phase diagram

The phase diagram for hydrogen in niobium from Walter and Chandler (1965) is shown in figure 4.1a. The hydrogen is generally thought to occupy tetrahedral interstitial sites in the B.C.C. lattice of niobium. [Recently however, Kistner, Rubin and Sosnowska, 1971 have found evidence from neutron scattering experiments that neither the tetrahedral nor octahedral interstitial sites are apparently favoured.] In the α phase the jump frequency ν for the hydrogen interstitials is very high (at room temperature $\nu = 10^{11} - 10^{12} sec^{-1}$) and consequently the interstitials may be considered to behave like a gas in the host lattice. The point A at $T = 172^{o}C$ (figure 4.1a) is the critical point of the miscibility gap and may be interpreted as the critical point for a gas-liquid phase transition (Alefeld, 1969). In the α (gas) phase and the more hydrogen rich α' (liquid) phase the hydrogen is randomly distributed among the available sites and the overall average distortion of the niobium

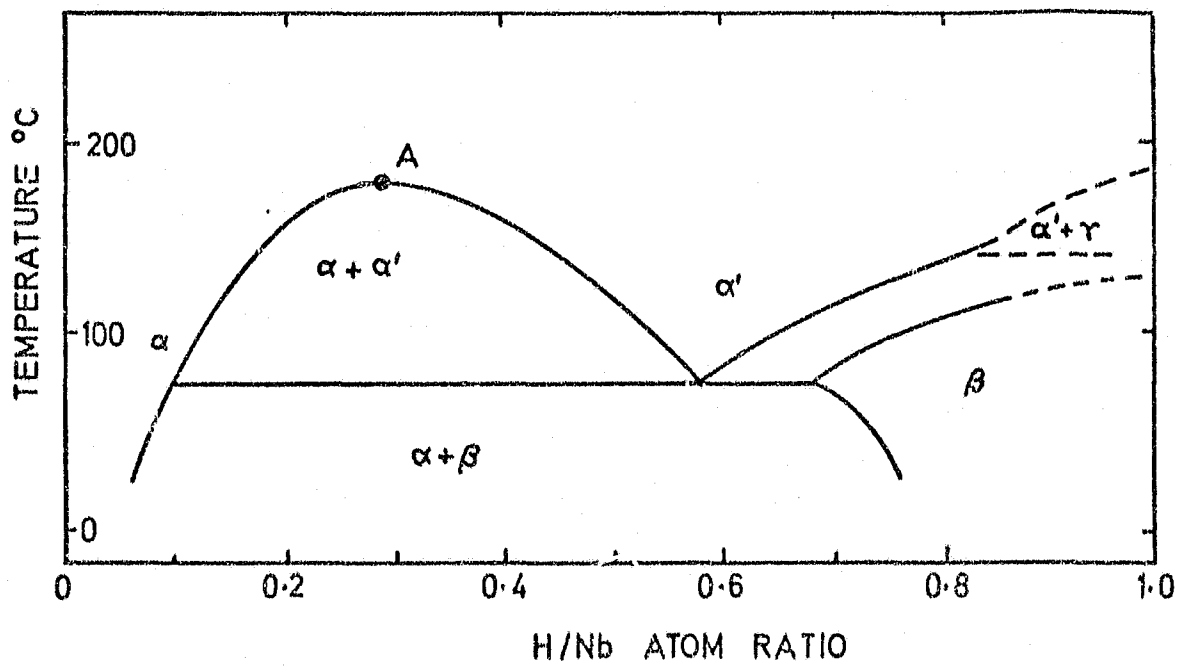


Figure 4.1a. Niobium-hydrogen phase diagram (from Walter and Chandler, 1965).

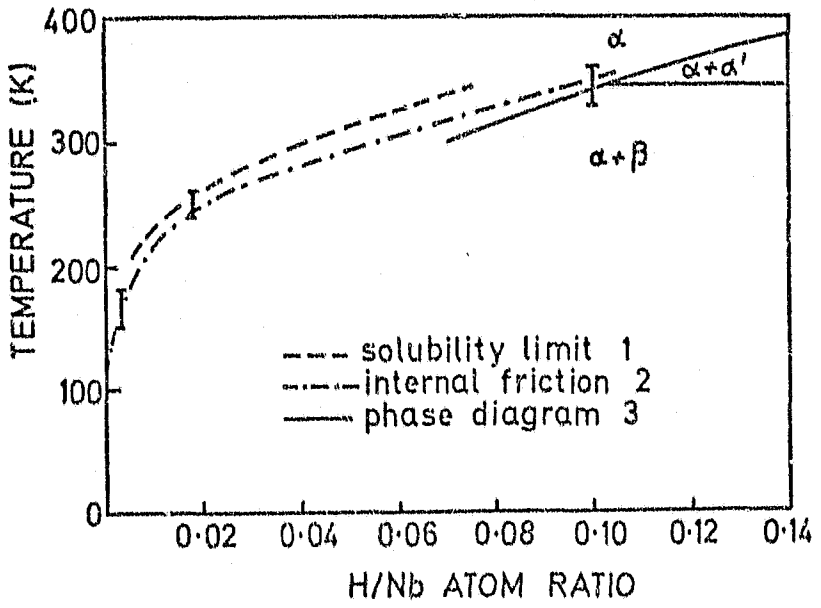


Figure 4.1b. The boundary between the α and α + β phases as obtained by various methods. (From Buck, Thompson and Wert, 1971.)

lattice is therefore isotropic. The β (solid) phase is a true precipitate with a composition in the range (0.2 to 0.8)H/Nb (Walter and Chandler, 1965) with an orthorhombic structure (Gorsky, 1935). The jump frequency in the β phase is lower by a factor of 40 relative to the α' phase. The ν phase is not relevant in the present investigation and will not be considered further.

The solubility limit, i.e. the phase boundary between the α and α + β phases has been determined experimentally by various methods. The results of some of these experiments are summarized in figure 4.1b which has been taken from the paper by Buck, Thompson and Wert (1971).

The phase diagram has not been established with certainty. There is evidence (see for example Hardie and McIntyre, 1972) that the hydride phase forms by an athermal martensitic or order-disorder transformation. Hardie and McIntyre investigate niobium containing less than 250 ppm hydrogen at sub-ambient temperatures and claim that their results, obtained by various methods, are consistent with a martensitic transformation requiring some diffusion ordering before precipitation. The precipitate was found to have a b.c. trigonal structure and not the expected orthorombic type. They suggest that the former structure may be a precursor for the latter and is stable at low hydrogen concentrations.

4.3 Low temperature diffusion

The microscopic jump model (see for example Fast, 1971) for the diffusivity of interstitials in the isotropic case (for example in B.C.C.) gives for the diffusion coefficient D

$$D = f\lambda^2\nu \qquad 4.1$$

where f is a constant which depends on the co-ordination of the favoured interstitial sites, λ is the jump distance between these

sites and ν is the jump frequency which is a strongly increasing function of temperature. It is therefore usual to make the substitution

$$D = D_o \exp(-\Delta H/RT) \qquad 4.2$$

where D_o contains the frequency factor and ΔH is an activation enthalpy. Both D_o and ΔH depend only weakly on the concentration of the solute. The Arrhenius plot of figure 4.2 (taken from the paper by Cantelli, Mazzolai and Nuovo, 1969) shows that the experimental results for D deviate from the predictions of equation 4.2 at temperatures below about 235K.

The two most common and straightforward methods of measuring D involve the Gorsky and Snoek effects.

The Gorsky effect (Gorsky, 1935) has its origin in the strain dilation of the host lattice due to the solute atoms. Thus, if a sample containing, for example, a mobile interstitial solute is stressed inhomogeneously, the solute atoms will migrate, under the influence of internal strain gradients arising from the applied stress, to regions of larger lattice parameters and so tend to relieve the internal stress. In these regions the solute atoms usually give rise to an additional or anelastic strain which is known as the diffusion after-effect. On removal of the applied stress this anelastic strain disappears at a rate which proportional to the diffusion coefficient. The relaxation time for long-range diffusion over some characteristic length d is given by

$$\tau_g = (d/\pi)^2 \; D^{-1} \qquad 4.3$$

For hydrogen in niobium with d = 1mm τ_g = 150 seconds at T = 290K. The relaxation strength is proportional to the interstitial concen-

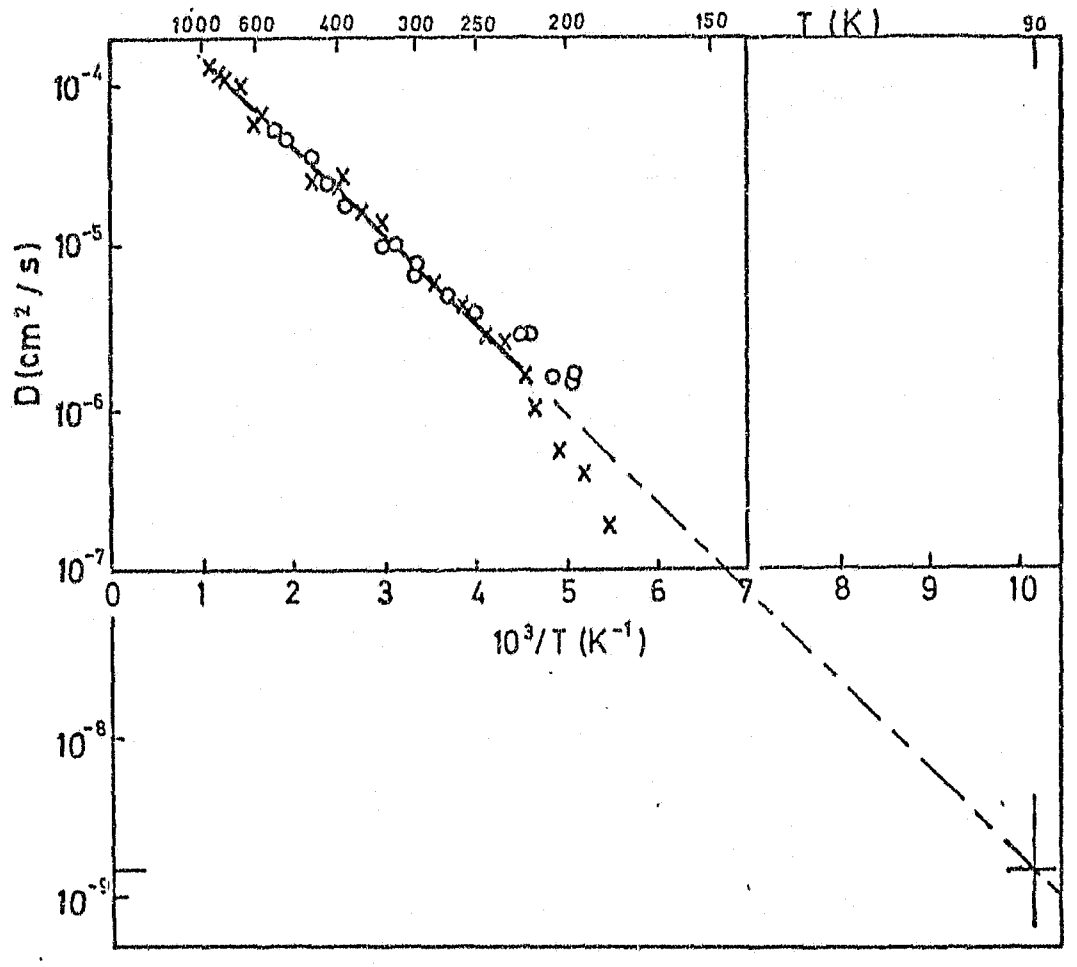


Figure 4.2. Arrhenius plot of the diffusion coefficient for hydrogen in niobium showing the deviation of the experimental results from simple exponential behaviour (from Cantelli, Mazzolai and Nuovo, 1969).

tration (1 per cent hydrogen gives a 1.6 per cent after-effect strain - see for example Walter and Chandler, 1965 and Buck, Thompson and Wert, 1971).

Westlake (1972) points out that measurements of D using the Gorsky effect and equation 4.3 may be in error at temperatures below solubility limit because reorientation of Nb-H platelets due to a cycling applied stress gives rise to orientation after-effects (which may involve a different - e.g. surface-diffusion coefficient) simultaneously with the diffusion after effects.

The Snoek effect has its origin in the preferential ordering of interstitial solute atoms into a particular class of interstitial site thereby producing a lattice distortion of lower symmetry (e.g. trigonal) than that of the host lattice (e.g. B.C.C.). Uniaxial or shear strain may therefore be relieved by this mechanism. Thus relaxation phenomena occur in a vibrating specimen when the frequency of an applied uniaxial stress corresponds to the inverse relaxation time for preferential ordering of the interstitials. In this case the interstitials are required to hop only between adjacent sites in the unit lattice cell (see Nabarro, 1967). The relaxation time τ_s is given by

$$\tau_s = (a^2/36)D^{-1} \qquad 4.4$$

where a is the lattice parameter.

Measurements of D_o and ΔH using this method are also subject to error. Thus if some of the hydrogen interstitials are associated with other insterstitials (e.g. H - H or H - O) then the resulting relaxation parameters, as experimentally determined, will be modified (Powers and Doyle, 1959).

4.4 Interstitial atmospheres on dislocations

Nabarro (1967) reviews this subject in some detail. The first calculations of the interaction between solute atoms and dislocations is due to Cottrell (1948) who calculates the potential $V(R,\alpha)$ of a solute atom in the hydrostatic stress field of an edge dislocation and obtains (see figure 4.3)

$$V(R,\alpha) = (4/3)\left[\mu\varepsilon r^2\lambda/R\right]\frac{(1+\nu)}{(1+\nu)}\sin\alpha \qquad 4.5$$

where μ is the shear modulus, $\varepsilon = \Delta V/V$ (i.e. the lattice dilation due to an interstitial atom), λ is the slip distance, ν is Poisson's ratio and r is the radius of the solute atom. Substituting $\alpha = \pi/2$, $\nu = 1/3$ and $\lambda = r = b_o$ (the Burgers vector) into equation 4.5 gives

$$V(R,\alpha = \pi/2) \simeq (8/3)(\mu\varepsilon b_o^4/R) \qquad 4.6$$

The conditions required for the formation of an atmosphere (Cottrell) are:

(i) an adequate concentration of solute. [The number of available solute atoms per dislocation per atomic plane is given by

$$n = c/\rho d^2 \qquad 4.7$$

where c is the atomic concentration of the solute, ρ is the dislocation density and d is the interatomic distance. Substituting $c = 5 \times 10^{-5}$, $\rho = 10^9 cm^{-2}$ and $d = 3 \times 10^{-8} cm$ gives $n = 50$.]

(ii) a sufficient time. [This depends on the diffusion coefficient and therefore on the temperature.]

(iii) that $V \geq kT$. [Equating $V(R,\pi/2)$ (equation 4.6) to kT gives the effective size R_c of the Cottrell atmosphere (see figure 4.3) as

$$R_c \simeq 4\mu\varepsilon b_o^4/kT \qquad 4.8$$

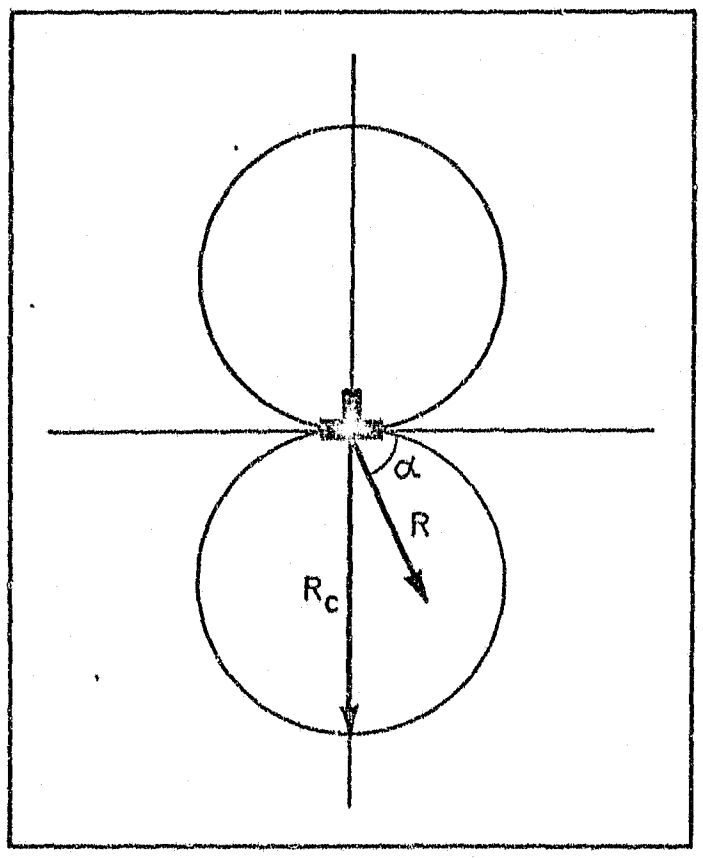


Figure 4.3. A schematic representation for the description of the hydrostatic stress field of an edge dislocation. In isotropic elastic continuum theory lines of constant stress are circles as shown.

Substituting $\mu = 3 \times 10^{-11}$ dynes cm^{-1}, and $b_o = 3 \times 10^{-8}$ (niobium) and $\varepsilon = 5 \times 10^{-2}$ (H in Nb) and T = 100K gives $R_c \simeq 350\text{Å}$. For $R > R_c$ the concentration of solute decreases approximately as $C \simeq C_o \exp(-V/kT)$.]

Schoeck and Seeger (1959) make a similar calculation for interstitial solute associated with the shear stresses on and about the glide plane of an edge dislocation and obtain

$$V(R) \simeq \beta b_o^4 \mu / 4\pi R \qquad 4.9$$

and therefore defining R_c^s as before gives

$$R_c^s \simeq \beta b_o^4 \mu / 4\pi kT \simeq \mu R_c / 16\pi\varepsilon \qquad 4.10$$

where βf is the shear strain due to the Snoek ordering of an atomic fraction f of the solute. [Recently Bockris, Beck, Genshaw, Subramanyan and Williams (1971) have derived a more exact formula for the concentration of interstitials in a Cottrell atmosphere. They calculate that in iron containing about 10^9 dislocations per cm^2 the existence of Cottrell atmospheres should increase the solubility of hydrogen by a factor of about 76 at room temperature .]

The rate of formation of a Cottrell atmosphere on an isolated edge dislocation in a region of initially dispersed solute has been calculated by Cottrell and Bilby (1949). They assume that the drift velocity of the solute atoms/ions in the stress field of the dislocation is greater than the diffusional drift velocity due to the solute concentration gradients which are set up by the stress fields. It is also assumed that the stress field of the dislocation is not affected by the accumulation of the atmosphere. (This latter assumption is patently not valid but other considerations compensate to allow this assumption.) The final result for the fraction f of the original solute which segregates to a dislocation in a time t when the dislocation density is ρ is given by

$$f(t) = 3(\pi/2)^{\frac{1}{2}} \rho[Adt/kT]^{2/3} \qquad 4.11$$

where $A \simeq V(R,\pi/2).R$ and therefore from equation 4.6

$$A \simeq 4\mu\varepsilon b_o^4 \qquad 4.12$$

Equation 4.11 is only expected to be valid in the very early stages of ageing. A semi-empirical equation has been proposed by Harper (1951), as an extension of equation 4.11, which is intended to take into account the effect of competing dislocations and extend the validity to longer times. The formula is given as

$$f(t) = 1 - \exp(-Bt^{2/3}) \qquad 4.13$$

where $B = 3(\pi/2)^{\frac{1}{2}}\rho(AD/kT)^{2/3}$

Harper (loc. cit.) obtains good agreement with experiment for carbon in iron and equation 4.13 has also been found to give reasonable agreement with experiment in a variety of systems. The refined consideration of Ham (1959) and Bullough and Newman (1959, 1961, 1962) however show that Harper's reasoning is untenable. However for situations where the elastic binding energy of the solute to the dislocation cores is large Harper's formula is fortuitously in agreement with the numerical calculations of Bullough and Newman (loc. cit.).

Finally solute, which is 'pumped' into the dislocation cores by the Cottrell-Bilby mechanism, diffuses along these cores and eventually forms discrete or rod like precipitates along them. According to the above model the volume of these precipitates should increase with time t as $t^{2/3}$. This has been confirmed by Dollins and Wert (1969) for nitrogen in niobium. These authors also find that for discrete precipitates, not associated with dislocations, the volume increases linearly with t.

4.5 Effects of interstitial solute on ρ_N, κ, T_c and H_c

The effect of a random distribution of solute is to disturb the regular periodic potential for electrons moving in the host lattice. Substitutional solute, especially when it has a valency different from that of the host, modulates both the magnitude and wavelength of this potential. Interstitial hydrogen is thought (Pryde and Tsong, 1971 and Hoffman and Cohen, 1973) to affect only the wavelength locally. The charge state of interstitial hydrogen in niobium is in any event not known (see Fast, 1971). The effect of the disturbed potential is to scatter electrons thus reducing their mean free path $\bar{\ell}$ and increasing the normal state resistivity ρ_N which is inversely proportional to $\bar{\ell}$.

Pryde and Tsong (loc. cit.) using Nordheim's model for the temperature independent change in the resistivity ($\delta\rho_N$) due to a concentration C of solute obtain

$$\delta\rho_N = k\, N_m C(1 - C/m) \qquad 4.14$$

where k is a constant which depends, inter alia, on the difference in potential between the filled and empty interstitial sites. N_m is the number of metal atmos per unit volume and m is the ratio of the number of interstitial sites to the number of metal sites per unit volume for the nearest stable phase.

For small C, $\delta\rho_N$ is proportional to C and for a concentration of 1 atomic per cent hydrogen in niobium $\delta\rho_N$ has been measured in the α phase to be about 0.8 micro-ohm cm (see for example Pryde and Titcomb, 1969). The dependence of the Ginzburg-Landau parameter κ on ρ_N is given (Goodman, 1961) by

$$\kappa = \kappa_o + 7.5 \times 10^3\, \gamma^{\frac{1}{2}} \rho_N \qquad 4.15$$

where ρ_N is in micro-ohm cm, $\kappa_o = 0.96\lambda_L(0)/\xi_o$ and γ is the

coefficient of the specific heat of the electrons per unit volume in the normal state in ergs cm^{-3} K^{-2}. Finnemore, Stromberg and Swenson (1966) find for pure niobium $\kappa_o = 0.78$ and $\gamma = 7.3 \times 10^3$ erg cm^{-3} K^{-2}. Substituting for γ and $\rho_N = 0.8C_1$ micro-ohm cm into equation 4.15 gives

$$\delta\kappa = 0.51\ C_1 \qquad 4.16$$

where C_1 is the concentration of the solute in atomic percent. This equation will not be valid however if applied to a region, containing an excess C_1 of solute, if it has a minimum linear dimension which is smaller than the local value of ξ_o. In this case coherence effects will tend to average κ over a region of radius ξ. The effective value of κ in the Cottrell atmosphere, for which $R_c < \xi_o$ will be given by

$$\delta\kappa_{eff} = 0.51\ C_1 (R_c/\xi)^2 \qquad 4.17$$

The effect of an interstitial solute on the critical temperature T_c in niobium has been experimentally investigated, inter alia, by Wiseman (1966) who obtains qualitative agreement with the theoretical expression of Claiborne (1963) for low concentration of solute (i.e. < one atomic per cent). This expression gives the change in T_c, resulting from a change in the superconducting energy gap due to the strain fields of solute atom ion, and is given (Claiborne, 1963) by

$$T_c \simeq kT_c\bar{\varepsilon}\ (2r_o) C_s^{1/3} \exp\left[\alpha - (C^{1/3} r_o)^{-1}\right] \qquad 4.18$$

where k is a constant, $\bar{\varepsilon}$ is the average strain due to the interstitial solute ion, r_o is the distance over which the strain extends, α is a constant of order unity and C_s is the concentration of the solute. The exponential term approaches unity as the solute concentration

approaches one atomic per cent. For higher concentrations Wiseman, in agreement with Morel (1959) obtains a change in T_c which is given by

$$\delta T_c \propto T_c(\delta V/V) \qquad 4.19$$

where $\delta V/V$ is the average relative change in the volume of the host lattice unit cell due to the presence of the interstitials.

Wiseman's experimental results are reproduced in figure 4.4.

The thermodynamic critical field H_c at $t = T/T = 0$ is given (Muhlschlegel, 1959) by

$$H_c(0) = 2.44\gamma^{\frac{1}{2}} T_c$$

and therefore

$$\delta H_c(0) = 2.44\gamma^{\frac{1}{2}}\delta T_c + 1.22\gamma^{\frac{1}{2}}T_c\delta\gamma \qquad 4.20$$

For small regions of modified H_c proximity and coherence effects must be taken into account. This is also problematical but need not be considered in this investigation as even without correction, in the case of Cottrell atmospheres, $\delta H_c(0)/H_c(0) << [\delta\kappa/\kappa]_{eff}$ (see chapter 5).

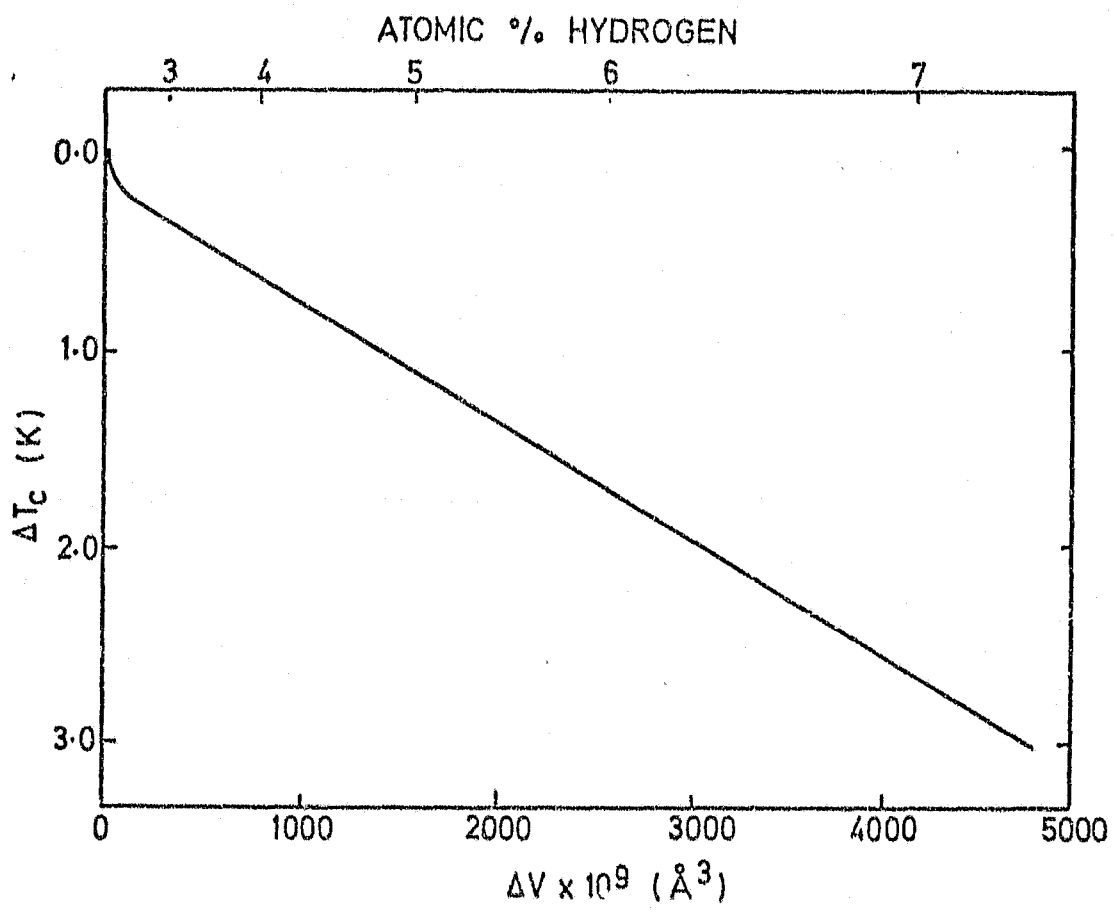


Figure 4.4. Variation in the critical temperature as a function of dilation of the unit cell in the niobium lattice and also of the hydrogen concentration in the nioboim lattice (from Wiseman, 1966).

CHAPTER 5

5. The Fluxon-Dislocation Interaction in Niobium

5.1 Introduction

In principle many of the theoretical considerations of chapter 3 have some experimental support. For pinning due to dislocations however there are areas of uncertainty in the theory. These include the relative importance of the various basic pinning site mechanisms, the method of summation and the related problem of the significance and validity of Labusch's (1969b) threshold criterion.

The results of previous experiments on pinning due to various dislocation configurations have been reviewed by Campbell and Evetts (1972) and by Dew-Hughes (1972). A brief outline of the experiments of particular relevance to this investigation will be given in this introduction. Other important results will be referred to when appropriate in the text.

Early measurements of the bulk pinning force density in cold worked niobium specimens (Narlikar and Dew-Hughes, 1964) indicated that an inhomogeneous dislocation distribution (i.e. braiding, tangles or cell formation) was necessary for strong fluxon pinning. These authors, Dew-Hughes (1966) and subsequently various other authors suggest that the basic pinning mechanism in cold worked materials is due to variations in κ between regions of tangled dislocations and regions relatively free of dislocations. Moreover since individual dislocations in a uniform distribution are known (see chapter 3) to interact with fluxons by a variety of mechanisms the increase in

pinning observed with the onset of dislocation tangling is not inconsistent with the concept of the threshold criterion. Enhancement of fluxon pinning has also been found, after suitable high temperature ageing treatment, in cold worked materials containing interstitial impurities (see for example Tedmon, Rose and Wulff, 1965).

Nembach (1966) and Freyhardt (1967, 1969, 1971) introduce screw dislocations into pure niobium single crystals, by torsional deformation about a <111> crystal axis, and investigate, from the magnetization behaviour of these crystals, the interaction between fluxons and a perpendicular screw dislocations. Freyhardt (loc. cit.) measures the pinning force density as a function of the induction B and temperature T for various degrees of torsional deformation. [The experimental method used, viz; determining the gradient dB/dr in the specimen from the areas of minor hysteresis loops, eliminates possible error due to surface pinning contributions.]

Apparent agreement is found between the experimental results and a model which uses Webb's (1963 and see also chapter 3) second-order elastic interaction model and a summation procedure based on Labusch's dilute-limit point-force approximation. The basic interaction apparently decreases with the reduced induction $b = B/B_{c2}$ as $(1 - b)$ as expected. However in Freyhardt's more heavily deformed specimens the dislocation distribution is certainly highly inhomogeneous and other basic pinning interactions, for example $\delta\kappa$, could be important (but see later). Moreover in this case, if the pinning is due to individual dislocation-fluxon interactions, the density of the pinning sites is too large for the dilute limit theory to apply (Campbell and Evetts, 1972).

Good and Kramer (1970) deform a pure single crystal cylinder of niobium (axial orientation <110>) in tension to 4 per cent strain

after (U.H.V. outgassing) to produce arrays of edge dislocations on the cross section {110} planes of the crystal. The pinning force density P_v is then determined as a function of B at T = 4.2K by measuring the critical transport current density J_c along the [110] axis of the crystal specimen with the applied field in the (110) plane. [J_c is defined by the appearance of a potential drop of 200 nanovolts with J_c held constant and H_o increasing from zero.] By rotating H_o in the (110) plane $P_v(B)$ is measured for various orientations of the dislocations with respect to the fluxon lattice. A maximum in J_c and hence in $P_v(B)$ for H_o along $[1\bar{1}0]$ (i.e. along the direction of the edge dislocations) and a slightly smaller broad maximum along [001] are found. This latter maximum is found to exhibit rectification effects and is ascribed to pinning of fluxons at the points of emergence of the dislocations in the specimen surface near the 110 poles.

A detailed comparison of the results of Good and Kramer with theory is not possible due to the lack of measurements on the temperature dependence of P_v. It is however significant that the dependence of P_v on $b = B/B_{c2}$ is apparently (i) invariant with the orientation of H_o with respect to the dislocations and (ii) is consistent with a dilute-limit point pinning force model for which Good and Kramer derive an expression using the dynamical summation approach (see chapter 3). The basic pinning sites are assumed to be associated with regions of dislocation braiding (which are evident in the electron micrographs of Good and Kramer (loc. cit.)) and to comprise mainly point like sites possibly acting cooperatively. It is also suggested that some edge dislocations segments are sufficiently long and straight to act as line pinning sites. No definite conclusion is reached

regarding the pinning site mechanism however.

In the present investigation the dislocation structure is similar to that of Good and Kramer (but see section 5.2.2). The presence of interstitial hydrogen in the niobium combined with measurements of the temperature dependence of the bulk pinning force density however permits a much more detailed investigation in the present case. In particular it will be demonstrated that isolated 'clean' edge dislocations (i.e. dislocations free of interstitial atmospheres) are apparently not effective as pinning sites in agreement with the expectation of Labusch's threshold criterion. For the deformation structure obtaining in the present case the results suggest that for 'clean' dislocations only regions of dense dislocation tangling act as the basic pinning sites. However if the dislocations have associated Cottrell atmospheres they become effective when parallel to the fluxon lattice and give rise to an overall pinning behaviour which is similar to that which is normally only obtained in much more heavily deformed specimens (see for example Campbell and Evetts, 1972).

5.2 Experimental

5.2.1 Sample preparation

The starting material used in this investigation was single crystal niobium as supplied by the Metals Research Corporation, New York, U.S.A. Interstitial and substitutional impurity concentrations are specified to be less than 50 ppm (by weight) each, with the exception of tantalum which is given as about 200 ppm. The crystal was in the form of a 1/4 inch diameter rod with the cylindrical axis aligned within one degree of a <110> orientation. The measured residual resistivity ratio R_{300}/R_{10} of the starting material was approximately 850.

From this crystal three specimens were prepared for deformation as follows: By spark erosion (Servomet Spark machine), with gradually decreasing spark intensity, the crystal rod was machined to be uniformly cylindrical along most of its 2 inch length. The final diameter of the cylinder was then approximately 6mm. The central region of the crystal was then sectioned (again by means of spark erosion) into three virtually identical cylinders, each 12mm long, and two discs each 1.2mm thick. The ends of the 12mm crystals were then planed, by spark erosion, to be flat, parallel and normal to the cylindrical axis of the crystals.

Surface damage due to spark erosion was minimized by using the finest cutting ranges for most, and in particular, the latter parts of the machining. This damage was subsequently removed by a light chemical polish in a solution of 55 per cent HF and fuming HNO_3 (ratio by volume 30:70). After polishing, the three crystals were deformed in uniaxial compression to nominal strains of 1 per cent, 2 per cent and 4 per cent respectively. This was accomplished by means of a special compression jig which was designed for use with the available tensometer. The polished stainless steel anvils of the jig were not lubricated prior to the compression procedures as this has been shown previously to give the best results (Taylor and Christian, 1967).

The tensometer is a screw driven Polyani type machine which was constructed by E.J.H. Wessels and P.J. Jackson (ex this department), with some modifications, from a design by Basinsky (see White, 1959). The linearity and calibration of the tensometer were checked by hanging known weights from the load cell. For deformation of the present specimens the cross-head velocity was set to be 2.5×10^{-3}mm sec^{-1}. The actual deformation rate was somewhat lower due to the 'softness'

of tne tensometer. This was established to be approximately 6×10^{-4}cm Kgm^{-1}. The stress-strain curve (after correction for machine softness - but not resolved onto the operating slip systems) for the specimens is shown in figure 5.1. The arrows in the figure indicate the actual final strain (along [110]) for each specimen. The absence of any yield point phenomenon in the curve is expected but is not significant because of the machine softness. These results are similar to those obtained elsewhere under similar deformation conditions (see for example Bowen, Christian and Taylor, 1967).

After deformation the crystals were slightly elliptical in cross section and they were again machined to be uniformly cylindrical over a region of several millimeters near their equators. From this region, in each case, three discs were cut (thickness > 1mm) normal to the cylindrical axis. These discs, together with the two 1.2mm thick discs of undeformed crystal mentioned earlier, were then planed, using the finest range available on the Servomet, on both faces to be uniformly 1mm thick.

Two discs of each set (i.e. for the 0 per cent, 1 per cent, 2 per cent and 4 per cent (nominal) deformed crystals) were then aligned by X-ray methods so that rods (1 x 1 x 6mm) could be cut from the discs with their long axes along $[1\bar{1}0]$ and [001] directions respectively for each set. Thus, for each deformation case, rectangular rods were obtained with edge dislocation debris lying predominantly along or at right angles to their long axes (see section 5.2.2).

The rods and remaining discs were then chemically polished for two minutes to remove surface damage. The time required to remove all spark damage was determined in a separate experiment where the magnetic hysteresis in undeformed specimens was measured as a function of polishing time.

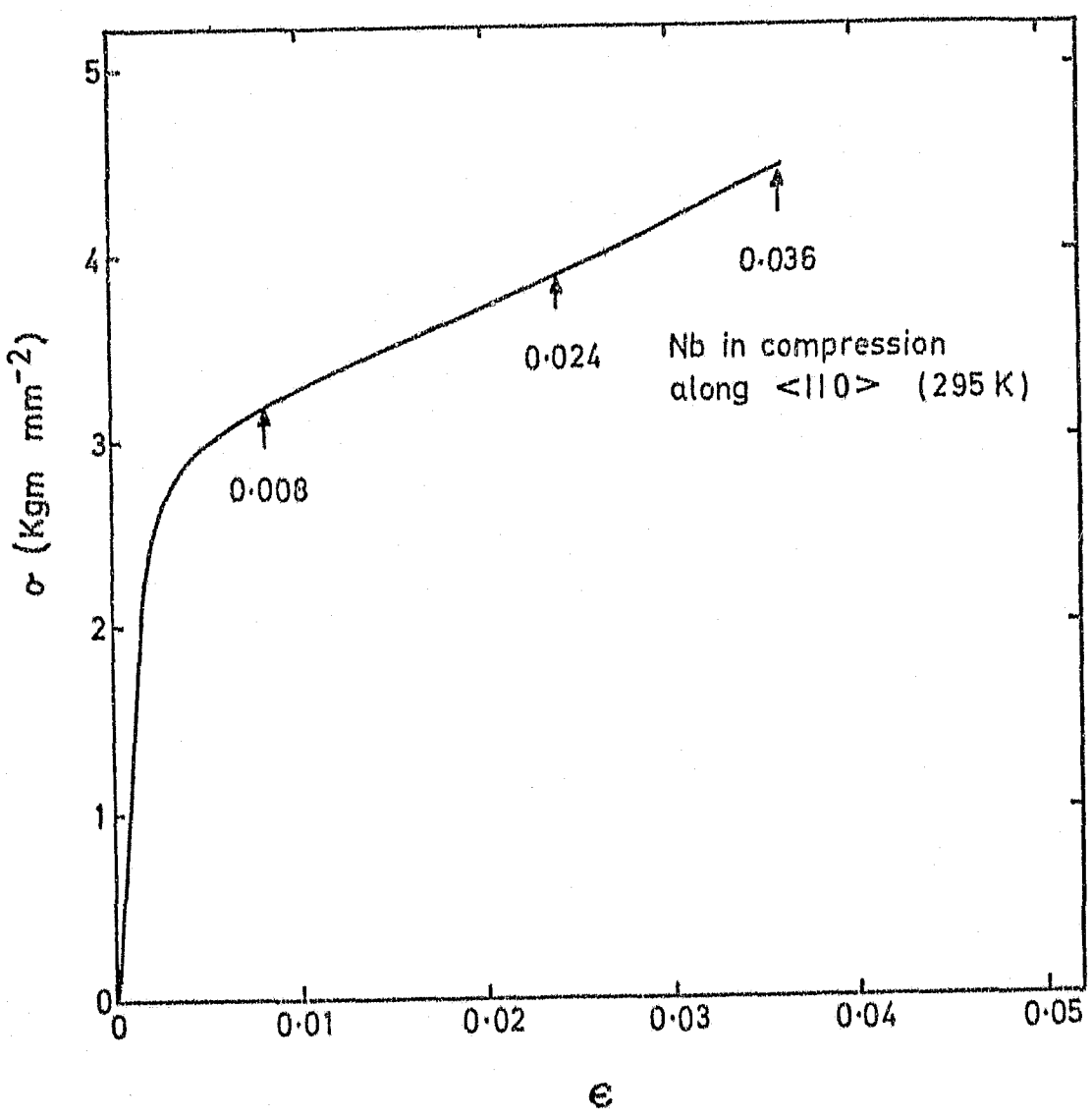


Figure 5.1. Stress-strain curves obtained for the niobium single crystals in compression along <110> at 295K. The arrows indicate the terminal strain for each crystal.

5.2.2 Deformation and the dislocation configuration

For uniaxial stress along the [110] direction in niobium it is known (Foxall, Duesbery and Hirsch, 1967, Bowen, Christian and Taylor, 1967, and Taylor and Christian, 1967a, b) that deformation occurs by double glide on the $[11\bar{1}]$ (112) and $[111]$ $(11\bar{2})$ systems which are symmetrically disposed to the [110] tensile axis. For deformation in tension any small imbalance in the Schmid factors on these two systems gives rise to a tendency for the tensile axis to rotate back to the [110] axis. In compression this tendency will be reversed, but in practice the tensile axis is stable providing it is initially within a few degrees of [110] (Christian and Taylor, 1967a).

The dislocation debris resulting from this type of deformation at room temperature is predominantly edge in character with the dislocations aligned along the $[1\bar{1}0]$ direction in the (110) plane. The Burgers Vector is $b = \frac{a}{2}[111]$ (see for example Taylor, 1966, Bowen, Christian and Taylor, 1966 and Taylor and Christian, 1967b). According to Foxall, Duesbery and Hirsch (loc. cit.) 80 per cent of the dislocation segments lie within 10 degrees of pure edge and about 0.5 per cent lie within 10 degrees of pure screw orientation. There is a strong tendency in this type of deformation for the formation of loose dislocation braids (see for example Taylor and Christian, 1967b) which extend for relatively long distances along the $[1\bar{1}0]$ direction. This tendency is apparently less marked in specimens deformed in compression than in tension.

A general feature of deformation in niobium is the existence of small regions of tightly tangled dislocations (typically 0.05 to 0.5 microns in diameter) which apparently consist predominantly of edge dipoles or multipoles.

Finally the dislocation density in niobium specimens deformed 4 per cent in this manner has been measured (Good and Kramer, 1970) as 1.5×10^{9} cm^{-2}.

5.2.3 The magnetization measurements

The magnetometer and a basic outline of the method of operation have been described in chapter 2.

Preliminary magnetization measurements on the rectangular rod specimens indicated an apparently irreproducible behaviour which was related to the manner in which the temperature of the specimen had been cycled between 300K, 80K and 4K. Various considerations and experiments established that this irreproducible behaviour was associated with configurational changes of interstitial hydrogen solute in the specimens at sub-ambient temperatures. The low temperature behaviour of interstitial hydrogen has been discussed in chapter 4 where it was demonstrated that the mobility of interstitial hydrogen in niobium is virtually zero at temperatures below 20K. Consequently rapid and reproducible quenching from room temperature to 4K should result in a uniformly dispersed hydrogen configuration, with partially formed Cottrell atmospheres 'frozen' onto the dislocations, and therefore to reproducible hysteretic behaviour. In practice this was found to be the case. The specimens were therefore always quenched to 4K in the same manner. The method of quenching has been described in chapter 2 and in figure 5.2 the highly reproducible cooling-time characteristic for this quenching process is shown*. Also shown in

---

* The quench time from 300K to 4K is limited to a minimum of approximately 150 seconds by the relatively low thermal conductivity between the calorimeter and the helium bath.

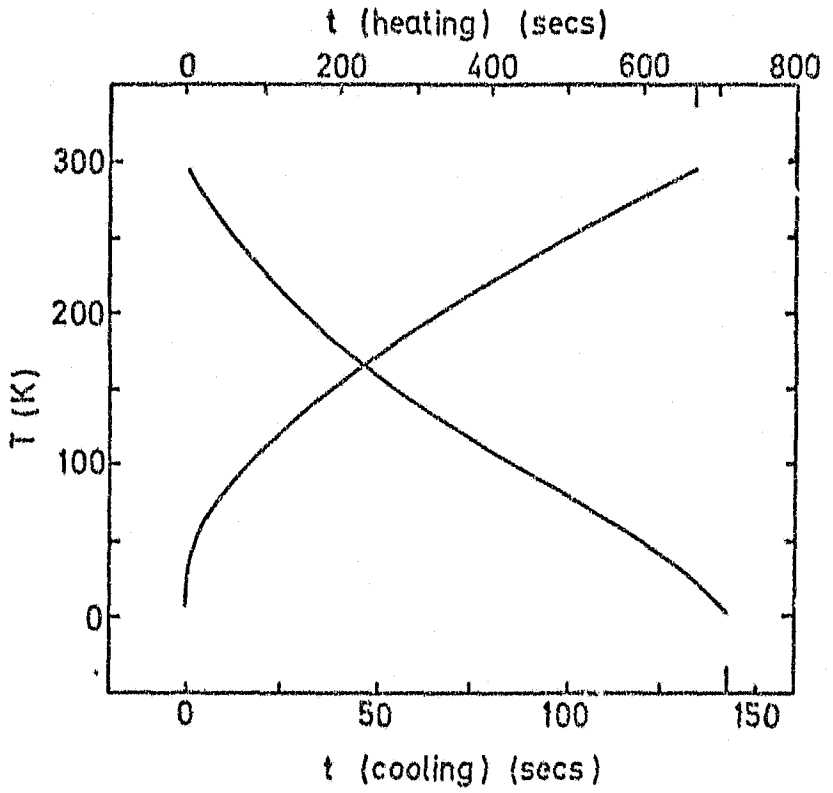


Figure 5.2. Heating-time and cooling-time characteristics for the temperature controlled specimen stage (see text).

the figure is the heating-time characteristic. These characteristics were obtained using the special temperature regulated specimen stage (see appendix A2 and A3) which was used in the ageing experiments (which will be described later). The slightly l[illegible]er thermal mass of this stage compared with the usual specimen holder is not expected to affect the rate of cooling (as indicated in figure 5.2) by more than a few per cent.

Thus magnetization (M) measurements were made on the rod-specimens in the as-quenched state as described above (and initially in the Meissner state), with the applied field (H_o) parallel to their long axes, for increasing and decreasing H_o and at various temperatures for a large number of intervals in the range $4K \lesssim T \lesssim 9.3K$. Although temperatures as low as 2.2K could be obtained by pumping on the helium bath it was not considered worthwhile to extend the measurements this temperature.

Magnetization measurements on the disc-specimens were made only at 4.05K with the applied H_o in the plane of the discs for various orientations of H_o with respect to the $[1\bar{1}0]$ direction. After each magnetization measurement on the disc-specimens it was necessary to remove the specimen from the cryostat, reorientate it, and then to quench it back to $T = 4.2K$ again for the next measurement. The specimen holder and jig for aligning these specimens are described in appendix A2.

To determine the effects of the configurational distribution of the interstitial hydrogen on fluxon pinning in a systematic manner isochronal ageing experiments were conducted on the rod-specimens at ageing temperatures T_a at equal intervals in the range $4K < T_a < 300K$. This was done as follows: The rod specimen was mounted in the

temperature regulated specimen stage and quenched to T = 4.05K. A magnetization loop was then recorded. The helium exchange gas was then pumped from the specimen chamber and the temperature of the specimen stage was raised to, and maintained at, some level T_{a1} for 10 minutes. Helium gas was then rapidly re-admitted into the specimen chamber, restoring the pressure to atmospheric, and the heater on the stage was simultaneously switched off. When the specimen had quenched to 4.05K a magnetization loop was again recorded. This process was repeated at an ageing temperature $T_{a2} > T_{a1}$ and so on for ageing temperatures up to $T_a = 300K$. A similar set of isochronal ageing experiments was then conducted at a constant temperature ($T_a = 90K$) for several periods of 15 minutes duration.

The hydrogen concentration in the rod specimens was subsequently determined by Mr R.P. Badenhorst of the South African Iron and Steel Corporation (Pretoria) to be approximately 50ppm (atomic). The small size of the specimens precluded an exact determination. For this hydrogen concentration, especially as the hydrogen is mostly associated with the dislocations at low temperatures, the effect on the bulk properties of niobium are very small (see chapter 4).

Attempts to measure the oxygen and nitrogen concentrations in the specimens by neutron activation analysis (also at the South African Iron and Steel Corporation) yielded inconclusive results but suggested only a few ppm in each case.

5.3 Experimental results

A few representative magnetization curves for the variously deformed rod-specimens (as-quenched) at various measuring temperatures are shown in figures 5.3a to 5.3d. The curves for all the rod-

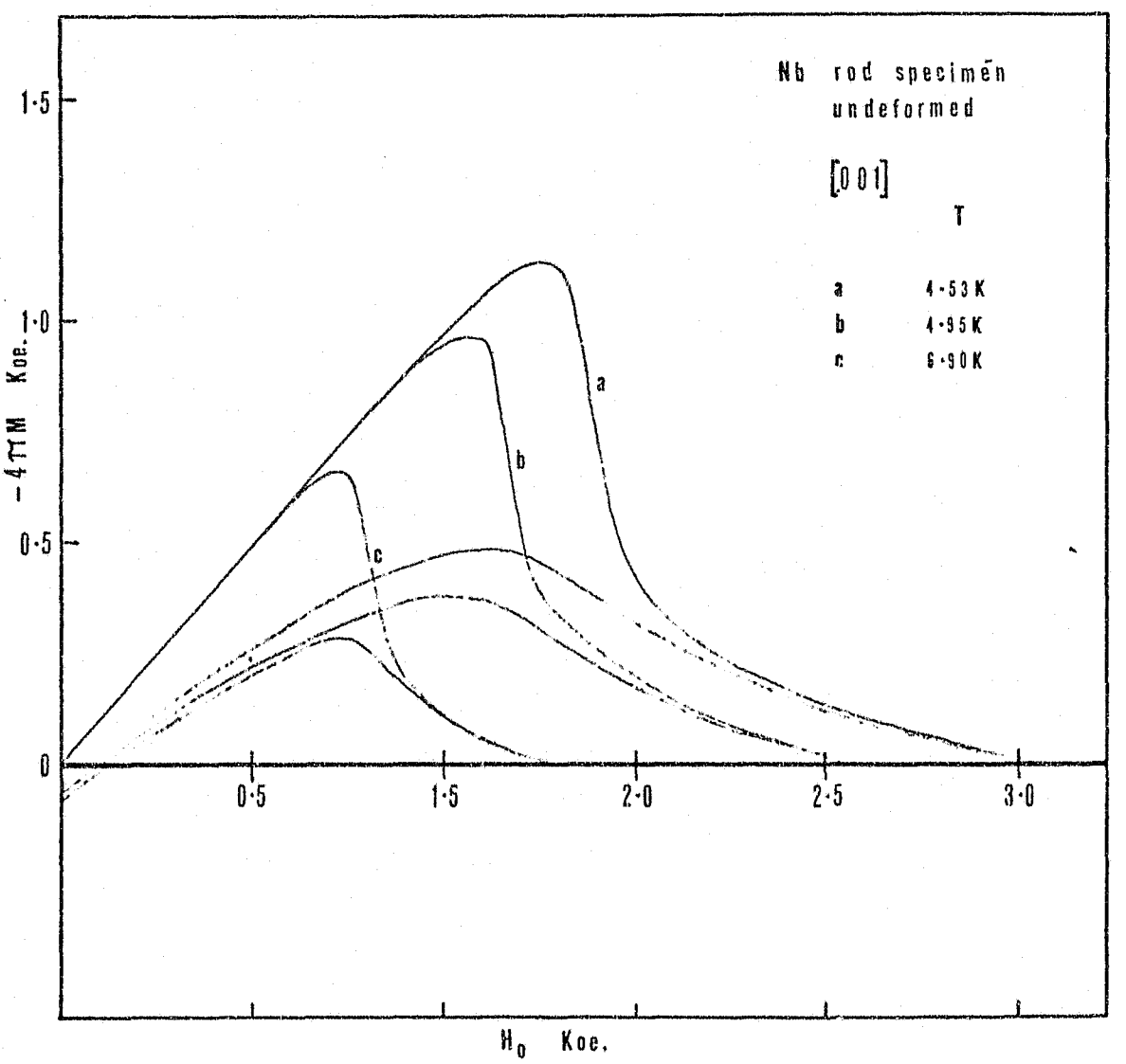


Figure 5.3a. Magnetization curves for the [001] undeformed niobium rod specimen and a few of the temperatures of measurement.

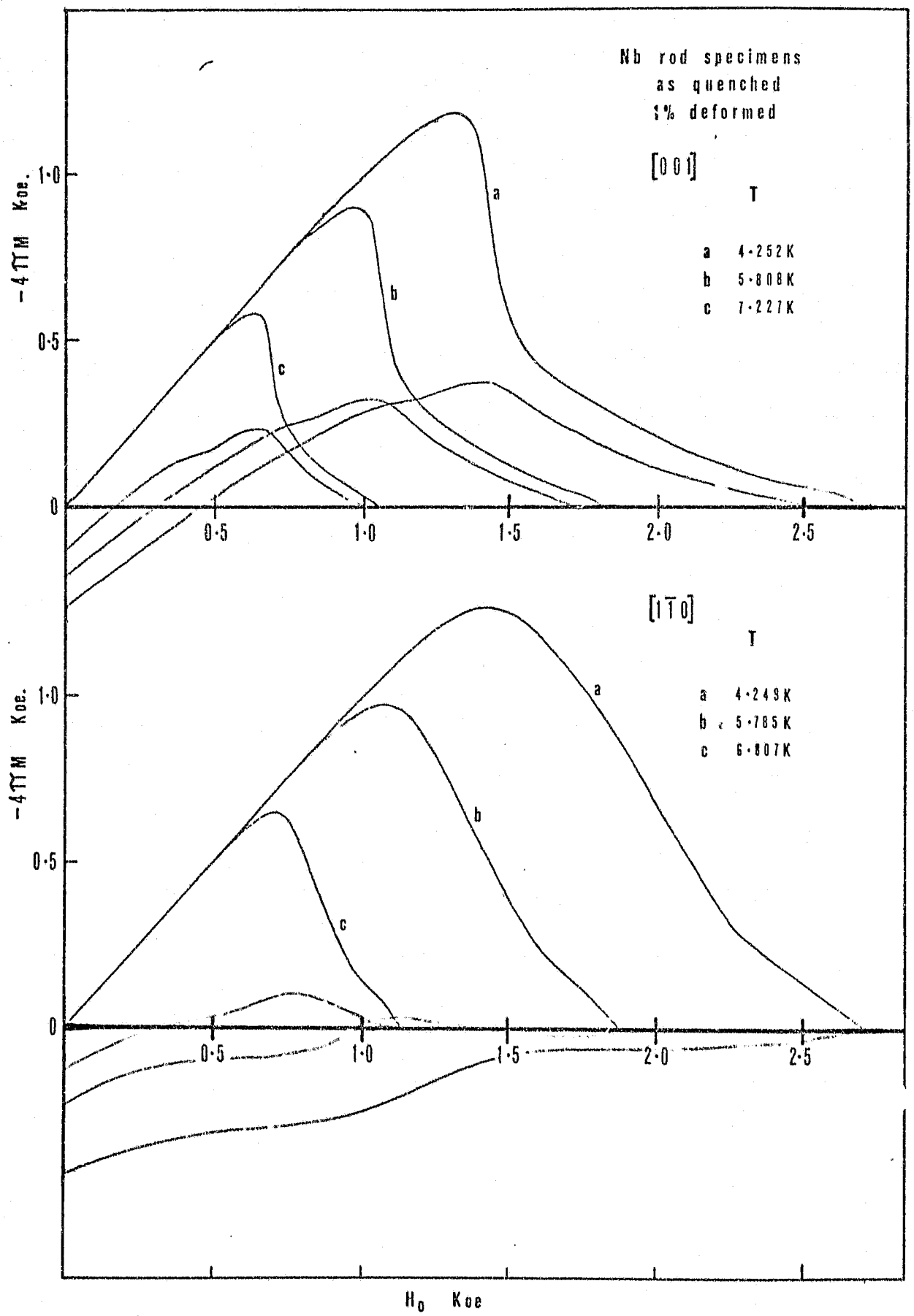


Figure 5.3b. Magnetization curves for the [1$\bar{1}$0] and [001] 1 per cent (nominal) deformed rod specimens.

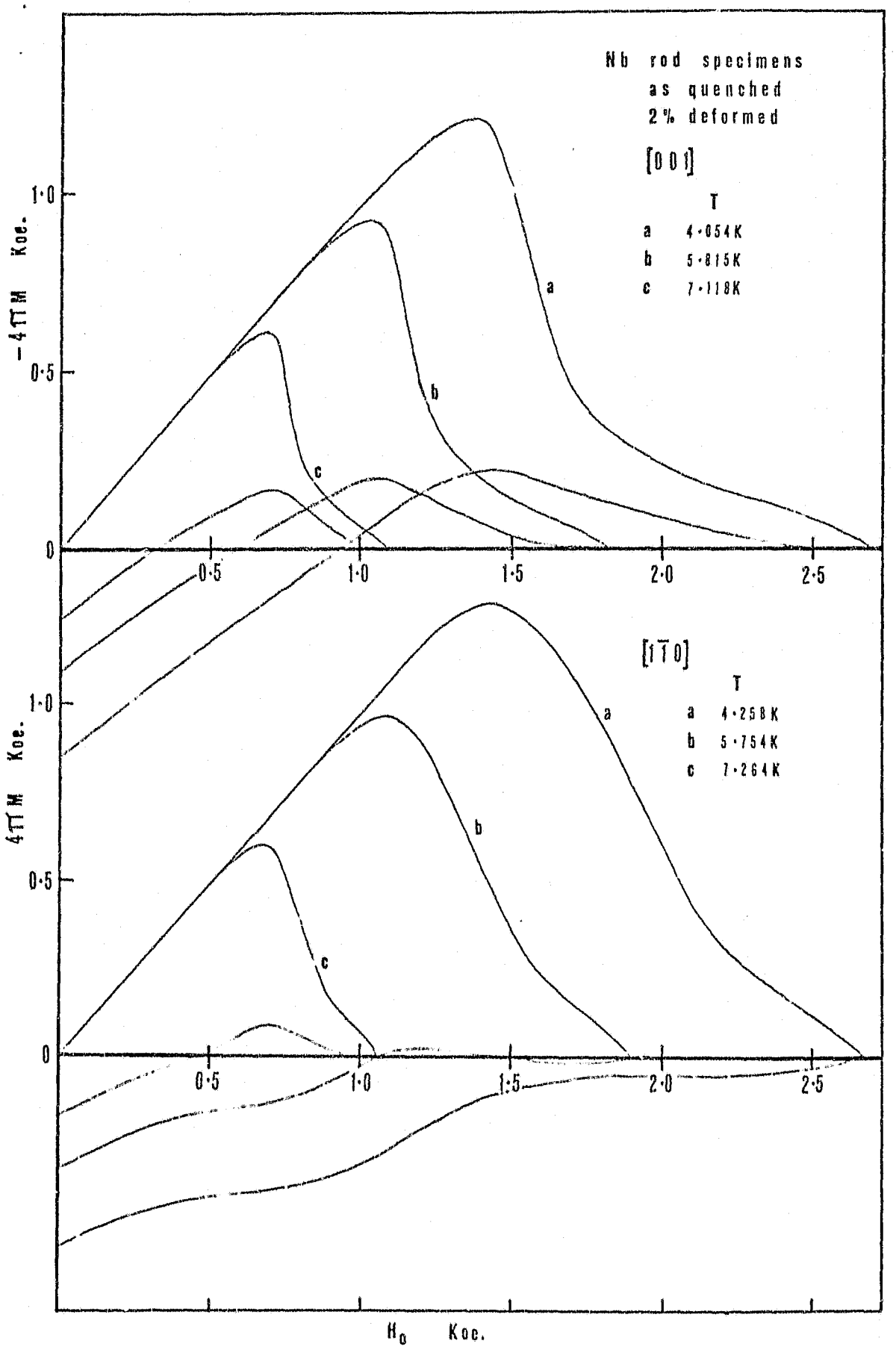


Figure 5.3c. Magnetization curves for the [1$\bar{1}$0] and [001] 2 per cent (nominal) deformed rod specimens.

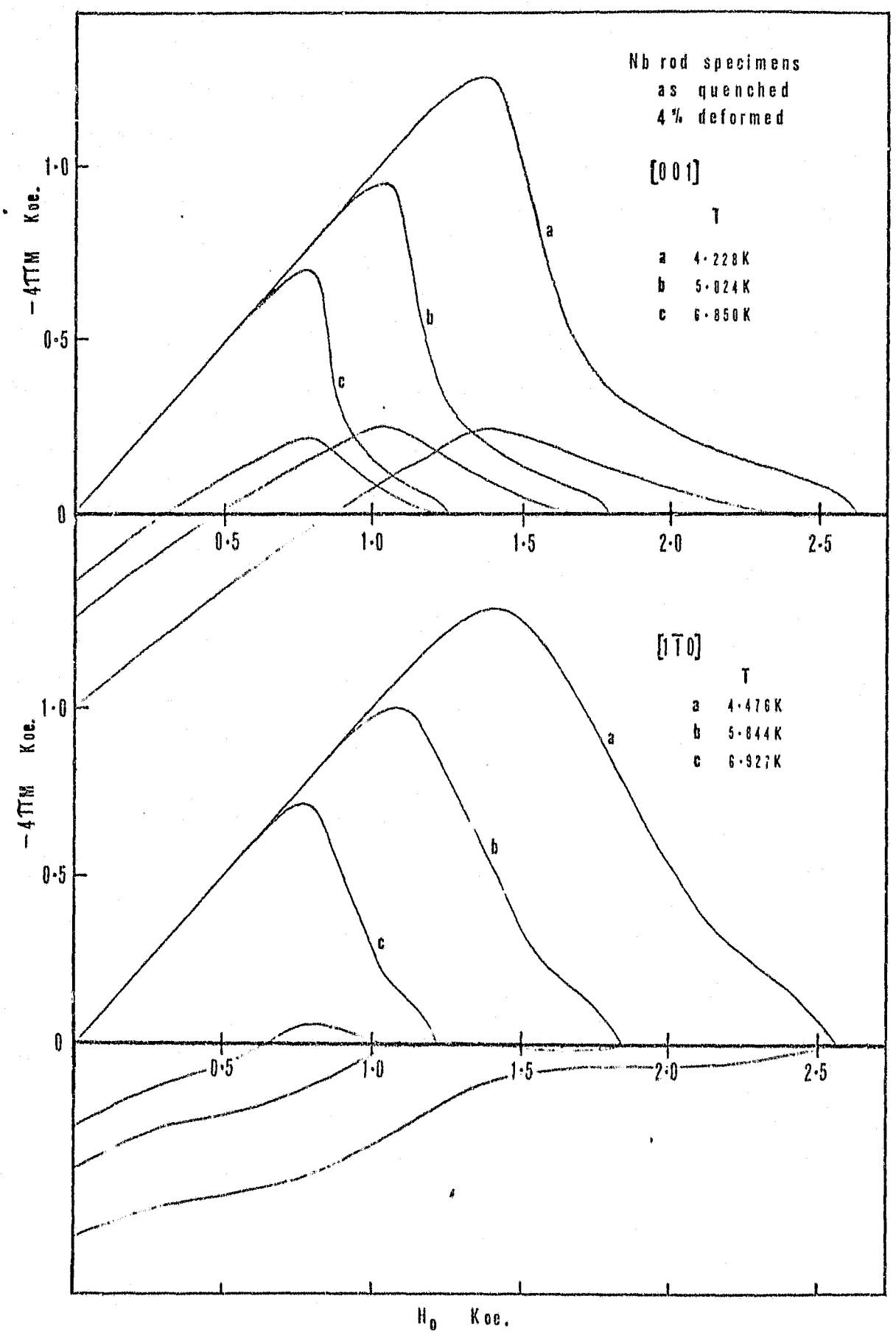


Figure 5.3d. Magnetization curves for the [1$\bar{1}$0] and [001] 4 per cent (nominal) deformed rod specimens.

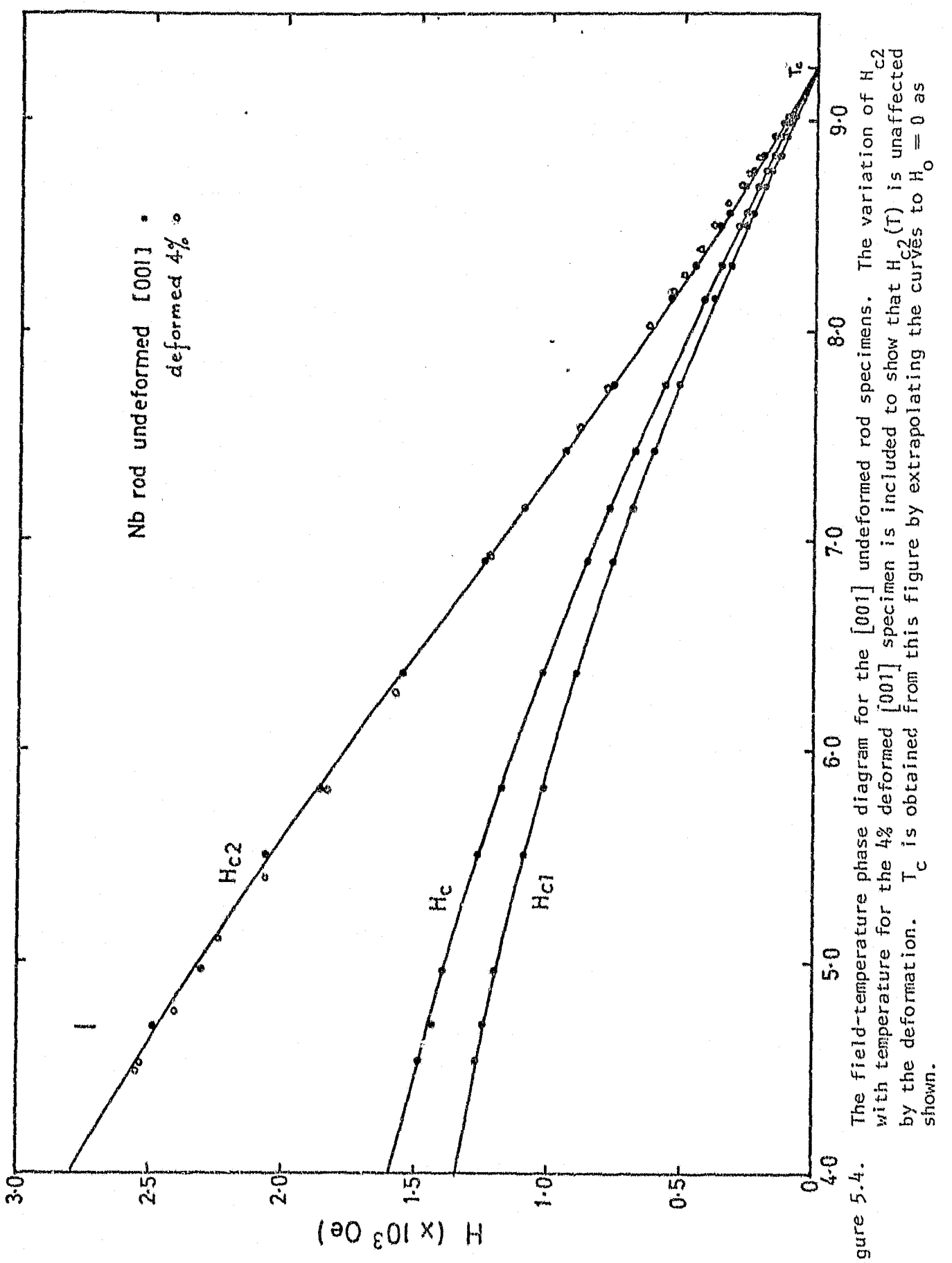


Figure 5.4. The field-temperature phase diagram for the [001] undeformed rod specimens. The variation of H_{c2} with temperature for the 4% deformed [001] specimen is included to show that $H_{c2}(T)$ is unaffected by the deformation. T_c is obtained from this figure by extrapolating the curves to $H_o = 0$ as shown.

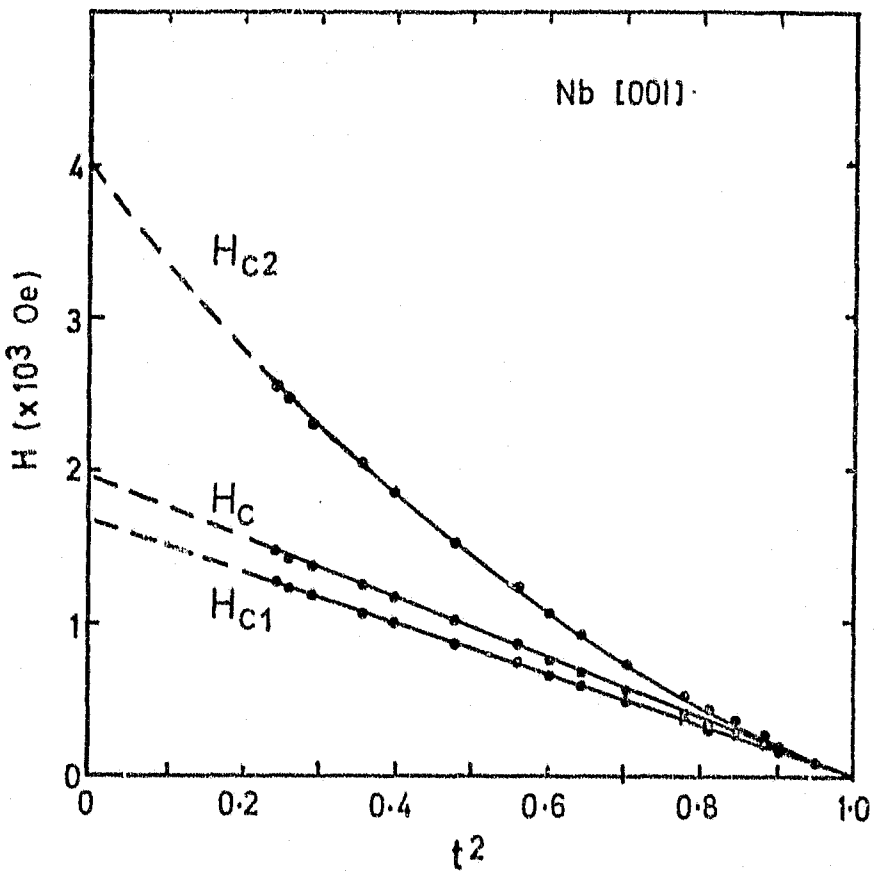


Figure 5.5. The variation of the critical fields H_{c1}, H_c and H_{c2} with t^2 where $t = T/T_c$. Extrapolation of the curves to $t^2 = 0$ gives $H_{c1}(0)$, $H_c(0)$ and $H_{c2}(0)$.

specimens show considerable hysteresis for $b \lesssim 0.35$. This hysteresis is due predominantly to the sharp corners of the rectantular specimens (see chapter 6). Since however, in low κ materials, large uncertainties exist in the theory of pinning for $b \lesssim 0.4$ (see for example Campbell and Evetts, 1972) the tedious and possibly hazardous procedure of attempting to remove the corners was not considered worthwhile. For $b \gtrsim 0.35$ the magnetization behaviour is almost reversible in the undeformed specimens (figure 5.3a) and the analysis of the pinning force density in the deformed specimens will therefore be confined to the region $b \gtrsim 0.35$. The reversible behaviour of the undeformed specimens and various other considerations which will become apparent also indicate that the various surface pinning effects (see chapter 1) are not significant in the present specimens in this regime.

In figure 5.4 $H_{c1}(T)$, $H_c(T)$ and $H_{c2}(T)$ for the [001] undeformed (as-quenched) rod-specimen are shown as functions of T. [$H_{c2}(T)$ and $H_{c1}(T)$ are obtained from the magnetization curves by extrapolation as shown in figure 5.3a.]

Extrapolating the critical field curves in the region $H \lesssim H_{c2}$ to $H = 0$ (see figure 5.4) gives, for the critical temperature, $T_c = 9.25 \pm 0.01$K. Also shown in figure 5.4 are the results for $H_{c2}(T)$ for the [001] 4 per cent deformed rod-specimen. The increase in $H_{c2}(T)$ due to the deformation is apparently not significant. In figure 5.5 the results of figure 5.4 are replotted against t^2, where t is the reduced temperature T/T_c. Extrapolating the curves to $t^2 = 0$ gives $H_{c2}(0) \cong 4.00 \times 10^3$ oersted, $H_{c1}(0) \cong 1.67 \times 10^3$ oersted and $H_c(0) \cong 1.96 \times 10^3$ oersted.

The Maki parameters $\kappa_1(t)$ and $\kappa_2(t)$ have been determined as a functions of t from the magnetization curves for the [001] undeformed specimen using equations 1.5 and 1.6. In the inset of figure 5.6 $\kappa_1(t)$ and $\kappa_2(t)$ are plotted against t^2 in the vicinity of $t = 1$ in order to determine the Ginzburg-Landau parameter κ which is given by $\kappa = \kappa_1(t = 1) = \kappa_2(t = 1)$. According to this plot $\kappa = 0.785$. Using this value for κ the reduced Maki parameters κ_1/κ and κ_2/κ were then calculated and are plotted against t^2 in figure 5.6. These results are very similar to those obtained elsewhere by other authors (see for example Finnemore, Stromberg and Swenson, 1966).

The method for the determination of the critical current density $J_c(B)$ and hence the bulk pinning force density $P_v(B)$ from the magnetization loops is given in appendix A1(e). The dependences of J_c on the reduced induction b for the various deformed specimen-rods at various temperatures is shown in figures 5.7 to 5.12. In figures 5.13 to 5.16 the dependence of P_v on b is similarly shown. Figure 5.17 shows qualitatively the an'sotropy in the magnitude of $P_v(b = 0.6)$ in the (110) plane for the 1 per cent, 2 per cent and 4 per cent deformed disc specimens (solid curves) and $P_v(b = 0.8)$ for the 4 per cent deformed disc specimen (points) with the applied field in the plane of the discs. The small asymmetry is presumably due to a slight mis-alignment of the disc axes from [110]. [The geometry of the disc-specimens precludes a quantitative determination of P_v]. The anisotropy of H_{c2} ($T = 4.05$) in the (110) plane is shown in figure 5.18.

According to figure 5.17 $P_v(b = 0.6)$ is strongly peaked (in the as-quenched specimen) when the applied field is in the $[1\bar{1}0]$

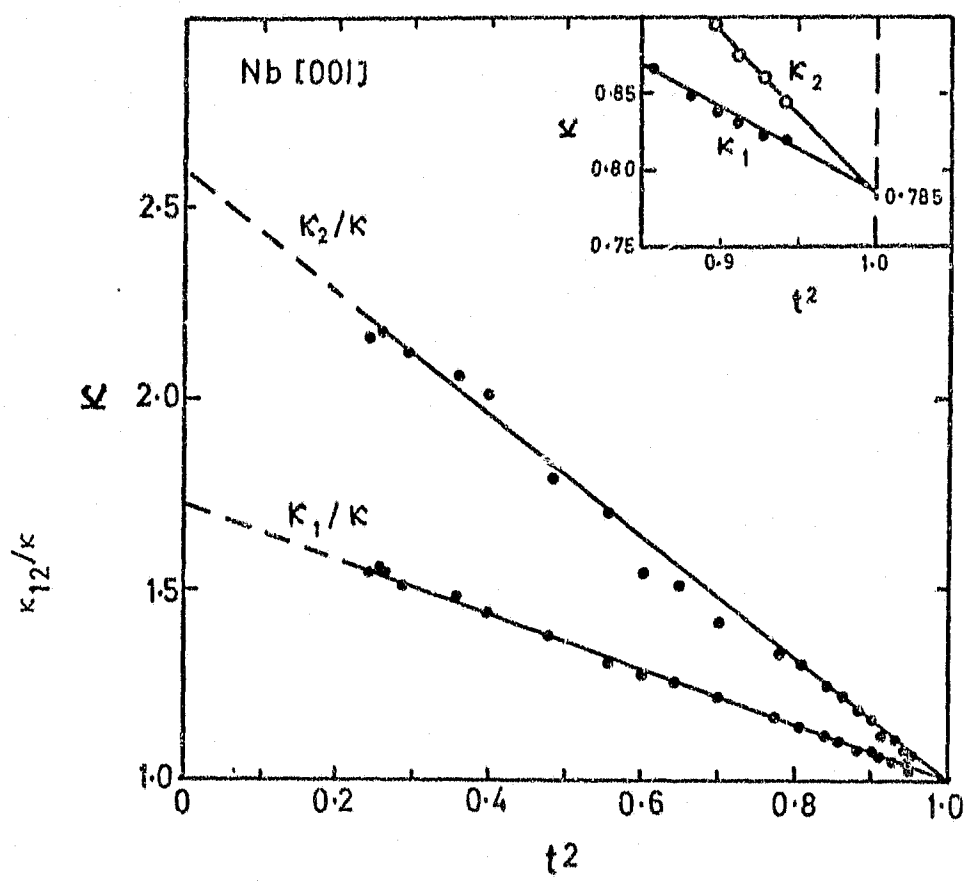


Figure 5.6. The variation of the reduced Maki parameters κ_1/κ and κ_2/κ with the square of the reduced temperature. The inset shows the variation of κ_1 and κ_2 with t^2 near $t = 1$ and gives the Ginzburg-Landau parameter κ $[\kappa = \kappa_1(t = 1) = \kappa_2(t = 1)]$ as 0.785.

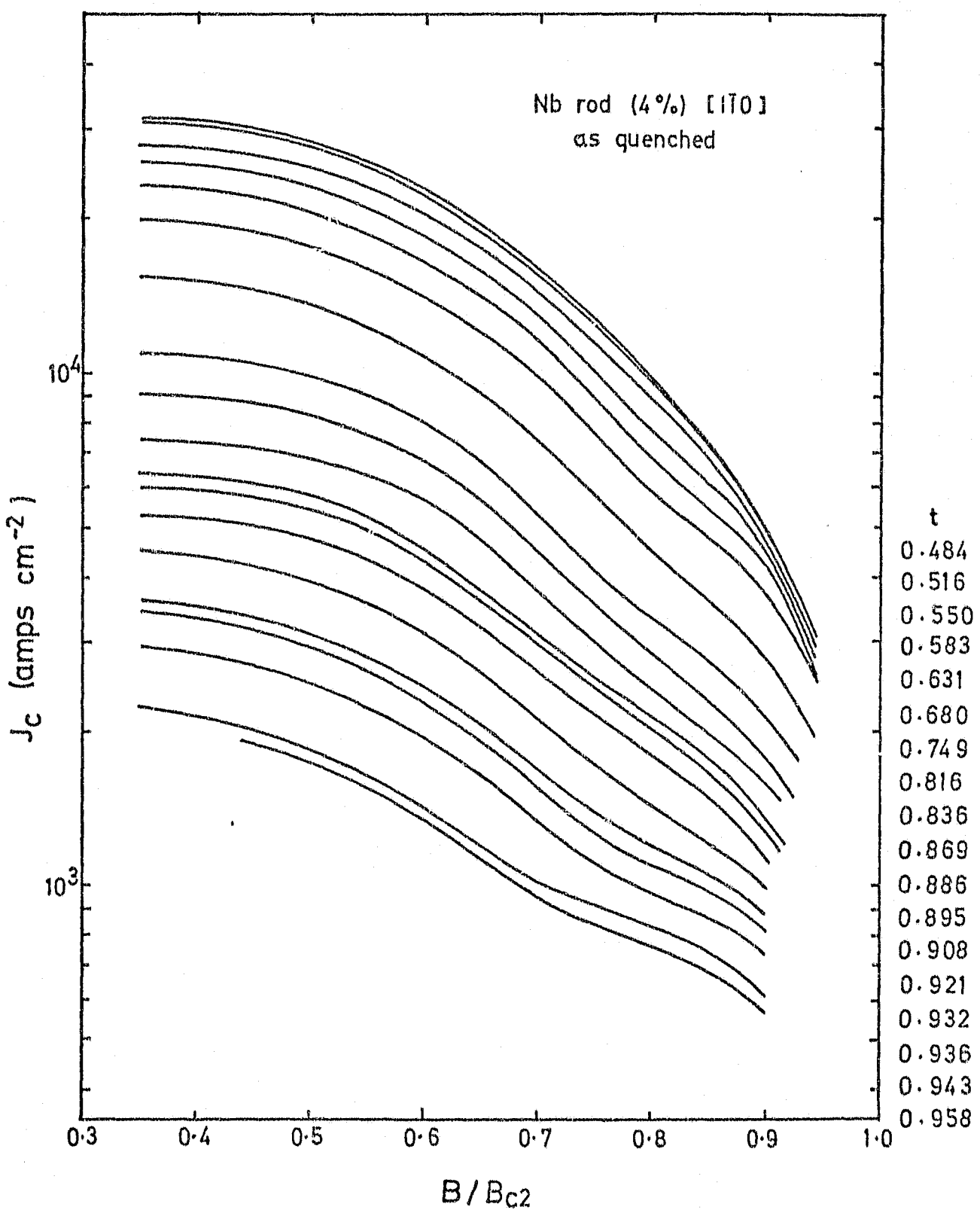


Figure 5.7. The variation, at various reduced temperatures, of the critical current density with reduced induction for the as-quenched [1$\bar{1}$0] 4% deformed rod specimen.

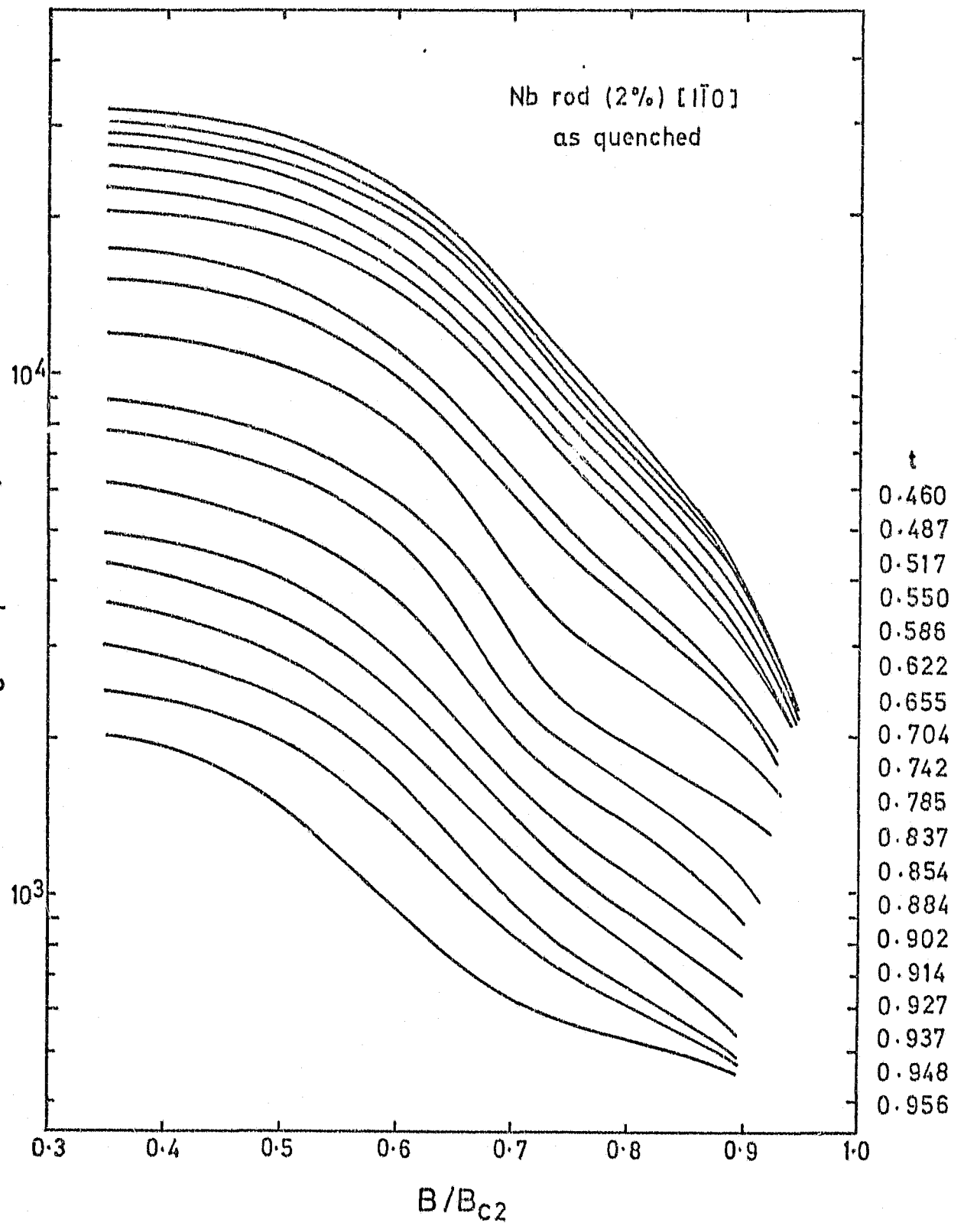


Figure 5.8. As for figure 5.7 for the as-quenched [1$\bar{1}$0] 2% deformed specimen.

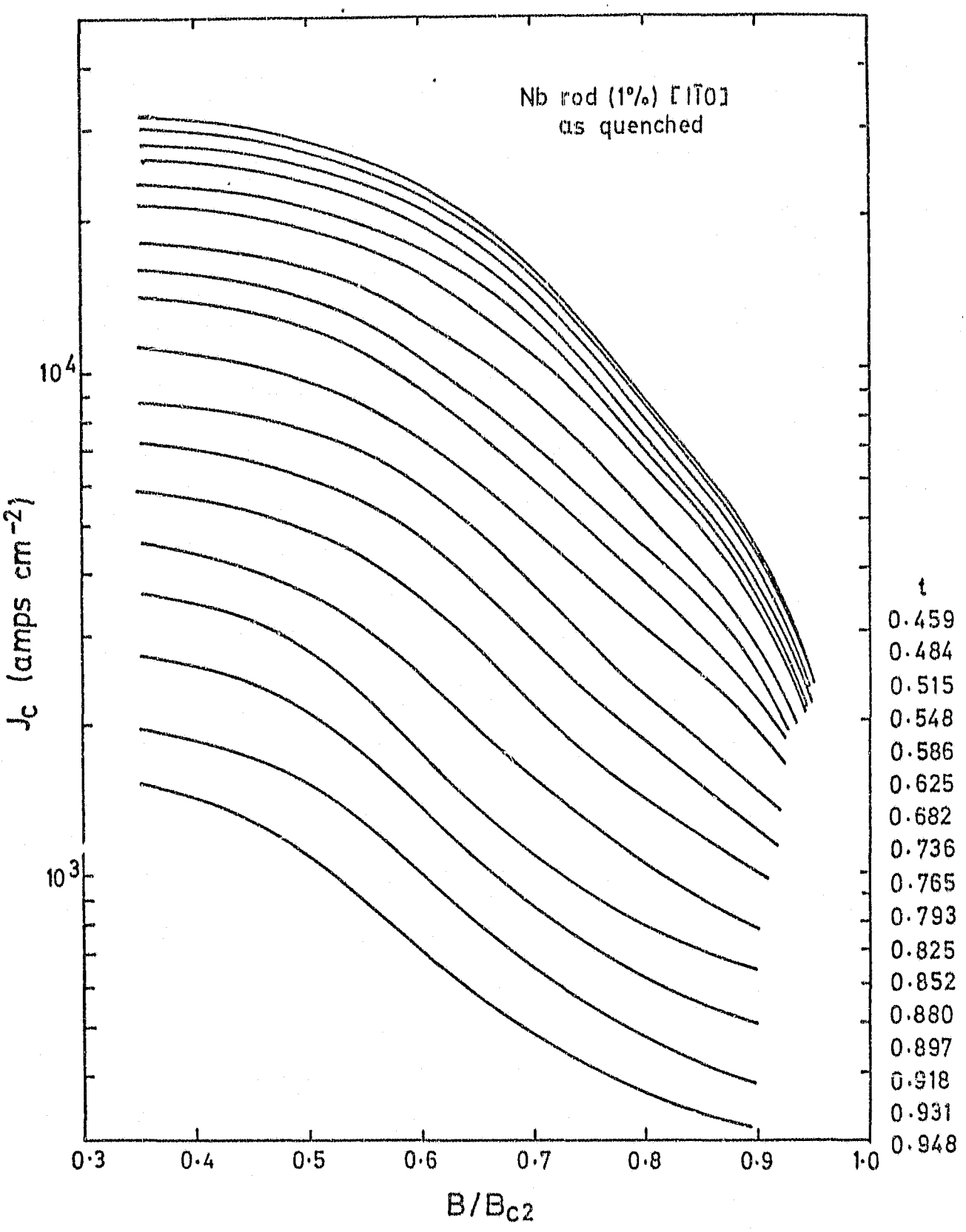


Figure 5.9. As for figure 5.7 for the as-quenched [1$\bar{1}$0] 1% deformed specimen.

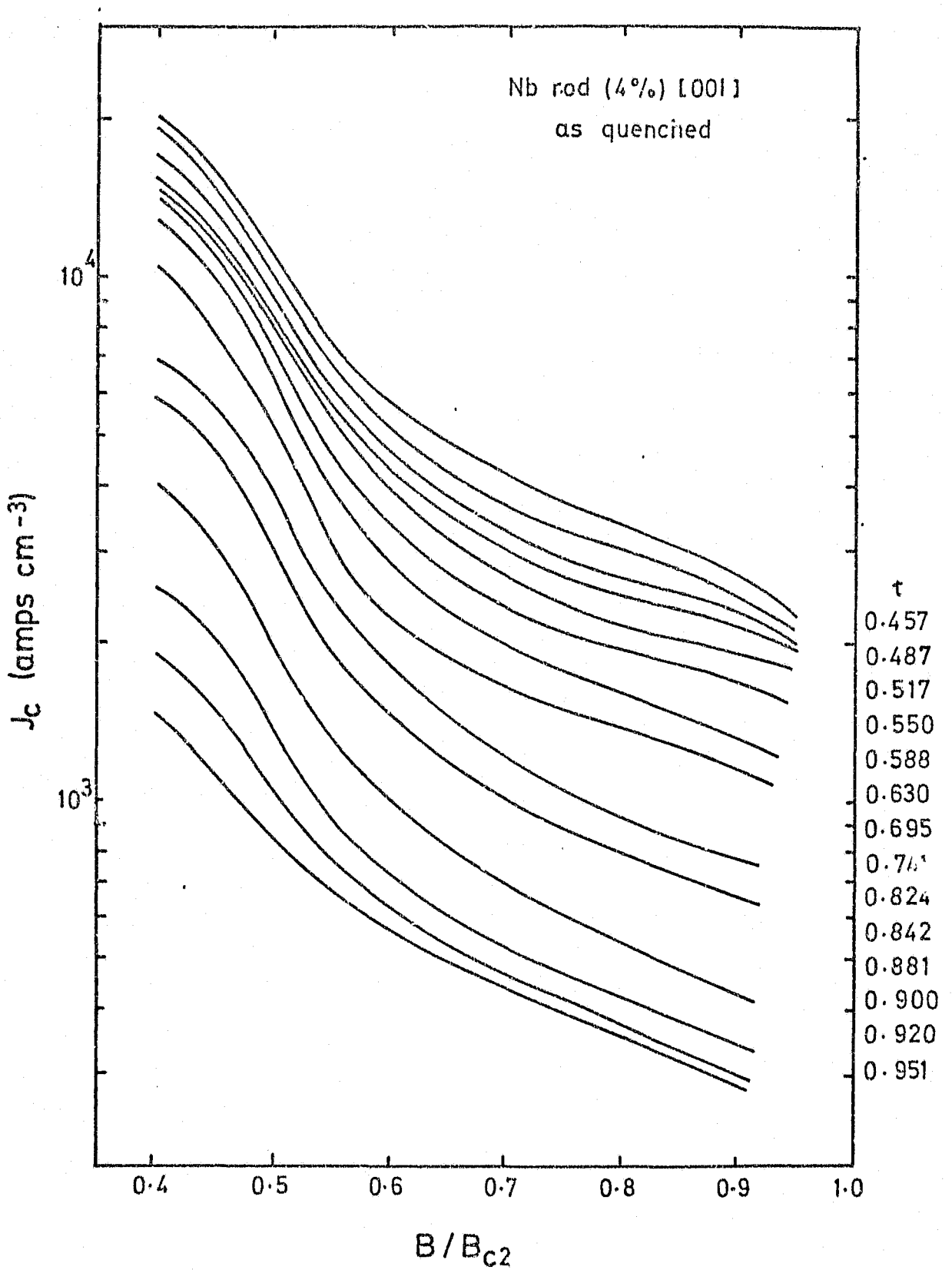


Figure 5.10. As for figure 5.7 for the as-quenched [001] 4% deformed rod specimen.

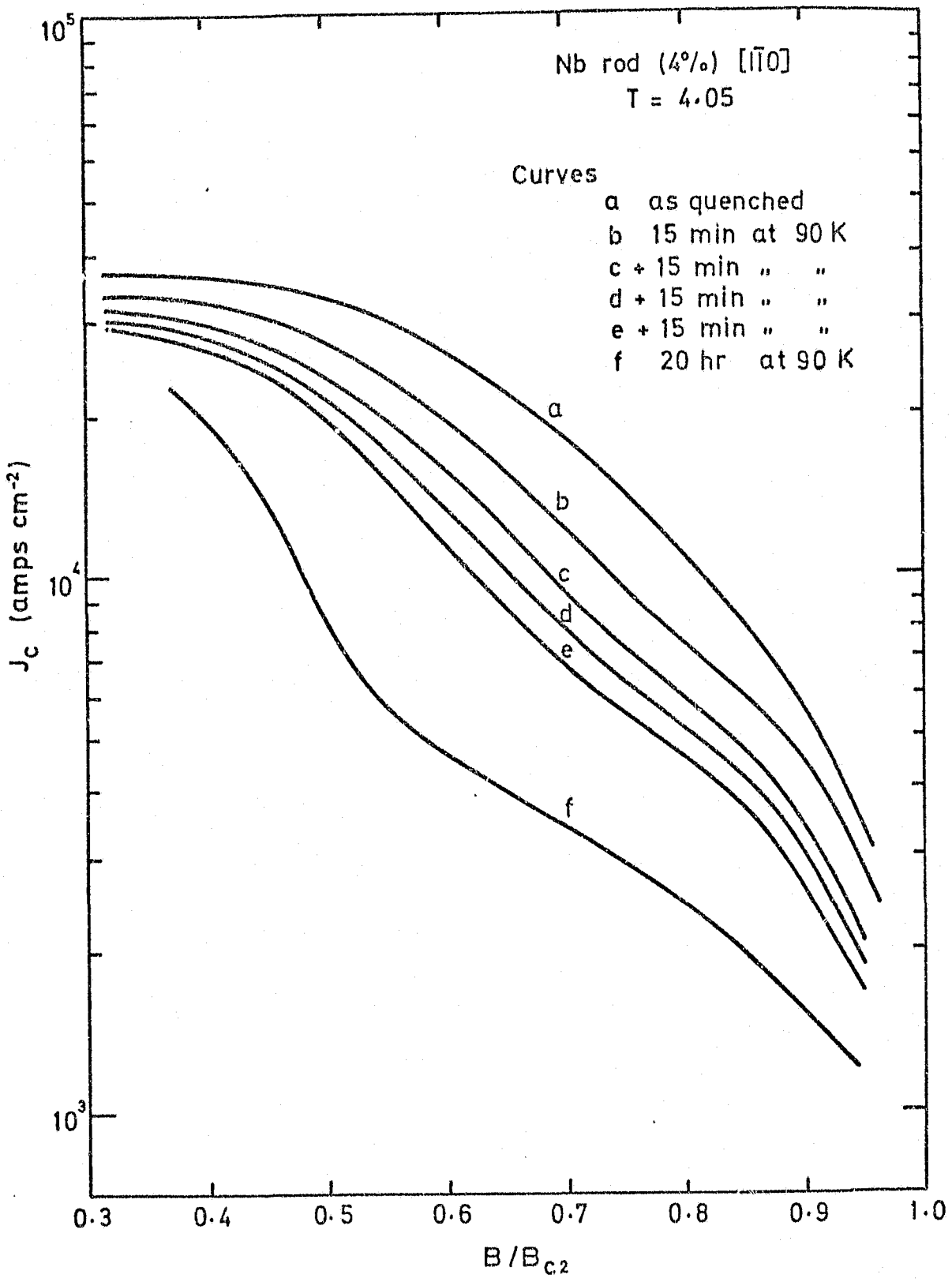


Figure 5.11. The variation at T = 4.05K of the critical current density with reduced induction for the $|1\bar{1}0$, 4% deformed rod specimen after various isochronal ageing treatments.

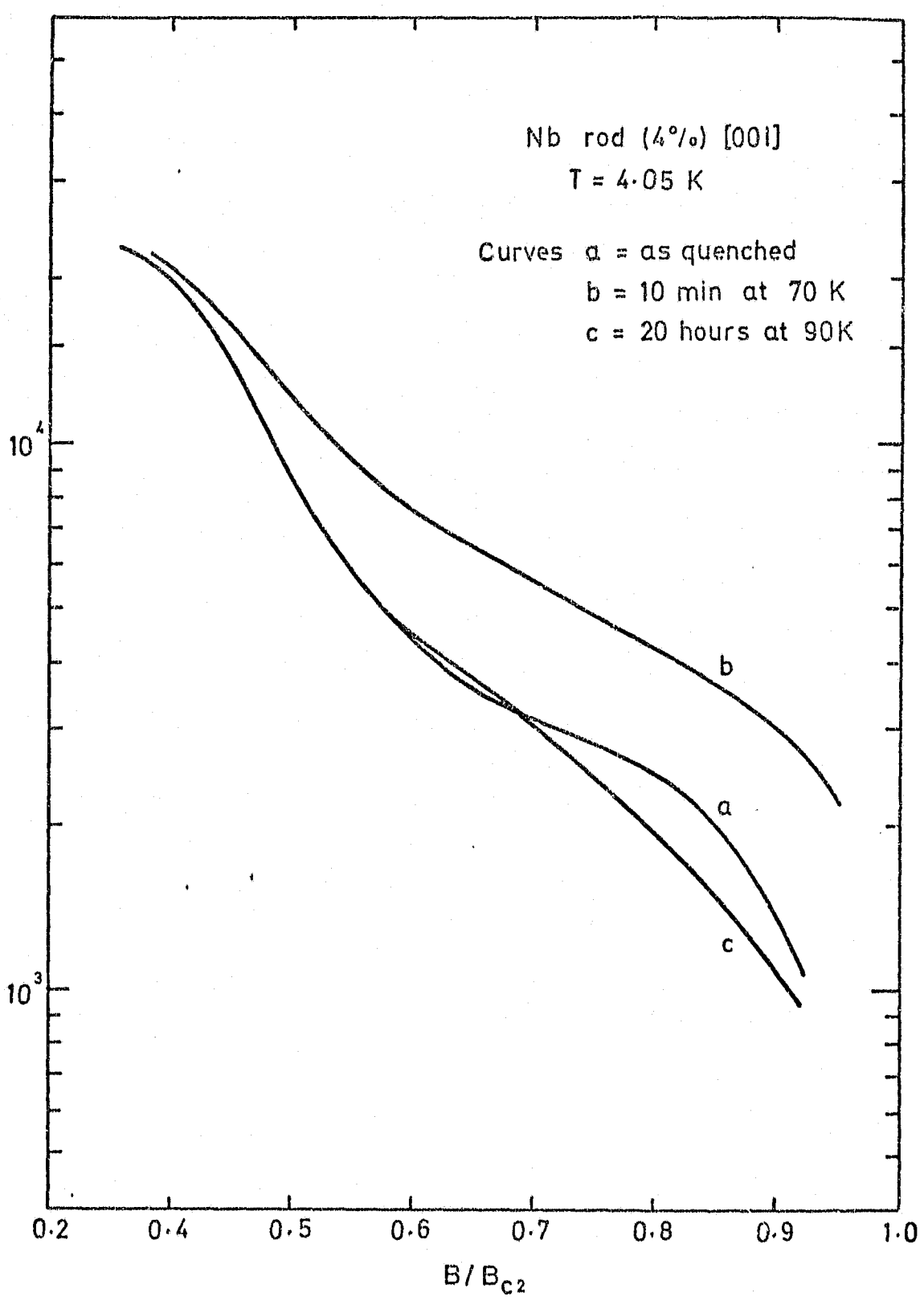


Figure 5.12. As for figure 5.11 for the |001| 4% deformed specimen.

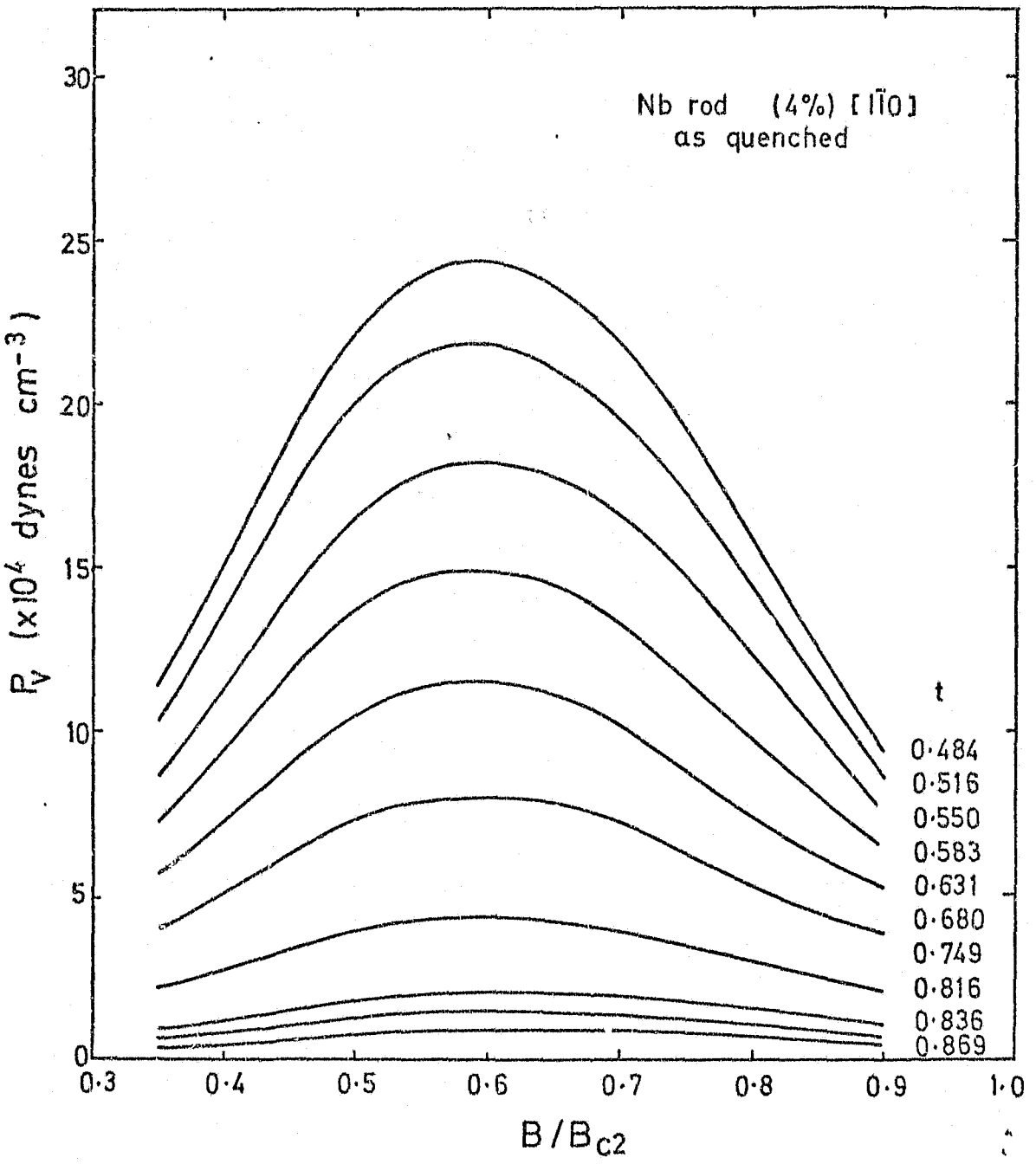


Figure 5.13a The derived variation of the bulk pinning force density with reduced induction for the as-quenched [1$\bar{1}$0] 4% deformed rod specimen at various reduced temperatures.

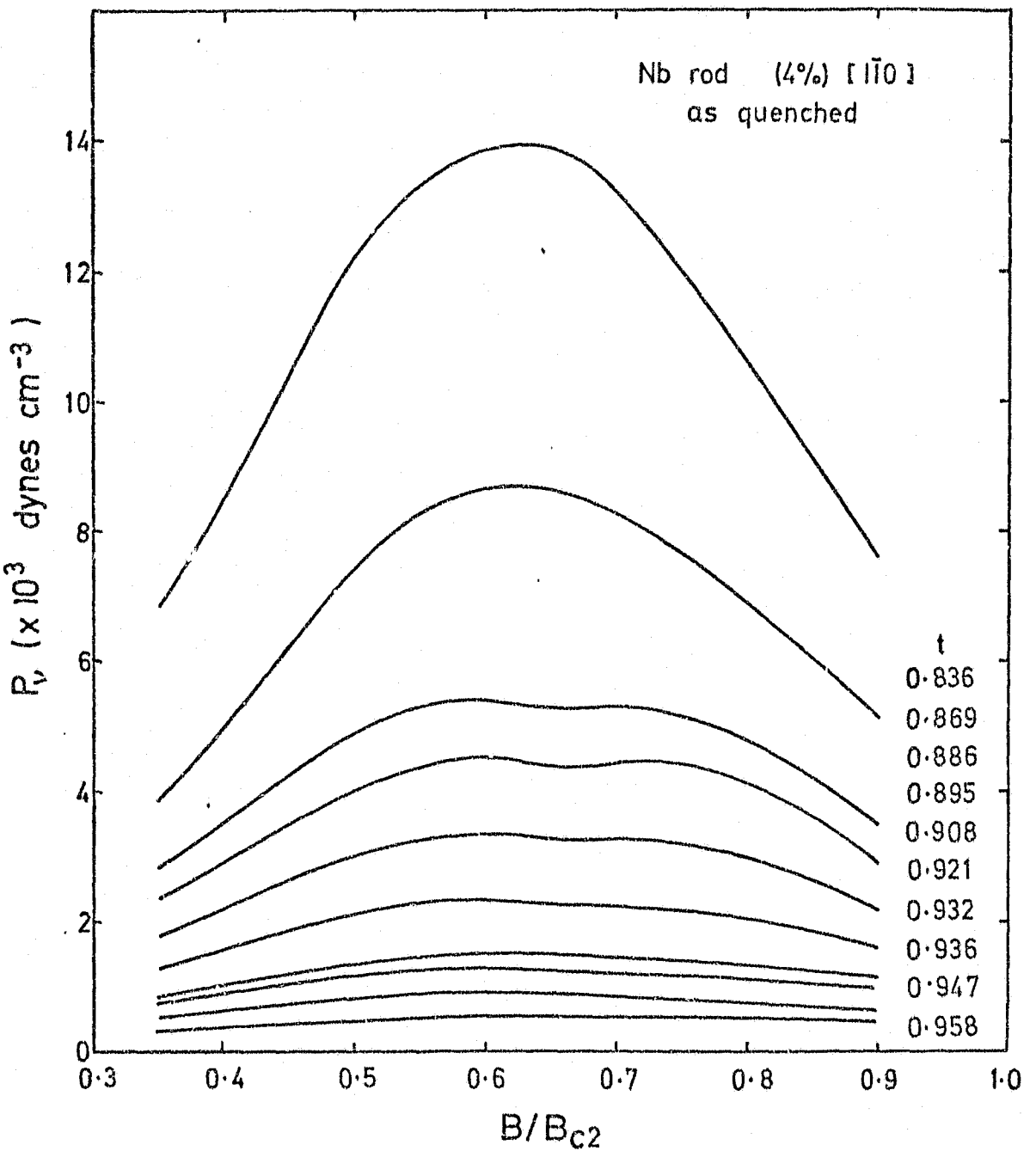


Figure 5.13b. The derived variation of the bulk pinning force density with reduced induction for the as-quenched [1$\bar{1}$0] 4% deformed rod specimen at various reduced temperatures.

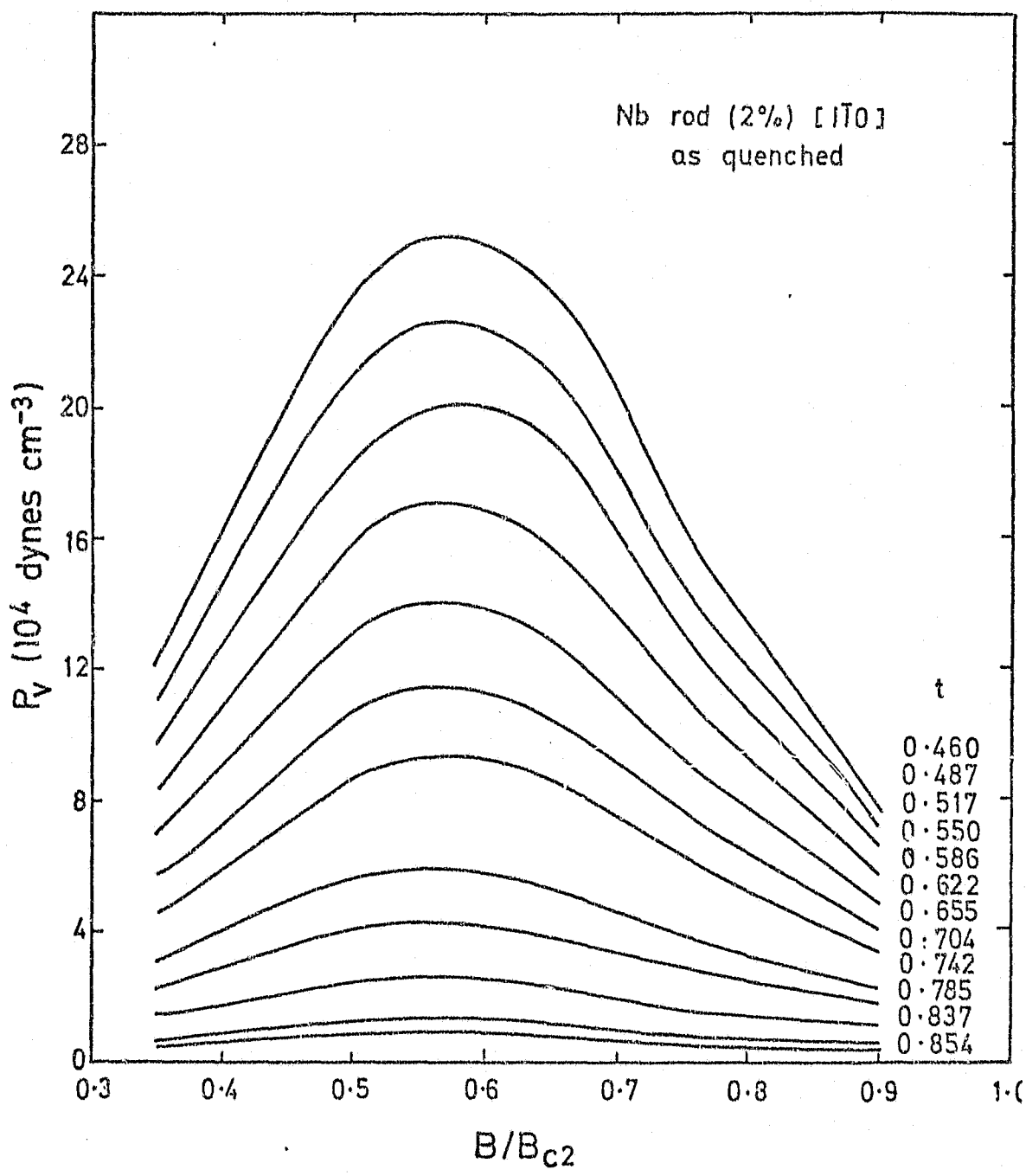


Figure 5.14a. As for figure 5.13 for the as-quenched $[1\bar{1}0]$ 2% deformed specimen.

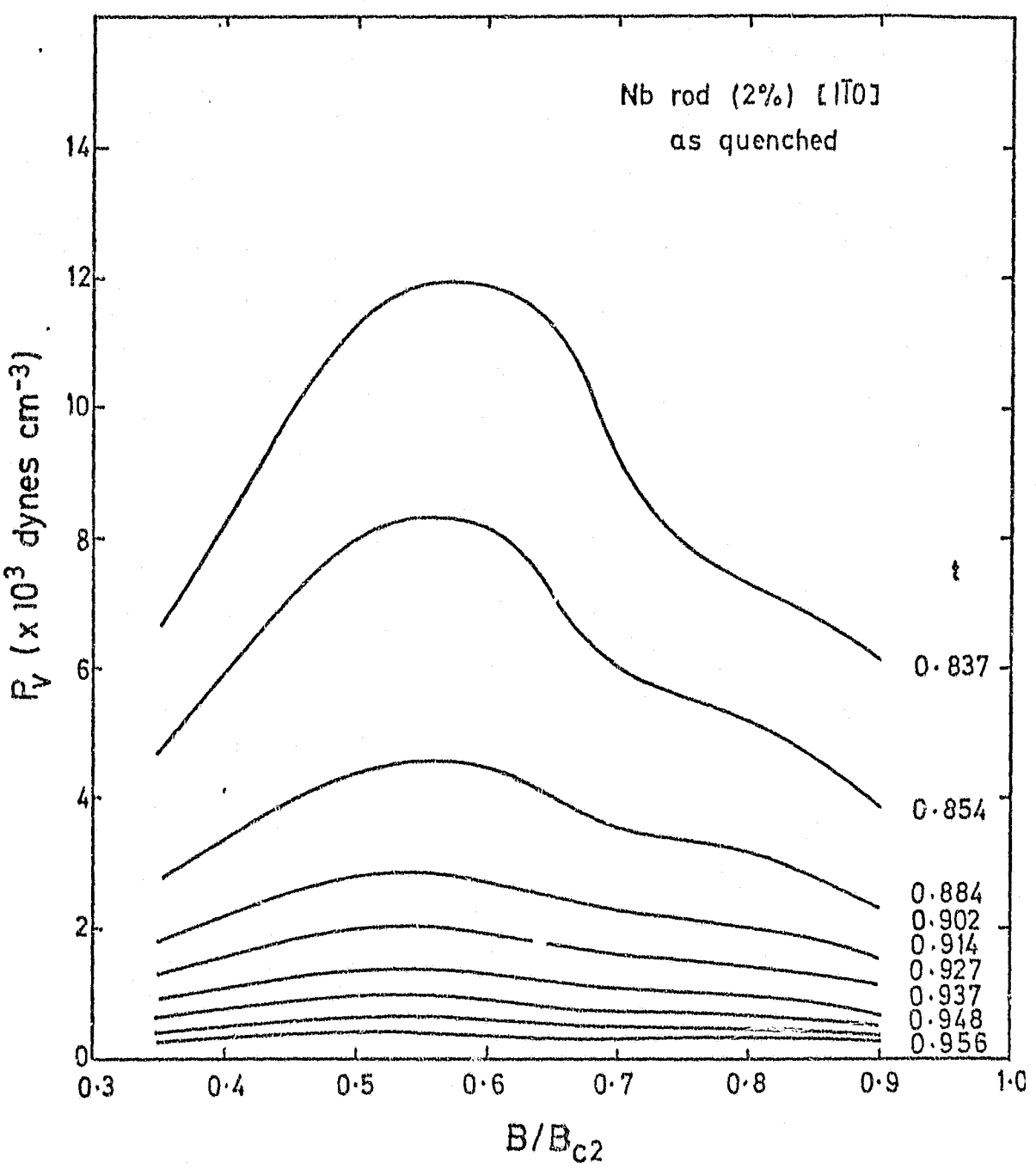


Figure 5.14b. As for figure 5.13 for the as-quenched [i10] 2% deformed specimen.

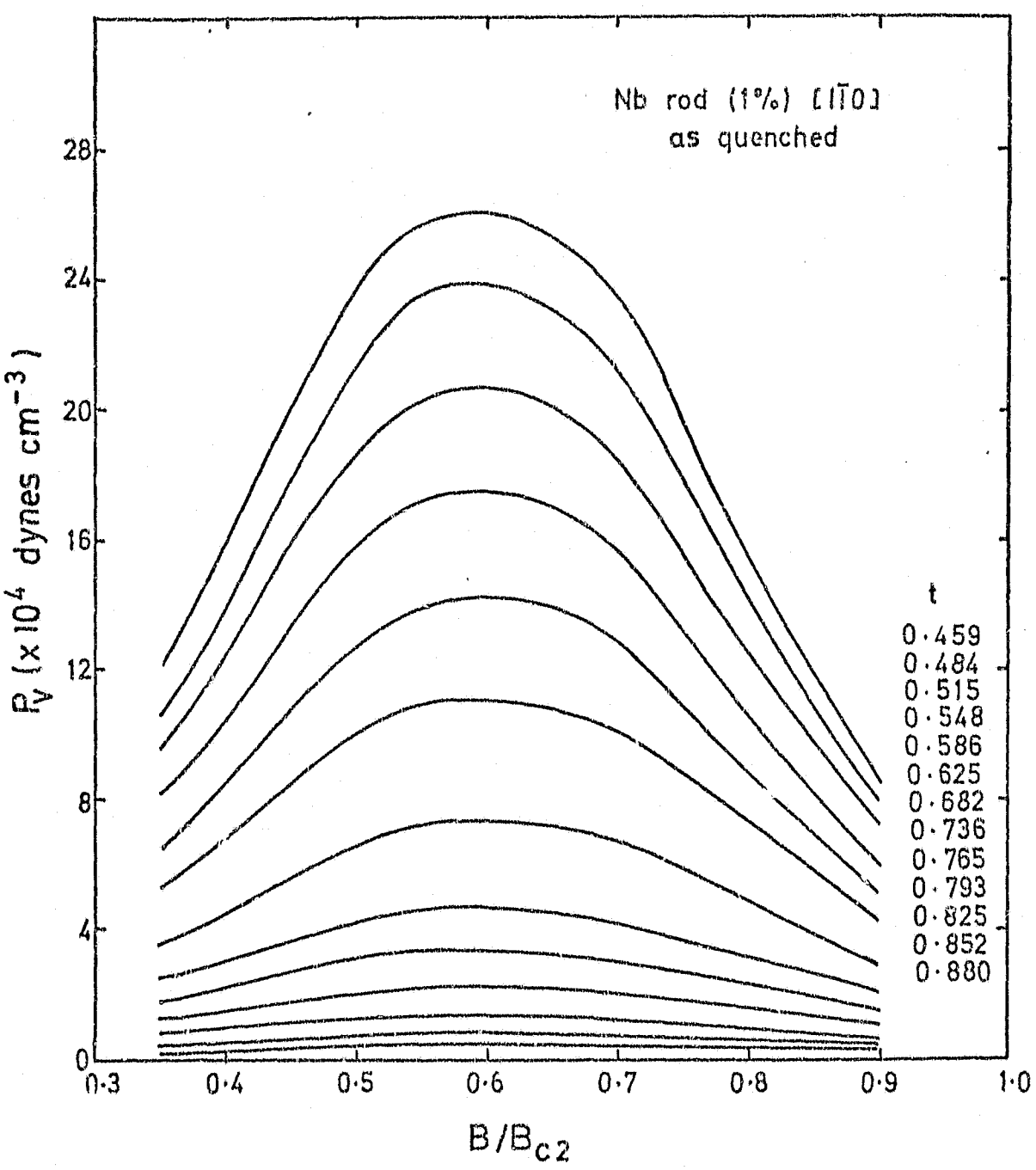


Figure 5.15a. As for figure 5.13 for the as-quenched [1$\bar{1}$0] 1% deformed specimen.

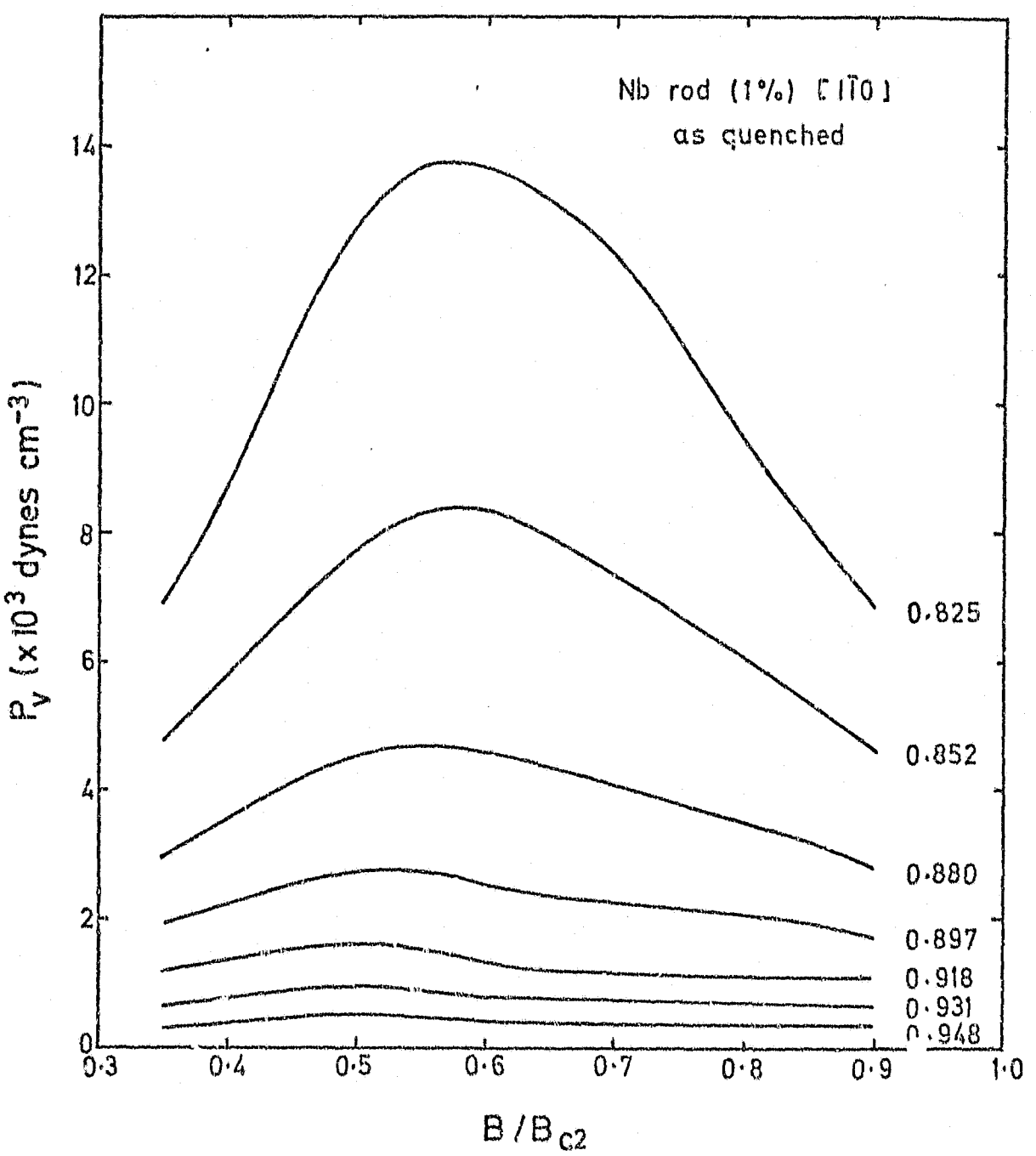


Figure 5.15b. As for figure 5.13 for the as-quenched [1$\bar{1}$0] 1% deformed specimen.

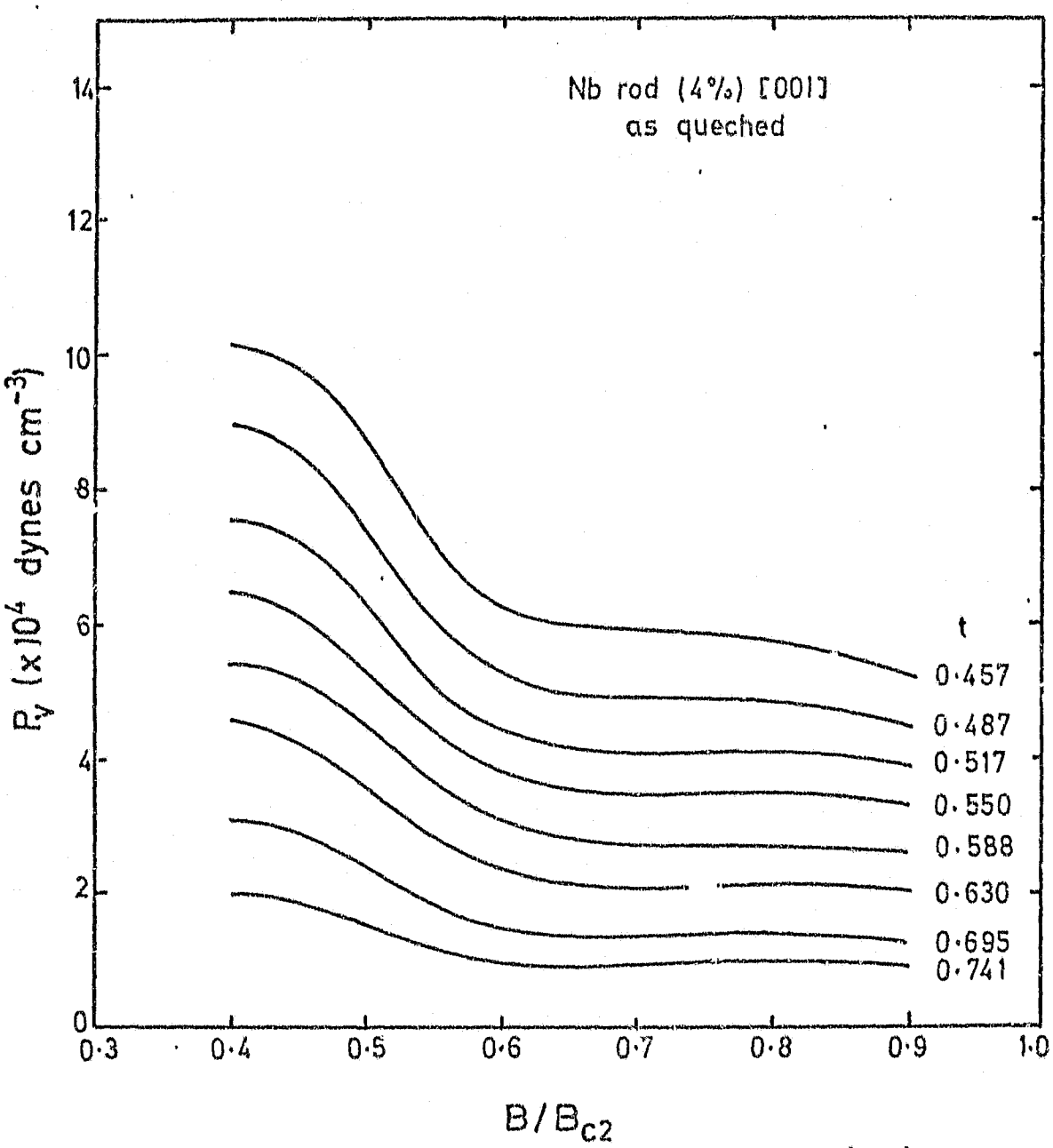


Figure 5.16a. As for figure 5.13 for the as-quenched [001] 4% deformed specimen.

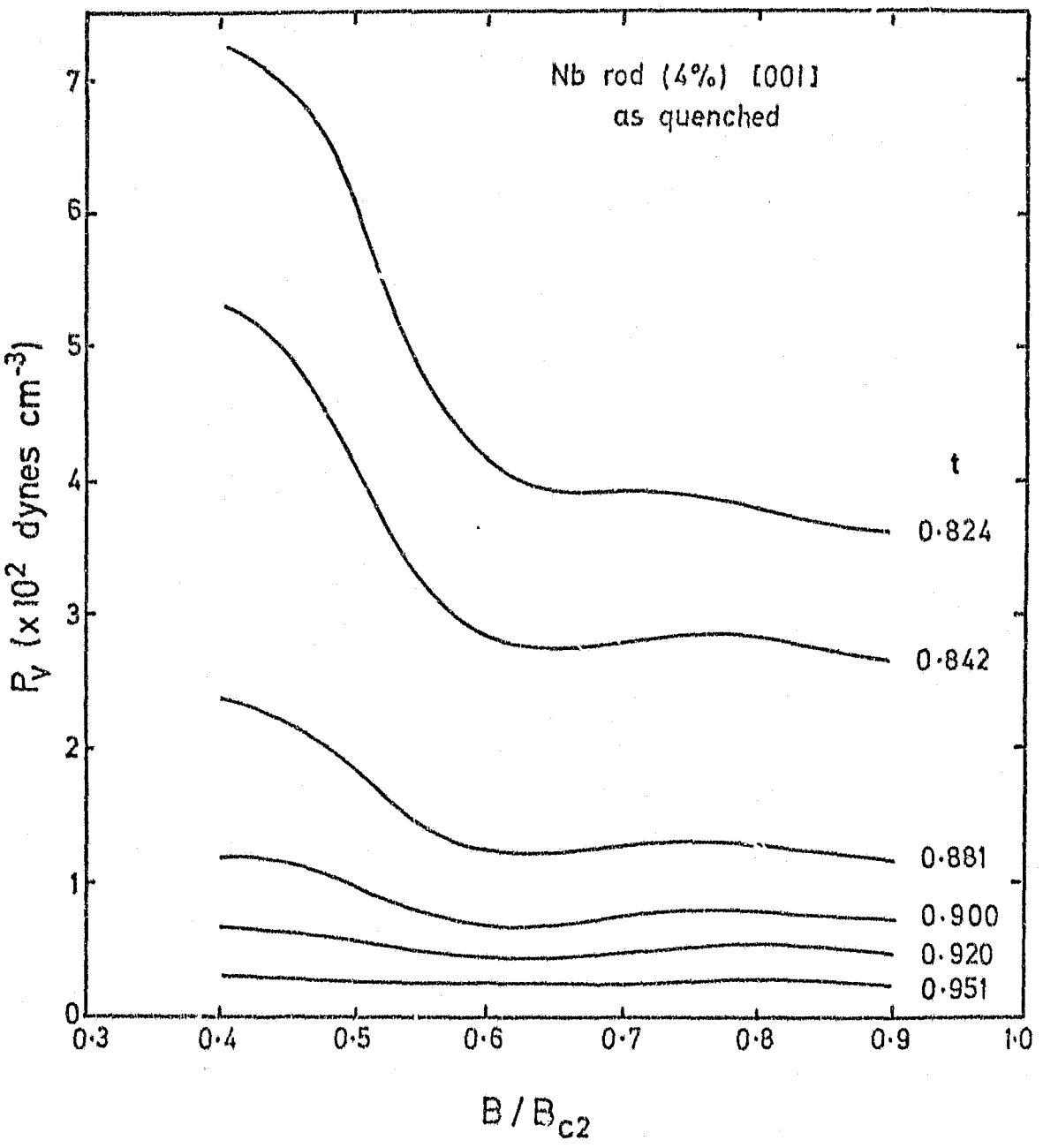


Figure 5.16b. As for figure 5.13 for the as-quenched [001] 4% deformed specimen.

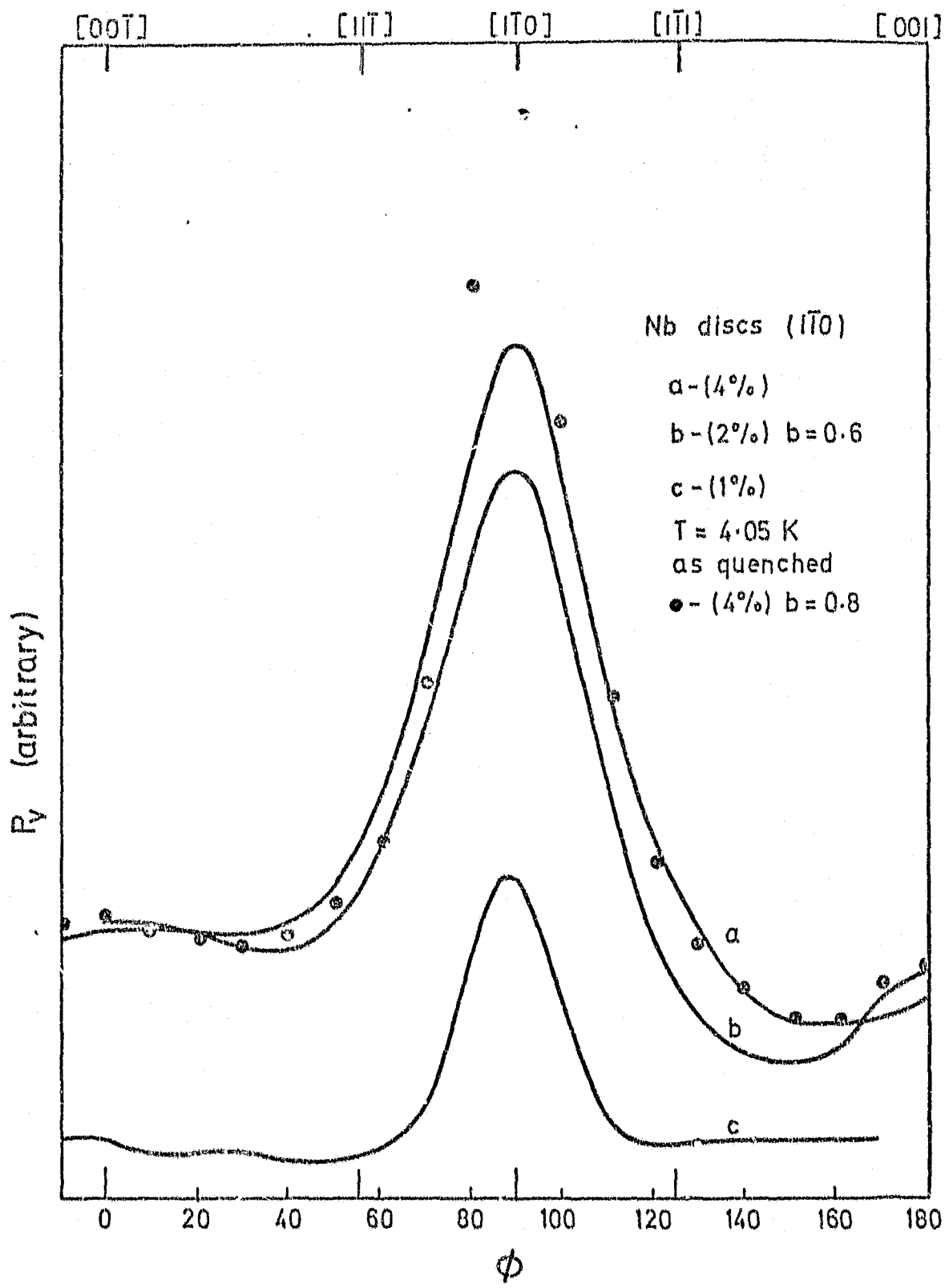
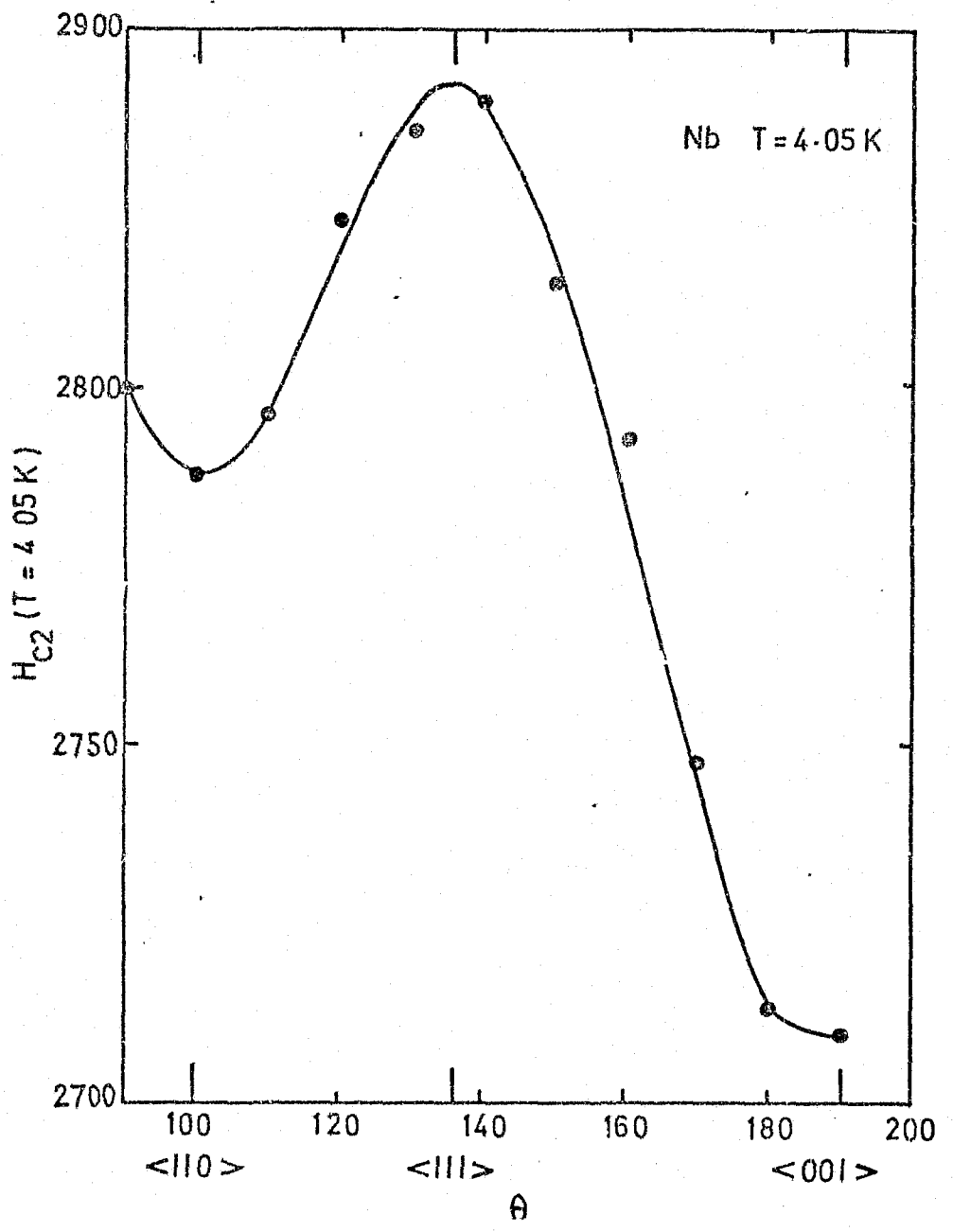


Figure 5.17. The anisotropy of the bulk pinning force density with the applied field in the (110) plane for the as-quenched deformed disc specimens at $T = 4.05K$ and $b = B/B_{c2} = 0.6$ (soli· curves) and $b = 0.8$ (points).



Figur. 5.18. The anisotropy of the upper critical field in the (110) plane of the as-quenched disc specimen at T = 4.05K.

direction, i.e. when the fluxons are parallel to the dislocations. There is also some suggestion of a maximum in $P_v(b = 0.6)$ near the $[00\bar{1}]$ and $[001]$ directions. This result is significantly different from that of Good and Kramer (1970) as described in section 5.1. However, the results of the isochronal ageing experiments, which will now be discussed, show that this discrepancy is principally a consequence of the interstitial hydrogen in the present specimens.

In figure 5.19 $P_v(b = 0.6)$ for the undeformed and 4 per cent deformed $[1\bar{1}0]$ and $[001]$ specimens is plotted against ageing temperature T_a in the range $4K < T_a < 300K$. With increasing ageing temperature $P_v(b = 0.6)$ remains constant up to $T_a = 40K$. $P_v(b = 0.6)$ then shows a narrow maximum centred at $T_a = 70K$. With further increase in the ageing temperature $P_v(b = 0.6)$ decreases rapidly to exhibit a broad minimum centred at $T_a = 200K$. When T_a reaches 300K $P_v(b = 0.6)$ is again, as expected, back to its as-quenched value. The overall magnitude of the ageing effects on P_v increases on deformation and is much larger in the $[1\bar{1}0]$ than in the $[001]$ deformed specimens. Prolonged ageing at temperatures in the range $80K < T_a < 140K$ causes a further decrease in P_v with a time constant of about 5 minutes. In figure 5.20 the effect of the 10 minute isochronal ageing experiments on the b dependence of P_v in the $[1\bar{1}0]$ 4 per cent deformed specimen is shown for various increasing ageing temperatures and also for a 20 hour anneal at $T_a = 90K$. Figure 5.21 shows the results obtained, for repeated 15 minute ageing experiments at $T_a = 90K$, on the same specimen and includes the result for the 20 hour age. This latter result cannot be modified by any further ageing at temperatures below approximately 140K. [These results are consistent (see chapter 4) with the expectation that the configurational

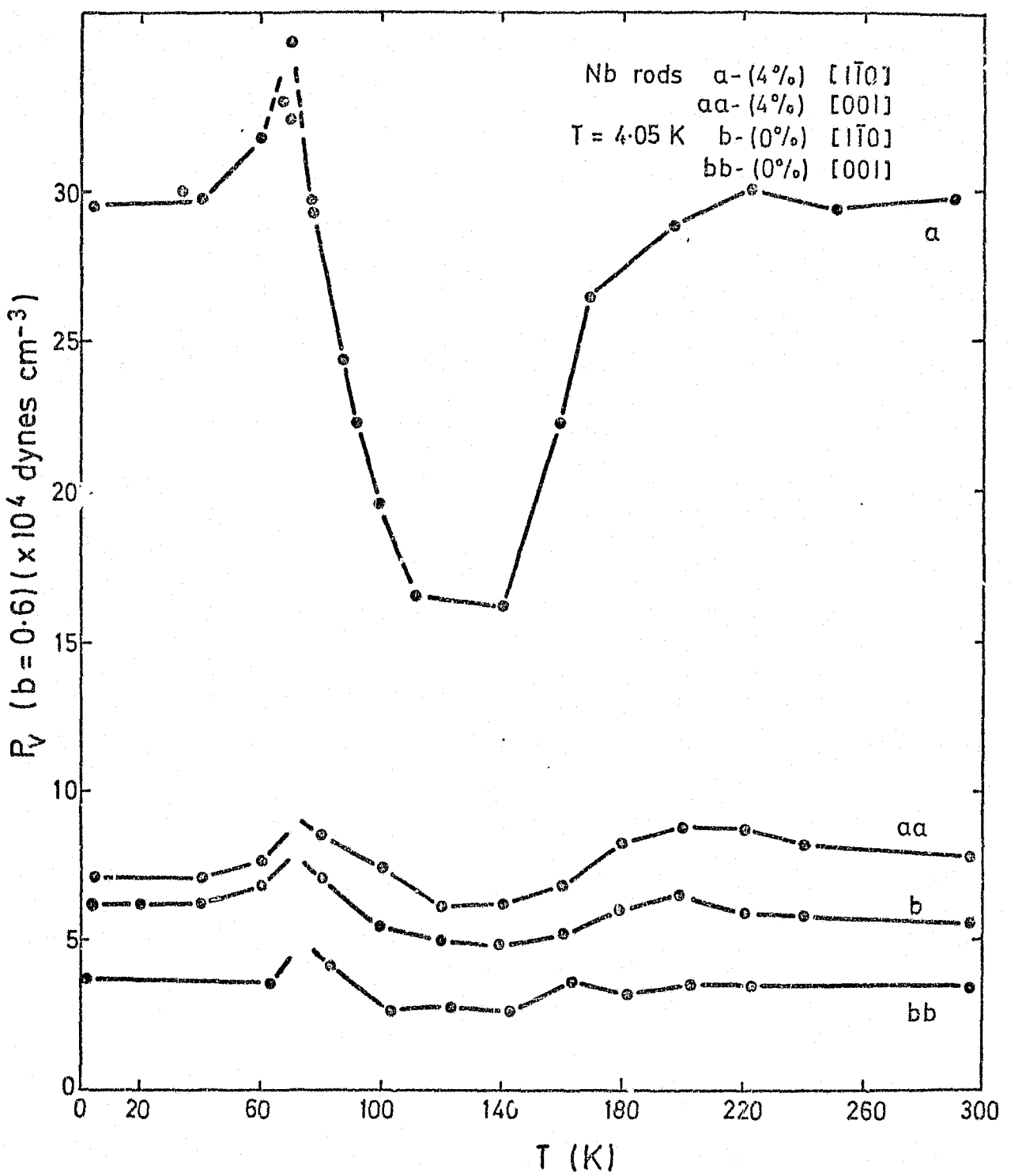


Figure 5.19. The variation of the bulk pinning force density, at b = 0.6, with ageing temperature in the isochronal ageing experiments on the undeformed and 4% deformed [001] and [1$\bar{1}$0] rod specimens.

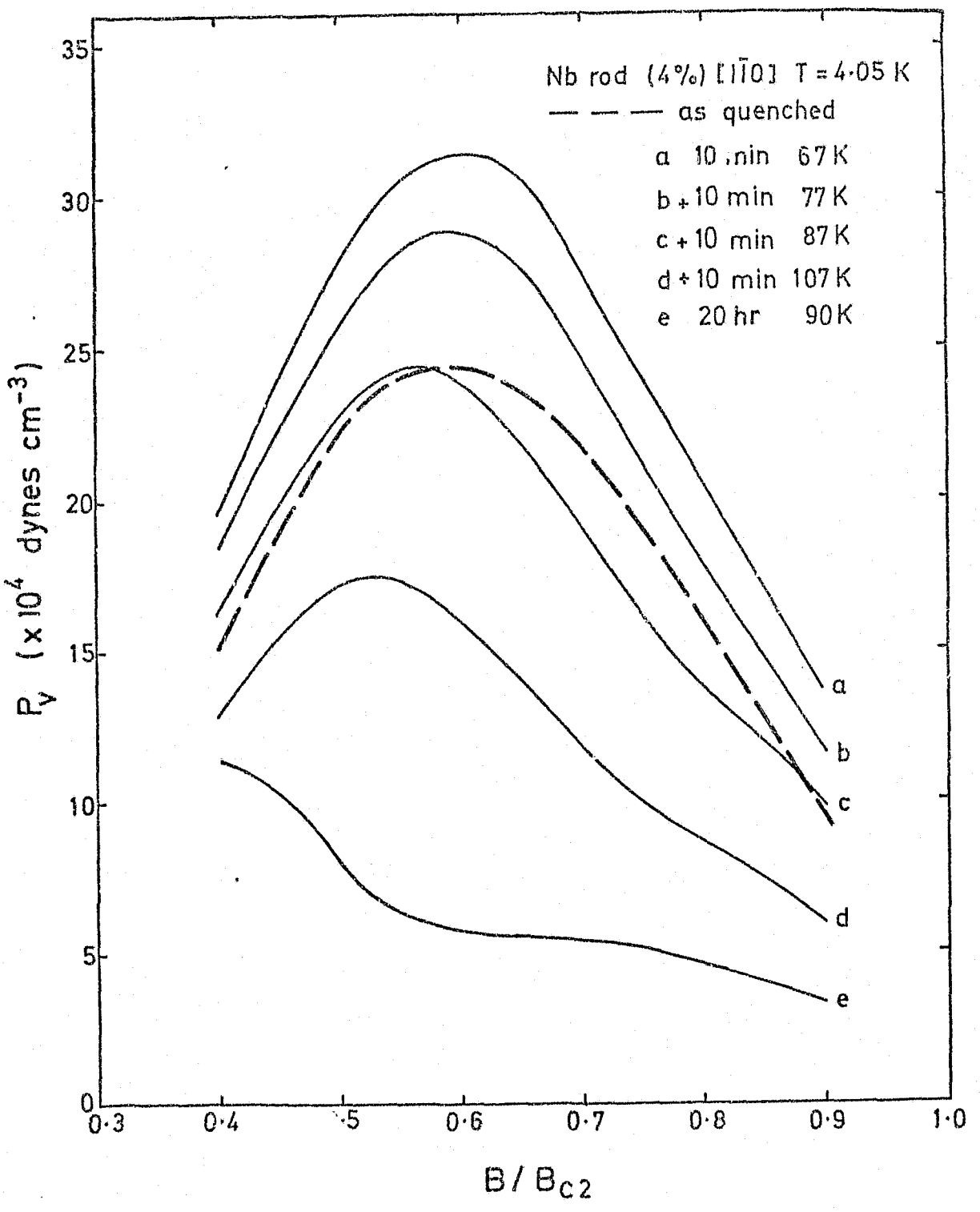


Figure 5.20. The variation in the bulk pinning force density with reduced induction, after 10 minute isochronal *ageing procedures at various temperatures*, for the [110] 4% deformed specimen. Included is the result for a 20 hour anneal at 90K.

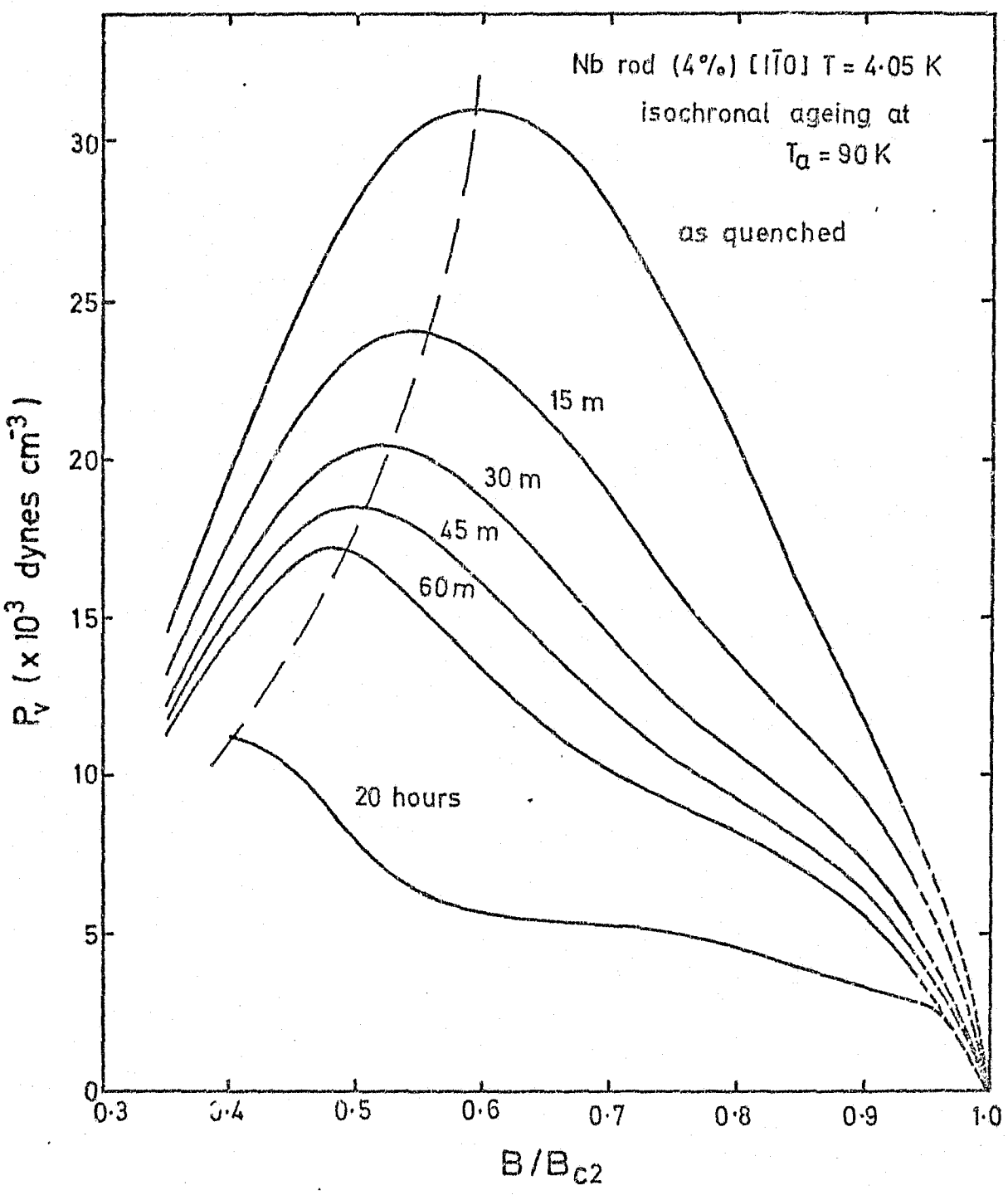


Figure 5.21. The variation in the bulk pinning force density with reduced induction, after successive 15-minute isochronal ageing procedures at 90K.

distribution of interstitial hydrogen influences the pinning effectiveness of the deformation induced microstructure. Prolonged ageing at a suitable temperature, i.e. 20 hours at $T_a = 90K$, causes all the available hydrogen to be pumped (by the Cottrell-Bilby mechanism) into the dislocation cores where it precipitates as small β phase hydride particles. For a hydrogen concentration of 50ppm, these discrete particles must necessarily be very small and well separated and their influence on P_v is expected to be insignificant. The dislocations in this condition are considered to be 'clean', i.e. free of Cottrell atmospheres.]

The effect of long ageing on $P_v(b)$ for the [001] 4 per cent deformed specimens is shown in figure 5.22 (compare curve c, which is the as-quenched result, with curve b, which is the result obtained after ageing for 20 hours at $T_a = 90K$). The ageing process in this case apparently has a relatively small effect on the $P_v(b)$ dependence and magnitude compared with the case for the $[1\bar{1}0]$ specimen. Also shown for comparison in figure 5.22 are the results for the saturation aged $[1\bar{1}0]$ 4 per cent deformed specimen (curve a) and the results of Good and Kramer (1970) for an approximately equivalent microstructure situation (curve d) (but see sections 5.1 and 5.22). Comparison of the former result (curve a) with the result for the saturation aged [001] specimen (curve b) shows in either case an almost identical dependence of P_v on t, with $P_v(b)[1\bar{1}0]$ only 20 per cent larger than $P(b)[001]$ on average. The result of Good and Kramer (curve d) has a dependence which is similar to the above (neglecting the small 'peak' effect at $b = 0.9$), but is about 40 per cent lower on average than curve a. This latter discrepancy is not considered to be serious because of the difference in the starting material, deformation procedure

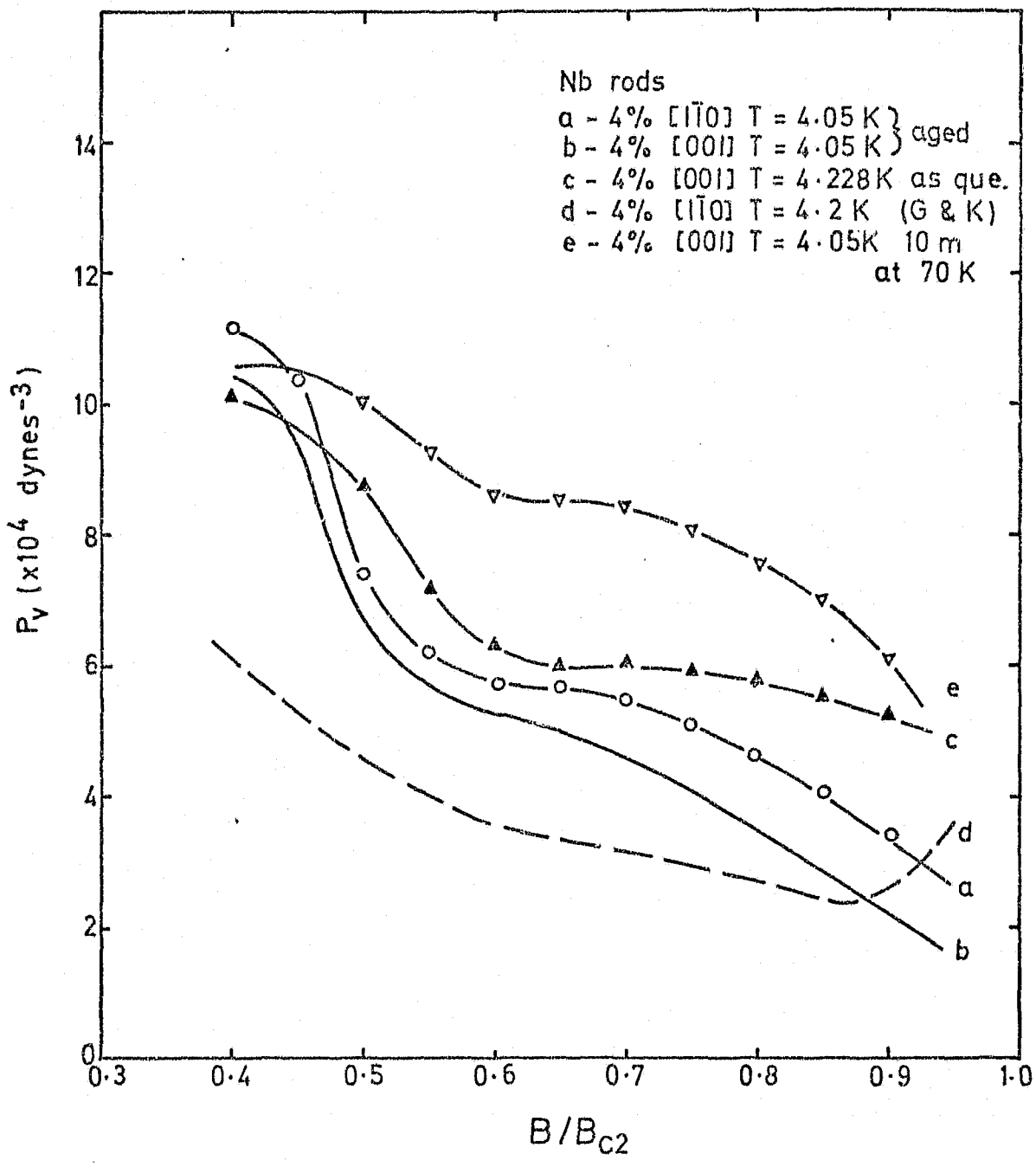


Figure 5.22. The variation of the bulk pinning force density with reduced induction in class (i) (see text).

and measuring technique employed in the two investigations.

In figure 5.23 P_v versus b curves are given for the 1 per cent, 2 per cent, and 4 per cent nominally deformed specimens in the as-quenched condition at T = 4.5K. $P_v(b)$ for the $[1\bar{1}0]$ specimens is apparently almost independent of the extent of deformation. In contrast the [001] specimens show a more or less linear dependence of $P_v(b)$ on the actual percentage strain (viz: 8:24:36 - see figure 5.1).

Neglecting, for the moment, a few small anomalies which will be discussed later it is obvious from the foregoing that the pinning behaviour found in the various specimens may be divided into two distinct classes. These are manifested respectively by (i) the [001] deformed specimens as-quenched or aged and the $[1\bar{1}0]$ deformed specimens after saturation ageing and (ii) the $[1\bar{1}0]$ deformed specimens as-quenched and also in the initial stages of ageing.

In accordance with the theoretical considerations of chapter 3 and with usual practice the results obtained for $P_v(b,t)$ from experiment in these two classes will now be examined to establish whether they scale in the manner predicted by equation 3.61, viz:

$$P_v(b,t) \propto G\, g(b)\, B_{c2}^n(t)/\kappa^m(t) \qquad 3.61$$

It is apparent from figure 5.23 that changes in the extent of deformation (and hence in G) within each class (shown respectively by curves aa,bb,cc and curves a,b,c) do not significantly influence the dependence of P_v on b at constant temperature. In either case therefore G is apparently independent of b. In the former case (class (i) - curves aa,bb and cc) G is apparently approximately proportional to the extent of deformation and in the latter case (class (ii)) there is no significant dependence. Moreover for the experimental results to be

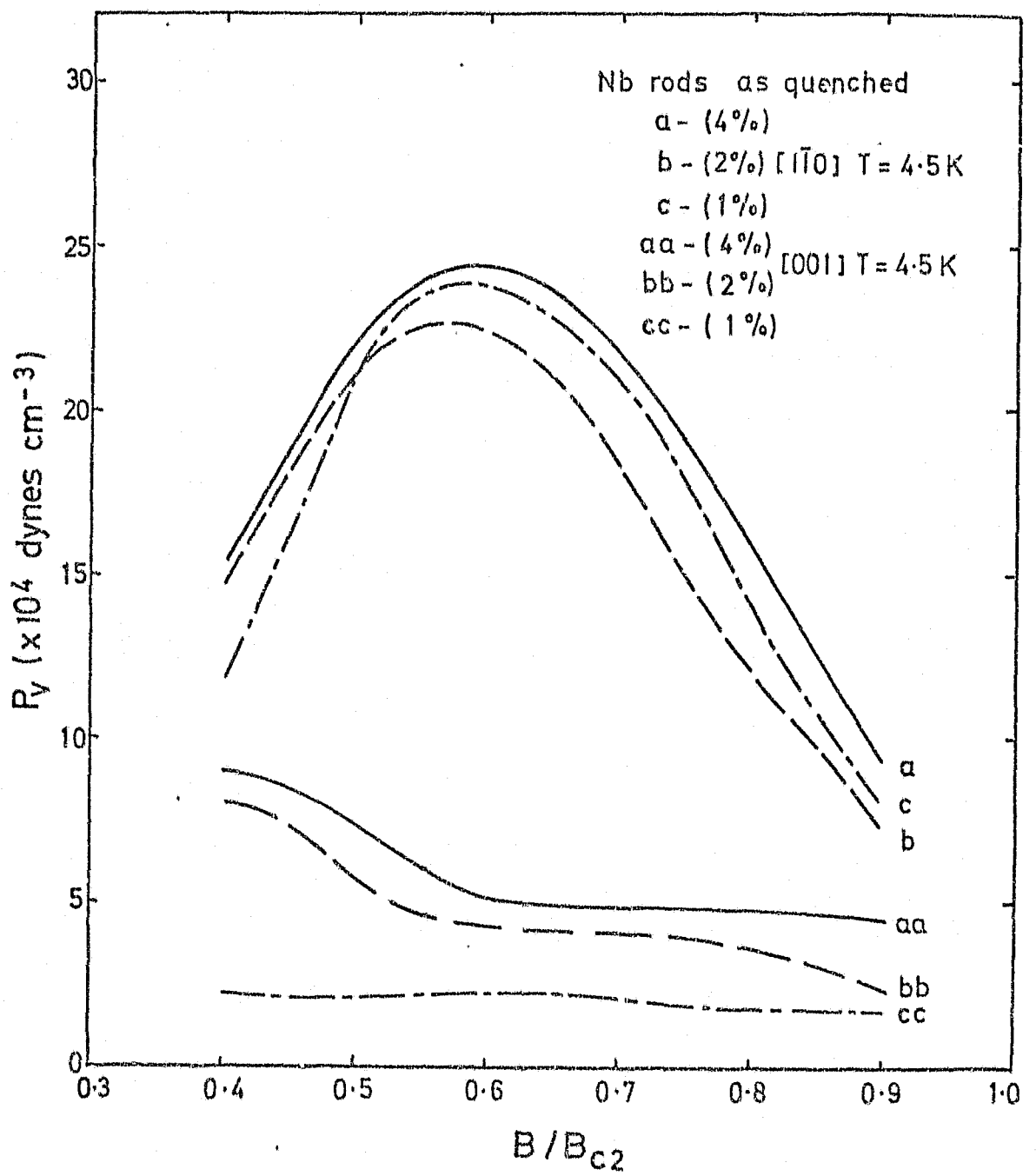


Figure 5.23. The variation of the bulk pinning force density with reduced induction for the deformed specimen at T = 4.5K showing the difference in behaviour between the [1$\bar{1}$0] (class (ii)) and the [001] (class (i)) as-quenched specimens.

consistent with the form of equation 3.61 the dependence of P_v on the microstructure and on b must also be temperature invariant for all b. [Failure in this respect would indicate the need for a fairly elaborate theoretical treatment unless it could be accounted for by some relatively straightforward effect such as the matching effect (see chapter 3) or by the existence of two or more pinning mechanisms with different scaling laws acting simultaneously.]

In figures 5.24a and 5.24b, therefore $P_v(b,T)$ (from figures 5.16 and 5.13 for the 4 per cent [001] and [1$\bar{1}$0] as-quenched specimens respectively) have been normalized at $b = 0.4$ and $b = 0.6$ respectively and the results are shown for a few reduced temperatures in both cases. It is apparent from these figures that for $b \leq 0.6$ the results scale with t in both cases. For $b \geq 0.6$ however there is a relatively small overall departure from the scaling law which is apparently associated with a small anomaly centred at $b \simeq 0.8$. This anomaly will be considered later. Similar results are obtained for the as-quenched 2 per cent and 1 per cent [1$\bar{1}$0] deformed specimens as shown in figures 5.25a and 5.25b. The latter figure however shows a further anomaly (see the curve for $t = 0.897$).

Thus it has been established, if the anomaly at $b = 0.8$ is neglected for the moment, that some function $G\,g(b)$ can be found from the experimental results in each class which does not depend significantly on temperature.

All that now remains for an experimental fit to equation 3.61 is to verify that $P_v(T)$ can be expressed in terms of $H_{c2}^n(t)\kappa^m(t)$ for each class of behaviour.

Previously it has been the practice to neglect the relatively small temperature dependence of κ and to determine the exponent n (in

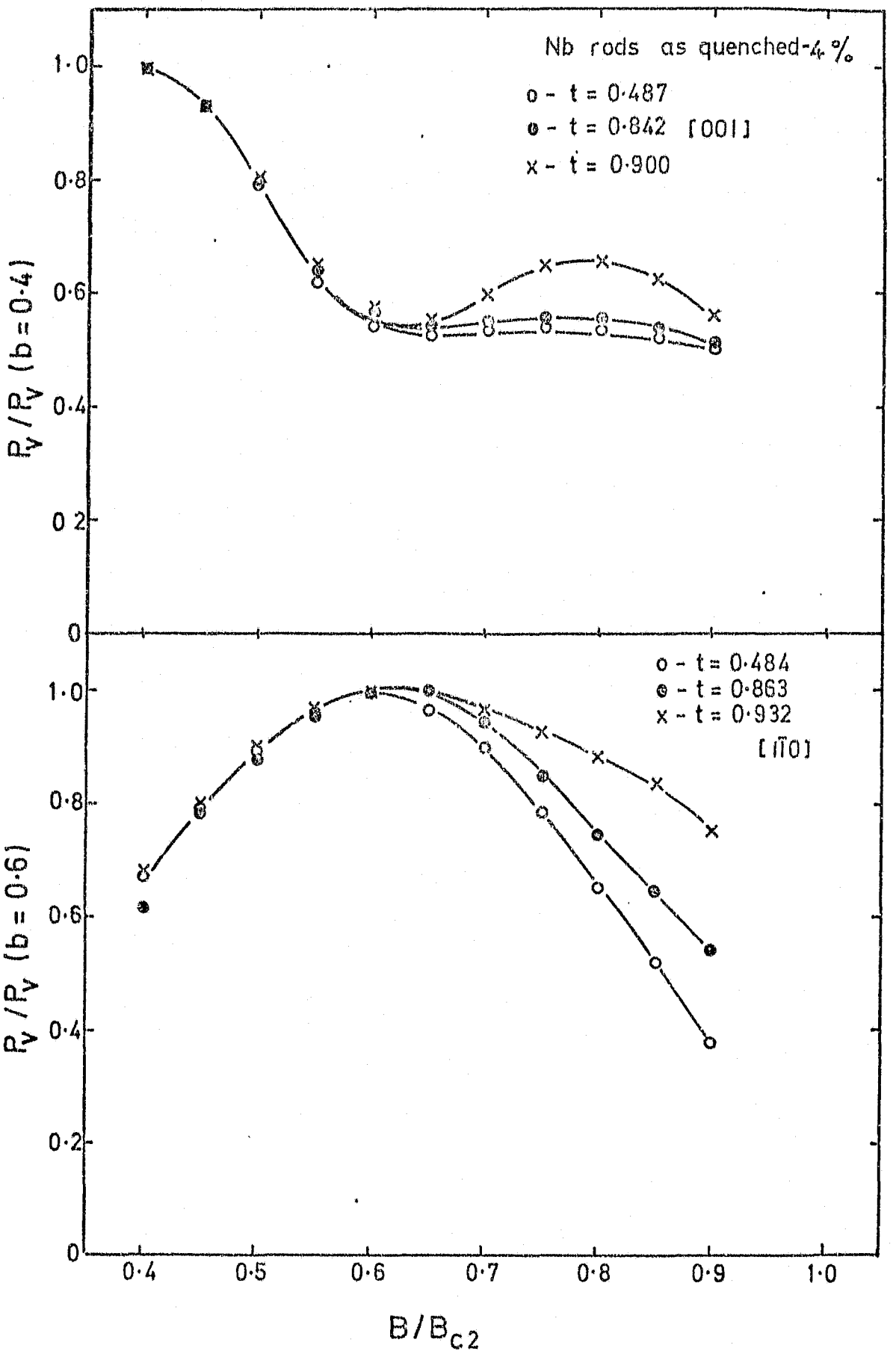


Figure 5.24a. The variation of the bulk pinning force density, normalized at b = 0.4, with the reduced induction b for the [001] 4% deformed specimen, as-quenched and aged for 20 hours at 90K, showing class (i) behaviour and the anomaly at b = 0.8.

Figure 5.24b. As for (a) but normalized at b = 0.6 for the [1$\bar{1}$0] 4% deformed specimen as-quenched showing class (ii).

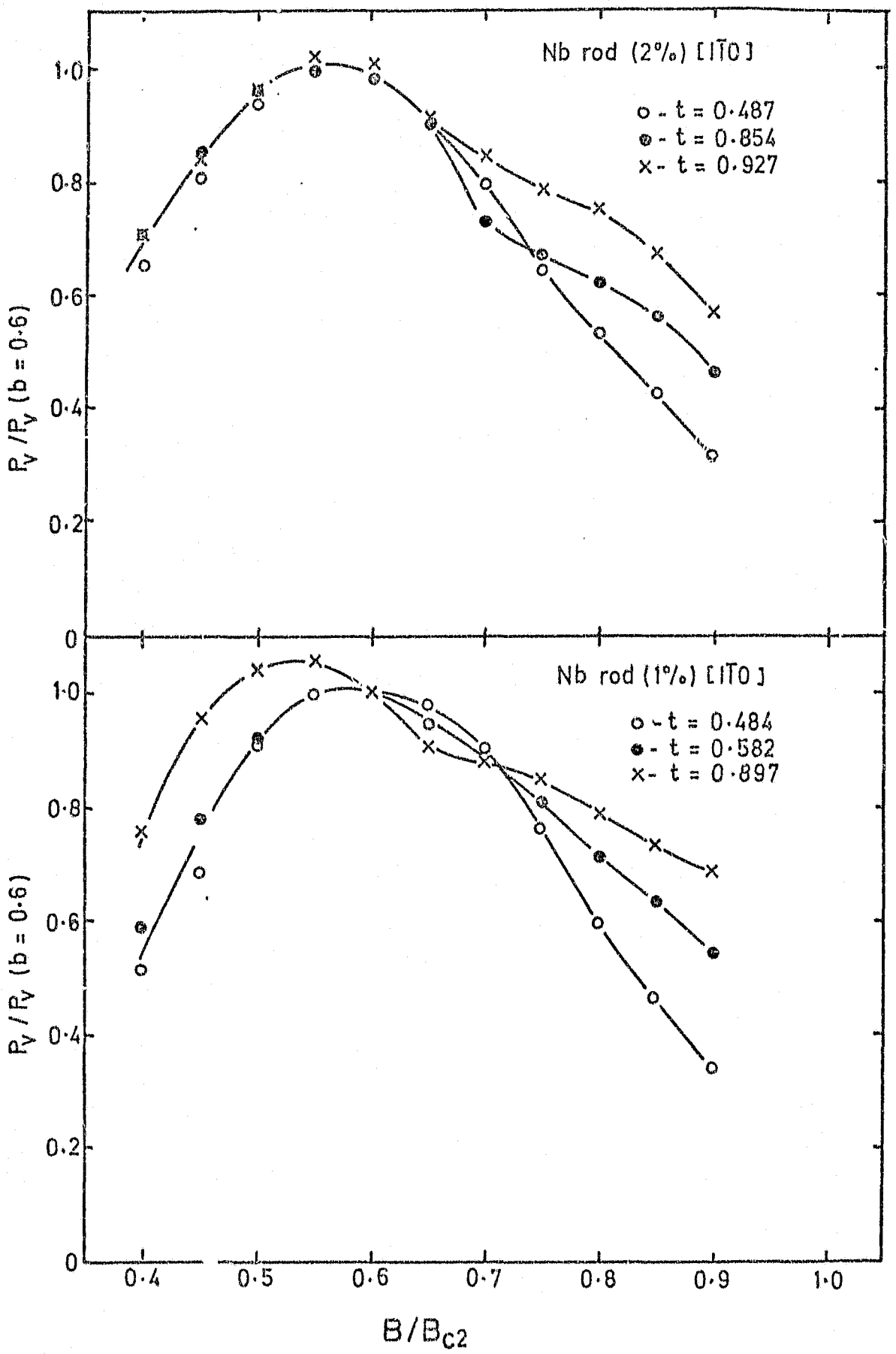


Figure 5.25a and 5.25b. As for figures 5.24b and for [1$\bar{1}$0] 2% and 1% deformed specimens respectively.

equation 3.61) from the experimentally determined temperature dependence of P_v and H_{c2}. In low κ materials (for example niobium) the temperature variation of κ with respect to that of H_{c2} is not insignificant however and such a determination of n will not be sufficiently accurate but may nevertheless be useful in the formulation of a model for $P_v(b,t)$. If the model predicts an equation of the form of equation 3.61 with $H_{c2}(t)/\kappa(t)$ given explicitly it should then be possible to obtain an experimental verification of this expression for the temperature dependence.

In figure 5.26 therefore $\log[P_v(b,t)]$ has been plotted against $\log[B_{c2}(t)]$ for the various specimens at various values of b. In every case an approximately linear relationship is found. The exponents n, which are given by the slope of the plot in each case, are tabulated in figure 5.26 and lie in the range $2.3 < n < 2.8$.

Thus finally: it has been established that the experimental results show two classes of behaviour which each approximately, neglecting the κ dependence, obey a scaling law like equation 3.61 and also show an anomaly centered at $b \simeq 0.8$ which is similar in both classes. Since, however, the temperature dependence of P_v in each class is very similar (see figure 5.26) any admixture of one class of behaviour with the other will still result in an overall $P_v(b,t)$ behaviour which scales approximately with t for all b. It is therefore not possible, except in certain circumstances, to state a priori from the experimental results the true behaviour of the function g(b) for the pinning mechanism possible for each class of behaviour.

The problem will be discussed in more detail in the next section where the experimental results will be considered in relation to the dislocation debris due to deformation and the effects of the ageing

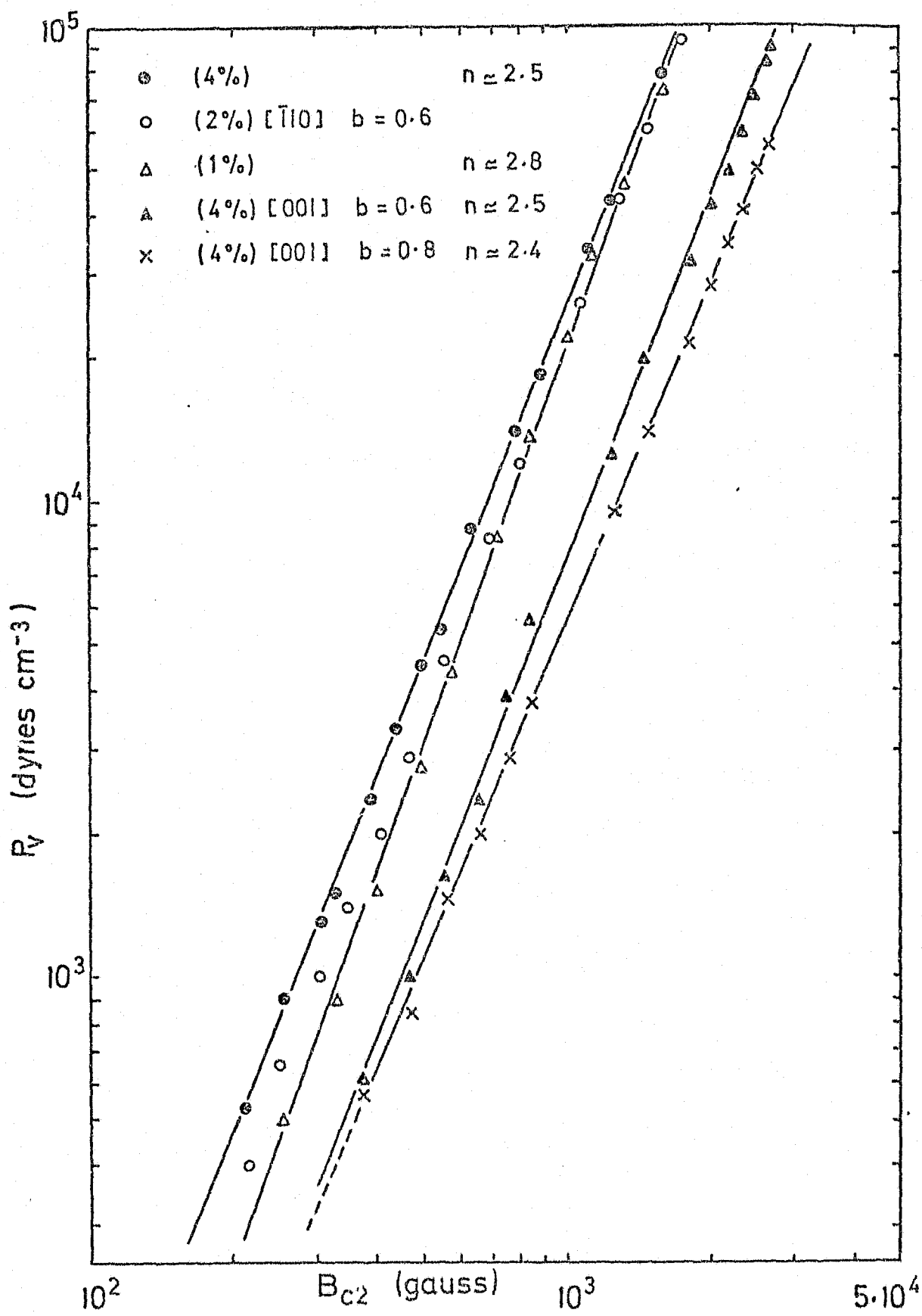


Figure 5.26. log-log plots of the bulk pinning force density at b ≃ 0.6 versus the upper critical field (induction for various specimens and also at b ≃ 0.8 for the [001] 4% deformed specimen. From these plots the temperature dependences of the bulk pinning force density have been obtained approximately in terms of an exponent n, i.e. $P_v(t)\ B^n_{c2}(t)$, which is given in the figure for the various plots.

procedures on the configurational distribution of the interstitial hydrogen in the specimens. It will then be possible to summarize the experimental results in two completely distinct classes of behaviour and to postulate models for the pinning mechanisms involved in each case.

5.4 Theoretical considerations

5.4.1 The basic pinning sites

The results of the preceding section show that both classes of pinning behaviour depend on the presence of dislocation debris (it will become apparent later that point defects and point defect clusters resulting from the deformation need not be considered in the explanation of the observed pinning behaviour). The dislocation distribution resulting from the particular mode of deformation used in the present investigation has been described in section 5.2.2. In essence it consists of edge dislocations aligned predominantly along the $[1\bar{1}0]$ direction with some braiding and isolated small (5.10^2 - 5.10^3Å) regions of tightly tangled dislocation dipoles and/or multipoles. From the considerations of chapter 3 it would appear therefore that the deformation produces two principal types of pinning site, viz: (i) parallel segments of edge dislocations (line forces) for which only the parallel interaction with a fluxon is appreciable and (ii) the regions of tightly tangled dislocation (point-like forces). Another possible site might comprise regions (with dimensions much larger than the fluxon lattice parameter a_o) in which the local dislocation density is relatively high (see for example Fietz and Webb, 1969). In this latter case it is assumed that the pinning forces due to the individual dislocation segments in the region may be summed linearly to give the nett basic pinning force per site. The very elongated regions of loose braid presumed to be present in the deformed specimens (see section 5.2.2) would appear to meet the requirement of this type of site. How-

ever, the absence of a large anisotropy (but see later) in P_v for class (i) behaviour suggests that, for clean dislocations, this type of site may not be operative in the present instance. This will be discussed in more detail in section 5.5.2(b).

It has also been shown in the preceding section that the measured pinning force density is influenced by low temperature ageing (and therefore by the configurational distribution of the interstitial hydrogen) in a manner which depends on the presence of dislocations (which are edge type in the present investigation - see section 5.2.2) and their orientation with respect to the fluxons.

The two classes of pinning behaviour which were found, viz: class (i) and class (ii) obey different scaling laws and occur respectively in (i) all specimens when the hydrogen has been completely precipitated out of solution or otherwise when the dislocations are far from parallel interaction with the fluxons and (ii) in the $[1\bar{1}0]$ specimens (dislocations parallel to B) as-quenched and in the initial stages of ageing. In class (i) the pinning force density P_v is only moderately anisotropic* with a maximum when B is parallel to the $[1\bar{1}0]$ direction.

---

* Class (i) was only measured with H_o along the [001] and $[1\bar{1}0]$ directions. The existence of maxima for both these orientations is possible and therefore the actual anisotropy near the $[1\bar{1}0]$ direction may be larger than the 20 per cent difference between the $[1\bar{1}0]$ and [001] directions quoted in the previous section. Good and Kramer (1970) (see also section 5.1) do indeed find such maxima but their maximum along the [001] direction is apparently associated with a strong surface pinning mechanism which does not seem to be present in this investigation (see figure 5.17). In any event it will become apparent, after the pinning sites responsible for class (i) are identified, that some anisotropy is inevitable.

Class (ii) behaviour however is strongly anisotropic with P_v reduced by a factor of two within approximately ±20 degrees of the $[1\bar{1}0]$ direction (see figure 5.17).

On the reasonable assumption that the summation procedure (see chapter 3) will not influence the argument the above considerations are consistent with the following tentative proposals for the basic pinning sites responsible for either class:

For class (i): the pinning sites are associated with the small regions of tangled dislocation. There is no a priori reason to suppose that the whole of such a region or only a small extra highly strained portion of the region acts as the effective pinning site. The apparent low anisotropy of P_v and also the relatively small influence of the distribution of the hydrogen on P_v in class (i) suggests that such regions interact with the fluxons either by isotropic stress independent (e.g. $\delta\kappa$) pinning mechanisms or by the second-order elastic interaction (see chapter 3). This type of site will be called the 'multiple dislocation site' and it is not inconsistent with the considerations of other authors (see for example Campbell and Evetts, 1972). It is probable that this type of site will be somewhat elongated parallel to the dislocation lines of the predominant dislocation system and that, in consequence, the pinning force density will be anisotropic. For class (ii): the pinning is associated with edge dislocation segments (isolated or in braids and aligned predominantly along the [110] direction) or, more precisely, with the Cottrell atmospheres associated with them. The experimentally observed pinning behaviour in class (ii) however is due to the effective operation of both the 'Cottrell atmosphere' sites and, to a lesser extent, the multiple dislocation sites which will always be effective

Class (ii) behaviour however is strongly anisotropic with P_v reduced by a factor of two within approximately ±20 degrees of the $[1\bar{1}0]$ direction (see figure 5.17).

On the reasonable assumption that the summation procedure (see chapter 3) will not influence the argument the above considerations are consistent with the following tentative proposals for the basic pinning sites responsible for either class:

For class (i): the pinning sites are associated with the small regions of tangled dislocation. There is no a priori reason to suppose that the whole of such a region or only a small extra highly strained portion of the region acts as the effective pinning site. The apparent low anisotropy of P_v and also the relatively small influence of the distribution of the hydrogen on P_v in class (i) suggests that such regions interact with the fluxons either by isotropic stress independent (e.g. $\delta\kappa$) pinning mechanisms or by the second-order elastic interaction (see chapter 3). This type of site will be called the 'multiple dislocation site' and it is not inconsistent with the considerations of other authors (see for example Campbell and Evetts, 1972). It is probable that this type of site will be somewhat elongated parallel to the dislocation lines of the predominant dislocation system and that, in consequence, the pinning force density will be anisotropic. For class (ii): the pinning is associated with edge dislocation segments (isolated or in braids and aligned predominantly along the [110] direction) or, more precisely, with the Cottrell atmospheres associated with them. The experimentally observed pinning behaviour in class (ii) however is due to the effective operation of both the 'Cottrell atmosphere' sites and, to a lesser extent, the multiple dislocation sites which will always be effective

regardless of the hydrogen distribution. Thus, in agreement with experiment, complete precipitation of the hydrogen in solution (i.e. in the Cottrell atmospheres) by suitably ageing should eliminate class (ii) and restore class (i) behaviour. The mechanism of interaction between the Cottrell atmosphere site and a fluxon will be discussed later but it is obvious that the pinning force due to this type of site will be appreciable only when $\underline{B}$ is parallel to the dislocation segments (i.e. to the $[1\bar{1}0]$ direction).

These tentative proposals for the basic pinning sites are remarkable insofar as clean isolated dislocation segments (i.e. free from Cottrell atmospheres), either parallel or perpendicular to $\underline{B}$, have been excluded as effective pinning sites in either class. It is moreover difficult to find a proposal, compatible with the experimental results, which would allow for their inclusion. This is in accordance with Labusch's threshold criterion (see section 3.3) and with the findings of several authors (see section 5.1) that inhomogeneous dislocation networks are necessary for strong fluxon pinning.

The final justification of the present choice of pinning sites depends inter alia (see later) on an unambiguous choice of an appropriate summation model and thus eventually to the formulation of a scaling law which correctly predicts the experimentally obtained pinning behaviour in each class. For class (i) this should be relatively straightforward because the pinning sites are more or less homogeneous in character and the dilute limit summation approximation is expected to be applicable (see later). However in class (ii) the summation problem is, in principle, expected to be complex because two different types of pinning site are operating simultaneously. This problem was alluded to in the previous section. Thus, depending on

the relative strengths and densities of the two types of pinning site, the overall response of the fluxon lattice and therefore the product G.g(b) in the scaling law (equation 3.61) will be intermediate between the limiting cases obtaining when the pinning sites are either of one type or the other. The pinning behaviour associated with these limiting cases will now be defined into two new classes, viz: Class I which is equivalent to the old class (i) and is for the multiple dislocation sites only and class II for the Cottrell atmosphere sites only. Class (ii) is therefore some complex combination of Class I and class II behaviour. Since however the configurational distribution of the hydrogen affects class I and, albeit much more strongly, class II and since both classes apparently (from the experimental results) have approximately the same temperature dependence it is not in general possible to determine a priori the relative contributions due to each class from the experimental results. Fortunately however, in the present instance, it can be shown that the function G.g(b) found for class (ii) is close to some limiting form which is most probably that appropriate for class II. This may be inferred from the following: Consider figures 5.20 and 5.21: with progressive ageing class (ii) becomes less prominent until eventually only class (i) behaviour remains. The dashed curve in figure 5.21 illustrates the tendency of g(b) (or more precisely the value of b for which $P_v(b)$ is a maximum) to reach a limiting value at short ageing times and it is apparent that the as-quenched result is very close to this limiting value. It has also been experimentally established (see figure 5.23) that in class (ii) the magnitude of $P_v(b)$ and the function g(b) are not significantly dependent on the extent of deformation. This implies that the product G.g(b) is approximately

invariant with deformation. Various models may be postulated to account for this result but only one model is entirely consistent with the overall observed behaviour, viz; that the fluxon lattice response is determined solely by the Cottrell atmosphere sites (i.e. class II) and that G is proportional to the product of the total dislocation length and the concentration of the interstitial hydrogen in the Cottrell atmospheres. It will be argued later that this product is a constant in the present specimens. Thus the functional dependence of G.g(b) on dislocation density (or deformation) and on b, as determined experimentally in class (ii), is expected to be similar to that pertaining in class II. However while this is apparently a good working hypothesis in the limit of the as-quenched $[1\bar{1}0]$ specimens it is still not possible to make an a priori prediction of the behaviour, intermediate between class II and class I, which occurs with specimen ageing. Such a prediction is desirable since it makes possible an independent test of self-consistency between the Cottrell atmosphere site, the summation method which depends on the basic pinning force as approximately p_m^2 or p_m in the dilute or concentrated limit respectively and the effect of the ageing procedures on the Cottrell atmosphere development. Anticipating later results it is supposed, for the present purposes, that the intermediate behaviour may be approximated by a linear combination of class I and class II and, moreover, that the relatively small dependence of class I on ageing may be neglected for the purpose. Thus the estimated class II behaviour after various ageing treatments is shown, in this approximation, in figures 5.27 and 5.28 which have been obtained by subtracting the curve for $P_v(b)$ after 20 hours ageing at $T_a = 90K$ (i.e. class I) from each of the other curves for $P_v(b)$ in figures 5.20 and 5.21 respectively.

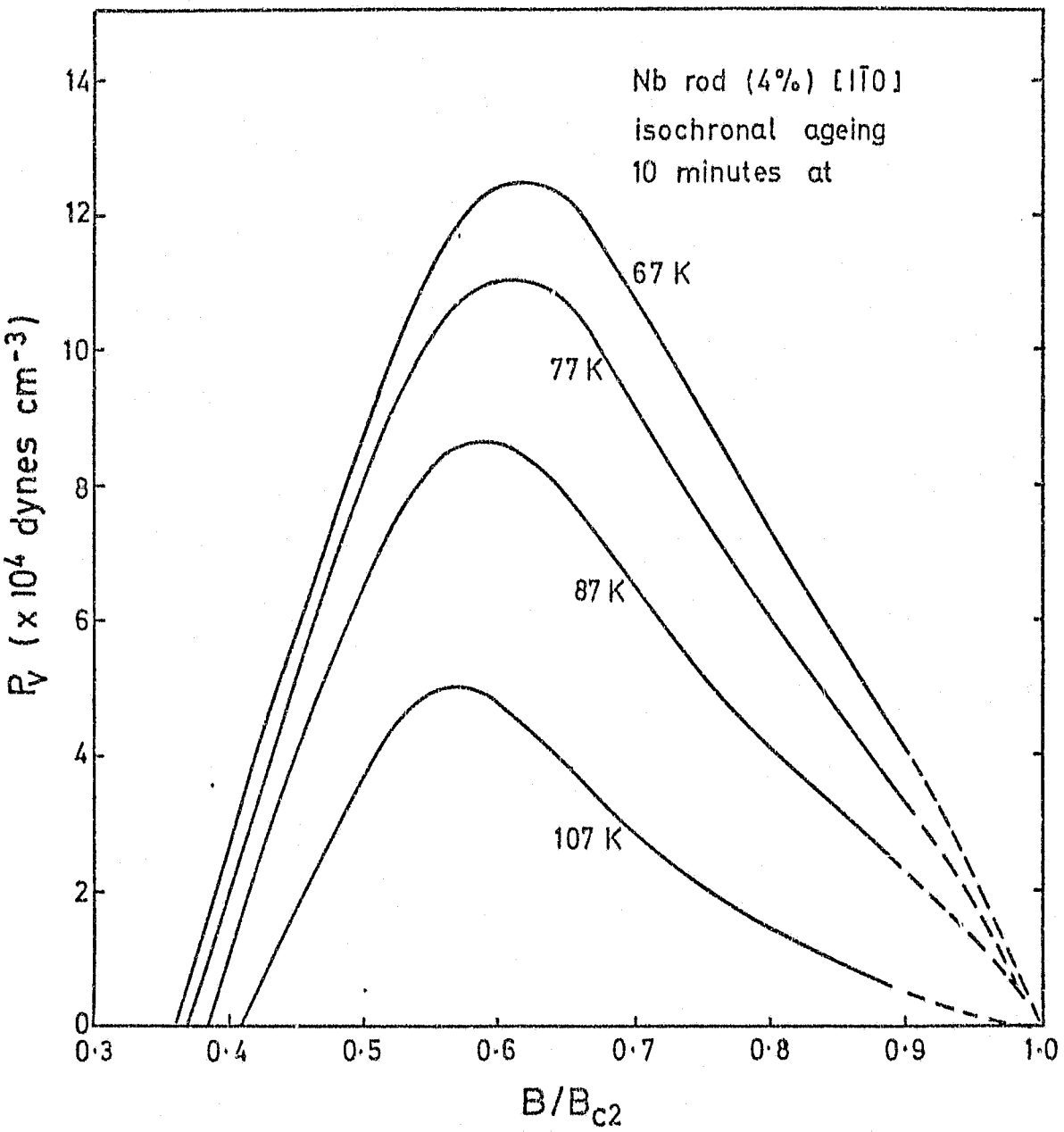


Figure 5.27. The variation of the bulk pinning force density at T = 4.05K with the reduced induction in class II (see text) after isochronal ageing at various ageing temperatures.

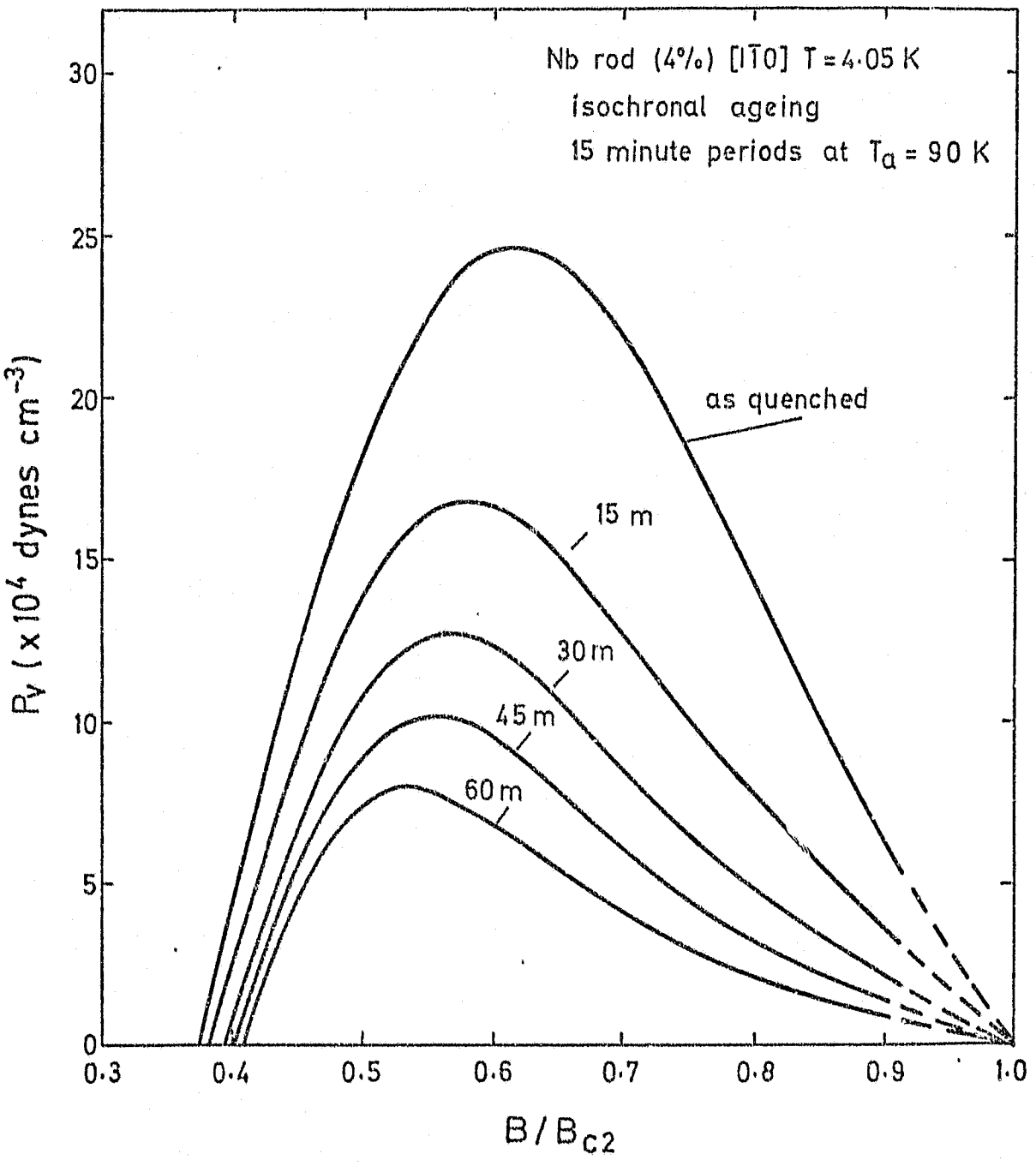


Figure 5.28. As for figure 5.27 after successive isochronal ageing for 15 minute periods at an ageing temperature Ta = 90K.

It is now possible to examine the relationship between the pinning force density in class II and the amount of hydrogen solute available for Cottrell atmosphere formation or, specifically, the fraction (1-f) where f is the fraction of solute which has segregated into the dislocation cores in a time t in accordance with Harper's formula (equation 4.13). [On the basis of previous considerations regarding the low concentration of hydrogen in the specimens it may be assumed that all the hydrogen is associated with the Cottrell atmospheres.] There is however a minor complication which is obvious on examination of the $P_v(b)$ curves of figure 5.28, viz: the curves do not scale exactly with ageing time. This is due in part to the approximation used in obtaining these curves but there may also be physical reasons. This will be considered in more detail later. The results are distinctly suspect for $b \simeq 0.45$ but scale well for $b \geq 0.7$. The relationship between $P_v(b)$ and (1-f) will therefore be investigated at $b = 0.5$, 0.6 and 0.7. In figure 5.29 therefore $\ln[P_v(t)/P_v(t=0)]$ (from the results of figure 5.28) for each of the above values of b has been plotted against $t^{2/3}$. [$P_v(t=0)$ in each case was determined from a separate plot (not shown) of $P_v(t)$ versus t taking the as-quenched value of t to be 60 seconds and extrapolating the curves to $t = 0$.] In each case a linear plot is obtained and consequently if Harper's formula is valid in this case it may be asserted (since the slopes of the plots are not excessively different*)

---

* The slopes of the plots in figure 5.29 fall in the range 0.783 ± 0.25. The fact that a single plot is not obtained for the three values of b may be a consequence of the inadequecy of the assumption that class (ii) is a linear combination of class I and class II behaviour or that the b dependence of P_v in class II varies slightly with the concentration of hydrogen in the Cottrell atmospheres.

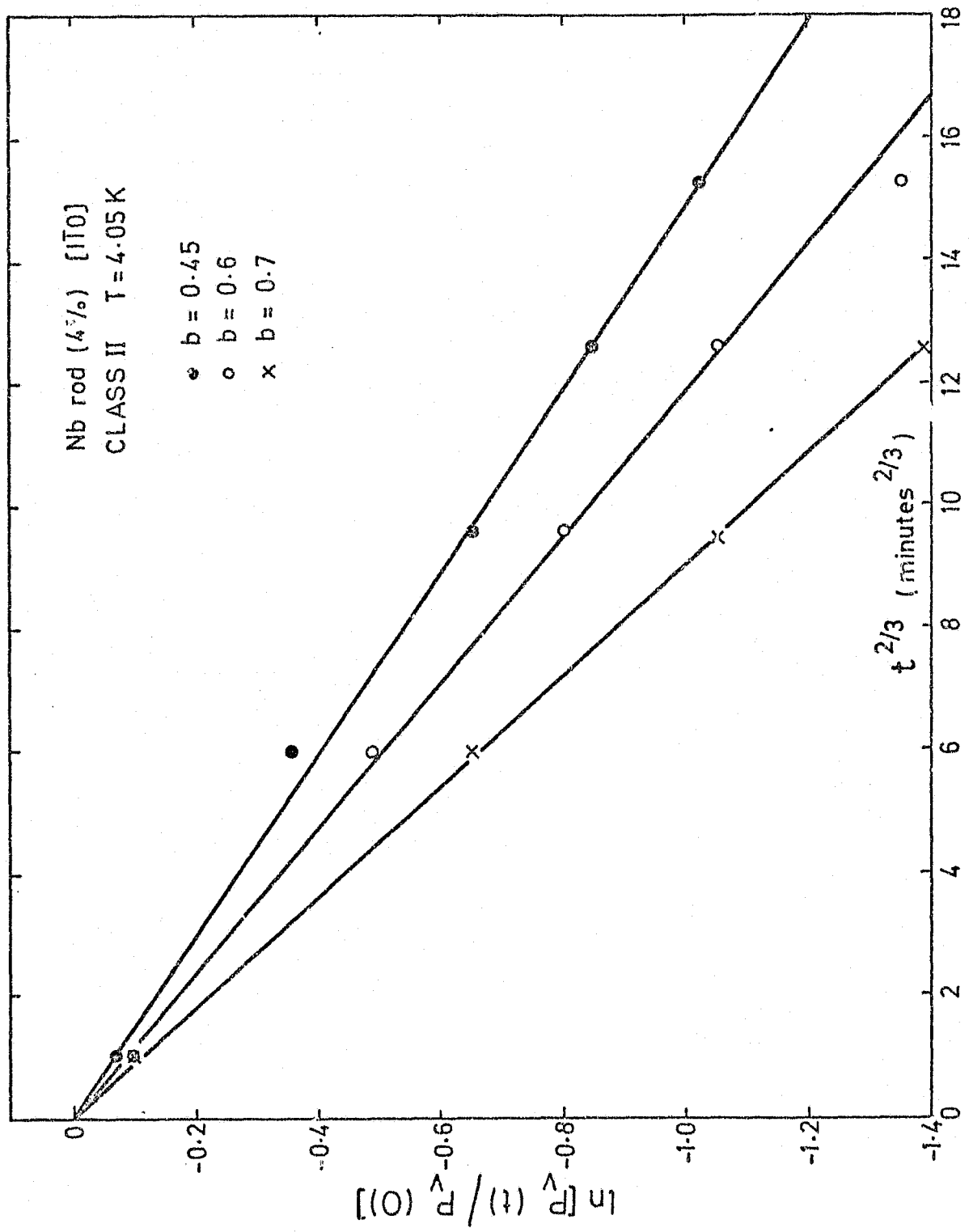


Figure 5.29. The variation of the natural logarithm of the ratio of the pinning force density, after a time t and at t = 0, with $t^{2/3}$ at reduced inductions b = 0.45, 0.6 and 0.7 (at T = 4.05K-from the class II results of figure 5.28). The average gradient $\Delta[\ln(\overline{P}_v(t)/\overline{P}_v(0)]/\Delta t^{2/3}$ is S = -0.783 ± 0.25 seconds$^{-2/3}$.

that

$$P_v(t)/P_v(0) \simeq [1-f]^{\beta} \qquad 5.1$$

where β is a constant which will be shown later to be unity. This result is consistent with the postulate of the Cottrell atmosphere site.

It is now possible to calculate the diffusion coefficient D for hydrogen in niobium at T = 90K. Thus from equations 4.13 and 5.1 the gradient S of the plot of $\ln[P_v(t)/P_v(t=0)]$ versus $t^{2/3}$ is easily seen to be given by

$$S = d[\ln(P_v(t)/P_2(0))]/d[t^{2/3}] = -\beta B$$

$$= -3(\pi/2)^{\frac{1}{2}}\rho(AD/kT)^{2/3}\beta.$$

Rearrangement gives for D:

$$D = [kT/A][-S/(3(\pi/2)^{\frac{1}{2}}\rho\beta)]^{3/2} \qquad 5.2$$

Substituting $S = -0.783\pm0.25$ sec$^{-2/3}$ (from figure 5.29), $\rho = 10^9$cm^{-2}, T = 90K, $A/kT = R_c \simeq 350$Å at 90K (see equations 4.8 and 4.12) and $\beta = 1$ gives $D \simeq 0.9\pm0.5\ 10^{-9}$cm^2 sec^{-1} (T = 90K) which compares favourably with the value predicted by extrapolation of the linear portion of the Arrhenius plot of figure 4.2 to $1/T = 1.11 \times 10^{-2}$, viz: 1.5×10^{-9}cm^2 sec^{-2}.

5.4.2 The detailed low temperature behaviour of the interstitial hydrogen

From the considerations of chapter 4 and the previous two sections the interstitial hydrogen is thought to behave as follows:

At room temperature the mobility of the hydrogen is very high and the concentration (i.e. approximately 50ppm-atomic) is below the solubility limit. Consequently a certain fraction of the hydrogen is uniformly distributed among the dislocations in stress relieving

atmospheres and the remaining fraction is in solid solution (α phase) between the dislocations.

At 4K both the solubility and the mobility of the hydrogen are virtually zero and consequently a sufficiently slow quench from room temperature should cause complete precipitation of the hydrogen, via the Cottrell-Bilby mechanism, into the dislocation cores along which, by pipe diffusion, β phase hydride particles would then form. The quench rate obtaining in the present case (i.e. 300K to 4K is approximately 150 seconds - see figure 5.2), is too rapid to allow significant β phase precipitation. As the specimen cools however the critical radii of the Cottrell and Schoek-Seeger atmospheres (see equations 4.8 and 4.10) increase and a greater fraction of the available hydrogen becomes associated with them. With further cooling the mobility becomes too low for further migration and only short range (e.g. Snoek) ordering of the hydrogen is now possible. The hydrogen in the atmospheres tends to adjust for optimum stress relief and some martensitic transformation is also possible. Eventually the mobility becomes virtually zero and the atmospheres are effectively 'frozen' onto the dislocations.

(The parallel interaction between a sufficiently long, straight edge dislocation segment and this frozen-in atmosphere (i.e. the Cottrell atmosphere site) is apparently effective for pinning (i.e. dissipative) whereas the interaction with a clean dislocation segment apparently is not.)

Consider now the results of the isochronal ageing experiments as shown in figure 5.19:

Curve (a) shows the magnitude of $P_v(b = 0.6)$ for the $[1\bar{1}0]$ 4 per cent deformed specimen as a function of ageing temperature T_a, with T_a

increasing from 4K, and ageing periods of 10 minutes. Ageing at temperatures T_a < 40K has no effect on P_v indicating that the mobility of the hydrogen is virtually zero at these temperatures. At T_a = 70K however P_v shows a sharp maximum which is presumed to be due to an extension of the short-range ordering process (previously alluded to), which must further reduce the elastic stress energy of the dislocations. This effect apparently increases their scattering cross-section for normal electrons. [Hoffman and Cohen (1973) measure the resistivity of iron-carbon martensites after isochronal annealing and find an anomalous increase in the resistivity when the annealing temperature is increased to a value which is just sufficient to allow short-range ordering of the carbon interstitials. They formulate a model for this effect which shows that the interstitial solute inevitably redistributes so as to increase, on average, the static displacement of the host lattice atoms thereby increasing the resistivity*.] Ageing in the range 80K < T < 140K causes precipitation of the hydrogen in the atmospheres into the dislocation cores (as β phase particles) in accordance with Harper's formula for the Cottrell-Bilby mechanism. The quantity of hydrogen in the atmospheres decreases with ageing time and their pinning effectiveness therefore also decreases. A calculation of the effective radius of the Cottrell (or Schoek-Seeger) atmospheres is problematical since the

---

* Professor Nabarro points out that the current is carried by electrons in the S band which if only partially filled implies that dE_F/dk_F and therefore the kinetic energy E_{k_F} of the electrons at the Fermi surface is small. For appreciable electron scatter under these conditions large regions of coherent strain are required.

radius will not, in general, be given by equations 4.8 (or 4.10) on substitution of the appropriate ageing temperature T_a unless the quenching rate from each ageing temperature and the remaining available solute are sufficiently high (see section 4.4).

Ageing at T_a > 140K leads to a progressive resorption of the hydrogen, from the β phase precipitates along the dislocations, back into the Cottrell atmospheres with a consequent increase in their pinning effectiveness. Finally ageing at room temperature restores the hydrogen to its original configuration.

The similar, though much smaller, effect of ageing on the [001] 4 per cent deformed specimen (class (i) - curve b - figure 5.12) is presumably due to a small enhancement of the effectiveness of the multiple dislocation sites due to associated interstitial atmospheres.

5.4.3 Summary

The basic pinning sites responsible for class I and class II behaviour (i.e. the multiple dislocation and the Cottrell atmosphere respectively) have been established with some confidence. From the considerations of characters 3 and 4 it should in principle be possible to make quantitative predictions for the magnitudes of the basic pinning forces due to the various possible interaction mechanisms (i.e. $\delta\kappa$ or elastic) in each case. In practice however, because of uncertainties in the precise details of the pinning sites and to some extent in the theory, such predictions would not provide an adequate basis for an a priori decision concerning the predominant interaction mechanisms. Furthermore it will become apparent later that such an exercise is, under certain circumstances, somewhat artificial. The predominant interaction mechanism must therefore be determined from the temperature and field dependences which are required for the basic

pinning force p_m in order to obtain a self-consistent agreement between a suitable summation model and the experimentally determined scaling law in each class of behaviour. By implication, in the above statement, the inter-dependence between the basic pinning sites and the summation model has been re-stated and without an adequate knowledge of the density and geometry of the pinning sites no a priori assumption should be made about the summation model either. This problem will be dealt with in the following sections.

5.5 Models for the bulk pinning force and comparison with experiment

5.5.1 Introduction

In this section class I behaviour, class II behaviour and the 'anomalous' departures from the experimentally determined scaling laws in each class will be treated separately. The treatment will be neither exhaustive nor rigorous but will constitute an attempt to establish the salient physical processes involved in each case. It should also be stated here that the methods and conclusions of this section are a logical extension only of the theoretical considerations and deductions of the previous sections and chapters. Various other conceivable and published mechanisms which have not been mentioned herein have been omitted on the basis either of trial or of feasibility in the present experimental situation.

Finally the conclusions of this section will, where possible, be examined for compatibility with pertinent experimental results which have been reported elsewhere.

5.5.2 Class I behaviour

(a) The multiple dislocation site

The multiple dislocation site has been identified with regions of tightly tangled dislocations which (from the electron-micrographs

referred to in section 5.2.2) have overall dimensions (<R>) in a range between approximately 5×10^{2}Å and 5×10^{3}Å (for comparison: a_o varies between approximately 10^{3}Å at B = 2Kgauss and 10^{4}Å at B = 20 gauss) and may have between 5 and 20 dislocation segments associated with them. This implies a local dislocation density of order $10^{10} - 10^{11}$ cm^{-2} which is a factor of $10 - 10^{2}$ larger than the average dislocation density in the crystal. These regions, which should be distinguished from regions of dislocation braiding, apparently consist largely of edge dislocation dipoles and multipoles. Such regions are expected, from previous considerations, to interact with fluxons either by the $\delta\kappa$ or the second-order elastic interactions. For the former interaction the analysis of section 3.2.2 should be appropriate since it is well known (see for example Livingston and Schadler, 1964) that severe cold work does not influence H_c significantly. This factor also precludes the so-called 'core interaction mechanism' (see for example Campbell and Evetts, 1972). The first-order interaction mechanism is unlikely in this case because: (i) this type of site will not give rise to long range stress or strain fields (ii) within the site the strain changes sign several times within one coherence length and (iii) there is an apparent absence of a strong anisotropy in class (i) (but see footnote on page 166).

Presumably for a significant first-order interaction a dislocation pile-up is required. The local and long-range stress fields due to various pile-up configurations have been calculated by Hazzeldine and Hirsch (1967) and can be very large especially (Nabarro, 1967) when two pile-ups run into each other on two intersecting glide planes. However, although the existence of dislocation pile-ups is inevitible after deformation their concentration is apparently small.

Expressions for the basic pinning force, due to the $\delta\kappa$ and the second-order elastic mechanisms, which may be used or adapted for use with the multiple dislocation site, have been given in chapter 3.

(b) The summation problem

As discussed in chapter 3 the method of summation depends on the strength p_m, the geometry, the volume density N_v and the distribution of the pinning sites.

The multiple dislocation sites, in the present case, may be assumed to be randomly distributed. However, an estimate for the volume density of these sites is problematical on account of the relative paucity of published electron-micrographs (see section 5.2.2) for equivalent deformation conditions and also because the minimum size and/or dislocation content for a site to satisfy the threshold criterion (see chapter 3 and later) is not well known. It will be assumed however, that in lightly deformed materials N_v satisfies the dilute-limit criterion (equation 3.42). Thus if it may also be assumed that the multiple dislocation site behaves like an ideal point-like pinning site, vis-a-vis the fluxon lattice response, then the dilute-limit point-pinning site theories of chapter 3 should be appropriate.

The theory of Labusch (1969b) yields three expressions for the interaction force which are appropriate for various regimes of a parameter α which is a measure of the ratio of the interaction force and the fluxon lattice rigidity. With increasing α the expressions give the pinning force in the so-called 'lattice', 'fluid' and 'single fluxon' approximations. The lattice-approximation is normally considered to be appropriate and was reviewed in chapter 3. Equation 3.47 gives the final result for the bulk pinning force density for a particular form of the pinning potential due to a point pinning site.

The dynamical summation method in the dilute-limit predicts a result which is similar to or identical with equation 3.47 without specifying the form of the pinning potential however (see for instance Campbell and Evetts, 1972). Experimental results for a variety of pinning situations have been compared by various authors, with more or less apparent success, against some or all of the predictions of equation 3.47. In lightly deformed materials (see Freyhardt, 1967, 1969, 1971 (screw dislocations in niobium), Good and Kramer, 1970 (edge dislocations in niobium) and Coote, 1970 (predominently edge dislocations in Nb - 50 per cent Ta)) the dilute-limit point-site models appear to have some validity although certain inconsistencies are apparent which have not previously been resolved. The basis of these inconsistencies is apparently associated with Labusch's threshold criterion. Thus an important assumption of both the statistical model, and the dynamical models is that the basic pinning site is a point or short line force with a pinning potential width d such that $d << a_o$. This condition is reasonably satisfied by segments of dislocation. However, as previously mentioned and demonstrated in chapter 3, theoretical estimates suggest that the basic pinning force due to isolated segments of dislocation is at least an order of magnitude lower than the threshold value required for effective pinning. This problem has previously been either ignored or resolved by assuming that the basic pinning site consists of regions of local, relatively high density clusters of point-like pinning sites (see for example Fietz and Webb, 1969, Webb, 1971). These clusters are usually considered to arise through statistical variations in the defect density and the basic pinning force (P_m) of the cluster is assumed to be given by $P_m = mf$ where m is the number of

individual sub-sites in the cluster and f is the basic pinning force due to each of these sub-sites. It is not obvious that equation 3.47 should still be valid for this type of cluster however (see also Nabarro, 1972). Such sites are in any event not compatible with the present experimental results.

It has also been suggested that dislocation pile-ups and tangles (which therefore includes the multiple dislocation site proposed here) may be the basic pinning sites. In this case, as in the case considered above, however there are difficulties associated with the assumption in the models, viz: that $d \ll a$. To date no adequate proposals have been made to resolve this problem (see also Campbell and Evetts, 1972).

Before proceeding to a discussion of the implications of using Labusch's model in the case of a dilute random array of multiple dislocation sites it will be useful to test the predictions of equation 3.47 against the various relevant experimental results. To facilitate discussion and comparison of the experimentally obtained scaling laws with the predictions of equation 3.47 the approximate form for the elastic constant C_e^P from equation A.4.5 will be substituted into this equation. This gives, to a fair approximation, for $b > 0.4$:

$$P_V^T(b,t) \propto N_v\, p_m^2(b,t).b^{\frac{1}{2}}\kappa_2(t)/\left[B_{c2}^{\frac{1}{2}}(t)(1-b)\right] \qquad 5.3$$

The experimental scaling law in lightly deformed materials (e.g. in the above mentioned cases and also in class I), considering only the regime $b > 0.4$ and neglecting the peak effect anomaly at $b \lesssim 1$ and, for the moment, the $\kappa_1(t)$ and $\kappa_2(t)$ dependences, may be expressed approximately as

$$P_V^E(b,t) \propto N_v\, B_{c2}^n(t)b^m(1-b) \qquad 5.4$$

where m varies between 0 and 0.5 and n varies over a wider range as will be discussed in the following paragraphs.

Thus Freyhardt (loc. cit.) measures P_v in niobium for screw dislocations in normal incidence with the f · lattice and finds $n = 1$ in lightly deformed specimens and $n = 1.5$ at higher deformations. He concludes therefore from the exact model (but see also equations 5.3 and 5.4) that $p_m(b,t) \propto B_{c2}(t)(1-b)$ in agreement with Webb's (1963) model for the interaction between an isolated fluxon and a perpendicular screw dislocation.

Good and Kramer (loc. cit.) measure P_v in niobium as a function of the orientation of the fluxons with respect to an array of edge dislocations in their glide plane. They do not measure the temperature dependence of P_v however and obtain $P_v^E \propto (1-b)$ for $b > 0.4$ at $T = 4.2K$. Using the dynamical summation method they obtain an expression for P_v^T which differs from equation 3.47 by a factor of $a_o/d \simeq 1/d(B_{c2}.b)^{\frac{1}{2}}$. According to their model therefore $p_m(b,t) \propto (1-b)$.

Coote (1970) obtains $n \simeq 3$ and $m \simeq 0$ for $b > 0.4$ in a lightly deformed Nb-50 per cent Ta specimen. [Transmission electron micrographs by Coote (loc. cit.) and see also Campbell and Evetts, 1972, show regions of dislocation tangling which are apparently similar to the multiple dislocation sites proposed in the present investigation.] Comparison with equation 5.3 gives $p_m(b,t) \propto B_{c2}^{7/4}(t)b^{1/4}(1-b)$ [or if Good and Kramers model is used $p_m \propto B_{c2}^2.(1-b)$]. If this result is considered to adequately indicate the second-order elastic interaction then it becomes very difficult or impossible to account for Freyhardt's result.

In the present investigation the scaling law for class I behaviour gives $m \simeq 2.5$ and $n > 0$. According to the models therefore,

$p_m(b,t) \propto B_{c2}^{3/2}(t) b^{1/4}(1-b)$ or $p_m \propto B_{c2}^{7/4}(1-b)$. The remark made in the previous case applies equally in this case. The small difference in the exponent n on $B_{c2}(t)$ in these latter two cases (i.e. Coote and class I) will later be seen to be a consequence of the temperature dependence of the Maki parameters $\kappa_1(t)$ and $\kappa_2(t)$ which will appear in the final expression for $P_v(b,t)$. (This temperature dependence is much larger in the low κ niobium specimens than in the larger κ Nb-50 per cent Ta specimens of Coote.) The relatively larger difference in the exponent n, and therefore in the temperature dependence of P_v, between the latter two cases and that of Freyhardt is significant however. If the geometry of the basic pinning sites is similar in both cases this difference may be indicative that different basic pinning mechanisms are operative in each case, viz; the second-order elastic interaction in the case of the screw dislocations or screw dislocation tangles in Freyhardts specimens* and the $\delta\kappa$ mechanism in the case of the multiple dislocation site which consists of edge dislocations. A detailed comparison of experiment, in each of the above cases, with equation 5.3 using the basic pinning force expressions for the multiple dislocation site, i.e. equation 3.40b for the second-order elastic interaction and equation 3.12b for the $\delta\kappa$ interaction, shows this trend but is generally not good. Thus equation 5.3 consistently predicts a bulk pinning force density which depends too strongly on B by a factor of $B^{3/2}$. Now it can be argued that this discrepancy is due in part to an oversimplification in the

---

* In this case it will be recalled that the screw dislocations are in perpendicular interaction with the fluxons. The parallel interaction case will be considered, albeit only for $b < 0.3$, in chapter 7.

derivation and use of the above mentioned expressions for p_m. Thus, as mentioned in chapter 3, these expressions are valid only for sites, of localized potential, which have dimensions, normal to the fluxons, which are small relative to the interaction range d. For such sites d is determined by the range of variation in the order parameter $|\psi|^2$ and is therefore given approximately by $\xi(t)$ at low fluxon lattice densities and by $a_o/2$ at higher fluxon lattice densities after core overlap has begun. As mentioned in the previous section however, the multiple dislocation sites which have been proposed as the basic pinning sites in class I apparently have dimensions which are comparable with a_o. (It is also possible that many of the so-called multiple dislocation sites are too small physically and therefore possibly too weak to satisfy Labusch's threshold criterion (see chapter 3).) It is therefore necessary to formulate expressions for p_m due to multiple sites which have dimensions of the order of a_o. In appendix A1h a calculation has been done to determine the effect of site dimensions, relative to a_o, on the maximum pinning force p_m due to spherical and cylindrical sites on the assumptions that (i) the potential density Ω, for a given value of $|\psi|^2$, is uniform inside the site and decays rapidly to zero outside the site, (ii) that the fluxon lattice is rigid so that the result is valid in the lattice approximation only and (iii) that the integrated potential, i.e. the interaction energy, is a simple first harmonic periodic function of the fluxon lattice parameter a_o and the position of the site relative to the lattice. The calculation is therefore only expected to be valid in the regime $b > 0.4$, i.e. after fluxon core overlap has begun, in the present case. The results of the calculation (see figure A1.5) show, for a spherical or cylindrical site (parallel to the fluxons) of radius R and constant uniform potential density Ω inside

the site, that the pinning force has a very large maximum when $2R/a_o \simeq 0.7$ and drops to half its maximum value at $2R/a_o \simeq 0.25$ and at $2R/a_o \simeq 1.3$. This result has some important implications*, viz:

(i) A random array of nearly identical pinning sites, with a relatively narrow distribution in their dimension 2R (normal to $\underline{B}$) could give rise to very rapid changes in the bulk pinning force density P_v with changes in $B \propto (a_o)^{-2}$. Thus, according to figure A1.5, if $2R/a_o = 1.75$ initially and $2R/a_o = 1$ finally $\propto p'_m \equiv \left[F_y\right]_{max}$ would increase by a factor of 10 with a corresponding decrease in B of only a factor of 3. For changes in $2R/a_o$ in the regime $2R/a_o < 0.5$ p_m is an increasing function of B, but the variation is slower. This type of behaviour is analogous to the so-called matching effect which was mentioned in chapter 3.

(ii) In a random array of sites which has a broad distribution in size R but a uniform value for their intrinsic potential density Ω only those sites for which $2R/a_o \approx 0.7$ will contribute significantly to $P_v(B)$ at any particular value of B. According to the analysis of appendix A1h the maximum interaction force for a spherical site is given by $p'_m \equiv \left[F_y\right]_{max} \propto \beta R^3 \Omega \times$ (correction factor) where β depends on the basic interaction mechanism as defined in the appendix and the correction factor is a function of R/a_o and is the required factor for generalizing equations 3.11 and 3.39 for sites with $R << a_o/2$ to arbitrary R/a_o. For $2R/a_o \simeq 0.7$ the results of figure A1.5 give to good approximation (correction factor) $\propto (a_o/R)^2$.

---

* The following discussion is pertinent only if $R \sim a_o$. For $R >> a_o$ other effects must be considered since the basic pinning interaction is different and the fluxon lattice inside R is in local equilibrium.

(iii) For a random array of sites which has broad distributions in both R and Ω it is obvious that sites in a correspondingly broad range of R/a_o will make a significant contribution to $P_v(B)$ at any B. Some average correction factor is now required and inspection of figure A1.5 suggests that (correction factor) $\propto (a_o/R)^2$ is still a fair approximation.

Thus since the multiple dislocation site array probably constitutes an array of the type under either (ii) or (iii) above it is concluded that in order for the pinning force expressions 3.11-for the $\delta\kappa$ interaction and 3.39-for the second order elastic interaction to be applicable here they must be scaled in proportion to $(a_o/R)^2$. Before these modified expressions are inserted into the Labusch expression for $P_v(b,t)$ it is necessary to consider the effect in Labusch's model of increasing the pinning range from $d \ll a_o$ to $d \simeq a_o/2$. According to Campbell and Evetts (1972) this will only change the number of effective interactions, or alternatively the probability that a particular super-threshold site, is effective at any instant, by a constant factor. The effect on the response function $G'(0)$ in the model (see chapter 3) is expected to be small because the distortion of the fluxon lattice, in the lattice-approximation, extends over distances which are large compared with a_o and therefore also with d. It seems reasonable therefore to suppose that Labusch's model (see equation 3.47) will still give good qualitative results, in the regime $d \simeq a_o/2$, providing that d in the model is replaced by ξ or $a_o/2$ which, as previously stated, are the maximum ranges over which the interaction is assumed to occur, for the type of sites under consideration, in the low and high regimes of b respectively.

Thus finally, if the above considerations for the multiple dislocation site are taken into account, the Labusch expression (equation 3.47)

is now given, for $b > 0.4$ and $2d = a_o$, by

$$P_v = (1/2\pi^{\frac{1}{2}})N_v(bB_{c2}/\phi_o)^{3/2}\left[(C_{44}C_{11})^{-\frac{1}{2}} + (C_{44}C_{66})^{-\frac{1}{2}}\right] \times \left[\eta p_m^2(a_o/R)^2.a_o/2\right] \qquad 5.5a$$

$$P_v \propto \eta N_v p_m^2\left[(C_{44}C_{11})^{-\frac{1}{2}} + (C_{44}C_{66})^{-\frac{1}{2}}\right]/R^2 \qquad 5.5b$$

which on substitution for the effective elastic modulus term in the square brackets from equation Ad5 gives

$$P_v(b,t) \propto \eta N_v p_m^2(b,t)\kappa_2(t)\left[B_{c2}^2(t)b(1-b)R^2\right]^{-1} \qquad 5.5c$$

where η is some function of the pinning site size distribution which may have some dependence on a_o if the distribution is narrow or otherwise is not particularly smooth*, N_v is the volume density of multiple dislocation sites and is related to η and p_m is the product of the maximum attainable pinning force for a site of uniform potential density Ω within its volume in the limit $R \to 0$ and the actual volume $4\pi R^3/3$ of the site. It is therefore given by the appropriate expressions of chapter 3 (see appendix A1h).

Now substituting for p_m from equation 3.40b, for the second order elastic interaction due to a multiple dislocation site, into equation 5.5c gives, for $b > 0.4$:

$$P_v(b,t) \propto (1-b)\ B_{c2}(t)\kappa_2(t)/\kappa_1^2(t) \qquad 5.6$$

in good agreement with the results of Freyhardt (loc. cit.). Sub-

---

* In the present investigation the overall variation in $a_o \simeq (bB_{c2}/\phi_o)^{-\frac{1}{2}}$ with b and t is less than a factor of 5 and with b only a factor of 1.6. Considering the apparently wide distribution for the size of the multiple dislocation sites it is reasonable to expect that η is approximatly a constant (but see section 5.5.4).

stituting for p_m from equation 3.12b, for the $\delta\kappa$ interaction, gives, for $b > 0.4$:

$$P_v(b,t) \propto (1-b)B_{c2}^3(t)\kappa_2(t)/\kappa_1^4(t) \qquad 5.7$$

in good agreement with the results of Coote (loc. cit.) since, as previously discussed, the variation of κ_1 and κ_2 with t for Nb-50 per cent Ta is slow. For pure niobium this variation is more rapid and if ignored is expected to result in a measured exponent on $B_{c2}(t)$ which is smaller than the actual exponent. In class I of the present investigation $P_v(t) \propto B_{c2}^{5/2}(t)$ approximately and to compare this temperature dependence with the prediction of equation 5.7 it is convenient to express this equation in the form

$$(P_v(t)\kappa_2(t))/(B_{c2}^3(t)\kappa_1^4(t)) = F(G,b)$$

where $F(G,b)$ is a function of the pinning microstructure and reduced induction but is independent of t. The left hand side of this equation can now be evaluated for a specific specimen and value of b and for various values of t from the experimental results of section 5.3. This has been done for the [001] 4 per cent deformed specimens (as-quenched and after ageing - Class I) choosing $b = 0.6$ and using the results of figures 5.16, 5.5 and 5.6. The final results have been plotted against t^2 in figure 5.30 where the maximum departure from the expected t independent behaviour is shown to be less than 15 per cent in the range $0.2 \leqslant t^2 \leqslant 0.85$. (The behaviour for $t > 0.85$ will be discussed in section 5.5.4.)

It may be concluded therefore that the model is at least in approximately qualitative agreement with a variety of pinning situations For a more precise and quantitative assessment of the model it will be necessary to make a more detailed comparison of the predictions of equation 5.5a (with p_m for the $\delta\kappa$ mechanism - equation 3.11) with the

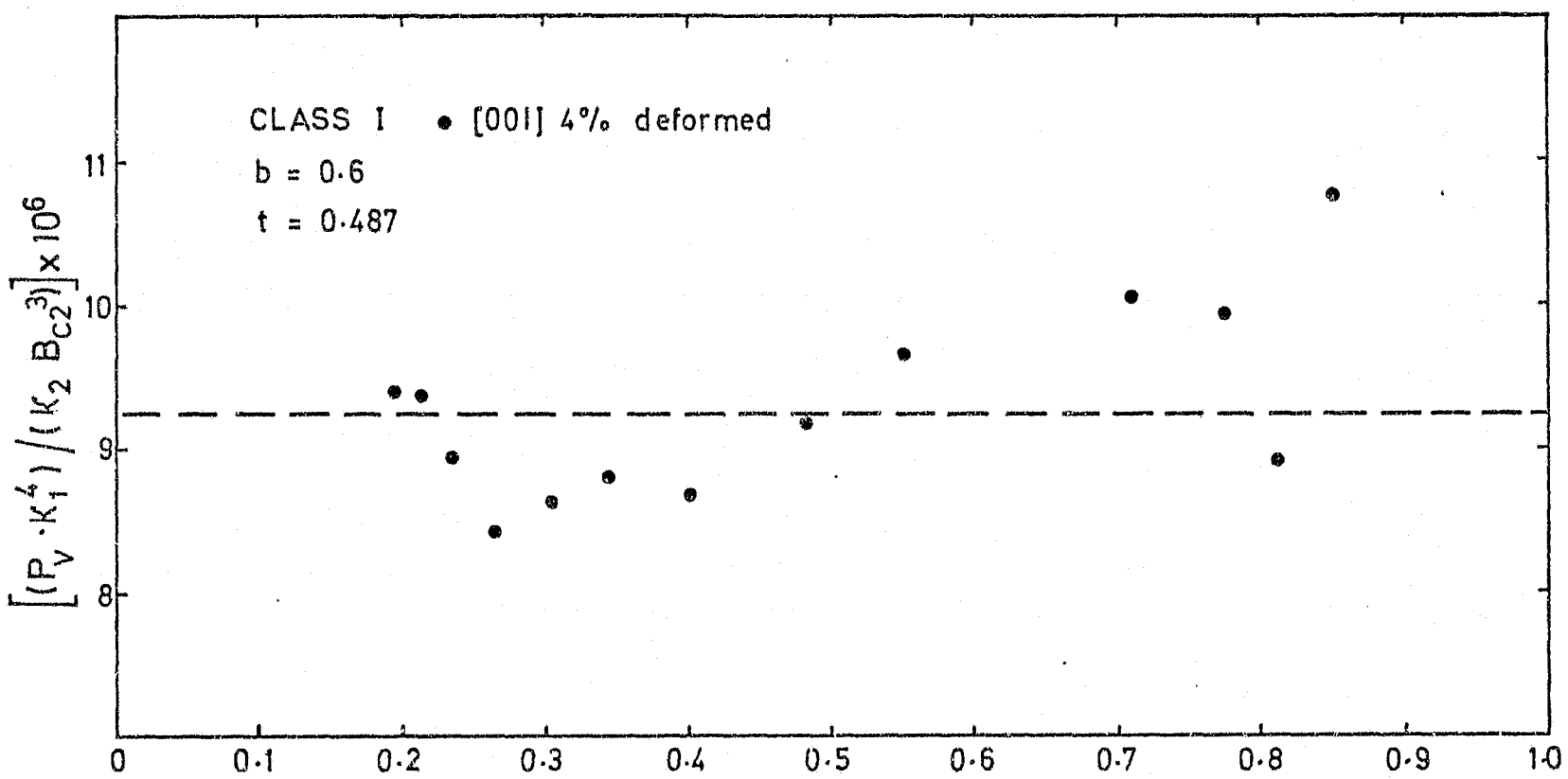


Figure 5.30. A plot of the temperature invariant component of the bulk pinning force density (in accordance with the model for class I), against t^2 showing a maximum relative deviation from theory of approximatly 10% (except near $t^2 = 1$).

scaling law obtained in class I. This is not altogether possible however as neither $\delta\kappa$ nor the product ηN_v for the multiple dislocation sites can be determined with any accuracy. For the present therefore it will only be possible to make an accurate qualitative comparison with the model. The complete explicit expression for the pinning force density, as predicted by the model (see above) is given for $b > 0.4$ (class I - $\delta\kappa$ mechanism) by:

$$P_v(b,t) \approx N_v(\eta/32(2\pi)^{5/2}R^2)(B_{c2}^4(t)/\kappa_1^4(t))\left[\delta\kappa/\kappa\right]^2_{\text{eff}} V^2$$

$$\times \left[\frac{d}{dr}(|\psi|^2 - |\psi|^4)\right]^2_{\max} \left[(C_{44}C_{11})^{-\frac{1}{2}} + (C_{44}C_{66})^{-\frac{1}{2}}\right] \qquad 5.8$$

In figure 5.31 P_v (class I) for $b = 0.5$, 0.6 and 0.7 (from figure 5.23) has been plotted against ε (i.e. the maximum strain to which the parent crystal specimens were strained in compression) on the assumption that $N_v \propto \varepsilon$. An approximately linear result is obtained with a residual value for $P_v(\varepsilon = 0)$ of approximately 10^4 dynes cm^{-3}. The temperature dependence of P_v in equation 5.8 is expected to be identical with the prediction of the approximate expression, viz: equation 5.5c and therefore need not be reconsidered*. Finally the predicted b dependence of P_v which is given only approximately in equation 5.5c has been obtained exactly (but see appendix A1h) for $b > 0.4$, from equation 5.8, using the results of figure 3.8 and table A1, and is compared qualitatively with experiment ([001] 4 per

---

* It has been established that the average diameter 2R for the effective multiple dislocation sites is approximately $0.7a_o$. Now $0.7(a_o/\xi) \simeq 0.7(2\pi)^{\frac{1}{2}}/b \simeq 1.75/b$ and therefore $2R > \xi$ for all b and t (except as $t \to 1$) and it is therefore reasonable to expect (see section 4.5 and Goodmans expression, i.e. equation 4.15) that $|\delta\kappa/\kappa|_{\text{eff}} = \delta\kappa/\kappa$ and is temperature invariant.

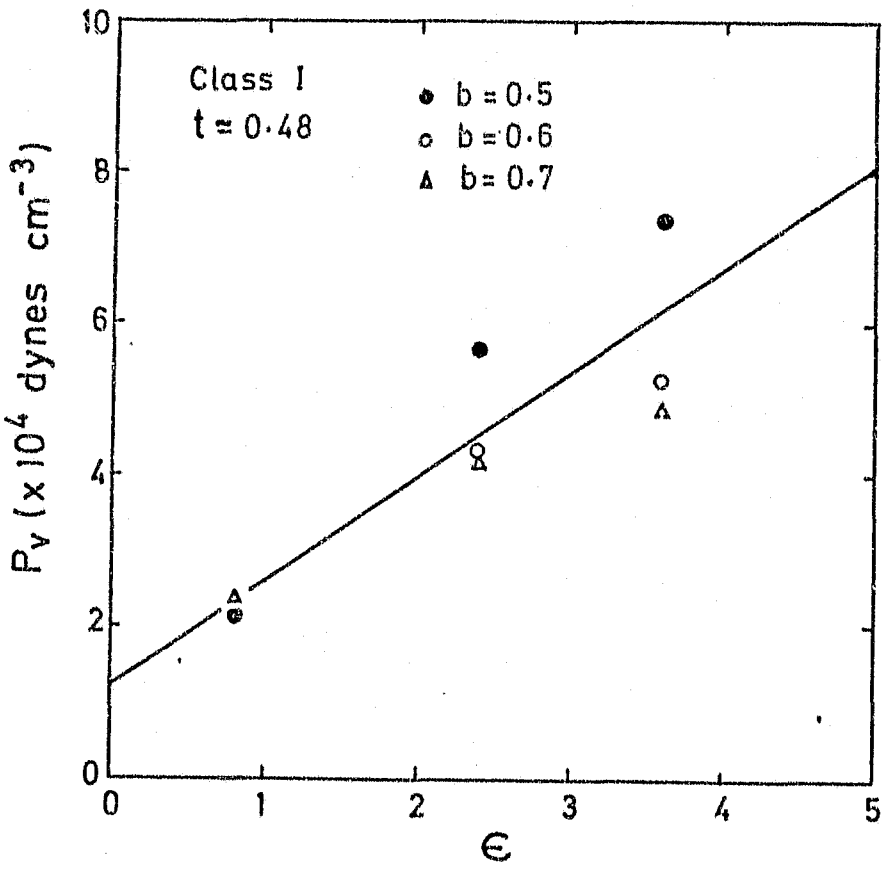


Figure 5.31. The variation of the bulk pinning force density with deformation ϵ, in class I at b = 0.5, 0.6 and 0.7, showing an approximately linear dependence.

cent deformed, as-quenched and saturation-aged) in figure 5.32. Also shown in the figure are the results of Good and Kramer (1970) (4 per cent deformed, H_o parallel to the [001] direction). (The various experimental results for $P_v(b)$ have been normalized at $b = 0.6$). For b in the range $0.5 < b < 0.9$ the qualitative agreement between the model and the results for the fully aged specimen is excellent. The as-quenched specimen and Good and Kramer's specimen show peak effect anomalies at $b \simeq 0.8$ and $b \geq 0.9$ respectively. For $b < 0.5$ the small positive deviation of all the experimental results from the prediction of the model is probably due to failure of the high field expression for the shear modulus C_{66} (see appendix A1d). Thus the low field expression for C_{66} (equation Ad3(a)) predicts a lower value for C_{66} in this regime and also that $C_{66} \to 0$ as $b \to 0$. Substitution of C_{66} from equation Ad3(a) into equation 5.8 would not provide a model for $P_v(b)$ which is valid as $b \to 0$, since other factors would need consideration, but would improve the validity in the regime $b < 0.5$ and, in particular, predict a larger value for $P_v(b < 0.5)$ in qualitative agreement with experiment.

Finally, for multiple dislocation sites which interact with the fluxon lattice predominantly by the second-order elastic mechanism, substitution of p_m from equation 3.40b into equation 5.5a leads to predictions for $P_v(b,t)$ which are in very good agreement with the results of Freyhardt (loc. cit.) in specimens containing predominantly screw dislocations.

It is therefore concluded; in agreement with the expectation that isolated clean dislocation segments fail to satisfy the threshold condition under any conditions (see chapter 3), that the pinning centres in lightly deformed materials are small regions of tangled dislocation which have only a localized pinning potential and have been called

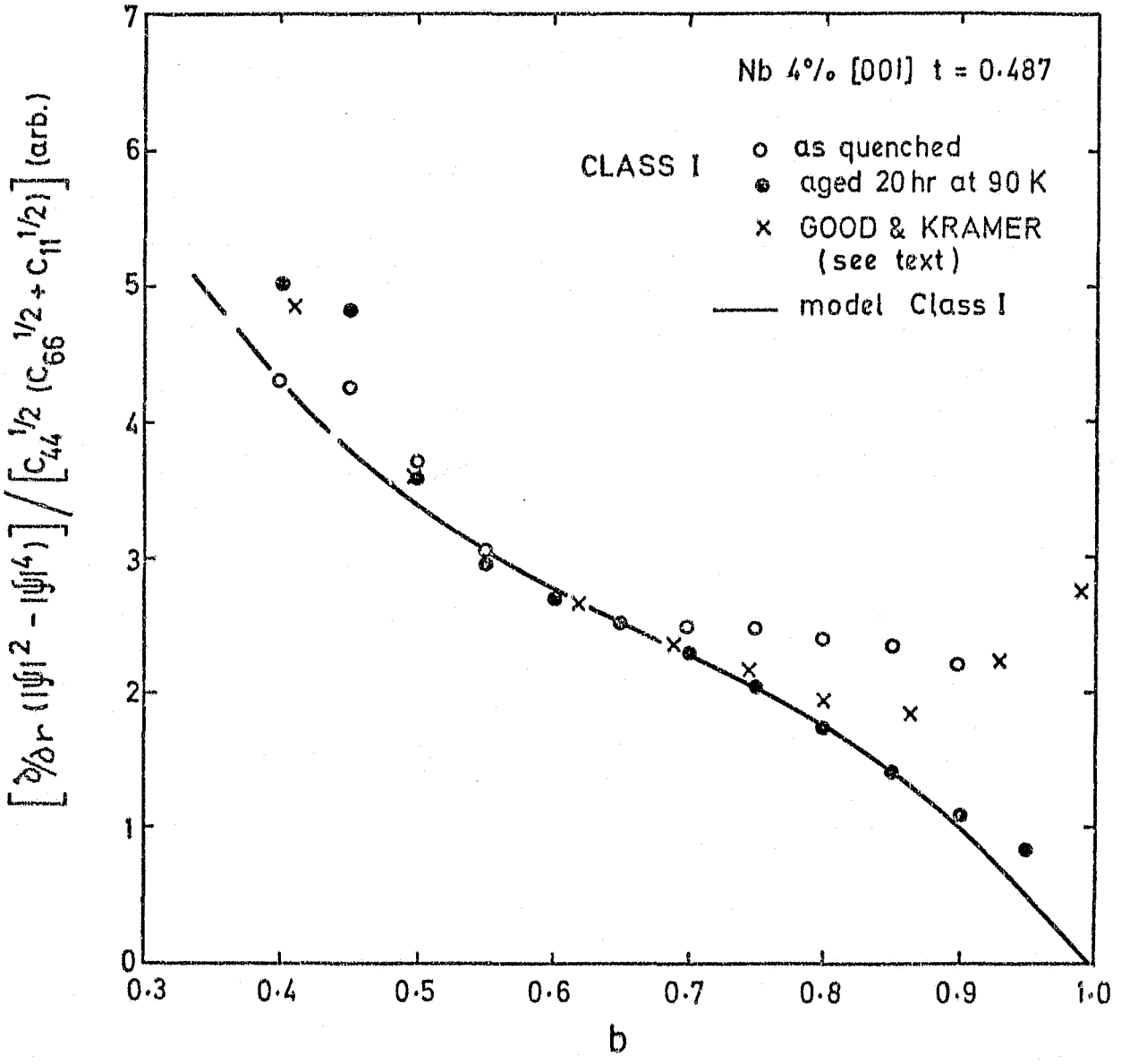


Figure 5.32. Comparison of the predicted b dependence of the bulk pinning force density, from the model for class I, with experiment on the as-quenched and aged [001] 4% deformed specimen (class (i)) and also with the experimental results of Good and Kramer at $t \simeq 0.48$.

multiple dislocation sites in the present investigation. Moreover, since at any particular value of the induction B only those sites for which $2R \approx 0.7a_o$ have a significant pinning force on the fluxon lattice, the dilute-limit lattice-approximation model for point-like pinning sites of Labusch (1969b) is still valid in this case. The relatively small anisotropy of pinning found in class (i) and by Good and Kramer (1970) is also readily accounted for by the above model if the multiple dislocation sites are slightly elongated along $[1\bar{1}0]$ i.e. along the direction of the edge dislocation.

5.5.3 Class II behaviour

(a) The Cottrell atmosphere site

The Cottrell atmosphere sites, which apparently give rise to class II behaviour in the present specimens, consist of atmospheres of interstitial hydrogen on segments of edge dislocation (see section 5.2.2) extended along the $[1\bar{1}0]$ direction. According to chapter 4 the Cottrell atmospheres should have a diameter $\langle 2R \rangle = R_c \simeq 350\text{Å}$. The effective length of a Cottrell atmosphere site, i.e. the mean length over which the sites may be considered to be straight and parallel with the fluxons, i.e. along $[1\bar{1}0]$, is not easily determined but is estimated from inspection of the electron micrographs referred to in section 5.2.2 to be of the order of 10^4Å. This question will be discussed in more detail later.

The strong anisotropy which obtains in class II is obviously due to the geometry of the Cottrell atmosphere site and need not necessarily have any relation to the interaction mechanism which may therefore possibly be due to the $\delta\kappa$ and/or an enhancement of the first or second-order elastic interaction for a clean dislocation. It is reasonable to assume however that the pinning effectiveness of the Cottrell atmosphere is locally much larger than that due to the

dislocation alone. The effective pinning mechanism will therefore be assumed to be entirely due to the atmosphere.

(b) The summation problem

The precise manner in which the basic pinning forces sum to give the bulk pinning force density in class II would appear to be fairly complex. Thus the Cottrell atmosphere sites may not be sufficiently long to promote a proper line-force response in the fluxon lattice and their distribution is non-uniform rather than random because of the tendency of the dislocation to form braids in the present specimens. Also, from the considerations of chapter 3, it is possible that the volume density of the Cottrell atmosphere sites lying close to the $[1\bar{1}0]$ direction may be sufficiently large, especially in the regions of braiding, that some concentrated-limit summation model may be appropriate.

The experimentally determined scaling law for class II behaviour may be summarized (see section 5.3) approximately as follows:

for $b < 0.3$

$$P_v \simeq 0$$

for $0.3 < b < 0.6$

$$P_v \propto B_{c2}^{5/2}(t)(b-0.3) \qquad 5.9$$

for $0.6 < b \leqslant 1$

$$P_v \propto B_{c2}^{5/2}(t)(1-b).b^{\frac{1}{2}}$$

Also $P_v \propto (1-f)^{\beta}$ (see section 5.4.1) where $(1-f)$ is the fraction of the interstitial hydrogen associated with the Cottrell atmospheres and β is a constant which has not yet been determined. P_v was also found to be approximately independent of the deformation and therefore presumably of the dislocation density ρ. [This pinning behaviour is remarkable and to this author's knowledge has not previously been

reported.]

The problem of a non-uniform site distribution in the concentrated limit has not been previously solved. Campbell and Evetts (1972) and Appleyard, Evetts and Campbell (1974) have made numerical calculations on computer models of random one-dimensional arrays of pinning sites in the concentrated limit and indicate that they are extending their calculations to two-dimensional arrays. Their method should be equally applicable to non-uniform two-dimensional arrays and probably offers the most useful approach to the problem. The model of Nabarro and Quintanilha (1970) and Quintanilha (1972) (see also chapter 3) is for a uniform two dimensional pinning potential and presupposes the elastic interaction mechanisms. It is possible that this model may have a limited validity in class II (for $b > 0.6$) in the regime where $\xi\rho^{\frac{1}{2}}$ is intermediate between the low and high limits for which explicit expressions for P_v are given (see equations 3.60a and 3.60b). It is not apparent how either of the above approaches can explain the low b behaviour in class II however.

The model of Kramer (1973) (see also chapter 3) is based on an assumed pinning site geometry which may be adequately similar to that obtaining in class II of the present investigation. Although this model has been formulated in the high κ limit, where it makes good predictions for $P_v(b,t)$ in certain experimental situations, it should nevertheless be possible to assess the qualitative validity of the basic premises of the mod in class II. The model is conveniently formulated and may easily be generalized to include the low κ limit and also different basic pinning mechanisms. Such an assessment is necessary, and will be useful, since the model makes predictions for $P_v(b,t)$ which are superficially in approximate agreement with the experimental results for class (ii) or class II (see equations 5.9

and following). Thus the model predicts $P_v(t) \propto B_{c2}^{5/2}(t)$ and for $\langle k_p \rangle \simeq 0.3 \langle k_s \rangle$ (see section 3.3.2) a $P_v(b)$ dependence which compares not unfavourably with experiment (see figure 5.34). There are however serious discrepancies between the model and the class II which are associated with the predicted dependence of P_v on the defect microstructure parameters. Thus the model predicts that the low field behaviour, the value of b for which $P_v(b)$ is a maximum and the magnitude of $P_v(b)$ at the maximum are all strongly varying functions of the microstructure parameters and in particular, of the density of effective pinning sites which are assumed to be line forces. This cannot be reconciled with class II behaviour even if plausible assumptions are made for various possible effects due to the interstitial hydrogen. It is concluded therefore, in spite of the fair predictions which are made for the b and t dependences of P_v, that the model is not appropriate in class II.

Finally the dilute-limit dynamical model of Good and Kramer (1970) (equation 3.53).for line forces parallel to the fluxons is also completely at variance with the observations in class (ii).

A consideration of reasons for the inapplicability of the above models in class II leads to the conclusion that the experimental observations can only be compatible with a model (i) in which P_v depends linearly on p_m and (ii) which involves an explicit mechanism to account for the rapid increase in the value of $P_v(b)$, from zero or some very small value, which occurs at $b \simeq 0.4$. It will be recalled from chapter 3 that the so-called matching and synchronous mechanisms may potentially satisfy these requirements. The former mechanism is obviously not applicable here since it predicts a maximum in P_v for a certain value of a_o and therefore of B. The synchronous mechanism, which involves a spontaneous relaxation of the fluxon

lattice in the force field of the pinning sub-structure (preferably line forces parallel to the fluxons) over a certain range of b - therefore producing a significant increase in P_v over the range, is obviously potentially applicable in Class II. The conventially accepted mechanism for the onset of synchronous pinning requires that either the pinning strength of the sites increases or the rigidity of the fluxon lattice decreases so that either the threshold criterion is satisfied or otherwise conditions become favourable for independent fluxon pinning. As stated previously in chapter 3 an example of this is the Pippard mechanism for the peak effect (see later) which depends on the quadratic decrease of the fluxon lattice shear modulus C_{66} with b near B_{c2}. This mechanism implies an increase in the Labusch parameter α, (Labusch, 1969b - or see chapter 3) and therefore the possibility that the fluid approximation should be appropriate in this case. For full synchronization it is obvious that the fluxon lattice should be sufficiently distorted so that the fluxons are able to interact independently with the pinning sites.

It will become apparent later that if the Cottrell atmosphere sites of class II interact with the fluxons predominantly by the $\delta\kappa$ mechanism a rapid increase in their pinning effectiveness is expected for $b \gtrsim 0.3$ which is approximately the regime of the large increase in $P_v(b)$. However, the maximum force which a Cottrell atmosphere site can exert on a fluxon under ideal conditions is expected to be not very much greater than that due to a clean dislocation and therefore only to be of the order of the threshold value. It is therefore reasonable to suppose that the sites will not be able to distort the fluxon lattice sufficiently to cause fluid behaviour and therefore independent fluxon pinning and possible synchronous behaviour.

Campbell and Evetts (1972) suggest however that mobile fluxon lattice defects (e.g. edge dislocations) may provide the necessary fluxon lattice plasticity to allow the fluxon lattice to relax synchronously in the force field of an array of line forces which are parallel to $\underline{B}$. According to Essmann and Träuble (1967) (but see also Campbell and Evetts, loc. cit.) any significant gradient in the fluxon lattice due to fluxon pinning can be accounted for by the presence of a suitable distribution of fluxon lattice dislocations. Thus if pinning sites begin to be effective, so that a gradient in the fluxon lattice occurs, fluxon lattice dislocations must be created simultaneously. It seems reasonable to postulate, in accordance with classical second-order perturbation theory (see for example Nabarro, 1972), that if these dislocations are sufficiently mobile their configurational distribution will continually adjust to reduce the total energy of the system thereby causing at least some of the fluxons to relax into available potential wells. This will allow an increased fluxon gradient and therefore more fluxon lattice defects and so on leading to either matching or synchronous behaviour.

On the basis of this postulate and on the assumption that a significant proportion of the total Cottrell atmosphere length is parallel to the fluxons and interacts with the fluxons predominantly by the $\delta\kappa$ mechanism a model can be formulated for class II which is in qualitative agreement with experiment in every respect.

Thus, in accordance with the considerations of the previous section, the Cottrell atmosphere sites are considered to behave as line forces, parallel to $\underline{B}$, of sufficient length to satisfy, under ideal conditions, such threshold requirements as obtain. Under these conditions the proportion of the total length of the edge dislocation, and therefore the Cottrell atmosphere, which is potentially effective for

pinning will be defined as Γ. [The sum total length of effective site is then $\Gamma\rho$ per unit volume where $\rho(cm^{-2}.cm^{3})$ is the total length of edge disiocation per unit volume.] It is postulated that Γ will not depend on the elastic properties of the fluxon lattice. The underlying assumption in this postulate is that the Cottrell atmospheres, which are apparently too weak to promote much local shear in the lattice, can therefore promote even less local bending since C_{11} and C_{44} for the fluxon lattice are both very much larger than C_{66}. The fluxons are therefore unable to bend and accommodate significantly to bends and deviations, from the direction of $\underline{B}$, in the Cottrell atmos- atmospheres. The actual physical diameter of a Cottrell atmosphere site ($R_c \simeq 350\text{Å}$) is always less than or of the order of the coherence length $\xi(t)$ in the present investigation. $(\xi(T) = (\phi_o/2\pi H_{c2}(T))^{\frac{1}{2}}$ so that at $T = 4K$ $\xi(4) = (2.07.10^{-7}/2 \times 2.75.10^{3})^{\frac{1}{2}} \simeq 350\text{Å}$ and at $T = 8K$ $\xi(8) \simeq 740\text{Å}$). Since coherence effects will average the electronic properties of the site over a range $\xi(t)$ the effective diameter 2R for the Cottrell atmosphere will therefore be $\xi(t)$ and the pinning potential density for a particular value of $|\psi|^2$ in the site will be assumed to be uniform within this diameter and zero outside.

The bulk pinning force density due to the above sites may now be expressed conveniently in the form

$$P_v(b,t) = \Gamma\rho\left[p_m^{\ell}(b,t)\right]_{eff} \nu_1(b,t) \qquad 5.10$$

where $\left[p_m^{\ell}\right]_{eff}$ is the force per unit length of Cottrell atmosphere site and ν_1 is the product of the probability and efficiency for an effective pinning event at any instant.

Now it is reasonable to assume that Γ will not have a strong dependence on the fluxon lattice parameter and therefore the rapid increase

in $P_v(b)$, which occurs at $b \simeq 0.4$ in class II, must be associated with a concomitant increase in p_m^{ℓ} and/or ν_1. Such a large increase is compatible only with a synchronous pinning mechanism however. As discussed previously this mechanism is postulated in this case to depend on mobile fluxon lattice defects and the existance of potential wells. The value of b at which synchronization begins may be expected to depend on the depth of these potential wells, i.e. on the pinning site interaction energy. In class II however, this value of b is found to vary by only a relatively small amount while the interaction energy is made to vary over a very much larger range by specimen ageing (see figures 5.27 and 5.28). It must be concluded, therefore, if the above considerations are valid, that in the absence of the synchronous mechanism the basic interaction energy for the site would still be a rapidly increasing function of b in this regime*. This immediately excludes the elastic interactions as the predominant mechanism for the Cottrell atmospheres in class II and suggests the $\delta\kappa$ interaction which will now be shown to be a strongly increasing function of b in this regime.

Thus: the interaction energy due to the $\delta\kappa$ mechanism is proportional to $-\int \delta\kappa \left[|\psi|^2 - |\psi|^4\right] d^3r$ (equation 3.5). Now it is apparent, from consideration of figure 3.3a (for $b < 0.6$) and equations 3.7, 3.8 and 3.9 (for $b > 0.6$), that three distinct regimes of behaviour for the interaction energy of a Cottrell atmosphere site (diameter $\xi(t)$) which is not perfectly straight or parallel with $\underline{B}$ may be distinguished, viz:

---

* These considerations may explain the different slopes which were obtained for $\ln[(P_v(b, \text{time}))/P_v(b,0)]$ versus $(\text{time})^{2/3}$ in figure 5.29.

(i) For $b < 0.3$: where $\left[|\psi|^2 - |\psi|^4\right]$ is large only in a narrow annulus (width approximately ξ) around each fluxon. The magnitude of the maximum interaction energy over the length of interaction along the site is therefore small.

(ii) For $0.3 < b < 0.6$: where the width of this annular region and therefore the magnitude of the interaction energy increases rapidly with b.

(iii) For $b > 0.6$: where $\left[|\psi|^2 - |\psi|^4\right]$ may be approximated by a simple periodic function with minima at the fluxons and maxima in the middle of the fluxon triangular cells and with an amplitude which now decreases with b as (1-b).

Thus the $\delta\kappa$ mechanism, in the range $0.3 < b < 0.6$ apparently provides the rapidly increasing attractive interaction which is a requirement for a synchronous pinning mechanism of the type postulated here. For $b > 0.6$ the synchronous mode, having been established, may still proceed but will be weaker because the magnitude of the interaction is now a decreasing function of b. The pinning force density $P_v(b)$ is therefore also expected to increase rapidly for some b in the range $0.3 < b < 0.6$ and reach a maximum in the region of $b \simeq 0.6$. This prediction is in good agreement with experiment (see figure 5.27 or 5.28).

Finally if the synchronous mode does extend into the regime $b > 0.6$ an expression can be formulated for $P_v(b)$ in this regime since p_m^{ℓ} and ν, in equation 5.10 can now be determined with some confidence.

Thus the effective diameter of the Cottrell atmosphere site is $\xi(t)$ and it is reasonable to assume for the $\delta\kappa$ mechanism that the pinning potential density Ω (see appendix A1(h)) is uniform inside the site and decays to an insignificant value, within a range which is less than $a_o/2$, outside the site. The considerations of appendix A1(h) are

therefore applicable in the formulation of an expression for p_m. Thus for the Cottrell atmosphere site $2R/a_o = \xi(t)/a_o(t) \simeq \left[(b.B_{c2}/\phi_o)(\phi_o/2\pi B_{c2})\right]^{\frac{1}{2}} = b/(2\pi)^{\frac{1}{2}}$ which is independent of temperature. In the range $0.6 < b < 1$ $2R/a_o$ therefore varies between approximately 0.24 and 0.4. According to figure A1.5, the correction factor, for generalizing the expressions of chapter 3, for p_m^{ℓ}, which are strictly valid only for $R \to 0$, varies to good approximation as $(a_o/2R) = (a_o/\xi)$ in this regime and is given approximately by $0.2(a_o/\xi)$. The use of this correction factor and the relevant expression for p_m^{ℓ} from chapter 3 is valid only for a Cottrell atmosphere site which is perfectly straight and parallel to the fluxons however. In real specimens it is probably reasonable to assume that a pinning site is a segment of Cottrell atmosphere which is sufficiently straight to be able to pin a particular fluxon along almost the entire length of the site. Slight waviness in the site, along its length, will result in a reduction in the pinning force relative to that for a straight site of the same length. It is reasonable to assume that the force per unit length will be reduced by a factor of order $(\sigma/d)^2$ where σ_1 is the radius of a hypothetical cylinder over which the pinning effect of the Cottrell atmosphere of a particular site can be considered to be averaged in consequence of its waviness and $d = a_o/2$ is the range of the pinning force in this case (i.e. for $b > 0.6$ and a pinning potential density of the form given in appendix A1(h)). The lower limit on the value of σ is obviously $\xi(t)$ and the upper limit is expected to be of order $a_o(t)/2$ since the pinning force will obviously begin to decrease rapidly if σ exceeds this value. The average value $\langle\sigma\rangle$ for all the Cottrell atmosphere sites should therefore have the same temperature dependence as ξ and a_o, i.e. as $B_{c2}^{-\frac{1}{2}}(t)$, and a dependence on b which will be slower than $b^{-\frac{1}{2}}$ and may therefore be neglected. Thus

it is reasonably assumed that $\langle\sigma\rangle \propto \xi(t)$ and that the above reduction factor, averaged over all the Cottrell atmosphere sites, is of order $(2\xi/a_o)^2 \simeq (\frac{2}{\pi}).b \approx b$. The final expression for the effective pinning force for an average Cottrell atmosphere site is therefore given, neglecting all the factors of order unity, by

$$\left[p_m^{\ell}\right]_{eff} \langle L\rangle \approx p_m^{\ell}(a_o/\xi).b^{-1}.\langle L\rangle \approx p_m^{\ell}.b^{-3/2}.\langle L\rangle \qquad 5.11$$

where $\langle L\rangle$ is the average length of a site and is postulated to be a constant of the dislocation structure and to be independent of the dislocation density ρ at low densities (so that the sum total of $\langle L\rangle$ for all the effective Cottrell atmosphere is $\rho\Gamma$) and p_m^{ℓ} is the product of pinning force per unit length in the limit $R \to 0$ and the volume of the site per unit length.

The determination of the factor v_1, in equation 5.10 is relatively straightforward. Thus, for synchronous pinning, the probability of a pinning interaction is expected to be unity (see Campbell and Evetts 1972 or chapter 3), but is more likely to have some value $0 < \omega < 1$ in the present case because the fluxon lattice is not fluid but only somewhat plastic. Again it is postulated that ω will depend only on the average dislocation structure and not on ρ.

The efficiency of the average interaction is expected (see chapter 3) to be given by $\langle u_o\rangle/d = 2\langle u_o\rangle/a_o$, i.e. the average displacement f the pinned fluxon divided by the range of interaction. For synchronous pinning u_o is apparently independent of the basic pinning force p_m because of the requirement of independent fluxon pinning and therefore a fluid or plastic fluxon lattice. According to Campbell and Evetts (1972) $u_o \ll a_o$ and u_o may also be assumed to be independent of a_o in this case. The efficiency factor is therefore assumed to be

given by k/a_o where $k << a_o$ is a constant with dimensions of length. Collecting the factors in ν_1 together therefore gives

$$\nu_1 = k\omega/a_o \simeq k\omega(bB_{c2}/\phi_o)^{\frac{1}{2}} . \qquad 5.12$$

Thus finally, substituting from equation 5.11 and 5.12 into equation 5.10 gives, for $b > 0.6$ - class II;

$$P_v(b,t) \approx k\omega\Gamma p p_m^{\ell} b^{-1}(B_{c2}/\phi_o)^{\frac{1}{2}} \qquad 5.13$$

The expression to be used here for p_m^{ℓ} is given by equation 3.11 with V replaced by A, i.e. the physical cross sectional area of the site, thus:

$$p_m^{\ell}(b,t) \simeq (B_{c2}^2/8\pi\kappa_1^2(t))\left[\delta\kappa/\kappa\right]_{eff}.A.\left[\frac{d}{dr}(|\psi|^2 - |\psi|^4)\right]_{max} . \qquad 5.14$$

For the Cottrell atmosphere site: since $\xi > R_c$, the effective cross sectional area is $A = \pi\xi^2/4$ and from equation 4.17;

$$\left[\delta\kappa/\kappa\right]_{eff} \simeq 0.51C_1(R_c^2/\xi^2(t))/\kappa \qquad 5.15$$

Now since the total concentration C_T of the hydrogen in the specimens is very small (approximately 50ppm-atomic) it may be assumed that at low temperatures this hydrogen is entirely associated with the dislocations, i.e. within the Cottrell atmospheres and precipitated into the cores of the dislocation. If the fraction in the atmospheres is (1-f) then the concentration C_1 of the hydrogen in the atmospheres will be given by

$$C_1 = 4 \times 10^2\left[(1-f)C_T/\pi R_c^2\rho\right] \qquad 5.16$$

where ρ is the dislocation density or the total length of edge dislocation per unit volume as before. Substituting for C_1 from this expression into the above expression for $[\delta\kappa/\kappa]_{eff}$ gives

$$[\delta\kappa/\kappa]_{eff} \simeq 2.04 \times 10^2[(1-f)C_T/\pi\rho\xi^2(t)]/\kappa \qquad 5.17$$

Author Doyle T B
Name of thesis Fluxon pinning and Geometrial effects in A type 11 superconductor 1975

PUBLISHER:
University of the Witwatersrand, Johannesburg
©2013

LEGAL NOTICES:

Copyright Notice: All materials on the University of the Witwatersrand, Johannesburg Library website are protected by South African copyright law and may not be distributed, transmitted, displayed, or otherwise published in any format, without the prior written permission of the copyright owner.

Disclaimer and Terms of Use: Provided that you maintain all copyright and other notices contained therein, you may download material (one machine readable copy and one print copy per page) for your personal and/or educational non-commercial use only.

The University of the Witwatersrand, Johannesburg, is not responsible for any errors or omissions and excludes any and all liability for any errors in or omissions from the information on the Library website.